UNIVERSITÀ DI TRENTO
Department of Industrial Engineering
XXXVI cycle

Doctoral School in Materials, Mechatronics and Systems Engineering

Multifunctional bio-composites for forestry and agricultural applications

Alessandro Sorze

January 2025

Multifunctional bio-composites for forestry and agricultural applications

Alessandro Sorze
e-mail: alessandro.sorze@unitn.it

Approved by:

Prof. Andrea Dorigato, Advisor
Dept. of Industrial Engineering
University of Trento, Italy

PhD. Commission:

Prof. Essi Sarlin
Faculty of Engineering and Natural Sciences
Tampere University, Finland

Prof. Francesco Mollica
Dept. of Engineering
University of Ferrara, Italy

Prof. Luca Fambri
Dept. of Industrial Engineering
University of Trento, Italy

University of Trento,

Department of Industrial Engineering

Date 15th January 2025

This project has received funding from the European Union's Horizon 2020 research and innovation programme under grant agreement No 101000406 – ONEforest: A Multi-Criteria Decision Support System For A Common Forest Management to Strengthen Forest Resilience, Harmonise Stakeholder Interests and Ensure Sustainable Wood Flows.

University of Trento – Department of Industrial Engineering
Doctoral Thesis
Alessandro Sorze – 2025

Cover image: Image of a topsoil cover based on xanthan gum and wood fibers (left) and an image of soil conditioner constituted of xanthan gum and cellulose fibers (right).

Abstract

In recent years, climate change has severely impacted forest ecosystems, leading to violent storms, wildfires, soil erosion, and increased insect and fungi infestations, clearing large forest areas. Restocking and restoring these forests is a challenge, particularly with the decrease in rainfall across Europe. Southern Europe faces at high risk of desertification due to over-exploitation of land and water, urban sprawl, tourism and unplanned industrialisation. To address these problems, it is necessary to develop technological solutions to support planting and forestry operations, even on degraded land.

On the basis of these considerations, this research developed innovative and sustainable solutions for supporting plant growth and revitalizing degraded forests within the scope of the H2020 European project ONEforest. Laboratory and field studies were conducted to design novel multifunctional topsoil covers (TSCs) and soil conditioners (SCs). TSCs are mulching films that regulate soil moisture and protect plants from weeds, while SCs enhance soil chemical, physical, and water regulation properties by being mixed into the planting hole. Both products were produced as wood-reinforced composite materials using xanthan gum, a bio-based polysaccharide, as matrix.

For the development of TSCs, various compositions of hydrogels based on xanthan gum reinforced with cellulose or wood fibers, and cross-linked with different agents, were tested. Hydrogels, especially those cross-linked with citric acid, showed excellent water absorption, retention, and stability. These hydrogels also demonstrated good water vapor permeability, weed growth inhibition, non-flammability and biodegradability.

For the development of SCs, several compositions of xanthan gum mixed with different types of cellulose fillers were tested to improve water absorption and retention properties of the soil. These SCs significantly enhanced soil-water holding capacity and delayed water loss, outperforming commercial alternatives. However, in saturated

conditions, high doses of SCs could negatively impact soil geotechnical properties. The local use of SCs in small quantities in planting holes could minimize these impacts.
Field experiments were performed to assess the effects of TSCs and SCs on tree growth under various climates. TSCs maintained excellent plant health but did not significantly enhance plant growth. In contrast, SCs improved plant growth, health, and reduced mortality rates.
Life Cycle Analysis (LCA) was conducted to identify the environmental impacts of the developed products. Furthermore, a cost estimate suggested that the current price for the production of TSC and SC was comparable to that of commercial products.

Considering the ease of the manufacturing process, the interesting outcomes of laboratory activity and the results obtained from practical experiments, these products have the potential to be upscaled to an industrial level and to be widely applied in forestry and agricultural applications.

Contents

List of Figures

List of Tables

List of Acronyms

BPST	Biopolymer-based soil treatment
CA	Citric acid
CSRs	Case Studies Regions
CTFC	Forest Science and Technology Centre of Catalonia
DSC	Differential scanning calorimetry
DTG	Derivative of thermogravimetric analysis
FT-IR	Fourier transformed infrared spectroscopy
FWVC	Forest-Wood Value Chain
HFM	Heat flux meter
LCA	Life cycle analysis
LCI	Life cycle inventory
LCIA	Life cycle impact assessment
LOI	Limit oxygen index
MWHC	Maximum water holding capacity
PAM	Polyacrylamides
PCM	Phase change material
PF	Phenolic resin
PP	Polypropylene
PU	Polyurethane
SEM	Scanning electron microscope
SC	Soil conditioner
STMP	Sodium trimetaphosphate
SWRC	Soil water retention curve
TA	Tannic acid
TGA	Thermogravimetric analysis
THRO	University of Applied Sciences of Rosenheim
TSC	Topsoil cover
UFR	University of Freiburg
ULJ	University of Ljubljana
UNITN	University of Trento
WF	Wood fibers

WHC	Water holding capacity
WL	Water loss
WVP	Water vapor permeability
WVP2	Water vapor permeance
WU	Water uptake
XG	Xanthan gum

List of Symbols

ρ_{app}	Apparent density	g/cm^3
A_L	Area loss	%
ρ_{bulk}	Bulk density	g/cm^3
P_{closed}	Closed porosity	%
c'	Cohesion	kPa
E_c	Compression modulus	MPa
σ_c	Compression stress	MPa
σ_v'	Effective vertical stress	kPa
E	Elastic modulus	MPa
E_f	Flexural modulus	MPa
σ_f	Flexural stress	MPa
φ'	Friction angle	°
ρ_{geom}	Geometrical density	g/cm^3
T_g	Glass transition temperature	°C
k	Hydraulic conductivity	m/s
LOI	Limit oxygen index	%
w_L	Liquid limit	%
T_{max}	Max degradation temperature (from DTG)	°C
T_m	Melting temperature	°C
M_i	Mass of samples during drying	g
M_{wet}	Mass of fully wet samples	g
M_w	Molecular weight	g/mol
P_{open}	Open porosity	%
wt%	Percentage by weight	%
m_{700}	Residual mass (from TGA)	%
$\dot{\gamma}$	Shear rate	1/s

σ	Shear stress	Pa
η	Shear viscosity	Pa·s
ρ_{th}	Theoretical density	g/cm^3
λ	Thermal conductivity	W/m·K
$w_{A\ 24\ h}$	Water absorption after 24 h	%
$w_{A\ MAX}$	Maximum water absorption	%
WHC	Water holding capacity	%
WVP	Water vapor permeability	g/(m·s·Pa)
WVP2	Water vapor permeance	g/(m^2·s·Pa)
σ_y	Yield stress	Pa

1 Introduction

1.1 ONEforest project: aim and scope

ONEforest is a European project funded by the European Union Horizon 2020 research and innovation programme, under Grant Agreement nº 101000406 with the name: A Multi-Criteria Decision Support System for a Common Forest Management to Strengthen Forest Resilience, Harmonise Stakeholder Interests and Ensure Sustainable Wood Flows. The general aim of the project is to ensure the sustainability of forest production systems under changing climate conditions and further develop and deploy technological advancements of environmental and micro/macroclimate-friendly wood-based value chains on the ground. In particular, as reported in Figure 1.1, four Case Studies Regions (CSRs) are established following Europe's biogeographical regions (Boreal, Alpine, Mediterranean and Continental), to study climate resilient silvicultural management practices and new methods of seeding and planting by the application of an own engineered topsoil cover based on wood fibers. Corresponding forest operations and concepts of actions in case of disturbances are developed under selected sustainability criteria. Stakeholders are activated in the participative process of socio-economic studies. Information are consolidated in Dynamic Value Chain Model to assess the impact of the Forest-Wood Value Chain (FWVC) on regional development quantified by a set of economic, environmental and social indicators. A new Multi-Criteria Decision Support System is developed, which visualizes decision-making by comparing Sustainable Forest Management, synergies and trade-offs of Forest Ecosystems, reliable wood supply, and stakeholder interests through FWVC indicators of social, economic, and environmental dimensions, by applying methods of Goal Programming. The easy-to-use software application will be available for Forest-Wood Value Chain stakeholders globally. All ONEforest results will be

implemented in new Model Forests, being part of the international Model Forest Network for regional adapted forest management concept.

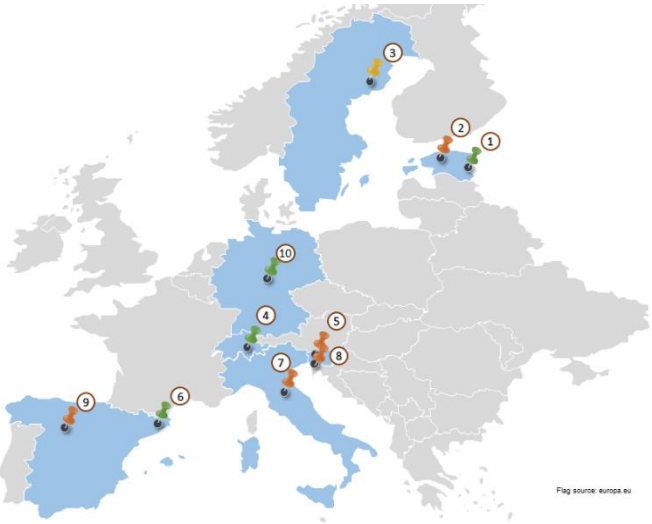

Figure 1.1 Locations of the four ONEforest CSRs (green pins), five supporting experimental sites (orange pins) across four biogeographical regions (source: europa.eu).

1.2 Motivation and objectives of the thesis

University of Trento was involved in the ONEforest project as part of the Work Package 5 (WP5), which accounted for the perspectives of forest operations and revitalization of degraded forests. Specifically, this Doctoral Thesis is presented to address Tasks 5.3 and 5.4 of the project, i.e., to conduct laboratory and field studies on selected test sites for the development and engineering of topsoil covers (TSCs) and soil conditioners (SCs). Both products aimed to support planting operations in Alpine, Mediterranean and Continental areas with high erosion risk and in regions subjected to temporary drought. The lab work was oriented to assess physical, mechanical and chemical

properties as well as the degradability of the produced TSC and SC compositions. The influence of the TSCs and SCs on the near-surface soil characteristics (e.g., permeability, evaporation and transpiration, erosion tendency, water storage capacity, microbiological activities) and their application methods have been also investigated in collaboration with the other project partners. Finally, a Life cycle Assessment (LCA) study on the developed TSCs and SCs was performed to assess their environmental impacts.

1.3 Thesis outline

This Doctoral Thesis is divided into ten Chapters:

- *Chapter 2* presents a detailed literature review on climate change related challenges and possible strategies to mitigate them, focusing on the advantages and disadvantages of the use of topsoil covers and soil conditioners.
- *Chapter 3* describes the materials and the experimental techniques used to prepare and characterize the samples.
- *Chapter 4*, *Chapter 5* and *Chapter 6* report the results of the main topics of the research activity, i.e., the "Development of TSCs", the "Development of SCs" and "Planting trials" performed within the ONEforest project, respectively.
- *Chapter 7* contains the evaluation of the environmental impact and cost for the production of the novel materials developed within the project.
- *Chapter 8* contains concluding remarks and the main recommendations for future research on this topic.
- *Chapter 9* reports the results of two side activities carried out during the PhD work.
- *Chapter 10* lists the scientific bibliography.
- Finally, a list of *publications*, *awards*, participation to *congresses* and *summer school*, a description of the *visiting period* spent abroad and of the *teaching activities* carried out during the Doctoral Program is presented.

2 Scientific Background

2.1 Climate change and related challenges

Climate change represents one of the most critical challenges of this century because of its broad, complex and often deeply intertwined consequences on the environment, the global economy and societies. For example, from a societal perspective, Massanza et al. reported in their review how climate change is related to an increased risk of mortality, suicide, suicidal tendencies, or psychiatric morbidity [1]. Furthermore, extreme weather events, that occurred between the years 2000 and 2020 are estimated to have caused millions of deaths and economic damages on the order of billions, if not trillions, of dollars worldwide [2]. Estimates of these deaths and damages are shown in Table 2.1.

Table 2.1 Direct health and economic impacts of different disasters calculated globally between 2000 and 2020 [2].

Extreme event	Deaths	Total Damage (USD)	Influence of climate on severity
Heatwaves	157’000	13.4 bn	Increase
Cold waves	14’900	31.3 bn	Decrease
Floods	111’000	610.0 bn	Increase
Droughts	21’300	119.0 bn	Increase
Wildfires	1570	94.3 bn	Increase
Storms	201’000	1.3 trillion	Increase

Extreme weather events are the first examples of the environmental impacts of climate change and global warming. They occur on an

almost immediate time scale rather than over a long period of time and their importance lies in the speed with which they occur. The extent of these effects varies widely among different parts of the world, as can be seen in Figure 2.1(a-c). However, it is difficult to attribute the occurrence of all extreme events directly to human activity, as measurements and documentations of these phenomena are not standardized. Moreover, representing a picture is made even more challenging by the scarcity of data in certain areas of the world (Figure 2.1(b,c)).

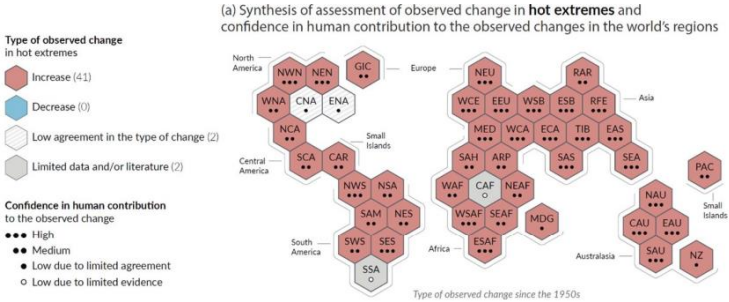

(a)

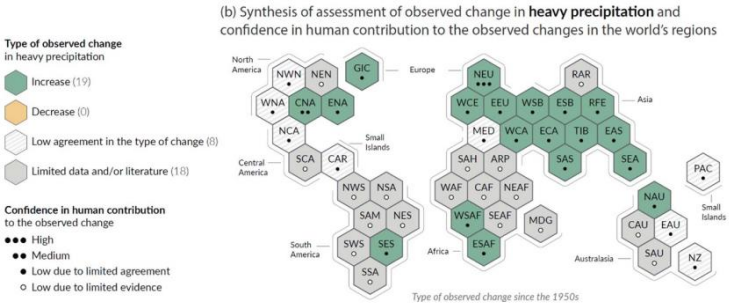

(b)

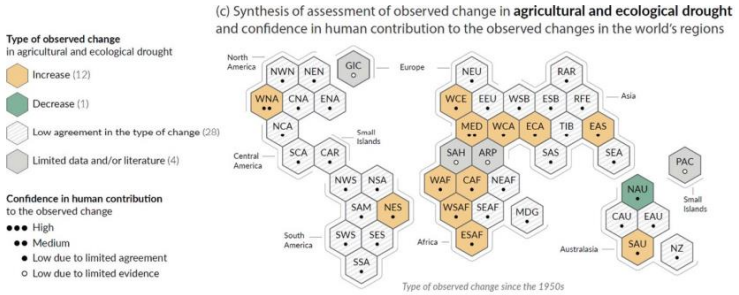

(c)

Figure 2.1 Schematic maps of occurrence of heatwaves (a) floods (b) and droughts (c) and confidence in human contribution as reported by Clarke et al. [2]. Changes observed since 1950.

It can be clearly stated how the occurrence of heatwaves is clearly correlated to global warming and human activity. The severity of these phenomena is increasing almost uniformly everywhere (Figure 2.1a). As noted in the 2021 Intergovernmental Panel on Climate Change (IPCC) report, heatwaves that would have occurred with a probability of 1/10 with the pre-industrial climate will occur almost three times more frequently, with an average temperature increase of 1.2 °C. Those that had a 1/50 probability of occurrence will occur 5 times more frequently with the same average temperature rise [3].
Flood events, on the other hand, are much more difficult to correlate to human activity, and their appearance and intensity varies by region and time of year (Figure 2.1b). For example, in Northern Europe these events will be much more pronounced during the winter season and will decrease in summer. Despite the difficulties in correlating them to human activity, floods are undoubtedly related to global warming, as an increase in global average temperature of 1 °C is associated with an 18% increase in the frequency of this phenomenon [4].
Other extreme events such as wildfires, droughts, land degradation and consequent loss or alteration of forests and vegetation-rich areas as a result of climate change are expected. These will be much more

accentuated in the Mediterranean basin, as temperatures in this region are projected to rise 20% higher than the global average (especially in summer and in its northern part). Moreover, precipitations are expected to decrease to a maximum of -7%/K [5], resulting in a decrease in soil water content, river runoff and water availability of lakes and reservoirs [6]. These phenomena are deeply intertwined with each other and will be treated more in detail in the following subsections. Furthermore, for the reason just explained, analysis of the problematic will be mainly focused on the Mediterranean basin.

2.1.1 Climate change and wildfires

Although wildfires are natural occurring phenomena, the increase in frequency and intensity with which they occur is clearly related them to climate change. As can be seen from Figure 2.2, the number of reported fires increased between the year 1970 and 2000 [7] and in recent times the trend has not changed.

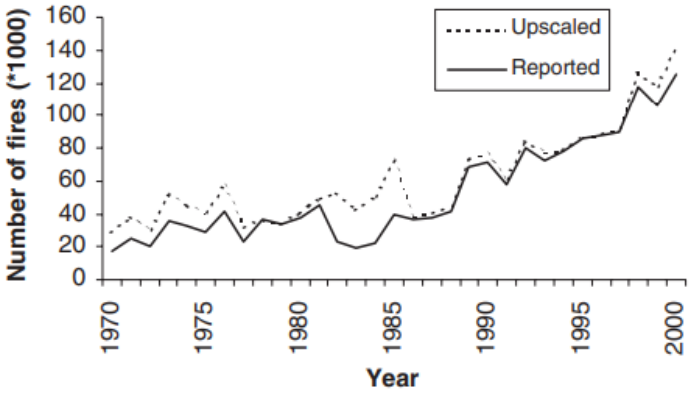

Figure 2.2 Number of wildfires in Europe from 1970 to 2000 as reported by Schelhaas et al. [7].

With the change in precipitation patterns due to global warming and hotter and drier summers, soil moisture is likely to evaporate more

rapidly, leading to drier vegetation and an increase in the amount of available flammable material. In addition, the increase in the number of heatwaves provides an increasing number of ignition sources and thus more favorable conditions for forest fires to occur [8]. Furthermore, the increase in surface wind speed recorded since 2010 aggravates the phenomenon by increasing its intensity and spreading [8]. The situation is then exacerbated in some areas such as Spain, Portugal, Southern Italy, and other parts of the Mediterranean Basin by sociological factors such as land abandonment and arson. In these regions, the abandonment of rural areas formerly devoted to agriculture or grazing is associated with unmanaged re-naturalization by flammable shrubs and bushes and with an increase in the critical land-urban interface, which is more prone to burning [9-11].

Although not a natural cause of forest fires, arson must be included among the sociological causes of the problem because of the scale of the phenomenon: voluntary fires are reported to be the cause of 59% of wildfires in Southern Italy between 1997 and 2007, with the most frequent motivation being finding employment in the seasonal fire-fighting force [12].

Fires are reported to affect 0.3% of the Mediterranean basin's forests each year and are estimated to have affected an area of 230'000 hectares each year in the period between 1960 and 2010 [7]. In recent years, the situation has worsened worldwide: it is calculated that more than 3.9 million hectares were burned in the Unites States and in Canada between 1960 and 2017 and the total cost of fighting these events exceeded 2 billion USD, although the real cost (including prevention measures, property damage, human life losses and other factors) is estimated to be 2 to 30 times higher [13]. By far the worst situation reported in literature is represented by the catastrophic wildfires occurred in Australia in Summer 2020, known as "Black Summer." These are reported to have damaged 18 million hectares of land and 3113 dwellings and to have killed 429 people and 3 billion animals, with a total economic damage of 110 billion USD [14]. The damage caused by wildfires is not only problematic in the short term,

but can also have effects on a longer time scale. For instance, wildfires are linked to increase soil erosion because, depending on their intensity and duration, they cause partial or complete burning of the soil organic matter, alter its morphology and structure (change porosity, increase bulk density and reduce aggregate stability). Moreover, they are associated with nutrient depletion and increased stormwater flow and water repellency [11]. Fires are linked to the loss of tree regeneration and forest resilience, with a potential displacement of wildlands from resilient forest, such as those composed of conifers, to shrub or grassland ecosystems. Stevens-Rumann et al. [15], indeed, reported how tree regeneration after wildfires in the 21st century was lower than that observed before the year 2000 due to warmer and drier conditions, which are correlated with higher post-fire water stress and lower seedling survival rate, and thus lead to an increase in forest vulnerability, especially in already dry environments.

2.1.2 Droughts, desertification and soil degradation

Desertification can be defined as the process that leads to the loss of the chemical, physical and biological capacity of the soil, gradually transforming a previously fertile area into a desert zone [16]. It is a complex phenomenon caused by many concomitant effects, such as soil degradation and droughts, which are observed to happen to a different extent in different areas of the world (Figure 2.1c) [17-20].
As previously stated, wildfires and post-wildfire soil degradation are one of the causes, but not the only one. In fact, one of the main factors related to soil degradation and subsequent desertification is the change in annual rainfall patterns and, thus, the decrease in water availability in a region. Rainfall patterns are closely linked to the location of desert boundaries [17]. Changes in the rainfall distribution and any related droughts could be connected to various factors; for example, droughts in the Sahel region that occurred during the 20th century were linked to the warming trends of the Pacific and Indian Oceans [19]. Deforestation and loss of vegetation were also linked to

the increase of desert zones, as their disappearance could increase the albedo of an area. This is associated to net radiative losses relative to the surrounding environment and, therefore, to the self-sustaining mechanism that fuels deserts. The higher radiative losses are balanced by descent of air which compresses adiabatically, and as compression decreases the relative humidity, it increases the dryness of the desert area [18]. Loss of vegetation is also associated with increased wind erosion of the land surface, which further favors the expansion of desert areas [21]. In addition, droughts negatively affect leaf transpiration and photosynthetic capacity of plants, leading to a reduction in plant growth rates (similar to what was described for wildfires) and to carbon losses from forests [22]. Furthermore, human-related causes such as overgrazing, intensive agriculture and land abandonment are related to soil erosion and desertification [17,20,23]. Overgrazing and excessive soil exploitation are, in fact, linked to the reduction of vegetation cover and to the consequent loss in plant variety and supply of dead organic matter to the soil, while trampling by large number of animals is associated to the disruption of the soil surface and to the reduction of its porosity [24]. Intensive agriculture, on the other hand, is associated with depletion of soil resources due to exploitation of deep water drainage, inefficient irrigation, pesticides use and, obviously, deforestation [20]. In addition, the deterioration of traditional agricultural systems is associated with an aggravation of land degradation as these practices played a role in ecosystem management and regeneration, especially in the Mediterranean region [20].

Desertification and land degradation become an obvious problem not only from the environmental point of view, as they are linked to the loss of biodiversity, but also from a social point of view, considering that drylands occupy more than 40% of the total land surface, are inhabited by more than 2 billion people and support about 50% of the world's livestock [21]. An increase in temperatures due to climate change will have a drastic impact on these areas. For example, an increase in temperatures between 1.5 and 3 °C in southern Australia

is expected to lead to an increase in the rate of soil evaporation between 2% and 8%, with strong detrimental effects on the agricultural sector and its associated economy [23]. Similar negative effects are expected around the Mediterranean Sea, especially in southern Europe, where livestock farming is associated with the production of value-added products such as cheese and meat [23]. The effects of land degradation and droughts on the agriculture also threaten the wheat (*Triticum aestivum*) production, which currently provides for 21% of food calories and 20% of proteins for 4.5 billion people worldwide [25]. Demand for this grain is expected to increase by 60% by 2050, but its production is being reduced by 29% due to this and other stresses [26]. For the same reasons, in certain areas of the world, cereal production is expected to decline by 45% if proper countermeasures are not taken [27]. Land degradation and desertification, as reported by Rodrigo-Comino et al. [20], are also linked in a vicious cycle to poverty in Mediterranean Europe. Land degradation encourages the abandonment of agricultural fields and shift of the population toward the cities causing, as previously stated, further soil deterioration. Less productive terrains receive less funding, causing further impoverishment of the population and land abandonment.

2.1.3 Effects of climate change on forests

Climate change is affecting forests and vegetation in several ways in addition to those previously listed. The type and effect of disturbances depend on the region affected and the type of forests in it. Figure 2.3 shows the types of forests on the European continent and their extent [28].

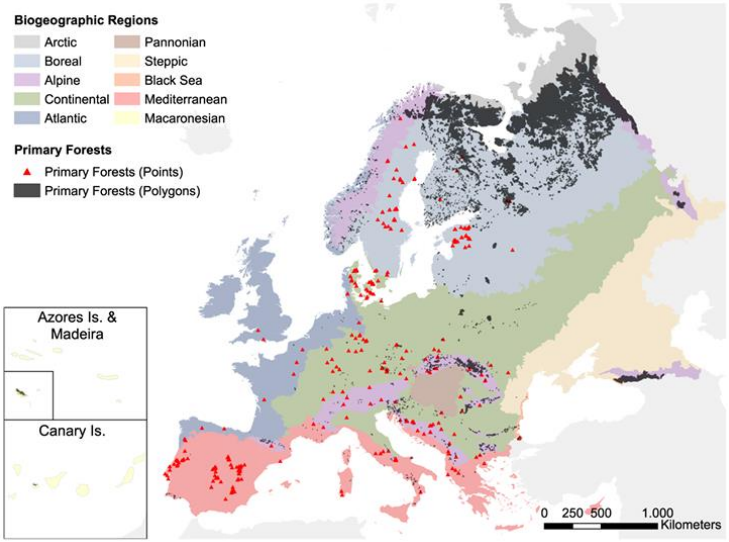

Figure 2.3 Types of forest in the European continent [28].

According to Figure 2.3, the most extensive forests on the continent are three. The first is the boreal forest, characterized mainly by conifers such as spruce (*Picea abies*), fir (Abies alba) and pine (*Pinus silvestris*) and a few broadleaf species such as poplar (*Populus tremuloides*) and birch (*Betula pendulax*). The second is the continental forest, characterized by spruces, beeches (*Fagus sylvatica*), oaks (*Quercus robur*) and other species. Finally, the Mediterranean forest characterized by perennial broadleaf trees, shrubs and bushes.

The various possible disturbances to forest ecosystems in Europe from 1850 to the year 2000 are estimated to have affected 35 million m^3 of wood [7] and many sources report how these ecosystems were drastically altered. For example, a decrease in the productivity and growth rate of *Fagus sylvatica* was observed in Europe due to increasing temperatures and decreasing annual precipitation, a phenomenon accentuated in the southern part of the continent [29]. Forecasts and models developed based on this behaviour predict,

depending on the area, a further decline ranging from -20% to -50% by 2090 [29]. Similarly, a 50% decrease in growth rate was observed in plants exposed to the 2003 heatwave. In particular, this phenomenon was observed to be much more pronounced in low-altitude broadleaf forests located in northern and central Italy [30]. The composition of Alpine Forest in Europe was also reported to be changing due to rising global temperatures [22,31]. Albrich et al. calculated that with a 2 °C increase in the temperature of alpine forest a tipping point will be reached: landscapes dominated by conifers will shift to those dominated by smaller broadleaf trees, even at higher altitudes [31]. The same study pointed out that this effect is highly dependent on the morphology of the terrain and the region to which it is applied (morphology can shift the tipping point from +2 °C to +3 °C), and, in addition, with an increase in temperatures of 6 °C, more than 2% of the current total forest area is expected to be lost.

How climate change will affect vegetation in different areas will depend strongly on the region. For example, in the Alps, where the effects are predicted to be twice as great as the global average, due to rising temperatures and retreating glaciers, there is an increase in thermophilic species and an upward migration of shrubs and trees at the expense of mosses and bogs. In the Mediterranean climate zone, on the other hand, rising temperatures are associated with a net loss of vegetation, with a drastic reduction in growth rates of shrubs and trees and a decrease in photosynthetic activity and leaf transpiration [22]. Storms, beetle outbreaks, and plant diseases are other phenomena that endanger forests and are likely to worsen [2,32,33]. Storm damage can take many years to repair. This was the case with the damage caused by storms "Vivian," "Weibke," and "Lothar," which occurred in the 1990s and affected more than 250 million m^3 of forests in the Bavarian region, with most of the affected trees being spruce (*Picea abies*). In the affected areas, birch forests replaced pioneer forests after 15 years [32]. On October 29th 2019, storm "Vaia" hit the northeastern regions of Italy. The storm affected 42’500 hectares of land in Trentino Alto Adige, Veneto, and Friuli Venezia Giulia. Its

strong sirocco winds, which reached speeds of 200 km/h, caused the loss of 8.5 million m^3 of woody biomass through breakage and uprooting [34]. Damages to the forest are shown in Figure 2.4 and are still being recovered to this day.

Figure 2.4 Damages from "Vaia" tempest near Carezza lake (Bolzano, Italy) in 2019 (image taken from SAPR of Bolzano Province).

Beetle outbreaks are projected to increase frequency as climate change is correlated with earlier swarming periods, increased reproduction, survival rates and voltinism (i.e., the number of broods or generations of an organism recorded in a year) [33]. Furthermore, increased temperatures are associated to more successful colonization of trees, which generally leads to plant death as hundreds of beetles attack the plant simultaneously and often infect it with phytopathogenic fungi that they need to metabolize wood [35]. There is evidence that these effects are strongly influenced by the morphology and altitude of the affected area [33]. In recent years, the damage caused by infestations reached unprecedented levels, as observable from Figure 2.5.

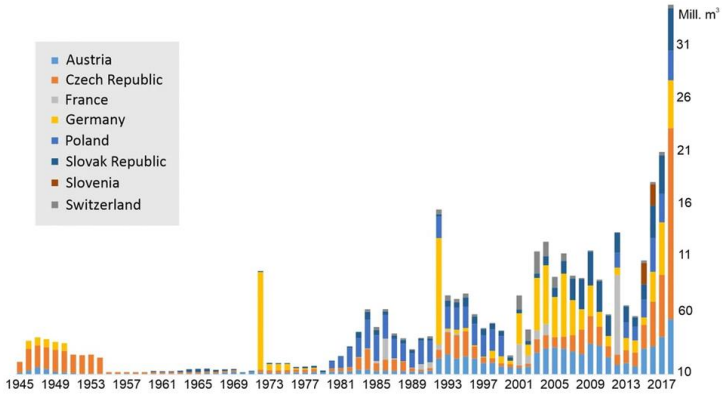

Figure 2.5 Volumetric damages induced by European spruce bark beetle (*Ips typographus*) from 1945 to 2017 [35].

Among the various species of beetles that infest trees, the spruce bark beetle (*Ips typographus*) is considered one of the most important, as it colonizes the most common tree in European forests (*Picea abies*) and has been associated with 8% of tree mortality between 1850 and 2000, with similar effects also recorded in the United States and Canada [35]. *Picea abies* is also one of the most economically important trees because of its use in pulp production and its use as a building material [36]. The total stock of this wood in Europe is estimated at 27.4 billion m^3 and is growing, but it is estimated that a quarter of this is exposed to damage from the colonization of *Ips typographus* [35]. Between 2004 and 2007 it is estimated that this beetle caused damages to 62'600 m^3 of wood in Trentino and to 18'795 m^3 in Friuli Venezia Giulia. Moreover, as a consequence of the "Vaia" storm, infestations are increasing [37,38].

The second most relevant beetle is considered the mountain pine beetle (*Dendroctonus ponderosae*), a native species of North America pine forests whose periodic outbreaks are associated with large-scale tree mortality with devastating effects on the environment. Between 2000 and 2020 outbreaks of *Dendroctonus ponderosae,* in British

Columbia (Canada), impacted 347'000 m^2 of forests and caused emissions from the decay of killed trees amounting to 270 Mt CO_2, thus transforming the forest from a net carbon sink to a large net carbon source [39]. Furthermore, the effects of these outbreaks have a short-term negative impact on the timber market and tourism [35].
Finally, another danger to forest ecosystems is represented by pathogens such as *Xylella fastidiosa* (Xf), which is considered one of the most dangerous plant pathogens in the world [40,41] as it causes a rapid decay syndrome in the infested plant and no effective curative therapy is yet available [42]. Between 2013 and 2019, Xf is estimated to have caused the Olive Quick Decay Syndrome in nearly 54'000 orchards in the Puglia region (Italy), reducing Italian oil production by 10% and causing estimated economic damage of 390 million euros in the short-term period [43]. Xf is also estimated to have decreased the flow of ecosystem services by 34% and general biodiversity by 28% [41]. The severity of the epidemic that affected this region was linked to both antropogenic factors [43] and rising temperatures and water scarcity, as disease spreads more if plants are subjected to water stress [42].

2.2 Climate change mitigation strategies

2.2.1 Forest management measures

Because of the deep intertwining of many of the above issues, the first important solution is a structural change in wilderness and forest management policies to account for the effects of global climate change. Indeed, many authors have stressed the need for policy changes and how plans can be used effectively to counter problems such as wildfires and beetle outbreaks [9,35,44-46]. For example, Fettig et al. [44] identified stand density, basal area, tree diameter, host density and tree growth rate (slower-growing trees are more affected) as primary attributes for beetle infestations and defined how carefully planned and defined how carefully planned and managed thinning can be seen as an effective outbreak prevention measure.

Furthermore, the authors stated that sunlight exposure of cut logs and removal of residual chips are associated with further reduction of beetle attacks [44]. Clearcutting, the practice of creating a mosaic of species and age of trees in a particular forest area, was also suggested by other authors as an effective way to reduce the impact of beetle damage. This practice improves stand density, growth and yield of the landscape where it is applied, thereby reducing the overall tree mortality and improving the resiliency to attacks [47].

In the broadest possible sense, forest management is defined as the set of forestry, decision-making and business practices designed to achieve a landowner's objectives by defining actions and goals based on past and present data and practical experience [48]. Currently forest management plans are based on centralized "command and control" directives which are based on long-term application protocols [35,45]. However, their effectiveness is questioned due to either: oversimplification of the problem and search for a "one-size-fits-all" solution [35], the lack of time horizons in which the policies have to be applied [45,48], the difficulty of applying centralized directives to a local context [45,49,50], or the inadequacy to the modern demands and visions on sustainability. So far, forests were managed mostly in the optic of economical revenue, whereas today there are demands to reconcile this with biodiversity conservation efforts [46,48].

It is undeniable that forest management requires long-term planning and strategic thinking, but a time frame of 20 to 30 years (required for tree maturity) is often considered too distant as time horizon to make meaningful and challenging decisions [45]. Moreover, the further the time horizon is pushed, the more difficult decision making is made by the increasing level of uncertainty in the system (important parameters remain known, but probability distributions become less and less) and the risks of failure due to different or unexpected outcomes [48]. In practice, a 15 years horizon seems the furthest that foresters can identify with. Therefore, it is suggested that decision makers set long-term goals rather than structured protocols [45] and compensate them with shorter-term plans, which not only decrease

uncertainty and risk in management but also allow for more flexible and adaptive planning [48].

The implementation of adaptive measures can only be achieved by including local (regional or national) stakeholders and forest owners in the planning of forestry policies, as highlighted by Bouriaud et al. [50]. Although institutionalized structures, rules, and legally enforced standards are undoubtedly necessary, regional stakeholders, local forest managers, and communities are what ultimately enable the implementation of adaptive policies, as not only does political decision-making slow down the implementation of such measures (especially when it comes to climate change), but also centralized directives may clash with local forest management. The study, therefore, suggested the development of centralized plans that take into account local stakeholders, their training, and define the boundaries within which managers can act to adapt to local conditions. Furthermore, it was highlighted how external stakeholders could take advantage of the situation and use their status to push their own policies [50].

Finally, the requirements for multi-functional management approaches that enable both economic exploitation and sustainability of forests are often not met, despite the claims of managers. This is due to the difficulty of assessing the parameters that define sustainable development, since these have always changed over time depending on the goals and strategies adopted and the principles and values on which they are based [46,48].

2.2.2 Wildfire prevention measures

Proper forestry practices can also help reduce the occurrence or the consequences of wildfires by addressing the problem proactively rather than reactively. A first example of these practices is the creation of green fire barriers (or green fuel breaks) within the forest. This technique involves the strategic planting of dense bands, 20 to 35 meters wide, of evergreen broadleaf trees belonging to naturally fire-resistant species [51,52]. It is widely used in China, where green

firebreaks occupy 2.08 million km², or 26.6% of the country's land area [52]. The working principle of green firebreaks is shown in Figure 2.6.

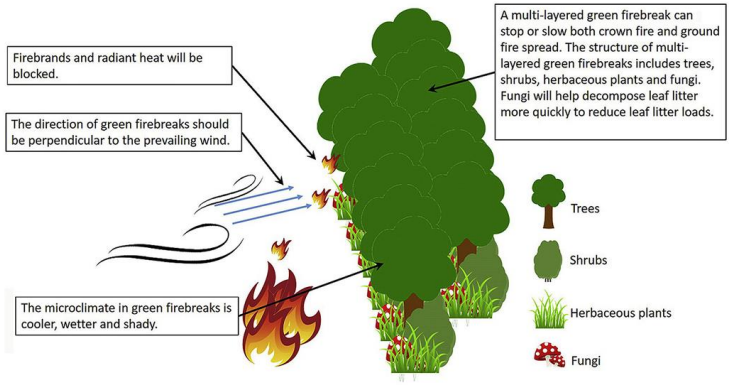

Figure 2.6 Working principle of green fuel breaks [52].

This type of planting raises the canopy level up to 30 m in height and creates a wetter and cooler microclimate with less fuel on the ground due to the canopy cover, thus hindering the spread of fires. Furthermore, this technique can be implemented in any territory with relative low costs and immediate effect [51]. As observable in Figure 2.6, for this measure to be effective, barriers must be placed perpendicular to the main wind direction in order to block it, as the wind could spread wildfires. Multilayered green fire barriers consisting of a combination of shrubs and trees are even more effective as the denser cover positively increases the microclimate [52]. Another traditional way to prevent wildfire risk is through the use of prescribed fire (or thin burning). Although it is controversial because of the obvious risks associated with it, when carried out in an appropriate environment and according to legislation and regulatory protocols [9], it does not affect soil erosion nor water run-off [53]. The long-term positive effects far outweigh the short-term negative ones, as prescribed fire is associated with increased water absorption

capacity in the soil, increased forage quality, and improved microbial activity in the soil [54]. This practice is particularly used in the Mediterranean region and, due to these positive effects, it was also used more frequently in North-American forests where it was proven to be an effective countermeasure to prevent beetle infestations [47,55].

2.2.3 Drought and desertification prevention measures

2.2.3.1 Drought resistant crop development

Although not a preventive measure, crop adaptation and the engineering of drought-tolerant crops could be a necessary response to climate change, especially with regard to the production of cereals such as rice and wheat, given their importance to the world's population (Subsection 2.1.2). Yan et al. [27] identified how the study of plant phenology and the identification of traits that are best adapted to projected climate scenarios can have beneficial effects and mitigate potential losses. Specifically, they stated that for regions where waterlogging stress is expected, selecting traits that lead to earlier flowering, larger grain size, and better radiation use efficiency by the crop, can reduce the effects of environmental stress by 15% when combined with improved crop management. For rice cultivated in rainfed lowlands, selection of traits that increase root length, increase root thickness and allow high leaf water potential to be maintained, was highlighted as a way to increase crop survival under drought conditions [56].

As grasslands cover 70% of the world's agricultural area and provide forage for grazing animals in both developed and underdeveloped countries, efforts are being made to select for traits that may contribute to resistance to dry environments. Norton et al. [23], identified how, to ensure the sustainability of perennial forage crops, the following traits are necessary and therefore breeding efforts should be directed toward their selection: a deeper and denser root system in order to enhance plant's "drought escape mechanism" and

delaying dehydration; earlier and enhanced seed production; disruption of the tradeoff between plant summer dormancy (the series of endogenously controlled processes that cause cessation of leaf growth and partial senescence of grasses) and yield productivity [23]. Although promising, selective breeding and genetic engineering of crops and forages are not always a viable option they may, for example, clash with legislation. Therefore, reforestation is a preferable alternative to address the risk of desertification.

2.2.3.2 Afforestation efforts

To achieve the ambitious goal set by the United Nations Convention on Climate Change (UNFCCC) of limiting temperature rise to +2 °C by the end of the century, it will be necessary to rapidly reduce greenhouse gases and remove CO_2 from the atmosphere. This will require both afforestation efforts and bioenergy coupled with carbon capture and storage (CCS), as these land-based mitigation strategies can address carbon emissions from agriculture and forestry, which, as mentioned above, account for 24 percent of total emissions [57-59]. Bioenergy and CCS are an attractive mitigation strategy as they allow CO_2 from biomass combustion to be sequestered and stored underground, requiring limited land use. Moreover, although this application depends on increased biomass production and future bioenergy development, the rate of increase in agricultural yield needed for energy production and to maintain food supply is estimated to be in the range of 1-1.4%/yr, which, considering historical data, is not an unlikely rate [57]. Unfortunately, CCS technologies are still being defined and are extremely expensive: compared with afforestation, the cost of bioenergy coupled with CCS is found to be much higher, while this difference becomes an order of magnitude with direct CCS [58]. Therefore, at the current state, this solution is not feasible on a large scale, although it remains an interesting solution in the future [57].

Afforestation, on the other hand, is a cheaper and more readily available mitigation option, as it does not require special technology

and is defined as the managed regrowth of natural vegetation from manually planted seedlings [57]. It is an advantageous technique that preserve and restores biodiversity, as saplings are selected from species endemic to the selected area, and it shows great mitigation potential of 4.95 $GtCO_2$/year already with a low investment of 200 USD/tCO_2 [59]. Furthermore, the increased carbon sequestration capacity comes from large-scale application of this measure in tropical regions of the globe, and many studies have established the positive effect in reducing temperatures when applied in these areas [58-60]. Large-scale afforestation becomes even more interesting when considering that more than half of the suitable lands, according to the clean development mechanism identified by the Kyoto Protocol, are located in these areas. Specifically, 46% in South America and 27% in Sub-Saharan Africa, most of which being located in savannas, shrublands or low-intensity agricultural fields [61]. Additionally, Trabucco et al. [62] showed that the use of this measure is linked to a reduction in water runoff ranging from -80% (for dryer areas) to almost no reduction for the 20% of possible cases. The positive or negative impact of this effect cannot be stated, as it is highly dependent on the area concerned, as it may compete with local water demand. However, for arid inhabited areas, it clearly identifies it as a possible countermeasure to desertification.

Large-scale afforestation, however, poses some concerns, first and foremost the possible competition with agricultural land due to expansion of forest area [59]. Figure 2.7(a,b) shows the possible effects of afforestation on land-use and the projected increase in food prices under different various scenarios identified by the study of Kreidenweis et al. [58]. Analyzed areas are identified as follows: Sub-Saharan Africa (AFR), Europe (EUR), Latin America (LAM), Pacific Asia (PAS), North America (NAM), Former Soviet Union (FSU) and rest of the world (ROW). Land-use type identified as "other" refers to non-classified natural vegetation. Current scenario identified as "Business As Usual" (BAU).

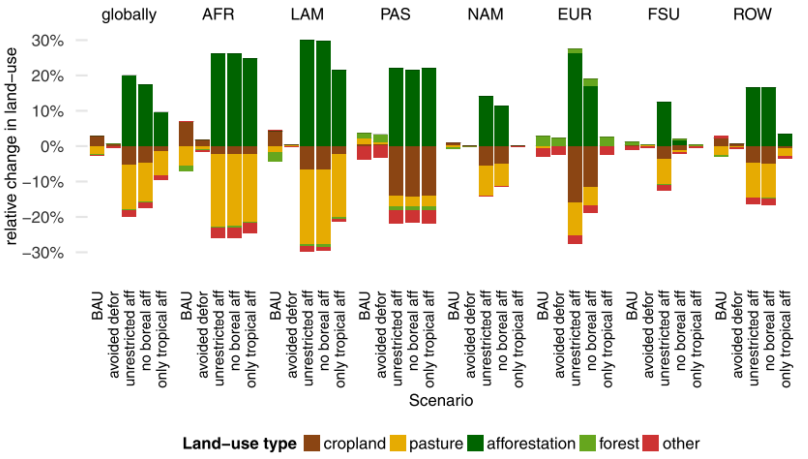

(a)

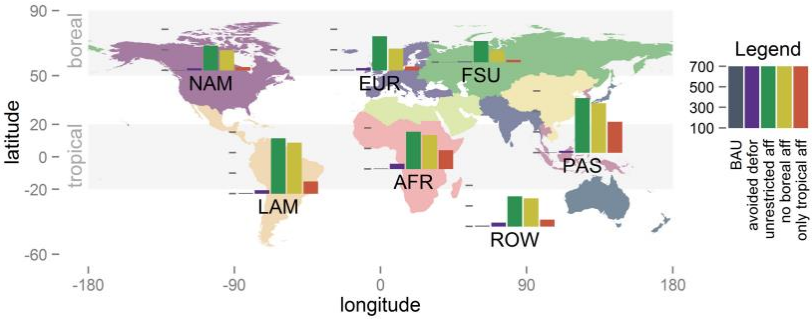

(b)

Figure 2.7 (a) Change in land-use and (b) predicted increases in food prices for different regions of the world [58].

Depending on the different case study, it is estimated that the transformation of land from fields to forests will be correlated with an overall increase in food prices of 80% by 2100 in the case of the unrestricted scenario (corresponding to an increase of forest area greater than 60%) due to a halving of the global cropland area. On the other hand, when limiting afforestation to the tropics, almost 60% of

the cumulative carbon capture obtained in the previous scenario was reached, and the increase in food prices was significantly lower and, most importantly, lower than the projected increase in wages [58]. Since it is generally agreed that sustainability goals should not be achieved at the cost of reducing food security [59], large-scale afforestation measures must be applied consciously. In addition, for these measures to be effective, deforestation must be stopped [58].
The final concern for large-scale afforestation stems from the effectiveness in implementing the measure. As of September 2011, only 0.75% of registered clean development mechanisms were actually such projects. This happened because proper effect of these measures is recorded when they are implemented on private areas. Landowners, however, prefer smaller ones to large tree plantations, which do not affect cultivated land or allow for income diversification [63,64]. Furthermore, most of the eligible areas identified for large-scale projects are in low- and middle-income regions, which are characterized by weak government and continued deforestation trends [59]. Nevertheless, it is suggested that by supporting projects with proper upfront funding, redirecting revenues from Certified Emission Reductions to local communities and having large organizations and experts working and leading the efforts, the effects of afforestation projects should improve [64].

2.3 Topsoil covers (TSCs)

One interesting approach to support afforestation and assist plant growth, especially under drought conditions, involves the use of topsoil covers (TSCs). TSCs are multifunctional mulching films, which aim to provide a more favorable environment for plant growth by increasing soil temperature [65,66], decreasing water evaporation and hindering the growth of competing weeds. The general advantages of mulching films are schematized in Figure 2.8 [67]. Due to its proven benefits, the adoption of this practice is increasing and applications can be found both in agriculture and in silviculture [68-71]. It is

estimated that more than 128'652 km² (approximately 1.0 Mt) of agricultural lands are globally covered with plastic films [72]. According to the Plasticulture magazine 2018 (International Committee for Plastics in Agriculture (CIPA), Paris), only in Europe the area of agricultural land covered with plastic films is estimated at about 40'000 km². In agriculture, the demand for plastic mulching films has increased from 1.2 billion to 3.2 billion pounds, with China accounting for 60% of the market and having a total covered area of 6.7 Mha. The use of TSCs in this country is mainly found in the cultivation of corn and cotton in arid soils [68]. Other users found in literature are Vietnam, Japan and in North-Eastern Spain [69-71].

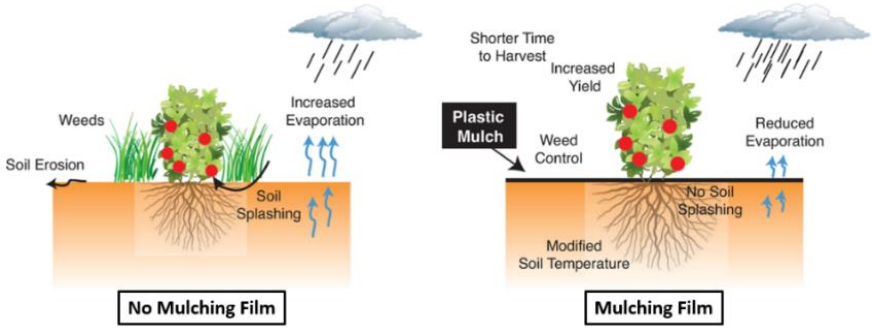

Figure 2.8 Schematization of the possible effects of mulching films on a common agricultural cultivation system (Adapted with permission from [67] Copyright © 2017 American Chemical Society).

TSCs usually consist of inexpensive and easy-to-produce materials which can range from natural to synthetic polymers; the latter are the most widely used in commercial applications [68,73]. Figure 2.9(a-c) shows some examples of TSCs materials in different applications.

(a) (b) (c)

Figure 2.9 Different types of mulching films in different applications: (a) synthetic TSC [74], (b) straw mulch in agriculture [75], (c) bark TSC in gardening [76].

Natural materials utilized for the TSCs production range from gravel to bark or straw [69,73,77]. Although they are extremely inexpensive, with straw costing 9 USD/ha [69], their large-scale use is rarely reported in literature and their main adoption is found in home gardening and horticulture.

The most widely used materials are synthetic plastics obtained through film casting, a manufacturing process in which a molten polymer is extruded through a flat die and subsequently stretched and cooled in air before being collected into rolls [78]. Despite having a greater cost than natural materials, plastic films remain incredibly cheap: polyethylene (PE) films are reported to have a cost of up to 96 USD/ha, while polypropylene (PP) films cost around 25 USD/ha [69]. The main material used for TSCs production is PE, in particular low-density polyethylene (LDPE) [68,73,79-81]. TSCs made of PE are sometimes produced with the addition of pro-oxidant additives or in starch blends to increase their biodegradability, although concerns for the actual capacity of these particular plastics to biodegrade are being raised [80,82]. Another commonly used material for TSC production is isotactic polypropylene (PP) [83].

Due to the rising concerns with plastic pollution associated to the use of synthetic TSCs [68,84,85], biodegradable bioplastics are being researched as a possible alternative, and some are already found on the market. Bioplastics reported to have been used for this application

are polyhydroxyalkanoates (PHAs), such as polyhydroxybutyrate (PHB) and polyhydroxyvalerate (PHV), and polylactic acid (PLA) [68]. PHAs are a class of semi-crystalline, optically active polyesters obtained through bacterial fermentation of sugars. As bacteria are put under stressful conditions in the reactor, they accumulate biopolymers in their cytoplasm in the form of discrete inclusions that are typically 0.2-0.5 μm big. These inclusions can make up to 90% of the dry-cell weight of the bacteria and, once they are extracted and purified, they can be processed as other plastics [86]. PLA is one of the most researched and utilized biopolymers by far [87]. It is a thermoplastic bioderived polyester obtained from ring-opening polymerization of lactide units obtained from bacterial fermentation of first-generation biomass such as sugars and starch [88]. Due to its low deformation at break, PLA is used in blends with a variable content of polybutylene adipate-co-terephthalate (PBAT) which in concentrations of 5-20 wt% greatly increases deformation at break and toughness [79]. Despite the fact that it is derived from renewable resources and its interesting properties, such as compostability and relatively high mechanical stability, application of PLA still remains limited in TSCs due to its relative high cost of 6 USD/kg [79].

2.3.1 Positive effects of TSCs

The two major positive effects reported for the use of mulching films are the increase in soil-water retention (SWR) and crop yield. Evaporation causes the loss of 90% of rainwater and of 25-50% of irrigation water [68,69]. Therefore, water use efficiency is a great issue, especially in arid regions, which accounts for a large portion of the earth's land surface and farming in arid lands is an indispensable practice for food production as population grows [89,90]. The use of TSCs is reported to increase water efficiency in soil by up to 90% [90] and, moreover, increasing the area covered from 35% to 90% can cause an additional decrease of 52% in soil evaporation [68]. Increase in soil water content due to lower evaporation is also associated to a more vigorous root system of the plant [79,91]. The increase in yield due to

use of TSCs varies depending on the considered crop and type of mulching used, with synthetic films providing better results. For example, Gu et al. [91] reported an increase in oil seed rape yield between 38% and 54% in fields covered with plastic mulching films and a slightly lower yield (6-14%) for those that used biodegradable TSCs. In Vietnam, on the other hand, an increase in groundnut production of 94% was observed with the use of PE mulching films and 70% with straw ones [69].

Another reason why topsoil covers are exploited is their ability to reduce competing species, such as weeds, so as to improve crop yields without the use of herbicides. Several studies have demonstrated the capability of both synthetic-based and biodegradable mulching films to control weed growth [92-94]. With regard to wood production of short-rotation trees, such as willows, the greatest increases in biomass volume were reported when there was also an adequate reduction of grass and weeds between the covered rows. Due to the larger root system of trees, weed growing in these areas competed with plant development, leading to a reduction of 32% in biomass volume [70]. It was reported that weed treatment is necessary until tree canopy establishment, as canopy closure will reduce competing grasses on its own [70].

Mulching is also reported to have beneficial effects on seedling survival and increasing in soil nutrient content. Especially in areas with high rates of seedling mortality such as post-mine Mediterranean soils, where it is estimated to be of 90% after 2 years after planting [95], the use of TSC can reduce mortality of 99% after one year [71], thus making it a truly promising practice for afforestation and reforestation efforts. As reported by Ma et al. [73], both PE mulching films and natural mulches such as straw are able to increase soil organic carbon content and the amount of limiting nutrients such as nitrogen and phosphorous. In particular, straw was observed to have better effects when compared to uncovered soil as the carbon and nitrogen content were found to be 9.7% and 7.8% higher. Furthermore, both material increased phosphorus limitation for bacterial activity, although by a

different mechanism. A schematic of the two mechanisms is reported in Figure 2.10.

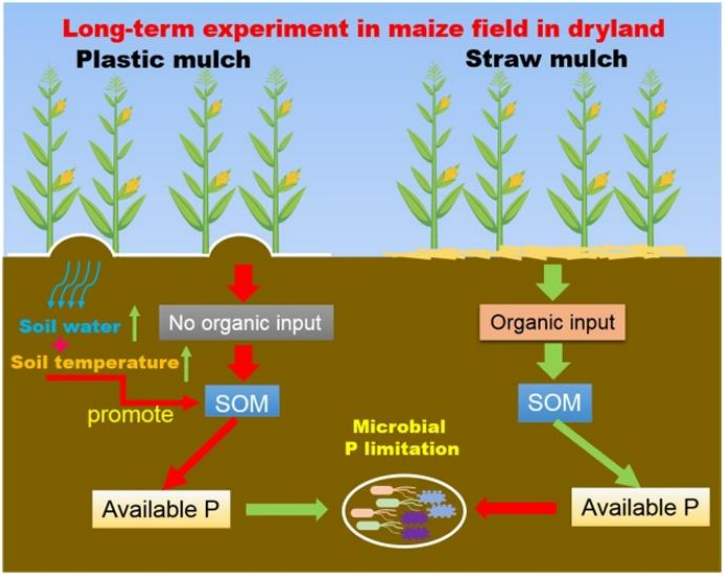

Figure 2.10 Mechanisms of bacterial activity improvement for PE and straw TSC [73].

For PE films, the recorded increase in soil moisture and temperatures promoted decomposition of soil organic matter (SOM), especially in the early years of the experiment, which ultimately decreased phosphorus availability for bacteria, whereas, for straw mulch, the decomposition of the layer was the one that provided this [73].
The last reported positive effect of using TSCs is the increase in soil temperature beneath the mulched surface. From a study carried out in northern Vietnam, Ramakrishna et al. [69] found that the use of TSCs maintained the soil temperature between 25.0 °C and 37.7 °C at a depth of 5 cm from the surface, this effect was independent from the type of cover used. In another study, under different conditions, it was found that plastic TSCs, compared with non-mulched soil, increased

the temperature from 0.5 °C to 1.8 °C and provided less fluctuation in this parameter [96]. Increased soil temperature is associated with more favorable conditions for root development and accelerated plant growth [79,90], but it might be associated with negative effects, such as root lignification and loss of activity, if temperatures exceed the optimal range for plant growth [96]. Biodegradable mulches are thought to be better in avoiding this problem [96]. Therefore, the choice of proper TSC should be made according to the type of plant or crop and environmental conditions.

2.3.2 Concerns with the use of TSCs

Despite the positive effects of the application of TSCs, due to the fact that most of them are made in PE and the size of their use in agriculture makes their recovery difficult, many concerns were raised because of the risk of plastic pollution to the environment and public health, as many farmers simply leave them in the field and then integrate them in the soil through rototilling, or, even worse, burning them [68,80]. The effects of plastic pollution due to use of synthetic TSC can be observed in Figure 2.11.

Figure 2.11 Residual of TSC on a tobacco field in China [68].

The release of macro-plastics (pieces larger than 2.5 cm) meso-plastics (size 5 mm- 2.5 cm) and microplastics (size < 5 mm) [82] from the

degradation of TSCs is the main concern when dealing with this kind of pollution. Zhang et al. [97] clearly reported how prevention of these residue is imperative and how it is inversely related to the film thickness and to its time of use. Increasing thickness correlates with increased TSC strength, while decreasing time of use reduces exposure to deteriorating environmental effects (such as UV light). Microplastics were extensively studied and correlated with adverse effects in marine ecosystems [98], but they also have negative impacts on soil properties and plant growth [81,84]. Qi et al. [81] demonstrated how both biodegradable and LDPE TSCs released debris microplastics during their experiment and how these had noticeable negative effects such as decreasing the bulk density of soil, decreasing the aggregate stability index, and increasing soil water repellency. These effects were found to be dependent on the size and concentration of debris and to be worse for the biodegradable TSC tested. Moreover, microplastics have negative effects on the plant growth both above and below ground: in a different study, Qi et al. [84] found how these significantly decreased root growth, leaf area, number of leaves per plant, and stem diameter; this effect was found to be worse in the starch-based biodegradable TSCs used in the test. The presence of earthworms was found to be beneficial in counteracting these effects but not sufficient. Furthermore, plastic fragments and residues have been associated to accumulation of pesticides, toxins, various heavy metals and phthalates in soil [85], thus posing severe risk for human health. Phthalates are used as plasticizer in plastics and are related to various health risks, such as abnormalities in the development of the male reproductive tract, increased risk of testicular cancer, endometriosis, increased risk of premature birth, respiratory obstruction, and other general risks [99]. As previously said, the problem of residues and microplastics, is being addressed by the production of starch-based blends (mainly starch/PE) or PE films with pro-oxidant additives [80,81,84], which are sold as biodegradable materials. Soil biodegradability, as defined by ISO 17556, ASTM D5988, and UNI 11462 standards, requires the

evolution of 90% of the original material mass into CO_2 within 24 months [100] and these commercial TSCs do not always meet this requirement. This is the case of the PE films with pro-oxidant agents studied by Briassoulis et al. [80]: the materials tested did not significantly degraded significantly after a period of 8.5 years in real field conditions. These blends could thus make more harm than good as the compounds that favor their degradation also lower their recyclability. Thus, much research is underway to produce fully biodegradable PHA or PLA films, but, as anticipated earlier, due to extremely high costs, these are not yet a viable solution.

2.4 Soil conditioners (SCs)

Another promising solution to support plant growth could be the use of soil conditioners (SCs), products specially developed to be mixed with the soil with the main aim of improving its chemical, physical and water regulation characteristics [101].
According to Shinde et al., SCs can be categorized according to the composition (organic and inorganic) or the origin (synthetic or natural) of their constituent materials [102]. Organic SCs consist of materials derived living organisms, such as plants or animals. The most used organic product is compost [103], but organic conditioners also include crop residues, manures, peat, bone meal, blood meal, compost tea, coir, biochar, sewage sludges, coffee grounds, farmyard manure (FYM), sawdust lignite, humate and vermiculite [104-107]. Inorganic soil conditioners are either mined or manufactured byproducts and may be natural occurring or synthetically produced. They include the mineral conditioners such as gypsum, lime, pyrites, crushed rocks, fly-ash, sulfur and zeolites [104,105,108].
Another category of soil conditioners are the synthetic conditioners, which include super-absorbent polymers characterized by long-chains and high molecular weight, such as synthetic polysaccharides (PSD), polyacrylamides (PAM) and potassium polyacrylates [109,110]. Thanks to the carboxyl, amine and hydroxyl groups in their

polymer structure, these materials are able to absorb water up to 300 times their dry weight, turning into hydrogels [111].
However, the use of synthetics in soil could raise environmental issues. Therefore, as with TSC applications, the use of biopolymers in soil conditioning applications may be an interesting strategy to solve these problems. Specifically, in literature is possible to find different studies on soil treated with natural polysaccharides such as starch and cellulose, proteins such as gelatin, casein, and silk, marine prokaryotes and materials derived from chemical synthesis of microbial activities (e.g., xanthan gum, gellan gum) or plant activities (e.g., guar gum) [112-116].

2.4.1 Positive effects of SCs

As previously stated, the main aim of soil conditioners is to improve the properties of the soil. In particular, they could be employed in dry and sandy soils to improve the water retention capacity, infiltration, percolation and permeability of water. Soil conditioners create a healthy environment in soil which helps to attracts useful microorganisms and earthworms in soil. Moreover, they could enhance the soil aeration, water retention, root development, and thus allowing plants to grow healthier, stronger and yield more [102].
Organic SCs are applied to enhance water infiltration and retention, promote soil particle aggregation and microbial activity, improve soil aeration and increase resistance to compaction and crusting [102]. In particular, compost is used to increase the organic carbon content and microbial activity in the soil and, thus, it can be a source of plant nutrients like N, P K and Mg [103]. Moreover, compost is a promising strategy to immobilize heavy metals in soils through changing the physicochemical property of soils and reacting with heavy metals [117,118].
Inorganic soil conditioners are characterized by improving the soil physical properties, with a consequent more effective utilization of soil and water resources [102]. Inorganic soluble conditioners undergo physico-chemical reactions with soil constituents, especially the clay

fraction. Thus, their application result in improved particle aggregation, soil porosity, water infiltration and hydraulic conductivity, and at the same time decreased bulk density and water permeability [119,120].

Synthetic polymer-based SCs have been used for improving aggregate stability, maintaining fertility and reducing soil erosion. The addition of small amounts of these polymers (10–20 kg/ha), either sprayed directly on to the soil surface or added to the applied water, has been observed to be effective in stabilizing and cementing the aggregates on the soil surface, and hence maintaining soil fertility [102]. Polyacrylamide, for example, was found to increase water retention in soil under drought conditions, enhance soil erosion resistance during irrigation and improve wind erosion resistance at construction sites [109,121].

Regarding the use of biopolymers, their direct mixing with soil forms uniform biopolymer-based soil treatment (BPST) mixtures that show instant strengthening due to the electro-static biopolymer-soil matrix formation [112]. As demonstrated by different studies in literature, this could reflect in a significant increase in the ultimate compression strength of soils (200 kPa–12.6 MPa) and interparticle cohesion (40–235 kPa), depending on soil type, biopolymer type, biopolymer content, and moisture condition [122-125]. Furthermore, treatment with biopolymers shows sufficient reduction of severe surface erosion and land degradation in arid, semi-arid, and highly degradable regions [115,116]. Another interesting advantage is that most of the hydrophilic biopolymers are able to turn into hydrogels that show high water-holding capacity, resulting in the improved water retention behaviour of BPSTs which could even benefit the growth of the plants under drought conditions [116]. Indeed, as reported in Figure 2.12(a,b), soil treated with biopolymers is able to store higher amounts of water during precipitations and release it more gradually during dry seasons. Finally, it is important to consider that biopolymers are environmentally friendly because they are mostly microbial hydrocarbons with a low CO_2 footprint compared to

conventional soil binders. Moreover, recent studies show that BPST promotes seed germination and the growth of vegetation in soil, which is a further advantage in terms of sustainability [112].

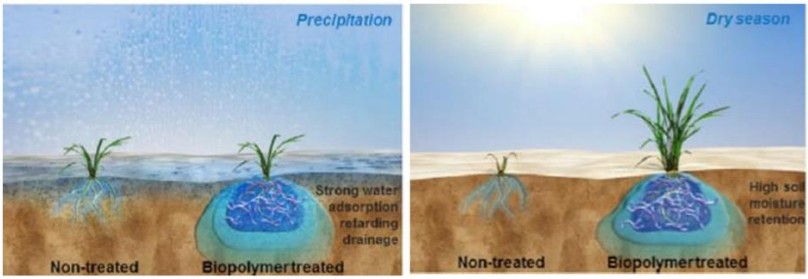

(a) (b)

Figure 2.12 Schematization of the working principle of biopolymers as soil conditioners: (a) water uptake during precipitation and (b) water retention during periods of drought [116].

2.4.2 Concerns with the use of SCs

Even for SCs, some drawbacks can occur due to the nature of the SCs with the consequent release of harmful substances, or the misuse by farmers, such as incorrect dosage and over-exploitation of land.
In particular, the effectiveness of organic SCs, such as compost, can be reduced if the degree of maturity of the compost is low and, in some cases, additional heavy metals can be introduced in the soil, which is detrimental to plant growth and microbes [126]. While compost merely immobilizes heavy metals in the soil and reduces their availability and uptake by plants, the heavy metals still remain in the soil. Over time, severe heavy metal pollution may occur due to environmental changes and the decomposition of organic matter Therefore, the large-scale use of compost is limited in agriculture in many cases.
The use of synthetic polymers as SCs could lead to environmental pollution problems due to their non-biodegradable nature. Moreover, some studies have shown that the residual monomers of PAM

generate toxicities that can impact the nervous system, increase cancer risks and even damage DNA [127-129].

The major drawback related to the use of biopolymers regards the economic feasibility of these materials. However, as it is possible to see from Figure 2.13, the increase in their production and their continuous expansion in different applications (e.g., medicine, cosmetics, food, farmland irrigation, construction, and geotechnical engineering) are expected to gradually decrease their cost [114].

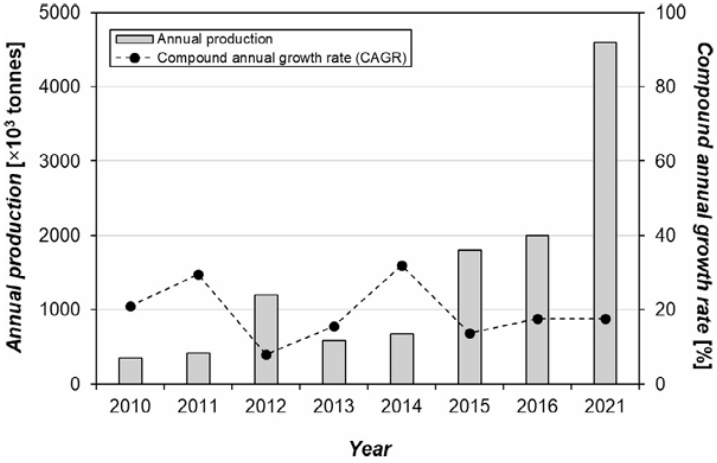

Figure 2.13 Global biopolymer market over the years [114].

Another possible issue related to BPST is that most of the studies have remained at the laboratory research level. Advanced studies are needed to develop in-situ implementation methods, design criteria and quality control guidelines, and to ensure the durability and reliability of BPST under real environmental circumstances. Moreover, as most biopolymers are hydrophilic and easily adsorb water and swell to hydrogels, there is a concern that BPST might lead to severe swelling and poor drainage due to biopolymer induced pore clogging [112]. For example, BPST could reduce the hydraulic conductivity of sand by up to three orders of magnitude, depending

on the type and content of biopolymers [130]. Therefore, the application of BPST must be used with caution considering site conditions and the final purpose.

2.5 Alternative materials for eco-sustainable TSCs and SCs

The following sections give examples of sustainable, multifunctional and innovative materials that could be good candidates for the production of topsoil covers and soil conditioners. In particular, these materials were chosen because they are bio-based, biodegradable, characterized by good water absorption and retention capacity and relatively low cost.

2.5.1 Xanthan gum

Xanthan gum (XG) is a complex bacterial polysaccharide obtained from the plant pathogenic *Xanthomonas campestris* through fermentation of glucose, sucrose, starch, molasses or corn syrup [131]. Figure 2.14(a,b) shows the bacteria *Xanthomonas campestris* the chemical structure of this bacterial polysaccharide.

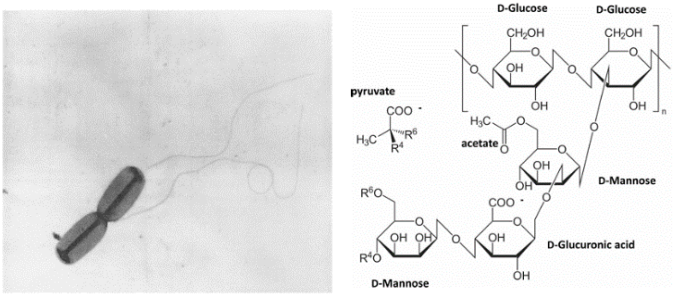

(a) (b)

Figure 2.14 (a) Transmission electron microscopy of *Xanthomonas campestris* [132] and (b) chemical structure of XG.

As observable from Figure 2.14b, XG is composed of repeated pentasaccharide units made of glucose, mannose and glucuronic acid units in a molar ratio of 2:2:1 arranged in a main chain presenting trisaccharide ramifications. Main chain has identical chemical structure to cellulose, with β-D-glucose units linked at 1 and 4 positions; while side chains are made of one D-glucuronic acid unit in between two D-mannose ones. Pyruvic acid units are found in one half of the terminal D-mannose units on the side chains while acetyl groups are observed with an unknown distribution in the main chain [132]. Due to its properties, XG has become one of the most important biopolymers in the food and cosmetic industries, and the most important microbial polysaccharide produced, with an estimated worldwide production of 30'000 tons per year and an increasing rate of 5-10%/year [133,134]. Classified as ADI-non specified (Acceptable Daily Intake) by the World Health Organization on food additives, and listed by the European List of Permitted Food Additives as E 415 [135], currently the main applications are found in the food industry where it is used as a thickener, an emulsifier or as a stabilizer in foods [132,136]. Other reported uses in cosmetics, where it is used as a thickener or a stabilizer in toothpastes, lotions and shampoos; in the pharmaceutical and biomedical sectors where it finds applications as an excipient, in development of drug delivery systems and in the production of scaffolds for tissue regeneration [136]. Moreover, XG is reported to be used by the oil industry in enhanced oil recovery system, in the production of food and packaging, and also in agricultural applications, mainly as a soil conditioner to enhance soil-water retention [133,136].

2.5.1.1 Production of xanthan gum

The most common method for XG production is through precipitation with isopropanol of a fermentation liquid followed by pasteurization and purification of bacterial cells [131]. A schematic of this production process is reported in Figure 2.15.

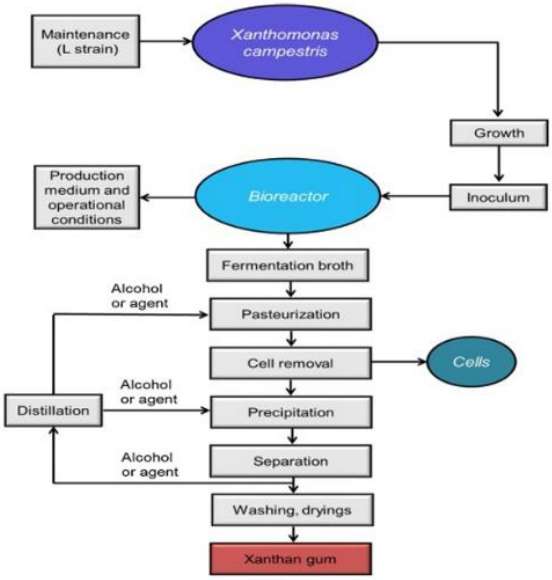

Figure 2.15 Schematic of the production process of XG [136].

Fermentation broth is a complex mixture consisting of bacterial cultures of *Xanthomonas campestris*, carbon sources (starch, molasses, corn syrup and those previously listed), a nitrogen source, which can either be soybean meal, yeast hydrolase or distiller solubles, and other various micronutrients. Liquid fermentation is carried out in the temperature range 25-34 °C and pH of the reaction varies overtime from neutral conditions to 5 due to the acid groups in the biopolymer. Although not mandatory, acidity control with potassium hydroxide (KOH) or sodium hydroxide (NaOH) is suggested by some authors [132]. During fermentation process an increase in viscosity of the medium occurs, thus mechanically or air agitated tanks are used as reactors [131]. A schematic representation of a production plant for XG is reported in Figure 2.16.

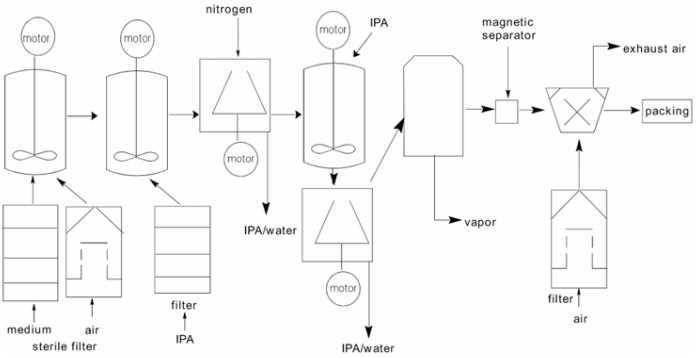

Figure 2.16 Schematic of a production plant for XG [133].

XG is produced as a biofilm between bacteria and production of this structure has three main functionalities: supports the growth of the bacterial colony, acts as a source of nutrients (as it is composed of polysaccharides) and protects the colony from potential environmental effects such as UV radiation and changes in pH [133]. Broth is thus pasteurized to kill bacterial colonies, then is washed and purified. Washing and purification mechanisms are expensive and vary accordingly to the desired purity degree of the product and economic factors [132]; precipitation with isopropanol, as anticipated, is often the preferred separation method [131,133]. The final broth has a concentration of XG ranging from 10 g/l to 30 g/l. The possibility to achieve greater yields depends on the possibility to design improved reactors and better compositions of the fermentation medium [132].

2.5.1.2 Main properties of xanthan gum

As previously stated, XG has many interesting properties which allow for its use in many applications. To begin with, being a naturally-occurring biopolymer, it is fully biodegradable and it is obtained from renewable resources. Moreover, it is resistant to cellulazes, despite having the same main chain as cellulose. This is attributed to the side chains which most likely form a barrier against enzymatic attacks

[137]. It is also non-toxic, non-sensitizing and non digestible, but safe for human consumption [136,137]. XG is soluble in both in cold and hot water but, as others hydrocolloids, it requires a lot of agitation to fully dissolve due to its tendency of forming lumps [132,137,138]. Solubility reaches a peak at a temperature of ~60 °C [132] and it is also dependent on pH, with the maximum solubility observed in 25% solution of phosphoric acid or acetic acid [138]. These parameters also influence rheological behaviour of XG solutions. Viscosity is observed to decrease as both temperature and pH are increased [132,138]. Solutions presents non-Newtonian shear-thinning behaviour (thus their apparent viscosity decreases as shear strain is applied) and present high gel-like viscosity even at concentrations of 1% [137]. Moreover, XG is observed to have emulsifying behaviour; for these reasons it finds large application as a thickening agent in various sectors. It is also reported to have great thermal stability and resistance to pH, with solutions recorded to being able to resist 100 °C and in the pH range 2-12 [138].

2.5.1.3 Xanthan gum hydrogels

Hydrogels are defined as lightly cross-linked hydrophilic three-dimensional polymeric networks with the ability to absorb up to hundreds of times their weight in water regardless of initial dried size. Their structure allows for rapid water absorption due to a combination of reduced resistance to permeation and high capillarity action [135,136]. This water absorption capability is correlated with the pH in which the gel is immersed and the effects depend on the type of hydrogel. For example, the water absorption capability of chitosan hydrogels decreases with increase of pH, while the opposite is true for XG ones [139]. Absorption, thus subsequent swelling capability could also be related to other effects such as the presence of determined ions or the osmotic effect. Cross-linking to obtain XG hydrogels can be obtained through either physical or chemical methods. Physical cross-linking occurs through the formation of interactions between polymers, these can be ionic, hydrogen bonds or

hydrophobic force interactions, and it allows for the production of both neat XG hydrogels or XG/biopolymer (notably, chitosan) without the need of a cross linking agent [136]. In literature it is found that chemical cross-linking of XG is obtained either with sodium trimetaphosphate (STMP) in alkaline environment or with citric acid (CA) [136,140]. STMP is a non-toxic and water-soluble cyclic triphosphate synthesized via electrolysis of sodium chloride (NaCl) solution into NaOH, followed by neutralization with orthophosphoric acid (NaH_2PO_4) and recrystallization. It is used as an additive in food and toothpaste [140,141]. Cross-linking with this compound occurs following the general cross-linking mechanism for polysaccharides, reported in Figure 2.17.

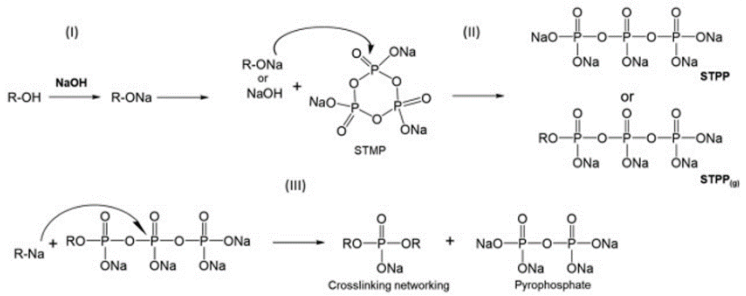

Figure 2.17 General cross-linking mechanism for STMP and polysaccharides [141].

Under alkaline medium hydroxyl groups (R-OH) of xanthan gum are deprotonized into $R\text{-}O^-$, STMP is thus subjected to the nucleophilic attack of this species or of NaOH and generating linear sodium tripolyphosphate (STPP) or monopolysaccharide graphted STPP. A subsequent nucleophilic from R-ONa causes the splitting of the intermediate into Pyrophosphate and a cross-linked XG/STMP network [141]. Tao et al. [140] reported how this reaction occurs in a temperature range between 25 °C and 37 °C. Cross-linking due to carboxylic acids occurs through the esterification of carboxylic groups (R-OOH) and R-OH groups found in XG, forming a stable ester bond

(R-OO-R) and releasing water as a byproduct [139,140]. CA is a weak organic acid obtained through fermentation of various bacterial strands and substrates, is the most produced acid in the world with a global production in 2007 of 1.6 billion tons [142]. Being a carboxylic acid, it is able to give esterification reaction with XG and the reaction is reported to occur at 165 °C following the mechanism reported in Figure 2.18.

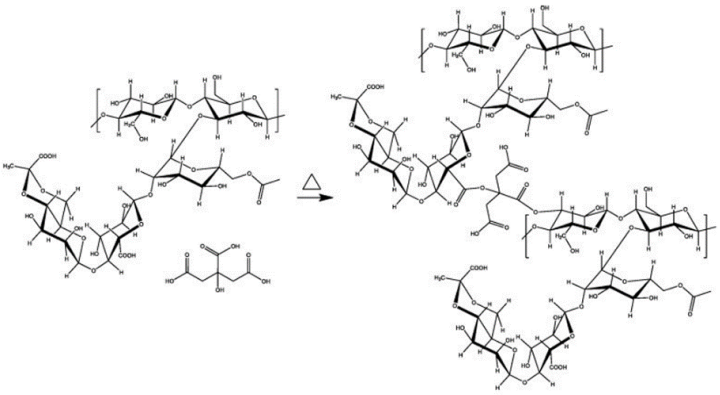

Figure 2.18 Esterification reaction mechanism between CA and XG [139].

Reaction follows the Fischer–Speier esterification process: interaction between the R-OOH group in D-glucuronic unit of XG and the only R-OH group in CA leads to the removal of the OH group from carboxyl and of the hydrogen in the hydroxyl group in the form of one water molecule and to the formation of one ester bond. Afterwards, one of the R-OOH groups in the newly formed complex interacts with one of the R-OH functionalities found in the backbone D-glucose unit of a different XG molecule completing the cross-linking reaction. Again, the reaction is associated with the removal of the OH from the carboxyl group and of the hydrogen atom from the hydroxyl. Esterification reaction only requires the simultaneous presence of both R-OOH and R-OH, it could occur if a big enough molecule presents both these functionalities within itself; in this case, the process takes

the name of intermolecular esterification. This phenomenon is observed when heating XG at 165 °C [139,141]. Mechanism for this reaction is reported in Figure 2.19.

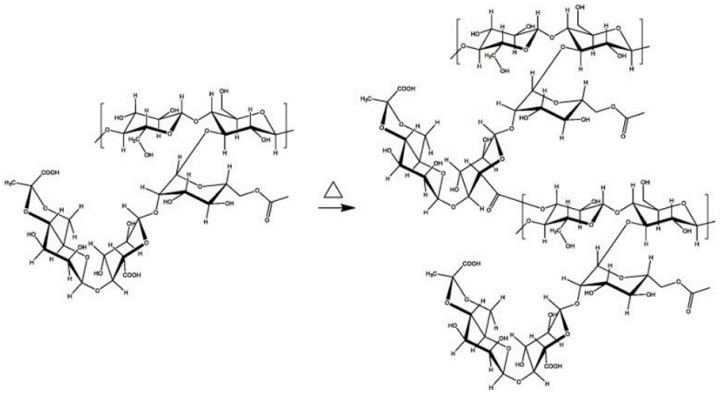

Figure 2.19 Intermolecular esterification reaction of XG [139].

Esterification reaction follows a similar mechanism to that explained when using CA as a cross-linking agent: R-OOH or pyruvyl groups found in the terminal D-mannose units directly interact with R-OH functionalities in backbone D-glucose unit; stable ester bond is formed with the removal of one OH from the most sterically cumbersome functionality and of the hydrogen atom from the hydroxyl which are expelled as one water molecule.

2.5.2 Gelatin

Gelatin is a natural protein traditionally produced by treating collagen-containing by-products of animal origin with acids or bases [143]. Collagen, the most abundant class of protein in both animals and humans, differs from spherical globular proteins because it is composed of linear fiber-like structures, as shown in Figure 2.20(a,b) [143,144].

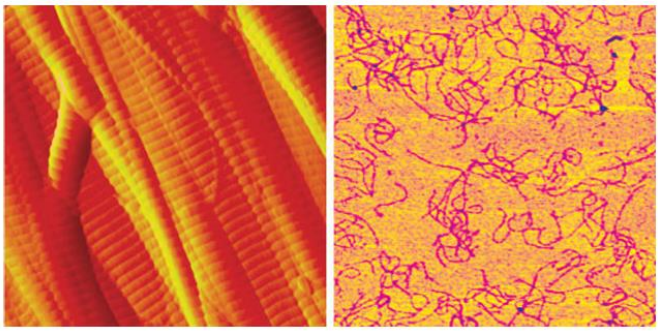

(a) (b)

Figure 2.20 Collagen consists of linear fiber-like structures. (a) Collagen from a rat tail tendon, (b) kangaroo tail collagen [143].

The primary structure of animal collagen (type I), used in gelatin production, consists of about 1014 amino acids linked in a chain with a molecular weight of about 100'000 g/mol. These alpha chains consist of 334 repeated units with the general sequence glycine-X-Y. Moreover, collagen and gelatin are characterized by a high content of the amino acids proline (~12%) and hydroxyproline (~10%) as well as the presence of hydroxylysine (~0.5%) (Figure 2.21).

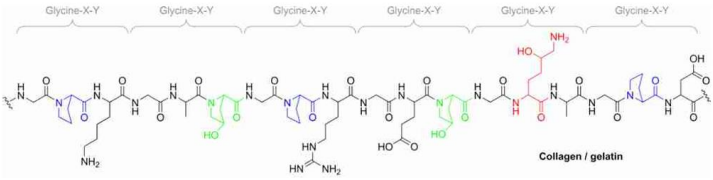

Figure 2.21 Schematic illustration of the glycine-X-Y sequence of collagen and gelatin. Proline, hydroxyproline and hydroxylysine residues are highlighted in blue, green and red, respectively [145].

Proline and hydroxyproline are responsible for limiting the rotation about the amino acid backbone, thus leading to the stabilization of the unique triple helix structure of collagen [143]. For gelatin, partial

renaturation at lower temperatures leads to the formation of the well-known thermo-reversible gels, which are characterized by a gelling power within the range of 50–300 bloom [145].

2.5.2.1 Gelatin hydrogels

In addition to warm water solubility and gel formation, gelatin is able to form strong films and displays adhesive properties [143,146,147]. However, in order to withstand humid or wet conditions for prolonged periods, it becomes necessary to cross-link its structure in order to produce gelatin hydrogels. Commonly, phenols, such as tannins, are used as cross-linking agents, which strongly interact with proteins [148-152]. Tannin is a class of compounds contained in plants such as oak and in oak galls presenting antioxidant properties. As shown in Figure 2.22, the most important classes of tannins are the hydrolyzable tannins, which comprise gallo-tannins and ellagi-tannins and the condensed tannins or proanthocyanidins.

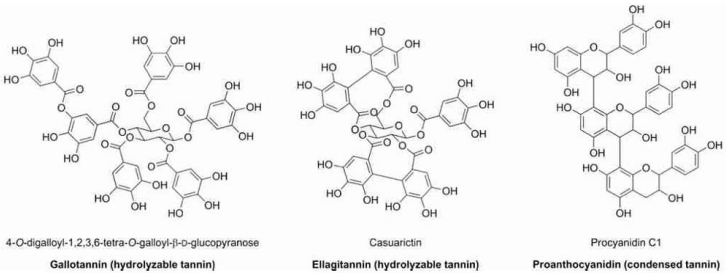

Figure 2.22 Examples of gallotannin (hydrolyzable tannin, left), ellagitannin (hydrolyzable tannin, mid), and proanthocyanidin (condensed tannin, right) [145].

The literature describes two primary pathways for strong interactions between tannins and proline-rich proteins such as gelatins. The first pathway involves a complex series of noncovalent interactions, including the hydrophobic stacking of phenolic rings against proline rings (σ-π attraction) and the formation of hydrogen bonds between

phenolic hydroxyl groups and carbonyl groups linked to proline amine groups [148]. The second pathway involves the formation of covalent bonds between tannins and gelatins under oxidative conditions [148,149,153]. This sequence is facilitated in basic environments, where the phenolate anions of tannins are readily oxidized to form electrophilic quinone species that react with nucleophiles, such as the lysine side chains in gelatins [145].

2.5.3 Wood-based composites with biopolymer matrix

Wood-based composites with biopolymer matrices represent a significant advance in sustainable materials engineering, combining the renewability and low environmental impact of wood with the ecological properties of biopolymers. Moreover, the economic feasibility of wood fibers and particles allows the production of composites with relatively low manufacturing costs [154].
In Figure 2.23 a representative scheme of the structure of wood fibers is shown.

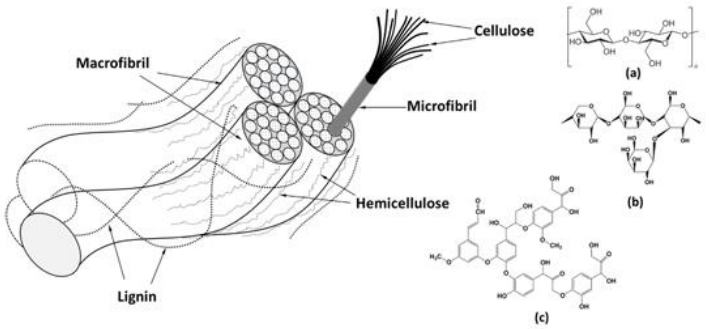

Figure 2.23 Structure of wood fibers and their constituents: (a) cellulose, (b) hemicellulose and (c) lignin [155].

Microstructurally, natural wood fibers are constituted mainly of hollow cellulose fibrils bound by a matrix of lignin and hemicellulose [156,157]. The cellulose fibrils, with a diameter of about 10-30 nm,

consist of concatenated cellulose molecules aligned along the length of the fiber, which provide considerable mechanical strength (tensile and flexural) and stiffness [158]. Lignin acts as a protective layer, preventing degradation of the fiber's internal structure by microorganisms. As a biopolymer, cellulose, together with hemicellulose, influences the fiber's ability to absorb moisture [159]. The reinforcing efficiency and the behaviour of wood fiber is linked with the nature of cellulose and its crystallinity degree [160].

Certain property and processing limitations of biopolymers can be overcome by incorporating wood fibers. In fact, studies in the literature have shown that wood fibers increase the tensile strength of biopolymers and the addition of wood flour reduces shrinkage and deformation of injection-moulded products [161]. Another example is related to starch-based polymers. Indeed, starch is a biopolymer, which tend to absorb water and have poor mechanical properties, resulting in limited long-term stability. As reported in the literature, the addition of wood flour to thermoplastic starch leads to an increase in tensile strength and elastic modulus and a decrease in elongation at break [162]. The improvement in mechanical properties is due to the strong interfacial bonds that wood and thermoplastic starch form due to their chemical similarity, eliminating the need for bonding agents. As the wood content increases, the moisture absorption of the composite decreases, improving long-term stability. As a result, thermoplastic starch and wood form a wood polymer composite that is suitable for use in non-humid environments, such as indoors, while reducing the environmental impact of disposal.

Moreover, the integration of wood fibers or particles in biopolymers not only improves the mechanical properties and durability of composites, but also reduces their carbon footprint and dependence on non-renewable resources [163,164]. This synergistic combination takes advantage of the natural strength and biodegradability of both components, resulting in materials that are not only high-performing but also environmentally friendly.

3 Experimental Part

Chapter 3 – Experimental part introduces the materials employed for the production of TSCs and SCs, and describes the main characterization techniques used to investigate the prepared samples. The techniques for sample preparation are, instead, described in Chapter 4 and Chapter 5.

3.1 Materials

In this section, all the materials employed in the Thesis are listed. For the production of both TSCs and SCs a biopolymer matrix constituted of xanthan gum was used and different cellulose-based fillers were studied as reinforcement. Different cross-linking agents were used and tested only for the development of TSCs.

3.1.1 Xanthan gum (XG)

XG was provided by Galeno Srl (Prato, Italy) and used in form of powder. It is a water-soluble, bio-derived polysaccharide obtained from bacterial fermentation of *Xanthomonas campestris* from corn. XG had a purity > 91%, molecular weight (M_W) of $1 \cdot 10^6$ g/mol, degree of pyruvate = 0.38 and degree of acetyl = 0.41.

3.1.2 Fillers

Different cellulose-based fillers were kindly provided by J. Rettenmaier and Söhne Gmbh (Rosenberg, Germany). Their main characteristics are listed in Table 3.1. Commercial wood fibers, Steico Flex 036, were kindly provided by University of Applied Sciences of Rosenheim (Rosenheim, Germany) (THRO) and milled for 30 s before use.

Table 3.1 Main features of the cellulose-based fillers utilized in this work [165,166].

Type of Filler	Basic Raw Material	Cellulose Content (%)	Oxide Ash (%)	Av. Fiber Length (μm)	Aspect Ratio
Arbocel R	Pure cellulose	>99	0.5	200–300	9.9
Arbocel FT 400	Technical cellulose	75	2	1200	34.4
Arbocel ZZC 500	Technical raw cellulose	80	15	400	8.8
Cellugrün	Technical raw cellulose	80	15	1400	31.1
Arbocel ZZ 8-2 CA1	Technical raw cellulose	50	50	1000	22.2
Arbocel Adsorb 2	Cellulose dextrose derivate	-	-	30–250 (particles)	- *
STEICO flex 036 (milled)	Wood fibers	-	-	9000–30′000	25.0

* Arbocel Adsorb 2 is constituted by very fine powder, with no info on the aspect ratio provided by the supplier.

3.1.3 Cross-linking agents

3.1.3.1 Citric acid (CA)

Citric acid monohydrate was provided by Riedel-de Haën GmbH (Seelze, Germany). It is a non-toxic, water-soluble organic acid with a M_W of 210.1 g/mol, supplied in the form of a white powder with a purity of 99.5% and a density of 1.53 g/cm^3.

3.1.3.2 Sodium trimetaphophate (STMP)

Sodium trimetaphosphate was produced by Thermo Fisher Scientific Inc. (Massachusetts, USA). It is a colourless, non-toxic compound with

a M_W of 305.9 g/mol, provided as a solid powder with a density of 2.49 g/cm^3.

3.1.3.3 Tannic acid (TA)

Tannic acid was supplied by Galeno Srl (Prato, Italy). It is a non-toxic, water-soluble powder constituted by a mix of esters of glucose with gallic acid and 3-galloilgallic acid. Powder had a purity of 97%, M_W of 1701.2 g/mol and a residual solvent content ≤ 60 ppm.

3.1.4 Glycerine

Vegetable glycerol (or glycerine) produced by Farmalabor Srl (Assago, Italy) was used as a plasticizing agent in order to grant flexibility to the produced TSCs. This is a syrupy, colourless water-soluble liquid obtained by double distillation of a mixture of vegetable oils (rapeseed, palm, sunflower and castor oils) with a purity of 98-101%, M_W of 92.1 g/mol and density of 1.26 g/cm^3.

3.1.5 Casein

Casein was supplied by Thermo Fisher Scientific Inc (Massachusetts, USA) and used in solution as protective coating for the TSCs. The material is a non-toxic white powder with a purity ≥ 92% and a density of 1.20 g/cm^3. Casein presents a micellar structure, which makes it hydrophobic in neutral pH, but it becomes water-soluble in basic conditions. For this reason, casein was dissolved in a 1 M solution of sodium hydroxide (NaOH).

3.1.6 Gelatin

GELITA IMAGEL® LB, a type B gelatin powder with Bloom 113 (gel) and viscosity of 2.29 mPa·s (6.67%, 60 °C), was purchased from GELITA AG (Eberbach, Germany). This material was used by THRO as matrix for the production of TSCs.

3.1.7 Materials used as reference

During the experimental analysis in the laboratory and in the field, different commercial products were tested as reference.

For some laboratory tests on TSCs, a commercial woven polyethylene (PP) mulching film (Rama S.p.A, RE, Italy) was used (0.25 mm of thickness).
For the field experiment with TSCs, a commercial groundcover, Thermodisc® TD-16 produced by MYC-5 (Girona, Spain), composed of 90% natural fibers and 10% synthetic fibers, being fully biodegradable in 6-18 months (according to the producer technical data-sheet) was applied. Moreover, woodchips produced by chipping wood residues of the nursery, and applied as a 40 mm layer, were also used.

As a benchmark for tests on SCs, two commercial potassium polyacrylate-based products were used. Idrogea [167] purchased by Endofruit Srl (Verona, Italy) and Be-Grow Boost M [168], kindly provided by the University of Freiburg (Germany) and produced by Be-Grow GmbH (Neustadt an der Weinstraße, Germany). According to the technical datasheet, Idrogea is a solid powder constituted by 95% of potassium polyacrylate (CAS 25608-12-2). It has a relative density of 0.7 g/cm^3, pH of 7.7 and an absorption capacity of at least 300 times its weight in water and a cation exchange capacity of not less than 460.00 m_{eq}/100 g. According to the suppliers, the concentration of Idrogea to be used in the soil is 0.13 wt%, while for Be-Grow is 0.4 wt%.
A field trial with SCs was carried out using a commercial product containing water-absorbing, growth-stimulating and nutritional components, called TerraCottem Arbor® produced by TerraCottem Intl. SL (Cadiz, Spain).

3.2 Experimental techniques

In this section, a comprehensive overview of the experimental techniques utilized for the characterization of the prepared materials is presented. A first subsection describes the specific techniques, procedures, and instrumentations employed in the investigation of TSCs, while a second subsection is dedicated to the investigation of SCs. In both cases, specific tests were carried out to investigate and verify whether the produced formulations met the requirements and were suitable for use as innovative TSCs and SCs.

3.2.1 Characterization of topsoil covers (TSCs)

3.2.1.1 FT-IR spectroscopy

Fourier-transformed infrared spectroscopy (FT-IR) tests were conducted in attenuated total reflectance (ATR) mode using a PerkinElmer Spectrum One spectrometer (PerkinElmer, Waltham, MA, USA), in the wavelength number range of 650–4000 cm^{-1}, obtaining each spectrum from the superposition of four scans. The analyses were performed on topsoil cover samples in order to investigate the effect of the cross-linking agent on the structure properties of the materials.

3.2.1.2 Microstructural characterization

Micrographs of the surface and of the cryofractured cross-section of the TSC samples were obtained using a field emission scanning electron microscope (FESEM) Zeiss Supra 40, operating at an accelerating voltage of 3.5 kV inside a chamber under a vacuum of 10^{-6} Torr. Prior to the observations, the samples were dried in a fan oven at 50 °C for 48 h and then coated with a thin electrically conductive Platinum/Palladium (Pt/Pd) layer.

The density of the samples was measured to calculate the total, open, and close porosity. Specifically, the theoretical density (ρ_{th}) of samples without porosity was evaluated with the rule of mixture, by knowing the densities and the nominal weight fractions of each constituent, according to Equation (3.1):

$$\rho_{th} = \frac{1}{\sum_i \frac{W_i}{\rho_i}} = \frac{1}{\frac{W_{XG}}{\rho_{XG}} + \frac{W_{WF}}{\rho_{WF}} + \frac{W_{GLYC}}{\rho_{GLYC}} + \frac{W_{CX}}{\rho_{CX}}} \quad (3.1)$$

where W_{XG}, W_{WF}, W_{GLYC} and W_{CX} are the weight fractions of the xanthan gum, wood fibers, glycerine and cross-linking agents, respectively, and ρ_{XG}, ρ_{WF}, ρ_{GLYC} and ρ_{CX} their densities. ρ_{XG}, ρ_{GLYC} and ρ_{CX} were found on the technical datasheet, while ρ_{WF} was measured with a pycnometer, as reported hereafter for the apparent density.

The apparent density (ρ_{app}), which identify the volume together with only the closed porosity was measured using the AccuPyc 1330 helium pycnometer (Micromeritics Instrument Corporation, GA, USA). For every composition, a disc specimen with a diameter of ~8 mm and thickness of ~3 mm was tested and inserted in a chamber with a volume of 1 cm^3. Every measurement was collected at a constant temperature of 23 °C, and 99 measurements were performed for each specimen.

The bulk density (ρ_{bulk}), which comprise both the open and the closed porosity was calculated as the ratio between the mass and the volume of disc specimens with a diameter of 15 mm and thickness of ~ 3 mm. The dimensions of the specimens were measured with a digital caliper and the mass with an analytical balance. Three specimens were measured for each composition.

Finally, the total porosity P_{tot}, the open porosity P_{open} and the close porosity P_{closed} were calculated according to Equations (3.2), (3.3) and (3.4):

$$P_{tot} = 1 - \frac{\rho_{bulk}}{\rho_{th}} \tag{3.2}$$

$$P_{open} = 1 - \frac{\rho_{bulk}}{\rho_{app}} \tag{3.3}$$

$$P_{closed} = P_{tot} - P_{open} = \rho_{bulk}\left(\frac{1}{\rho_{app}} - \frac{1}{\rho_{th}}\right) \tag{3.4}$$

3.2.1.3 Water absorption properties

Water uptake tests were carried out in order to determine the behaviour of produced samples under extreme flood conditions. For each sample three specimens, approximately 30×50 mm² in size and thickness ~3 mm, were placed in a container filled with 20-30 mm of water and left immersed. Mass variation due to water absorption or hydrogel swelling was recorded over time after removing periodically specimens from water. Water uptake (WU), or swelling degree, of the samples was obtained according to Equation (3.5):

$$WU\% = \frac{M_t - M_0}{M_0} \cdot 100 \tag{3.5}$$

where M_0 is the initial mass of the sample and M_t is the sample mass at the time t. The test was carried out until complete rupture of the specimens or after a plateau in the absorption curve was reached.
After the samples were fully hydrated, they were placed in an oven at a constant temperature of 40 °C. In this way, by periodically measuring the weight of the samples, it was possible to calculate the weight loss (WL%), which indicates the water evaporation rate, according to Equation (3.6):

$$WL\% = \frac{M_i}{M_{wet}} \cdot 100 \tag{3.6}$$

where M_i is the mass of the sample during drying and M_{wet} is mass of fully wet samples.

3.2.1.4 Water vapor permeability

Water vapor permeability (WVP) is a very important property for mulching films because it affects the soil water preservation. This analysis was performed in accordance to ASTM E96 standard. For each sample two circular specimens (diameter ~40 mm, thickness ~3 mm) were placed on a small glass container filled with 20 ml of distilled water. Vases were closed with a lid presenting a circular hole with a diameter of 16 mm and sealed with Parafilm®. A commercial woven polyethylene (PP) mulching film (Rama S.p.A, RE, Italy) was also tested as a reference for this experiment (0.25 mm of thickness). Specimens were placed in a climatic chamber at 30 °C and 50% RH. Their mass was measured at regular time intervals over the span of two days. The water vapor permeance (WVP2) of the tested specimens was thus obtained through Equation (3.7):

$$WVP2 = \frac{\Delta M}{tA} \cdot \frac{1}{\Delta p} \quad (3.7)$$

where ΔM is the mass variation, A is the exposed area, t is the time over which ΔM occurs, while Δp is the differential water vapor pressure across the sample. It is important to emphasize that WVP2 is not water vapor permeability (usually indicated as WVP). On the contrary, it is a thickness-independent parameter and therefore allows a better comparison between inhomogeneous samples. From WVP2 it was possible to calculate the water vapor permeability (WVP) according to Equation (3.8):

$$WVP = WVP2 \cdot d \quad (3.8)$$

where d is the sample thickness. The measured WVP values were corrected for the resistance due to the still air layer and the resistance

offered by the specimen surface, according to ASTM E96 standard specifications.

3.2.1.5 Thermogravimetric analysis (TGA)

Thermogravimetric analysis (TGA) was performed via the thermobalance Mettler TG 50 (Mettler Toledo Inc., Columbus, Ohio, USA). Specimens of approx. 20 mg were subjected to a thermal ramp between 30 °C and 700 °C with a heating rate of 10 °C/min, under a constant nitrogen flow of 10 ml/min. This test allowed the determination of the degradation temperature (T_{max}), considered as the maximum of the first derivative of the TGA thermogram (DTG), and the residual mass at 700 °C ($m_{R,700}$).

3.2.1.6 Penetration resistance

Penetration resistance tests were performed to simulate the resistance offered by mulching films against weed perforation. The tests were carried out according to ASTM F1306 standard with an Instron 5969 (Instron®, Norwood, MA, USA) machine operating at 25 mm/min and equipped with a load cell of 100 N. The specimens were fixed with an appropriate sample clamping device and were perforated by a 3.2 mm diameter hemispherical probe. The maximum load to perforate the sample was determined and compared with that of a commercial woven PP mulching film. For each sample, five specimens with dimensions 76×76×3 mm^3 were tested.

3.2.1.7 Single flame source tests

Single flame source test was carried out at the University of Applied Sciences of Rosenheim (Germany) and performed according to EN ISO 11925-2 standard. Specifically, vertically clamped specimens were in contact at their underside with a 20-mm-high flame for 30 s. After the burner was removed, observation were done regarding whether ignition occurs, whether the flame tip reaches 150 mm above the

application point and the time at which this occurred. The analysis was performed on five specimens, for each composition, with dimensions of 250×90×10 mm^3.

3.2.1.8 Limit Oxygen Index (LOI)

LOI tests were carried out in order to measure the minimum concentration of oxygen, expressed as a volume percent, capable of sustaining flame combustion in a fluid mixture of oxygen and nitrogen. The measurements were performed according to ASTM D2863 standard, on at least 10 specimens, for each composition, with dimensions of 100×10×10 mm^3 by using CEAST oxygen index apparatus.

3.2.1.9 Weather conditioning in external environment

Weather conditioning tests in outside environment were carried out in order to qualitatively evaluate the dimensional stability and the biodegradability of produced hydrogels. A rectangular area of the garden in the Department of Industrial Engineering of Trento University (46.06° N, 11.15° E, altitude 398 m asl) was cleared from grass and weeds, then the selected samples (discs 160 mm in diameter, thickness ~3 mm) were laid on it at a distance of ~200 mm from one another. At least five specimens were tested for each composition. The soil, analysed by Fondazione Edmund Mach (S. Michele all'Adige, Italy), was a loamy, alkaline, very calcareous soil with a good content of organic matter (more information can be found in Table 6.16). Figure 3.1 shows the recorded weather conditions.

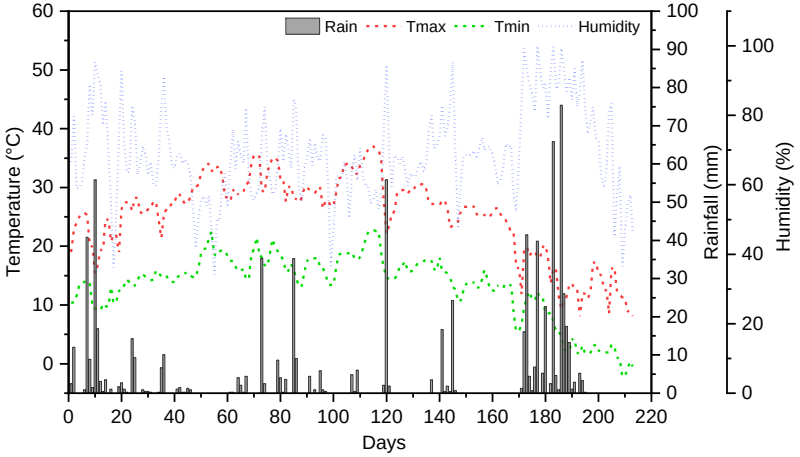

Figure 3.1 Meteorological pattern recorded during open field experiments. Day 0 corresponds to May 15th 2023.

The percentage of area lost over time (A_L) due to the exposure to outside weather conditions was evaluated through the use of a digital caliper (sensitivity 0.01 mm) according to Equation (3.9):

$$A_L = \frac{A_0 - A_i}{A_0} \cdot 100 \quad (3.9)$$

where A_0 and A_i are, respectively, the initial area and the area at time "i" of the specimens. The area of the specimens (hydrated state) was measured after a period of 1, 3 and 7 months. At the end the experiments the samples residues were collected, washed gently to remove attached soil, dried and weighed so that to calculate their residual mass. The test was also useful to qualitatively observe the ability of the samples to block weed growth.

3.2.1.10 Evaluation of the plant growth with TSCs

A preliminary practical experiment was carried out by evaluating the growth of tomato plants (*Solanum lycopersicum variety cerasiforme* purchased by Consorzio Agrario Trento, Italy) to study the possible

interactions of the topsoil cover in the soil and with plants. Monitoring duration was 80 days, comparing the increase in vegetation mass of plants and observing the biodegradability of TSC in the soil. Three tomato plants, 300 mm in height, were planted at a distance of 800 mm from each other in a common garden soil. 600 mL of water were provided daily to the plants and no fertilizers were used. Xanthan-based TSCs, with dimensions of 500×500 mm^2, were used as topsoil covers and applied at the base of two plants, while the third was planted without TSC and used as a reference. Specifically, the two topsoil covers utilized had the same composition, but only one of them was subjected to heat treatment in a furnace to perform the cross-linking reaction. This made it possible to verify the effectiveness of this treatment and to evaluate the influence of the cross-linking step for these materials in a practical case study. In Figure 3.2, the experimental setup utilized for the tomato plant cultivation is displayed.

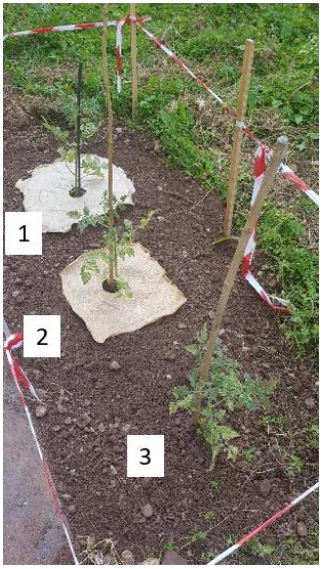

Figure 3.2 Experimental setup for the tomato plant cultivation with TSC. (1) not cross-linked TSC, (2) cross-linked TSC, and (3) without TSC.

3.2.2 Characterization of soil conditioners (SCs)

3.2.2.1 Rheological properties

The rheological properties of the wet SC samples were investigated using a Discovery hybrid rheometer DHR-2 (TA Instrument, DE, USA), adopting a plate-plate configuration and setting a gap distance of 1 mm. The tests were performed under steady conditions at a constant temperature of 30 °C, in order to measure the viscosity and the shear stress in a range of shear rate between 0.1 to 100 s^{-1}. From these tests, it was possible to determine the yield stress of the materials by fitting the data with the Casson model [169], which can be described by Equation (3.10):

$$\sigma^{1/2} = \sigma_y^{1/2} + (\eta\dot{\gamma})^{1/2} \quad (3.10)$$

where σ is the shear stress, σ_y is the yield stress, η is the shear viscosity and $\dot{\gamma}$ is the shear rate. The value of the yield stress was detected as the intercept with the y-axis of the linear fit of the data in the strain rate range from 0.3 to 2 s^{-1}.

3.2.2.2 FT-IR spectroscopy

Infrared spectroscopy tests were performed on SC samples with the same equipment and parameters described in Section 3.2.1.1. The test was carried out to investigate possible differences between the different cellulose fillers added in the SC formulations.

3.2.2.3 Optical microscopy

The different compositions in the wet or dry state were observed using a Nikon SMZ25 optical microscope, equipped with a Nikon DS-Fi2 digital camera. This analysis was performed to study the morphology of the prepared samples and to investigate the presence

of agglomerates in the solutions, assessing thus the feasibility of the mixing process.

3.2.2.4 Moisture absorption properties

Moisture absorption analyses were carried out on the fully dried samples. The analysis was conducted by periodically weighting the samples stored in a sealed box under constant humidity (RH = 80%) and temperature (25 °C) conditions. The mass of the samples was measured with a Gibertini E42 balance (resolution of 0.1 mg). The moisture absorption was calculated as the WU% for the TSCs described in Section 3.2.1.3, using Equation (3.5). The procedure described in Section 3.2.1.3 was followed also for the assessment of weight loss (WL%), using Equation (3.6). At least three specimens were tested for each composition.

3.2.2.5 Morphological analysis of the soil treated with SCs

Micrographs of the soil mixed with SCs samples were obtained with the same equipment and parameters described in Section 3.2.1.2. The soil was mixed with the SCs at 1.8 wt%. This weight concentration was selected after preliminary laboratory tests and on the basis of literature studies [112,170]. Prior to the observations, the samples were dried in a fan oven, so to remove any moisture, and then coated with a thin electrically conductive Platinum/Palladium layer. Measurements of particle and fiber sizes were carried out through ImageJ® software analysis.

3.2.2.6 Evaluation of the maximum water holding capacity (MWHC) of the soil

The evaluation of the water holding capacity of the soil treated with dry SCs was carried out by adapting the procedure of Yu et al. [171]. The test was performed on soil sieved through a 1.8 mm sieve and with an initial measured water content of 10 wt%. The untreated soil

was tested as a reference, and the soil mixed with commercial products was also analyzed as a comparison. All the samples were enclosed in perforated polyethylene films (160 m × 160 m × 0.1 mm), permeable to water but not to the soil. The soil envelopes were weighed (m_{dry}) and then placed in demineralized water for 15 min. Then, excess gravitational water was drained, sample weights were recorded (m_{wet}), and the MWHC was calculated using Equation (3.5). At least three specimens were tested for each composition.

3.2.2.7 Evaluation of the water retention capacity of the soil

The effect of the presence of SCs in the soil on the water retention capacity was evaluated by adapting the procedure utilized by Ni et al. [172]. 100 g of dry soil were filtered through a 1.8 mm sieve and mixed with the dried SCs. One hundred mL of tap water were then slowly added to the samples and weighed. Neat soil and soil treated with commercial products were also tested as reference. The samples were maintained at 30 °C in an oven and periodically weighed. The weight loss which corresponds to the water evaporation rate was calculated using Equation (3.6). At least three specimens were tested for each composition.

3.2.2.8 Determination of the soil water retention curve (SWRC)

In collaboration with the Faculty of Civil and Geodetic Engineering of the University of Ljubjana (Slovenia) (ULJ), soil water retention curves (SWRCs) were determined using the Hyprop evaporation method device (matric suctions up to approximately 100 kPa) and Dew Point Potentiometer WP4-T (total suctions higher than approximately 100 kPa). Figure 3.3 shows a schematic of the Hyprop device involving pressure head measurements at two depths (12.5 mm and 37.5 mm) within a 50 mm high saturated specimen with a diameter of 80 mm [173]. The evaporation rate was obtained by automated weighing. The assumption that changes in weight are equal to changes in the mass of water was used. This means that possible biodegradation during

the investigation, which lasted at least 1 month, was not taken into account. Water retention values were estimated from the average gravimetric water content and the average pressure measured by the two tensiometers. Untreated and treated soil specimens were prepared from the soil at natural water content with the addition of dry SCs and slightly compacted into the Hyprop mold. The specimens in the mold were then saturated by immersing them in water to their 4/5 height. Volume changes were reduced by porous discs on both ends of the specimen (at the upper and lower surface), and a pressure of 10 kPa was applied on the top of the specimen during the saturation process. After saturation was reached, tensiometers mounted on the Hyprop device were pushed into the specimen, and measurements started. To provide quasi-steady state conditions (constant flux and hydraulic gradient over the time interval), evaporation was slowed down by covering the specimens with a perforated plastic bag. In the high suction range, SWRC was measured using the potentiometer WP4-T, following the procedure described in ASTM D6836. The measurements were conducted on the remaining portion of the sample (soil or mixture), prepared for the specimens investigated in the Hyprop device. Using drippers, the samples were wetted to water content at or slightly below full saturation. At this point, the first specimen was prepared, and total suction was measured. The sample was then slowly dried stepwise at room temperature, and specimens were taken at various drying intervals. Before conducting the measurements, the prepared specimens were tightly sealed in special plastic containers for at least 24 h to ensure that the water content and the suction were equilibrated. Before the regular measurements started, the potentiometer WP4-T had been calibrated each day by using a standard solution of 0.5 M KCl. The dry mass of all specimens was determined after suction measurements by drying in an oven at 45 °C.

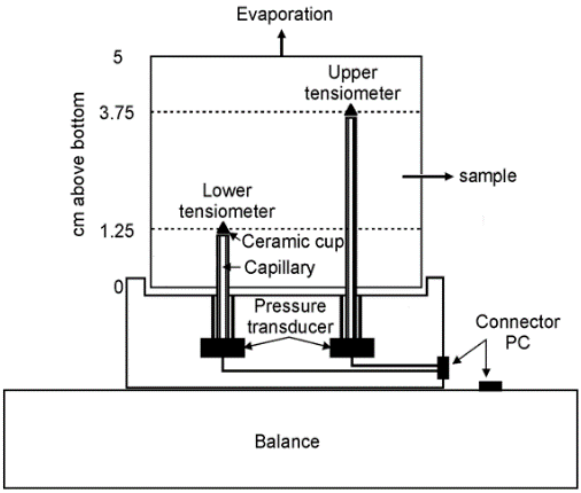

Figure 3.3 Schematic cross-section of the HYPROP evaporation method device [174].

3.2.2.9 Investigation of the geotechnical properties of soil

In collaboration with the Faculty of Civil and Geodetic Engineering of the University of Ljubjana (Slovenia) (ULJ), different compositions of xanthan-based soil conditioners have been applied on different soils to investigate the effect of SCs on the geotechnical properties of these soils. The test procedures and the evaluation of results was carried out out by ULJ following the standard test methods outlined in Table 3.2.

Table 3.2 List of laboratory investigations, associated standards, methods and devices used for investigations and investigation plan.

Parameter	Standard	Device/Method description
Liquid limit (w_L)	EN ISO 17892-12 [34]	
Gravimetric water content (w_0)	EN ISO 17892-1 [27]	Dried at 45°C
Water absorption (w_A)	DIN 18132 [30]	Enslin-Neff / 1 g specimen
Compressibility – oedometer	EN ISO 17892-5 [31]	70/20 mm fixed ring cell oedometer
Shear strength – direct shear test	EN ISO 17892-10 [32]	60/60/20 mm shear box
Hydraulic conductivity ($k_{10°C}$)	EN ISO 17892-11 [33]	Falling head, oedometer cell

The water absorption evaluated according to DIN 18132 standard allowed to calculate the water absorption capability of treated soils, through Equation (3.5), after 24 h ($w_{A\ 24\ h}$) and after the test was finished ($w_{A\ max}$). Dry conical specimens were placed on a filter disc using the funnel. The measurements of time and volume of absorbed water started when the first particles dropped onto the filter disc. Although the specimen holder was covered with a glass stopper during the test, the measured values were corrected to account for evaporation. The evaporation rate was frequently determined by measuring the time changes in water volume in the measuring capillary without a specimen on the filter disc

To enable the investigation of compressibility, shear strength and hydraulic conductivity in saturated state, the specimens assembled into the oedometer or direct shear cell were submerged under water and left to swell. Once swelling was complete, soaked specimens underwent consolidation in loading stages up to the highest selected effective vertical stress, 400 kPa in the case of the oedometer and 50 kPa, 100 kPa, or 150 kPa in the case of the direct shear test. Throughout the shearing stage, the vertical load was maintained constant, and specimens remained submerged. The rate of shear displacement ranged between 0.002 mm/min and 0.003 mm/min.

The number of conducted tests followed common geotechnical practice where one or two repetitions per specimen type are performed. However, for research purposes, the investigation of water absorption, compressibility and hydraulic conductivity were carried out with at least two repetitions for all specimens. The direct shear test was repeated for two sets of mixtures. Other tests were carried out without repetitions.

3.2.2.10 Evaluation of the grass germination with soil conditioners

The produced xanthan gum-based SCs were applied to the soil to investigate the effects of the biopolymers on the plant growth. The soil was mixed with the different compositions of soil conditioners at 1.8 wt%. The experimental procedure was adapted from a work of Chang et al. [116]. Three pots (length 40 mm × width 40 mm × depth 50 mm) for each sample were used. As reference, untreated soil and commercial product were also tested. In each of the 30 pots, the same number of grass seeds of *Nepeta Cataria* (HortuSì Srl, Italy) were planted. The seeds were covered with a thin layer (i.e., 5–10 mm) of soil and placed in a sealed chamber under constant thermo-hygrometric conditions (25 °C; 30%). Only 2 mL of water were supplied daily in each pot and no nutrients were applied. Seed germination of each soil/medium type was monitored periodically. Then, after 18 days, the daily water supply was cut off and the analysis was focused on which plants survived best under drought conditions.

3.2.3 Statistical analysis of the experimental results

All the experimental results were presented as mean ± standard error of the mean. Normally distributed data were analysed by using one-way analysis of variance (ANOVA) with significance level of 0.05. Pairwise differences between samples were assessed using the post hoc Tukey's test. Otherwise, a non-parametric Kruskal-Wallis analysis followed by the Conover's test was used.

4 Development of topsoil covers (TSCs)

Chapter 4 – Development of topsoil covers (TSCs) presents the methodologies and the experimental results referred to the production of multifunctional mulching films (topsoil covers) for forestry applications.

4.1 Xanthan-based TSCs reinforced with cellulose fillers

Published paper:

Sorze, A; Valentini, F; Dorigato, A; Pegoretti, A. Development of a xanthan gum based superabsorbent and water retaining composites for agricultural and forestry applications. *Molecules*, **2023**, 28 (4), 1952.

Biopolymers are eco-friendly materials that have been widely employed in food and medical applications [175,176]. Xanthan gum is one of the most promising materials, due to its biodegradability, soil-strengthening efficiency, film-forming ability, and high water-absorbing capability [133,135,136,170,177]. The use of fillers, based on wood or cellulose fibers, may offer the possibility of optimizing the performances of the materials, in terms of water absorption, water retention, and structural stability [178-181]. Despite the possible synergies derived from the combination of xanthan gum with cellulose fibers to produce materials for water retention applications, no study can be found in the open literature on this topic. Therefore, the aim of this work was to develop, for the first time, engineered bio-based hydrogels constituted of xanthan gum and cellulose fibers, in different concentration ratios, cross-linked with citric acid, to be used as topsoil covers (TSCs) for agricultural and forestry applications. The

choice of the materials and the methods adopted for the production of these composites have been optimized, so that they could be easily produced in large quantities for forestry and/or agricultural applications. The idea was to develop materials that are compatible with every type of soil (both sandy and clay), and that have better performances and comparable costs with products already present on the market.

4.1.1 Materials and methods

4.1.1.1 Materials

The materials employed in the production of topsoil covers are listed in Table 4.1. A more detailed description can be found in Section 3.1.

Table 4.1 List of materials employed for the preparation of TSCs.

Material	Label
Xanthan gum	XG
Cellulose fibers Arbocel R	R
Citric Acid	CA

4.1.1.2 Sample preparation

For the preparation of the topsoil covers, xanthan-based hydrogels were produced following the method described by Bueno et al. [139]. Citric acid was added to the 4 wt% xanthan gum solution, and after homogenizing it with the mixer for 3 min at 10'000 rpm, the solution was cast and dried at 45 °C overnight. The cross-linking reaction was performed by heating the dried samples in an oven at 165 °C for 7 min. In this case, four different samples were produced by tuning the amount of citric acid (0 wt%, 1 wt% and 2 wt% relative to the biopolymer matrix) and the amount of cellulose fibers (0 wt% and 2 wt%), as reported in Table 4.2.

Table 4.2 List of prepared the xanthan gum-based TSCs.

Sample	Xanthan Gum [wt%]	Cellulose Fibers [wt%]	Citric Acid [wt%]
TSC_A	4.0	2.0	1.0
TSC_B	4.0	2.0	2.0
TSC_C	4.0	0.0	1.0
TSC_D	4.0	2.0	0.0

4.1.1.3 Experimental techniques

The techniques used to characterize the prepared samples are listed in Table 4.3. A more detailed description can be found in Section 3.2.1.

Table 4.3 List of experimental techniques used to characterize the xanthan-based TSCs.

Technique	Parameters
Water absorption	Section 3.2.1.3
Evaluation of plant growth rate	Section 3.2.1.10

4.1.2 Results and discussion

4.1.2.1 Water absorption properties

For this analysis, only the cross-linked samples (TSC_A, TSC_B and TSC_C) were considered, because they kept their shape and consistency when immersed in water, while the not cross-linked sample (TSC_D) was completely dissolved in water after a few days. In Figure 4.1(a,b) the results of water absorption and release tests for the xanthan gum-based top soil cover are shown.

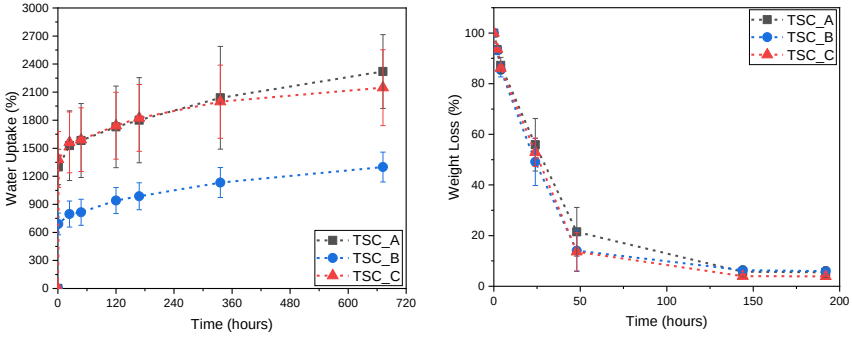

(a) (b)

Figure 4.1 Evaluation of the (a) water uptake and of the (b) weight loss for the prepared xanthan gum-based TSCs.

From Figure 4.1a it can be observed that the samples with a lower amount of citric acid (TSC_A and TSC_C) have a higher water absorption capability (up to 2000% after 700 h), compared to sample TSC_B, which has a higher citric acid content. In all the cases, the water uptake occurs in the first hours after immersion. It is also possible to observe that there are no evident differences between the results of samples TSC_A and TSC_C, meaning that the presence of cellulose fibers does not affect the water absorption tendency of the samples. However, from qualitative observations, the presence of the fibers in the hydrogels limits the volumetric shrinkage during drying.

4.1.2.2 Evaluation of plant growth rate with topsoil covers

For this experiment, TSCs constituted by 4.0 wt% of XG, 2.0 wt% of R and 1.0 wt% of CA have been selected and applied according to the methodology described in Section 3.2.1.10.
In Figure 4.2(a,b) the representative pictures of the plant cultivation with TSC at two different times are shown.

Figure 4.2 Representative pictures of the plant cultivation with TSC: (a) after 60 days and (b) after 80 days. (1) not cross-linked TSC, (2) cross-linked TSC, and (3) without TSC.

Figure 4.2(a,b) clearly show the effect of the TSC on plant growth. It is possible to observe that the two plants with the TSC (1 and 2) have a greater vegetation mass than the plant taken as a reference (3). This indicates that, in addition to not being harmful to plants, the selected TSC formulations could help to promote plant growth and improve the water regulating properties of the soil by slowing down the evaporation rate.

In Figure 4.3(a,b), the visual aspect of the TSC after 6 days and 80 days is displayed.

(a)

(b)

Figure 4.3 Visual aspect of the TSC (a) after 6 days and (b) after 80 days. (1) Not cross-linked TSC, (2) cross-linked TSC and (3) without TSC.

From Figure 4.3b it is possible to observe that after 80 days the TSC undergoes evident biodegradation with a volumetric shrinkage that is more significant for sample 1 (not cross-linked TSC), which means that heat treatment is useful for increasing the stability and the strength of the TSC. However, in both cases, the TSC works efficiently for a period of time that is comparable with the average lifespan of a tomato plant (2–3 months) making it suitable for this type of application. Moreover, it is important to point out that water was supplied to the plant every day, which results in the TSCs being subjected to many absorption/drying cycles that greatly stress the material with consequent accelerated biodegradation. For other applications, such as in forestry, in which the service life of a TSC is expected to be longer, it is important to note that the water supply would be determined only by the weather conditions and may not be supplied on a daily basis. In arid conditions (e.g, Mediterranean forests), this type of TSC would be less stressed by hydration/dehydration cycles, and its service life would be therefore increased. However, it is clear that the composition of these TSCs should be optimized, improving their durability and weathering stability for a period of at least 24 months, in order to make them suitable for real agricultural and forestry applications. Finally, it can be also observed from Figure 4.3b that the presence of the TSC on the soil helps to partially block the growth of competing weeds, showing

that the presence of a durable and stable TSC on the soil can be effective as expected, in this sense as well.

4.1.3 Conclusions

This work showed that novel bio-based hydrogel composites produced from xanthan gum and cellulose fibers could be effectively used to develop topsoil covers capable of promoting plant growth. The use of a biopolymer such as xanthan gum has proven to be very suitable for these applications due to its efficient water-absorbing properties. The cross-linking of xanthan gum with citric acid allowed the TSC samples to absorb water (up to 2000% after 700 h), while maintaining their dimensional stability and durability in the soil. From practical experiments conducted on the growth of tomato plants, it was observed that the presence of xanthan gum-cellulose fiber composites in the soil helped to better retain water, which was released to the plant more gradually than in untreated soil, thus enabling a more vigorous growth and an increased survival rate under drought conditions.

4.2 Xanthan-based TSCs reinforced with wood fibers

Published paper:

Sorze, A; Valentini, F; Burin Mucignat, M; Pegoretti, A; Dorigato, A. Multifunctional xanthan gum/wood fibers based hydrogels as novel topsoil covers for forestry and agricultural applications. *Carbohydrate Polymer Technologies and Applications*, **2024**, 7, 100520.

As described in Section 4.1, to further enhance water retention and mechanical stability of xanthan-based hydrogels, fillers based on cellulose microfibers can be successfully incorporated, reaching water absorption values up to 2000% after 700 h. However, cellulose microfiber-based fillers, although decreasing the volumetric shrinkage during drying compared to neat xanthan hydrogels, still undergo considerable volumetric shrinkage once used as TSC in practical applications. Moreover, they also have a high biodegradability in contact with soil (less than 3 months) and make the material too rigid. On the basis of these considerations, to provide alternatives to commercial fossil-based materials, with adequate technical performances, the present study is meant to improve the mechanical and dimensional stability of XG-based hydrogel formulations by changing the type of filler, i.e., by adding longer wood fibers. In particular, the aim of the work was to develop novel xanthan/wood fibers-based hydrogels and to study the effect of three different types of cross-linking agents (i.e., citric acid, sodium trimetaphosphate and tannic acid) on the morphology, water absorption, water vapor permeability and mechanical properties of the resulting materials. These optimized hydrogels could be potentially applied as multifunctional bio-based and biodegradable topsoil covers in agriculture and forestry, becoming valid alternatives to commercial products. The newly developed mulching films, thanks to their high water-absorption capability, will be able to absorb and

retain water, helping seedlings during dry periods and improving the water management in agriculture and forestry.

4.2.1 Materials and methods

4.2.1.1 Materials

The materials used in this study are listed in Table 4.4 and have been already described in Section 3.1.

Table 4.4 List of materials employed for the preparation of optimized TSCs.

Material	Label
Xanthan gum	XG
STEICO flex 036 (milled)	ST
Citric acid	CA
Sodium trimetaposphate	STMP
Tannic acid	TA
Glycerine	GLY

A commercial woven polyethylene (PP) mulching film (Rama S.p.A, RE, Italy) was also tested as a reference for some experiments (0.25 mm of thickness).

4.2.1.2 Sample preparation

Samples were prepared by mixing xanthan gum, wood fibers and glycerine. Glycerine and XG were used in a 1.2:1 weight ratio, while XG and WF were mixed in a 1:1 relative weight ratio. These ratios were chosen after preliminary laboratory tests. Glycerine and XG were mixed together to obtain a paste, then hot water (T ~ 60 °C) was added to the paste and mixed for 3 minutes with an industrial mixer (Fama Industries Srl, Italy), until a homogeneous and lump-free solution was obtained. Wood fibers were further reduced in size using a JK-IKA LABORLINK M20 grinder for 30 s, reaching an average

length of 9-30 mm, and then added to the solution. The compound was then stirred again until a homogeneous mixture was obtained. Different compositions were prepared by adding the three cross-linking agents (CA, STMP and TA), previously dissolved in 50 ml water solution at different concentrations, as reported in Table 4.5. A reference sample (XG_WF) without any cross-linking agent was also produced. The resulting mixtures were manually spread on a plate, dried at room temperature and then subjected to a thermal treatment of 165 °C for 3.5 minutes in oven, in order to perform the cross-linking reaction. These parameters and the selected cross-linking agent concentrations were identified after preliminary trials and on the basis of literature studies on xanthan hydrogels [139,182]. Table 4.5 reports the code identification and the composition, in terms of per hundred rubber (phr), of the different samples obtained.

Table 4.5 Sample coding for the prepared XG/wood fibers-based samples.

Code	**Xanthan Gum (phr)**	**Wood Fiber (phr)**	**CA (phr)**	**STMP (phr)**	**TA (phr)**
XG_WF	100	100	-	-	-
CA10	100	100	10	-	-
CA50	100	100	50	-	-
CA60	100	100	60	-	-
CA100	100	100	100	-	-
STMP50	100	100	-	50	-
STMP60	100	100	-	60	-
STMP150	100	100	-	150	-
TA5	100	100	-	-	5
TA20	100	100	-	-	20
TA50	100	100	-	-	50

4.2.1.3 *Experimental techniques*

The techniques used to characterize the prepared samples are listed in Table 4.6. A more detailed description can be found in Section 3.2.1.

Table 4.6 List of experimental techniques used to characterize the optimized TSCs.

Technique	Parameters
FT-IR	Section 3.2.1.1
Microstructural characterization	Section 3.2.1.2
Water absorption	Section 3.2.1.3
Water vapor permeability	Section 3.2.1.4
Penetration resistance	Section 3.2.1.6
Weather conditioning in external environment	Section 3.2.1.9

4.2.2 Results and discussion

4.2.2.1 *Fourier-Transformed Infrared Spectroscopy (FT-IR)*

Figure 4.4(a-c) present the FT-IR spectra of the cross-linked samples with CA, STMP and TA and compare them with the reference sample (XG_WF).

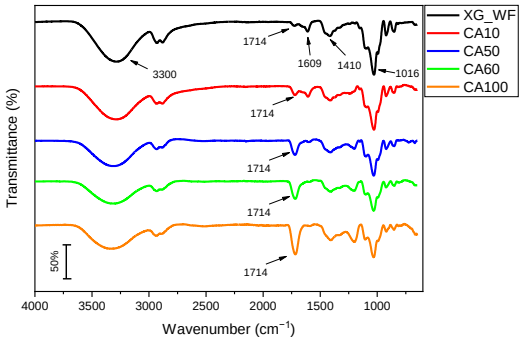

(a)

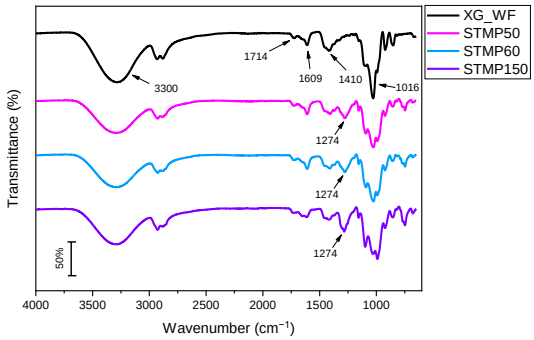

(b)

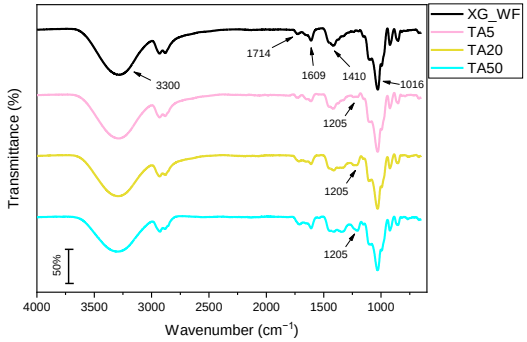

(c)

Figure 4.4 FT-IR spectra of XG/wood fibers samples cross-linked with different concentrations of (a) CA, (b) STMP and (c) TA.

For all the samples the broad absorption peak visible at 3300 cm^{-1} is ascribed to the O-H stretching vibration of hydroxyl groups, while the absorbance peak at 1016 cm^{-1} is associated to the C-O stretching vibration of the primary alcohol in XG and wood fibers. Peaks at 1410 and 1609 cm^{-1} are ascribed to the symmetrical and asymmetrical C=O vibration of the carboxylate anion ($-COO^-$), respectively, while absorbance peak at 1714 cm^{-1} is due to the presence of carbonyl groups of the carboxylic acid (-COOH) in XG and wood fibers. From Figure 4.4a it can be observed that the intensity of the absorbance peak at

1609 cm^{-1} gradually decreases with the concentration of cross-linking agent, while the intensity of the peak at 1714 cm^{-1} increases. This could suggest an increase in the cross-linking degree, since more ester groups are present in the chemical structure after the esterification reaction between citric acid and xanthan gum [183]. In Figure 4.4b samples cross-linked with STMP show an absorbance peak between 1250-1300 cm^{-1} whose intensity increases with the cross-linking agent content, this peak corresponds to the P=O stretching vibrations occurring from the reaction between STMP and XG and it is characteristic of the cross-linked polysaccharides [184]. From Figure 4.4c it can be noticed that the spectra of the TA cross-linked samples are very similar to that of the XG_WF sample. However, rising the TA content it is possible to observe an increase in the intensity of the peak at 1205 cm^{-1}, which can be associated to the C-O stretching vibration of the carbonyl groups of the aromatic esters of the tannic acid [185].

4.2.2.2 Microstructural characterization

SEM micrographs of the surface and of the cross-section of a dried xanthan/wood fibers-based hydrogel are shown in Figure 4.5(a,b). Since no morphological differences were found between the samples produced, only the micrographs of the reference sample (XG_WF) were reported.

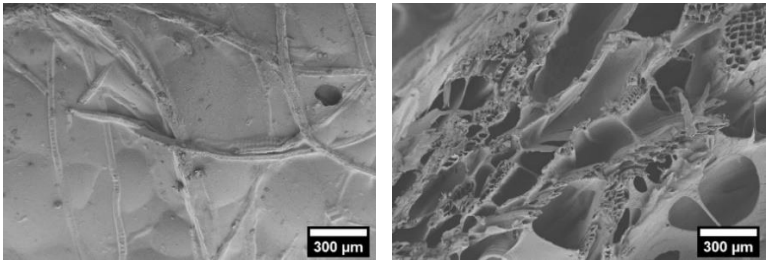

(a) (b)

Figure 4.5 SEM micrographs of dried XG_WF hydrogel. (a) Surface and (b) cross-section.

Figure 4.5a clearly shows that the surface of hydrogels is constituted by a network of wood fibers coated with xanthan gum. The result is a compact surface with few macropores. From Figure 4.5b it can be seen that the cross-section is characterized by lots of voids with dimensions ranging from 500 μm up to 10 μm. The presence of several pores facilitates the penetration and diffusion of water into the hydrogel network, resulting in a higher swelling capacity. Once in contact with water, the macropores fill with water first, resulting in a high initial water absorption rate. The micropores are then gradually filled, causing the hydrogel to absorb even more water [111]. It is also possible to clearly distinguish the cross-section of the wood fibers, consisting of lumens between 20 μm and 1 μm in size. These channels may improve the water storage capability of the hydrogels and increase their stiffness due to the formation of an intertwined network consisting of wood fibers.
In Table 4.7 values of density and porosity of the produced hydrogels, calculated according to Equations (3.1), (3.2) and (3.3), are reported.

Table 4.7 Values of density and porosity for the XG/wood fibers-based hydrogels.

Sample	ρ_{th} (g/cm³)	ρ_{app} (g/cm³)	P_{tot} (%)	P_{open} (%)
XG_WF	1.38 ± 0.01	1.01 ± 0.02	73.3 ± 1.5	63.2 ± 4.7
CA10	1.39 ± 0.02	1.16 ± 0.01	76.9 ± 2.2	72.4 ± 7.4
CA50	1.40 ± 0.02	1.19 ± 0.01	77.2 ± 1.4	73.1 ± 5.2
CA60	1.40 ± 0.02	1.22 ± 0.01	75.8 ± 1.1	72.1 ± 3.8
CA100	1.41 ± 0.02	1.21 ± 0.02	74.6 ± 1.2	70.3 ± 4.5
STMP50	1.47± 0.02	1.13 ± 0.02	74.9 ± 2.0	67.3 ± 6.6
STMP60	1.49 ± 0.02	1.21 ± 0.02	71.1 ± 1.3	64.3 ± 4.1
STMP150	1.61 ± 0.02	1.39 ± 0.01	70.8 ± 1.1	66.3 ± 3.0
TA5	1.39 ± 0.03	1.12 ± 0.02	69.1 ± 0.9	61.7 ± 2.8
TA20	1.41 ± 0.03	1.11 ± 0.02	75.9 ± 2.1	69.3 ± 7.4
TA50	1.45 ± 0.03	1.07 ± 0.01	75.2 ± 1.4	66.5 ± 4.3

It can be observed that overall, the samples are characterized by total porosity values ranging from 69% to 77% with no statistically significant difference at 0.05 level. Therefore, there is no clear influence of the type and content of cross-linking agent. In particular, the porosity of hydrogels is mainly an open porosity formed during the mixing phase of the production process, where air bubbles develop in the xanthan-based solution. Moreover, the introduction of wood fibers further contributes to increase the formation of pores in the structure, which can positively influence the final water absorption properties of the produced samples, but on the other hand can negatively affect their mechanical properties.

4.2.2.3 Water absorption properties

Water absorption properties were performed on the produced xanthan-based TSCs according to the procedure described in Section 3.2.1.3. Additionally, in this work, fully wet samples were left to dry at RT conditions. All specimens were subjected to three water absorption/desorption cycles, in order to investigate their behaviour on a longer time scale. In order to understand the diffusion mechanism of water molecules through the hydrogels structure, the diffusional coefficient n was evaluated, according to Equation (4.1) [186]:

$$\frac{M_t}{M_e} = kt^n \tag{4.1}$$

where M_t and M_e are the masses of water absorbed at a given time t and at equilibrium condition, respectively, and k is a constant. For values of n equal to 0.5 the diffusion mechanism is Fickian and the diffusion of water molecules within the matrix is not characterized by any physical or chemical interaction between the liquid and the solid phases.

Figure 4.6 (a-c) shows the water absorption curves of XG_WF sample and of the hydrogels cross-linked with CA, STMP and TA.

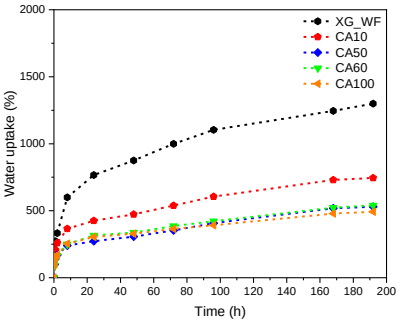

(a)

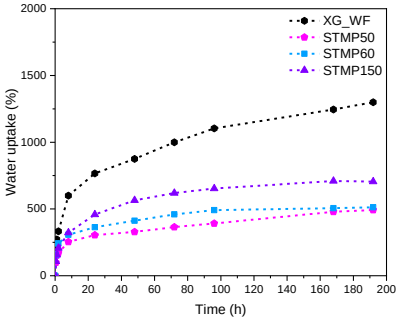

(b)

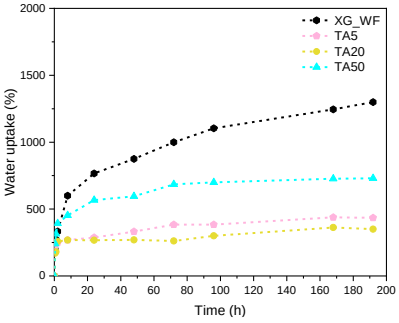

(c)

Figure 4.6 Water absorption curves of XG_WF sample and hydrogels cross-linked with (a) CA, (b) STMP and (c) TA.

All the tested specimens are able to reach a water uptake (WU) plateau and to resist in immersion for 8 days. The fact that the reference sample is insoluble in water and reaches a maximum value around 1300% confirms that an esterification reaction between the xanthan acid groups (pyruvyl or acetyl) and OH groups occurred during heat treatment, despite the absence of any cross-linking agent. However, for the cross-linked samples, the plateau achieved is lower than that of XG_WF, meaning that the presence of cross-linking agent increases the cross-linking density, which is inversely proportional to the swelling capacity [187]. Indeed, WU of samples made with CA ranges from 490% to 740% and it decreases with the cross-linking agent content. The opposite behaviour is instead observed for samples cross-linked with STMP. This can be attributed to the fact that, in addition to the cross-links, the reaction with STMP introduces more anionic charges into the XG chains. Therefore, the water uptake in STMP cross-linked hydrogels becomes greater due to the higher number of negative charges within the phosphorus species. Furthermore, the counter ions within these hydrogels, which neutralise the fixed charges on the polymer chains, lead to an increase of the osmotic pressure and result in a high swelling ratio [140,184]. WU of these samples reaches plateau values ranging from 490% to 700%, i.e., lower than that observed for CA cross-linked samples. For hydrogels cross-linked with TA, the increase of the cross-linking agent content leads to a higher concentration of hydrophilic groups in the hydrogel structure. Thus, the cross-linking density decreases with a consequent increase in water uptake and swelling [188]. For these samples the WU ranges from 360% to 800%. Although most of the curves in the Figure 4.6(a-c) have a parabolic trend, by fitting the data according to Equation (4.1) it is observed that the values of the diffusion coefficient n are lower than 0.5. This means that the diffusion mechanism that drives the water absorption is described as quasi-Fickian, and the water molecules pass through a preferential way inside interconnected pores of the hydrogel.

Table 4.8 reports the WU values of samples after multiple water absorption/desorption cycles.

Table 4.8 Values of the final water uptake measured for the prepared hydrogels after multiple water absorption/desorption cycles.

Sample	WU (I cycle) (%)	WU (II cycle) (%)	WU (III cycle) (%)
XG_WF	1300 ± 71 [a]	2826 ± 217 [a]	3669 ± 567
CA10	744 ± 29 [ab]	1569 ± 20 [abc]	1812 ± 108
CA50	530 ± 30 [abc]	1425 ± 23 [bc]	1558 ± 61 [b]
CA60	540 ± 25 [abc]	1549 ± 80 [abc]	1662 ± 138
CA100	491 ± 33 [bc]	1596 ± 29 [abc]	1730 ± 105
STMP50	486 ± 35 [bc]	2535 ± 49 [ab]	-
STMP60	513 ± 70 [abc]	2082 ± 139 [ab]	-
STMP150	704 ± 114 [ab]	2772 ± 23 [a]	-
TA5	434 ± 74 [bc]	1301 ± 202 [bc]	1904 ± 418
TA20	361 ± 23 [c]	875 ± 53 [c]	-
TA50	726 ± 188 [ab]	1747 ± 516 [abc]	-

Different letters in a column indicate that results are statistically different ($p<0.05$).

The first notable result is that WU of samples after the second absorption cycle is almost the double compared to the first one. This is related to the fact that, after the first cycle, part of the water-soluble mass, mainly glycerine, is washed away. However, this is not a problem for the intended application of these materials, as the glycerine acts as a plasticiser and it has been introduced only to facilitate the sample preparation by dissolving the xanthan gum without the formation of lumps, and to make the TSCs flexible to ease their placement around the plant. Nevertheless, all samples are able to reach again an absorption plateau after 8 days of immersion. In all

cases the plateau value reached is lower than that of XG_WF sample (2800%). Ultimate WU of samples cross-linked with CA is practically independent from the CA content, with values ranging from 1400% to 1500% after 8 days. For the STMP and TA cross-linked samples the values of WU after the second cycle are found to be independent from the concentration of cross-linking agent. From the results of the third absorption cycle it is possible to observe that the reference sample reaches an elevated WU value (3700%), because of the rupture of the sample, of the continuous leaking of material and thus of the continuous absorption of water, which lead to the almost complete loss of the sample itself. Samples obtained with CA, on the other hand, are all able to resist a full third cycle of immersion and show noticeable stability. Final WU values are comparable to those obtained during second cycle, and range from 1550% to 1800%. From these tests, considering the need for a topsoil cover to have good WU ability and, most importantly, high stability after different water absorption/desorption cycles, CA50, CA60 and CA100 are found to be the most promising compositions for the intended application. No significant difference at 0.05 level was found between these samples for all the cycles. This means that, for the amount of XG used, a threshold value of the degree of cross-linking was reached, beyond which, further increasing the CA content would not result in any significant improvement in properties. During the third cycle, STMP cross-linked samples and most of TA cross-linked hydrogels show instability and leakage due to excessive swelling, which lead in some cases to their breakage before reaching a plateau. Only TA5 should be kept into consideration due to its good WU behaviour.

4.2.2.4 Water vapor permeability

Values of WVP2 and WVP of the different xanthan/wood fibers based hydrogels, calculated according Equation (3.7) and (3.8), are reported

in Table 4.9 and compared with those of a commercial woven PP mulching film.

Table 4.9 Values of WVP2 and WVP of the xanthan/wood fibers based hydrogels and of a commercial PP mulching film.

Sample	**WVP2 × 10^{-6} (g/(m^2·s·Pa))**	**WVP × 10^{-9} (g/(m·s·Pa))**
XG_WF	14.7 ± 0.4	37.5 ± 1.2
CA10	11.4 ± 0.3	32.2 ± 0.7
CA50	10.2 ± 0.3	30.7 ± 0.1
CA60	9.9 ± 0.1	29.0 ± 0.1
CA100	9.1 ± 0.1	27.7 ± 0.1
STMP50	13.7 ± 0.4	40.7 ± 1.3
STMP60	14.8 ± 0.5	31.0 ± 2.8
STMP150	12.0 ± 0.5	34.3 ± 1.2
TA5	14.8 ± 0.4	31.9 ± 0.2
TA20	17.2 ± 0.5	38.8 ± 0.4
TA50	15.0 ± 0.4	37.6 ± 0.5
PP film	8.1 ± 0.1	2.1 ± 0.1

In general, the water-barrier properties of xanthan/wood fibers based hydrogels are rather poor due to the presence of hydrophilic groups, which increase the water absorption properties but also increase the water vapor permeability [189]. However, positive results can be seen by looking at the WVP2 values of the CA cross-linked samples, which are lower than that of XG_WF and comparable to that of the commercial woven PP mulch film. This can be explained by the fact that the cross-linking reaction between citric acid and XG reduces the amount of available hydrophilic groups in the structure and thus reduces the water vapor moving through the hydrogel structure, thus increasing the water barrier properties. However, the WVP values of the xanthan/wood fibers-based hydrogels are still one order of

magnitude higher than that of the commercial product. This can be explained by the fact that the permeability is strongly influenced by the thickness of the sample (increasing the thickness, the WVP increases [190]) and, in this case, the thickness of the commercial product is 10 times lower than that of the produced hydrogels. Furthermore, the presence of a plasticizer such as glycerol in the hydrogels increases the mobility of the polymer chains and thus further enhances the water vapor diffusion properties [191]. Samples cross-linked with STMP and TA show much higher WVP2 and WVP values with respect to the commercial mulching film, without any clear influence of the cross-linking agent content. This behaviour can be explained by the high swelling tendency of these samples once in contact with water [190]. For topsoil cover applications it would be important to have WVP values as low as possible, in order to limit the water evaporation rate from soil, as in the case of the commercial products. However, it is important to underline that the thickness of the hydrogels prepared in this work can be adjusted during the preparation phase in order to obtain the desired water vapor barrier properties.

4.2.2.5 Penetration resistance

Figure 4.7 shows the results of penetration resistance tests performed on the xanthan/wood fibers based hydrogels and on the PP commercial film, expressed in terms of maximum load sustained by the samples.

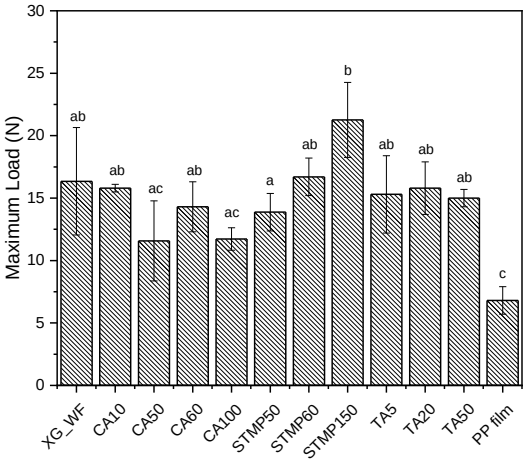

Figure 4.7 Penetration resistance of the produced xanthan/wood fibers-based samples and of the commercial PP mulching film. Different letters indicate that results are statistically different ($p<0.05$).

It can be seen that for all the samples produced the maximum penetration load is between 12 N and 20 N, and that their penetration resistance is mainly determined by the formation of a network of wood fibers that provides cohesion and improves the strength of the hydrogels. Considering the standard deviations values, there is no substantial influence of the type and concentration of the cross-linking agent on the penetration resistance and, overall, there is no significant difference at 0.05 level between samples. The only significant difference ($p<0.05$) can be found between STMP150, CA50 and CA100. CA50 is characterized by high standard deviation, while the behaviour of CA100 can be ascribed by its high CA content, which leads to a stiffening of the structure and a consequent lower penetration resistance. It is interesting to notice that some samples are statistically different ($p<0.05$) with respect to the commercial PP woven film, which shows a mean penetration resistance of 6.8 N. This difference may be attributed to the much lower thickness of the PP commercial film. However, for the purpose of this test, i.e., the

assessment of the ability of the TSCs to resist weed perforation, the absolute maximum penetration load should be considered, without any normalization. It is also important to underline that these penetration resistance values refer to dry samples which, in a practical topsoil cover application, would correspond to the initial condition in which the samples are placed around the plant. From this point on, the samples will be subjected to substantial variations of the environmental conditions (i.e., temperature, humidity, UV radiation) that may alter the structure of the hydrogel, causing swelling and thus changing its mechanical properties. Therefore, further investigations will be needed to study the mechanical resistance of these hydrogels under different environmental conditions.

4.2.2.6 Weather conditioning in external environment

The weather conditioning test was performed only on the compositions CA60 and TA5, as they proved to have efficient water absorption after multiple cycles, good water vapor permeability and interesting penetration resistance. The results are reported in Table 4.10.

Table 4.10 Results of outside weather conditioning tests after 1, 2 and 7 months on the prepared hydrogels with optimized compositions.

Sample	**A_L 1 month (%)**	**A_L 2 months (%)**	**A_L 7 months (%)**	**Residual Mass 7 months (%)**
CA60	22.1 ± 1.1	15.4 ± 2.3	50.7 ± 8.0	36.4 ± 6.6 [a]
TA5	22.2 ± 1.2	29.2 ± 2.1	46.5 ± 8.3	57.6 ± 8.9 [b]

Different letters in a column indicate that results are statistically different ($p<0.05$).

It can be seen that the area loss does not decrease steadily over time, but it can also increase. This is due to the fact that, in the presence of rainfall, the materials absorb water and swell, increasing their volume. In general, the samples show good stability after 2 months, as it has been already seen after multiple cycles of water absorption and desorption (see Section 4.2.2.3), due to the presence of the cross-linking agents. During the test, the samples show some warping and deformation, but substantially maintain their original shape. This is due to the presence of the network of long wood fibers (9-30 mm length) in the hydrogels, which limits shrinkage during drying periods. The values of residual mass indicate that samples underwent biodegradation, which is more prominent for the CA60 sample which shows a greater mass loss at the end of the test compared to TA5 sample ($p<0.05$). The development of fully biodegradable topsoil covers is of paramount importance to overcome the problems of end-of-use removal of commercial plastic mulch films. By tuning the size of TSCs and the cross-linking agent content, it would be possible to tailor the biodegradation time of the samples. In agricultural applications the maximum time required for the complete biodegradation of TSCs is only few months (seasonal planting), while in forestry applications their service time could be longer (1 or 2 years). It is also important to note that the growth of vegetation was completely inhibited in the area below the samples for the first 3 months, while grasses and weeds only grew in the area between them. After 7 months, due to weather effects and the biodegradation of materials, different weed filaments were able to perforate the samples.

4.2.3 Conclusions

In this work, multifunctional bio-based and biodegradable hydrogels constituted of xanthan gum and wood fibers were developed with the aim to produce novel eco-sustainable topsoil covers for the agricultural and forestry sectors, able to support plant growth and

increase their survival rate, especially under drought conditions. Different cross-linking agents, such as citric acid, sodium trimetaphosphate and tannic acid, were added in different concentrations to obtain cross-linked hydrogels with different physical properties. Water absorption tests highlighted the capacity of the developed hydrogels to effectively absorb water after multiple absorption/desorption cycles, especially in samples cross-linked with citric acid. These hydrogels also exhibited water vapor permeance values comparable to that of a commercial plastic mulching film along with good penetration resistance, an important property for mulching films to inhibit weed growth. On the basis of the results of outdoor weathering conditioning tests, it was assessed that citric acid cross-linked hydrogels manifested a good stability after 2 months and suitable biodegradability after 7 months, with a final mass loss of 63.6%.

4.3 Investigation of the TSCs flammability

Paper in preparation:

Sorze, A; Bösing, J; Hirschmüller, S; Dorigato, A. Investigation of the flame behaviour and thermal degradation of gelatin- and xanthan-based wood fibers composites used as topsoil covers for forestry applications.

Part of this study was carried out during the visiting period at the University of Applied Science of Rosenheim (THRO) in Germany from February 15th 2024 to May 15th 2024.

Considering that the purpose of topsoil covers is to support plant growth in forestry applications and that one of their main constituents is wood fibers, a primary concern may arise related to the risk of flammability of these products and the subsequent development of forest fires. Therefore, the aim of this study was to primarily investigate the flame behaviour of the TSCs produced in Section 4.2. Moreover, to improve the flame retardancy of the xanthan-based TSC, a variation in the previous composition has been introduced. Specifically, a casein coating has been applied on the surface of the TSC. Casein is characterized by high phosphorous and nitrogen contents, thus has been proven to be a potential bio-based flame retardant additive [192,193]. A comparative study was performed with the TSC samples based on gelatin produced by the University of Applied Sciences of Rosenheim (THRO). In this case, the high nitrogen content of amino acids in gelatin may suggest that it is a low-flammability material [194,195].

4.3.1 Materials and methods

4.3.1.1 Materials

The materials employed in the production of xanthan-based TSCs are listed in Table 4.11. A more detailed description can be found in Section 3.1.

Table 4.11 List of materials employed for the evaluation of the flame behaviour of TSCs.

Material	Label
Xanthan gum	XG
STEICO flex 036 (milled)	ST
Glycerine	GLY
Citric acid	CA
Tannic acid	TA
Casein	CAS
Gelatin	GEL

4.3.1.2 Sample preparation

The details for the production of xanthan-based TSCs are extensively described in Section 4.2.1.2. In particular, for this study the compositions CA60 and TA5 (Table 4.5) were tested. These compositions were selected as they showed the most promising results from tests described in the previous sections. Moreover, a third composition, coded as CA60_cas, was also prepared. This formulation was produced from sample CA60 and by applying a layer based on an alkaline solution of casein to the upper side of each sample. The casein coating was prepared according to the methodology described by Picchio et al. [196]. First, casein (10 wt%) was dissolved in 1M NaOH solution at 40 °C under magnetic stirring, glycerol (50 wt% of casein) was then added followed by incorporation of tannic acid (10

wt% of casein) previously dissolved in 500 μL of 1M NaOH. The solution was then mixed for 1 hour before use.
In this study, the samples produced by THRO have been also tested. These sample were constituted by gelatin-based composites which were prepared starting from two different batches (A and B): batch A composed of 12 wt% of the total amount of water, while batch B of the 88 wt%. Initially, NaOH was added to batches A and B to ensure a pH of 9, then tannic acid was added to batch A at room temperature and gelatin was added to batch B pre-heated at 55 °C. The mixing process continued for 120 minutes until complete swelling of gelatin in batch B was reached; NaOH was added to keep the pH at 9. Batch A was then gradually added to batch B under continuous mixing (pH is kept at 9), followed by the addition of wood fibers. Finally, the homogeneous solution was poured into a mould and cured under air flow for two weeks at room temperature. By changing the content of gelatin, tannic acid and wood fibers respect to water, five different compositions were produced, as reported in Table 4.12.

Table 4.12 List of the prepared gelatin-based TSCs.

Sample	Gelatin [wt%]	Wood Fibers [wt%]	Tannic acid [wt%]
ID5	8.0	6.0	1.0
ID6	15.0	6.0	2.0
ID7	8.0	12.0	1.0
ID8	15.0	12.0	2.0
ID9	11.5	9.0	1.0

Finally, in Table 4.13 a list of the tested samples is reported considering both samples produced from UNITN and THRO.

Table 4.13 List of samples use for the flame tests.

Base material	Code
Xanthan gum	CA60 CA60_cas TA5
Gelatin	ID5 ID6 ID7 ID8 ID9

4.3.1.3 Experimental techniques

The techniques used to investigate the flame behaviour of the prepared samples are listed in Table 4.14. A more detailed description can be found in Section 3.2.1.

Table 4.14 List of experimental techniques for the evaluation of the flame behaviour of TSCs.

Technique	Parameters
TGA	Section 3.2.1.5
Single flame source test	Section 3.2.1.7
LOI	Section 3.2.2.10

4.3.2 Results and discussion

4.3.2.1 Thermogravimetric analysis (TGA)

In Figure 4.8(a,b) and Table 4.15 the results of the thermogravimetric analysis are reported.

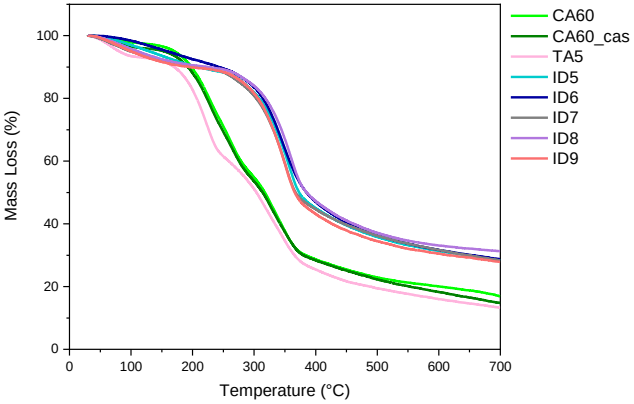

(a)

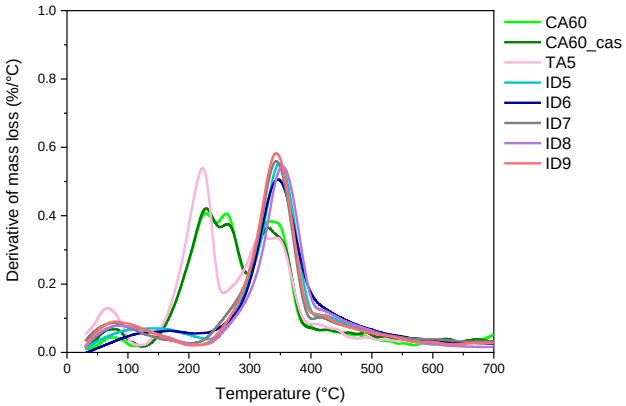

(b)

Figure 4.8 (a) TGA curves and (b) DTG curves of the TSCs samples.

Table 4.15 Results of the thermogravimetric analysis on TSCs.

Sample	$T_{max,1}$ (°C)	$T_{max,2}$ (°C)	$T_{max,3}$ (°C)	$T_{max,3}$ (°C)	m_{700} (%)
CA60	228.3	262.2	331.3	344.5	16.8
CA60_cas	229.2	263.5	328.6	348.3	14.8
TA5	222.2	-	321.5	345.5	13.2
ID5	-	-	-	356.5	28.4
ID6	-	-	-	347.5	28.7
ID7	-	-	-	351.0	28.3
ID8	-	-	-	360.2	31.3
ID9	-	-	-	350.5	27.9

From Figure 4.8a, for all the samples, it is possible to observe a first mass loss (around 7%) between 35 to 125 °C associated to moisture evaporation. As reported in Table 4.15, for the xanthan-based TSCs the first important mass loss (around 30%) is observed at 225 °C, associated to the degradation of the glycerine. The CA-cross-linked samples show a second DTG around 262 °C, corresponding to the degradation of the citric acid. Finally, the degradation of the XG and the wood fibers occurs in the range between 320 to 330 °C with two almost superimposed peaks due to the chemical similarity of these constituents. Overall, the casein coating does not significantly affect the TGA results of the CA-cross-linked samples.

For the gelatin-based TSC samples, it is possible to observe only a single degradation peak, between 347 to 360 °C, associated to the superimposed degradation of gelatin, wood fibers and tannic acid. For these compositions, there is no relevant difference in terms of degradation temperatures and residual mass.

4.3.2.2 *Single flame source tests*

In Figure 4.9 two representative images of TSCs samples during the single flame source test are reported.

Figure 4.9 Representative images during the single flame source test of TSCs samples: (a) CA60 (based on xanthan gum) and (b) ID5 (based on gelatin).

The results of the single flame source test show that all the gelatin-based TSCs do not burn but the flame self-extinguished as soon as it is removed from the sample. All samples produce a white smoke and it can be seen that the burnt part of the sample expanded in volume. This behaviour is specific to gelatin, which tends to expand during combustion process due to the release of gases during reaction, thus extinguishing the flame [197] .

About the xanthan-based TSCs, different behaviours can be observed for each composition. Samples cross-linked with citric acid do not burn and the flame self-extinguished after a few seconds after it is removed from the sample. The casein coating does not substantially affect the sample behaviour, as the composition CA60 and CA60_cas

behave in the same way. On the other hand, specimens cross-linked with tannic acid (composition TA5) failed the test, as the flame continued to propagate along the specimens and burnt out completely. This different behaviour compared to the citric acid could be explained by the different cross-linking mechanism of these acids with XG. However, at present, there is no evidence in the literature regarding this behaviour and further studies are recommended to investigate these aspects more thoroughly.

4.3.2.3 Limit Oxygen Index (LOI)

In Figure 4.10(a,b) two representative pictures of the TSCs samples during and at the end of the LOI test can be observed.

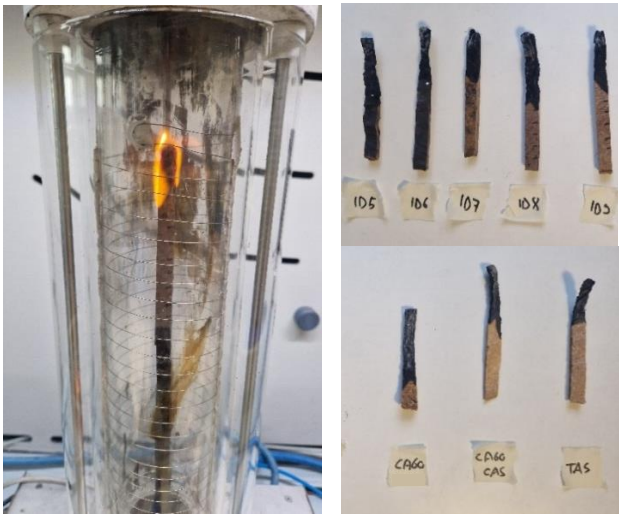

Figure 4.10 Representative images of TSCs samples (a) during the test and (b) at the end of test.

In Table 4.16 the results of the LOI tests for the TSCs samples are reported.

Table 4.16 Results of the LOI test. Different letters indicate that results are statistically different ($p<0.05$).

Sample	LOI [vol% O_2]
CA60	23.5 ± 0.1 [a]
CA60_cas	23.7 ± 0.1 [a]
TA5	22.4 ± 0.2 [a]
ID5	36.3 ± 0.1 [bc]
ID6	41.5 ± 0.1 [c]
ID7	31.2 ± 0.2 [ab]
ID8	33.6 ± 0.1 [abc]
ID9	33.3 ± 0.1 [abc]

From Table 4.16 it can be observed that the xanthan-based TSCs cross-linked with citric acid (CA60 and CA60_cas) have an oxygen index higher than the standard oxygen condition in air. On the other hand, the composition with tannic acid shows values very close to the oxygen concentration in air, thus meaning that this composition does not have a good flame behaviour.

The gelatin-based TSCs are characterized by statistically higher values of LOI ($p<0.05$), thus confirming their ability to resist combustion in air. Indeed, the LOI values are correlated to the sample composition. Specifically, increasing the gelatin-to-wood fibers ratio (as reported in Table 4.12) the LOI values are higher. This is highlighted by sample ID6, which is characterized by the highest gelatin-to-wood fibers ratio and highest LOI value. On the other hand, compositions constituted by a lower gelatin-to-wood fibers ratio (i.e., ID7) are characterized by slightly lower LOI values.

4.3.3 Conclusions

This study demonstrated the non-flammable behaviour of the produced topsoil covers, despite the presence of wood fibers in their

composition. The TGA results showed that the xanthan gum-based samples started to thermally degrade at around 220 °C, while the gelatin-based TSCs at around 350 °C. In both cases these temperatures are well above the typical working conditions of TSCs for the intended application. Single flame source tests revealed the flame self-extinguishing capability of both TA-cross-linked gelatin-based and CA-cross-linked xanthan-based TSCs. Gelatin-based samples showed higher LOI values, especially increasing the gelatin-to-wood fibers ratio. The addition of a casein coating on the surface of XG-based samples did not significantly affect the flame behaviour. However, it must be considered that the casein coating is a surface treatment and both performed flame tests required the flame to be applied to the edge of the specimen not coated with the casein layer. Further analysis should be performed in order to deeply investigate this aspect.

5 Development of soil conditioners (SCs)

Chapter 5 – Development of soil conditioner (SCs) presents the methodologies and the experimental results referred to the production of soil conditioners for forestry applications.

5.1 Optimization of the formulation

Published paper:

Sorze, A; Valentini, F; Dorigato, A; Pegoretti, A. Development of a xanthan gum based superabsorbent and water retaining composites for agricultural and forestry applications. *Molecules*, **2023**, 28 (4), 1952.

Soil conditioners are products that can be mixed with the soil in the planting pit to enhance its physical, chemical, mechanical, and water-regulating characteristics [101]. To counteract the problems caused by drought and water shortage, one of the main requirements for these products is the ability to absorb large amounts of water; therefore, superabsorbent hydrogels are widely used for this type of application [111,121]. However, traditional soil conditioners often rely on synthetic polymers, which come with significant drawbacks. In fact, these synthetic materials have limited bio-degradability and release harmful by-products into the soil, posing risks to both the environment and human health [111,127,128]. To address these concerns, researchers have considered various biopolymers as potential alternatives to traditional plastics for SCs [109,112,124]. For soil conditioning purposes, xanthan gum is one of the most promising materials, due to its biodegradability, soil-strengthening efficiency, film-forming ability, and high water-absorbing capability [133,135,136,170,177]. Xanthan gum is soluble in both cold and hot

water and therefore can easily form hydrogels and gel-like structures. The use of fillers, based on wood or cellulose fibers, may offer the possibility of optimizing the performances of the materials, in terms of water absorption, water retention, and structural stability [178-181]. Although the combination of xanthan gum and cellulose fibers for soil conditioning applications may offer potential synergies, there are no studies on this topic available in the literature. Therefore, the aim of this work was to develop, for the first time, engineered bio-based composites constituted of xanthan gum and cellulose fibers, in different concentration ratios, to be used as soil conditioners (SCs) for agricultural and forestry applications. Material selection and production methods for these composites have been optimized to enable large-scale production for forestry and agricultural applications. The goal was to create materials compatible with all types of soils, including the sandy and clay ones, that offer superior performance and cost comparable to existing products on the market.

5.1.1 Materials and methods

5.1.1.1 Materials

The materials employed in the production of soil conditioners are listed in Table 5.1. A more detailed description can be found in Section 3.1.

Table 5.1 List of materials employed for the preparation of SCs.

Material	Label
Xanthan gum	XG
Cellulose fibers (Arbocel R)	W

As a benchmark, tests on the soil were also performed using a commercial potassium polyacrylate-based soil conditioner, called Idrogea [167] and purchased from Endofruit Srl (Verona, Italy). According to the technical datasheet, it is a solid powder constituted

by 95% of potassium polyacrylate (CAS 25608-12-2). It has a relative density of 0.7 g/cm^3, pH of 7.7 and an absorption capacity of at least 300 times its weight in water and a cation exchange capacity of not less than 460.00 m_{eq}/100 g. According to the supplier, the concentration of this product to be used in the soil is 0.13 wt%.
The soil used in this study was sampled from a forest near the city of Trento (Italy). Appropriate analyses for the characterization were carried out by Fondazione Edmund Mach (San Michele all'Adige, TN, Italy), and its main properties are reported in Table 5.2.

Table 5.2 Results of the chemical analysis of the soil used in this work.

Determination	**Value**
Sand (2.0–0.05 mm)	595 g/kg
Silt (0.05–0.002 mm)	345 g/kg
Clay (<0.002 mm)	60 g/kg
pH (in water ratio 1:2.5)	7.2
Total limestone	668 g/kg $CaCO_3$
Active limestone	11 g/kg $CaCO_3$
Organic substance	257 g/kg
Assimilable phosphorus	45 mg/kg P_2O_5
Potassium	112 mg/kg K_2O
Magnesium	2238 mg/kg MgO

5.1.1.2 Sample preparation

For the preparation of the soil conditioners, xanthan gum powder was dissolved in water at three different relative concentrations (1 wt%, 2 wt% and 4 wt%). This biopolymer is soluble in cold water, so the procedure was carried out at room temperature by mixing the solution with the use of a Dispermat® F1 mixer (VMA-Getzmann Gmbh, Reichshof, Germany), operating at 5000 rpm for 15 min, in order to obtain a homogeneous mixture without lumps. During mixing, different amounts of cellulose fibers (0 wt%, 2 wt% and 5 wt%

relative to water solution) were gradually added. In this way, nine different compositions were obtained, as reported in Table 5.3.

Table 5.3 List of the prepared compositions used as SCs.

Sample	Xanthan Gum [wt%]	Cellulose Fibers [wt%]
X1	1.0	0.0
X2	2.0	0.0
X4	4.0	0.0
X1W2	1.0	2.0
X2W2	2.0	2.0
X4W2	4.0	2.0
X1W5	1.0	5.0
X2W5	2.0	5.0
X4W5	4.0	5.0

5.1.1.3 Experimental techniques

The techniques used to characterize the prepared samples are listed in Table 5.4. A more detailed description can be found in Section 3.2.2.

Table 5.4 List of experimental techniques used to characterize the SCs.

Technique	Parameters
Rheological properties	Section 3.2.2.1
Light microscopy	Section 3.2.2.3
Moisture absorption	Section 3.2.2.4
Morphological analysis of the soil treated with SCs	Section 3.2.2.5
Maximum water holding capacity (MWHC) of the soil	Section 3.2.2.6
Water retention capacity of the soil	Section 3.2.2.7
Evaluation of the grass germination	Section 3.2.2.10

5.1.2 Results and discussion

5.1.2.1 Rheological properties

In Figure 5.1(a–c) the results of the rheological analysis are displayed. In particular, in Figure 5.1c the values of yield stress obtained by fitting the viscosity data according to the Casson model (see Equation (3.10)) are reported.

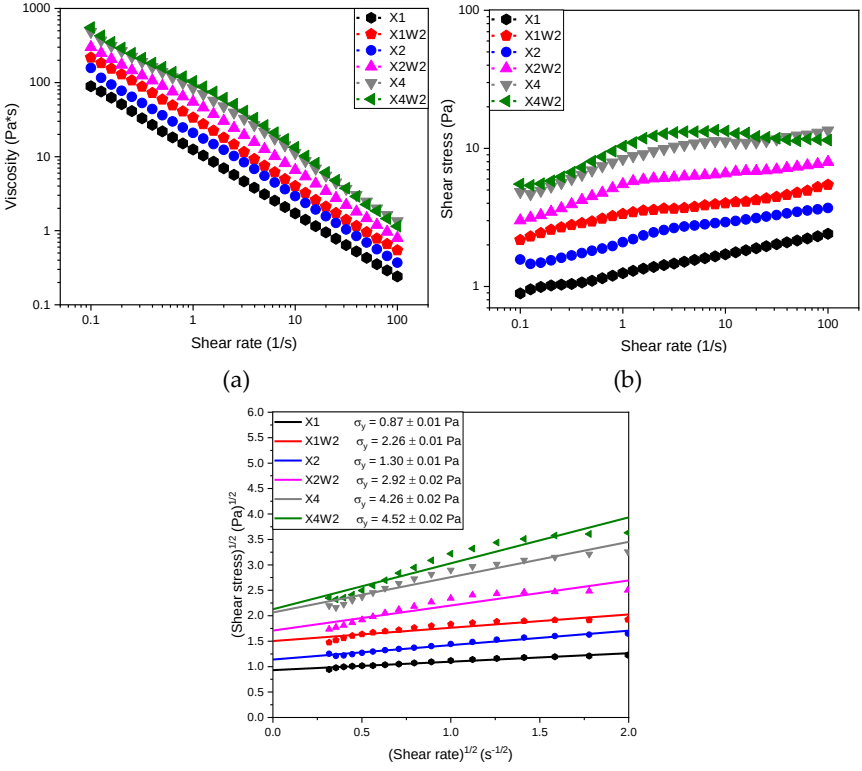

Figure 5.1 Rheological tests on the soil conditioners. Trends of (a) shear viscosity and (b) shear stress as a function of the shear rate. (c) Linear interpolation of shear stress values for the determination of the yield stress, according to the Casson model (see Equation (3.10)).

Rheological measurements show that by increasing the amount of the xanthan gum and cellulose fibers in the composites, the viscosity and the shear stress are increased up to one order of magnitude (from 100 to 1000 Pa·s and from 1 to 10 Pa, respectively). Moreover, from Figure 5.1b it can be observed that these composites show a yield stress, which indicates the minimum stress required for the material to flow. Figure 5.1c shows that the yield stress increases with the amount of XG and cellulose fibers in the solution. This means that the increase in the concentration of XG in the solution and the presence of the fibers leads to an increase in the ionic strength of the system and thus to the strengthening of the gel network, as also con-firmed by Talukdar et al. [198], who investigated the drug release behaviour of XG solutions.

5.1.2.2 Optical microscopy

Figure 5.2(a–i) shows the optical microscopy images for each sample.

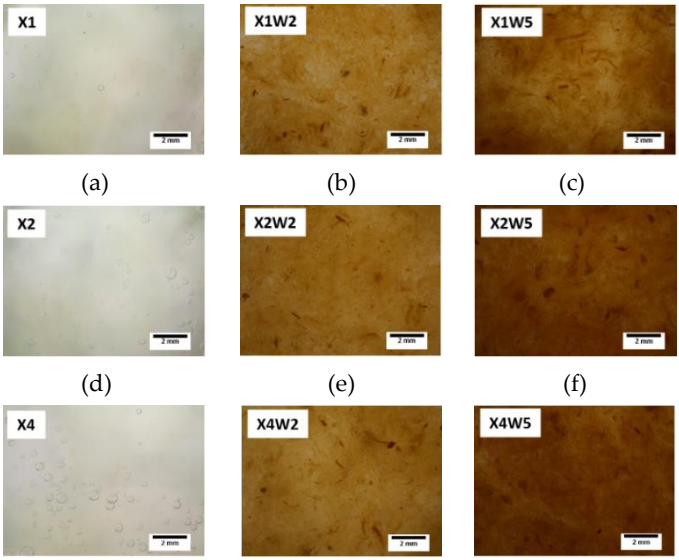

Figure 5.2 Light microscope images of the prepared samples: (a) X1, (b) X1W2, (c) X1W5, (d) X2, (e) X2W2, (f) X2W5, (g) X4, (h) X4W2, (i) X4W5.

It is possible to notice that an increase in the concentration of xanthan gum and cellulose fibers in the solution leads to a densification of the gel structure, passing from a very aqueous solution (X1) to a more viscous and denser one (X4W5). Moreover, it can be observed that the structure appears to be quite homogeneous in all of the samples, without the presence of evident lumps and agglomerates in the composites. This means that the mixing process was performed efficiently with an effective dispersion of the polymer and the fibers in the water solution. It can be hypothesized that the network of cellulose fibers within the sample structure may lead to a reinforcing and stabilizing effect of the material, when it is applied in the soil [199,200].

5.1.2.3 Moisture absorption properties

In Figure 5.3 the results of the moisture absorption and water release measurements for the different formulations are reported.

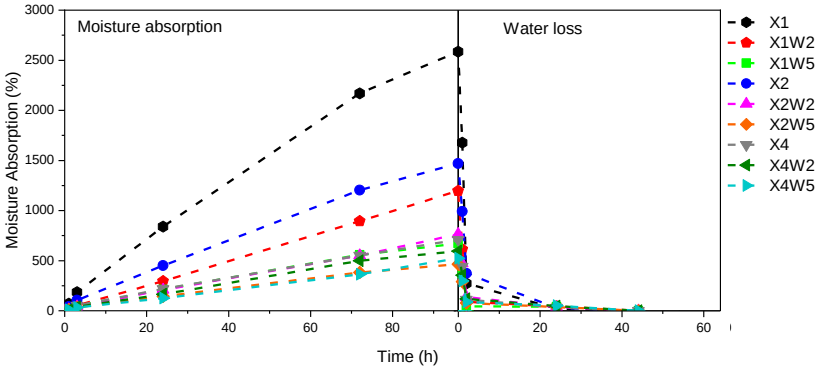

Figure 5.3 Evaluation of the moisture absorption (left) and of the water release (right) for the different formulations.

Figure 5.3 shows that the moisture absorption of the tested samples increases almost linearly with time and that the values of the moisture absorption capacity increase for the samples with a lower amount of xanthan gum and cellulose fibers. The increase in the concentration of

xanthan gum and cellulose fibers in the solution leads to a decrease in the moisture absorption capacity. This behaviour can be explained by the chemical similarity between xanthan gum and cellulose fibers which may lead to a good interfacial adhesion between the two components, which, to some extent, can slow down the diffusion of water molecules [179]. Moreover, increasing the amount of xanthan gum may result in the presence of lumps that may adversely affect moisture absorption. The analysis was concluded before reaching the plateau due to the formation of molds in the samples, which formed because the test was performed under elevated humidity conditions. In the right part of Figure 5.3, from the water retention test, the water loss mainly occurs in the first two hours, with an opposite trend with respect to water uptake measurements: an increase in the amount of fibers leads to a slight decrease in water release. Furthermore, from qualitative observation, the formation of a fiber network in the samples (see Figure 5.2) helps to limit the volumetric shrinkage during the drying, which is very high for samples without cellulose fibers. From these measurements, it can be concluded that the most promising formulations for practical application are those that couple a good water absorption capacity and a slow release of water, such as X1W2, X4W2 and X4W5 samples.

5.1.2.4 Morphological analysis of the soil treated with SCs

In Figure 5.4(a–f) the SEM micrographs of the neat soil and of the soil mixed with xanthan-based SCs are shown.

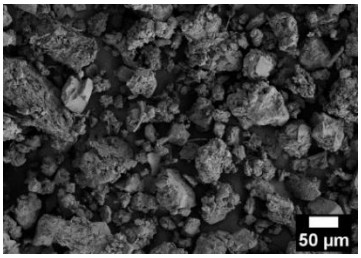

(a)

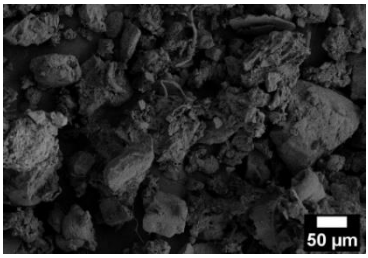

(b)

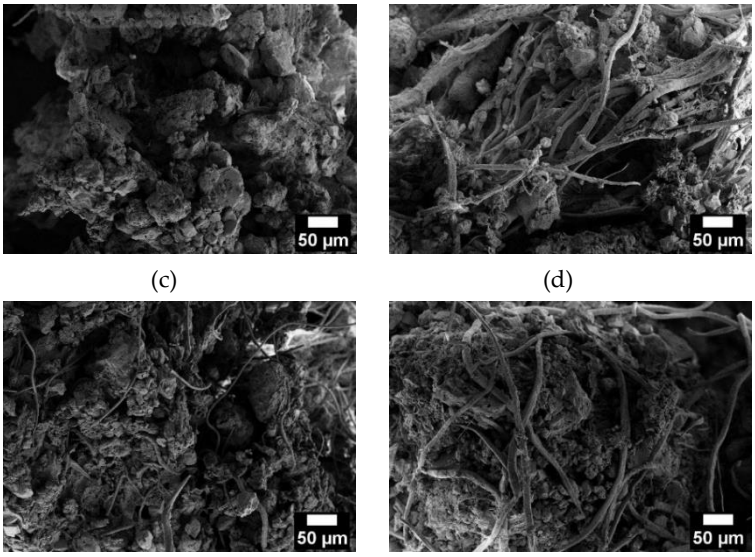

Figure 5.4 SEM micrographs of the (a) neat soil and soil mixed with (b) X1, (c) X1W2, (d) X1W5, (e) X4W2, and (f) X4W5.

From the SEM micrographs of the neat soil shown in Figure 5.4a, it is possible to observe that soil particles are mainly distributed within two-dimension ranges: the first with particles around 50 μm (47.8 ± 13.8 μm) and the second with particles around 10 μm (12.2 ± 4.3 μm). From Figure 5.4d and Figure 5.4f, it is possible to notice that the cellulose fibers have a diameter of 7.9 ± 2.4 μm and an average length of 300 μm. Comparing Figure 5.4a with Figure 5.4(b–f), it is possible to observe that mixing the soil with the xanthan gum-based SCs leads to an agglomeration of the soil particles, with the formation of an interconnected structure. The interconnection between the soil particles, xanthan gum, and cellulose fibers is even more evident by increasing the content of the biopolymer and filler mixed with the soil. This behaviour can be probably explained by the capability of xanthan gum to make hydrogen bonds with the fine soil particles, as observed by Chang et al. [170]. Moreover, from these micrographs it is evident

that the importance of cellulose fibers in forming an interconnected network may lead to beneficial effects in the case of real applications (e.g., soil stabilization, landside mitigation, and reduced water loss).

5.1.2.5 *Evaluation of the maximum water holding capacity (MWHC) of the soil*

The analyses were performed only on the soil with the composition X4W2, that, from the tests carried out in the first part of this work, showed the most interesting moisture absorption and water retention capacities, good rheological properties, and mold resistance. Specifically, the tests were performed on the soil mixed with two different concentrations of dried X4W2: X4W2_high (1.8 wt% relative to soil) and X4W2_low (0.4 wt% relative to soil). In Figure 5.5, the results of the MWHC tests of the soil mixed with different compositions are reported. In this plot, a comparison with the commercial product Idrogea is also reported.

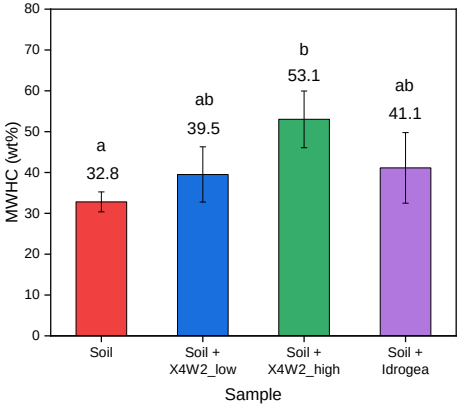

Figure 5.5 Maximum water holding capacity of soil mixed with X4W2 at different concentrations and Idrogea. Different letters indicate that results are statistically different ($p<0.05$).

From Figure 5.5 it can be recognized that the addition of SCs to the soil increases its maximum water-holding capacity (MWHC) value.

The MWHC of the reference untreated soil is 32.8%, meaning that the addition of 33 mL of water leads to the saturation of 100 g of soil. Soil treated with the dried X4W2_low and X4W2_high compositions increases MWHC values by 20.5% and 61.6%, respectively. Specifically, the X4W2_high sample reaches a maximum water holding capacity as high as 53.1%, while the soil treated with the commercial Idrogea shows an MWHC value of 41.1%, comparable with the value obtained for the X4W2_low sample. Moreover, the MWHC value could not be increased by further increasing the amount of Idrogea in the soil, because it would have resulted in a relevant increase in the soil volume, with consequent geological instability in practical applications (Section 5.3).

5.1.2.6 Evaluation of the water retention capacity of the soil

As for the evaluation of MWHC, this analysis was performed only on the soil treated with the composition X4W2 at two different concentrations: X4W2_high (1.8 wt% relative to soil) and X4W2_low (0.4 wt% relative to soil). In Figure 5.6 the results of the evaluation of the water retention capacity of the soil are reported.

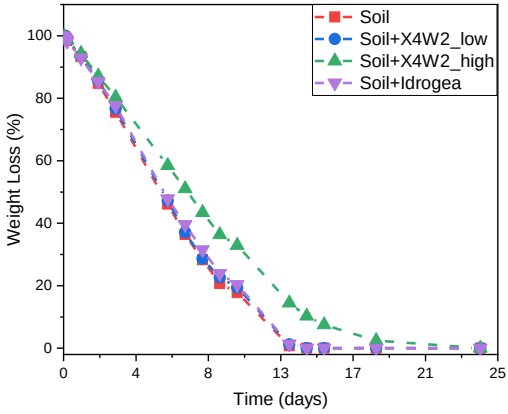

Figure 5.6 Water retention of the soil mixed with different amount of X4W2 and Idrogea.

Figure 5.6 shows that the addition of the xanthan-based samples to the soil leads to an increase in the water retention capacity, which means a slowdown in the water evaporation rate from the soil. The neat soil has a weight loss of 71.8% after 8 days, and becomes completely dry after 14 days. The soil treated with the two compositions of X4W2 possesses weight loss values of 71.4% (low) and 56.5% (high) after 8 days. In these cases, complete dryness is reached after 14 and 24 days, respectively. The addition of the commercial product Idrogea leads to a weight loss of 68.5% after 8 days and to complete drying after 14 days. Therefore, also from this test, the xanthan-based SCs show good performance in retaining water and thus are a suitable solution for soil conditioning applications, acting as a micro water reservoir for plants.

5.1.2.7 Evaluation of the grass germination with soil conditioners

In Figure 5.7, a schematization of the experiment for the evaluation of the grass growth and germination is reported.

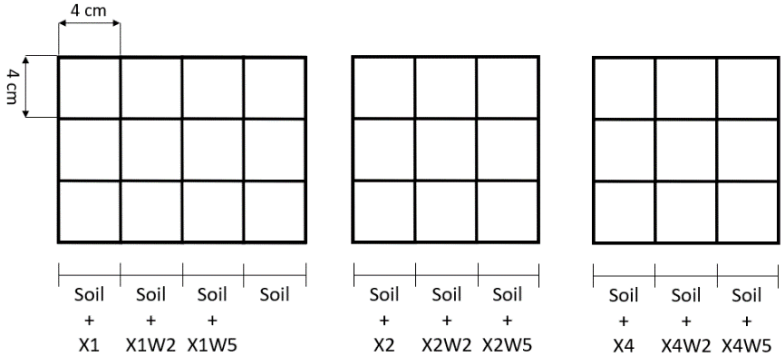

Figure 5.7 Schematization of the experiment for the evaluation of the grass growth with soil conditioner.

In Figure 5.8(a–d) the results of the plant cultivation experiment with soil conditioners are reported.

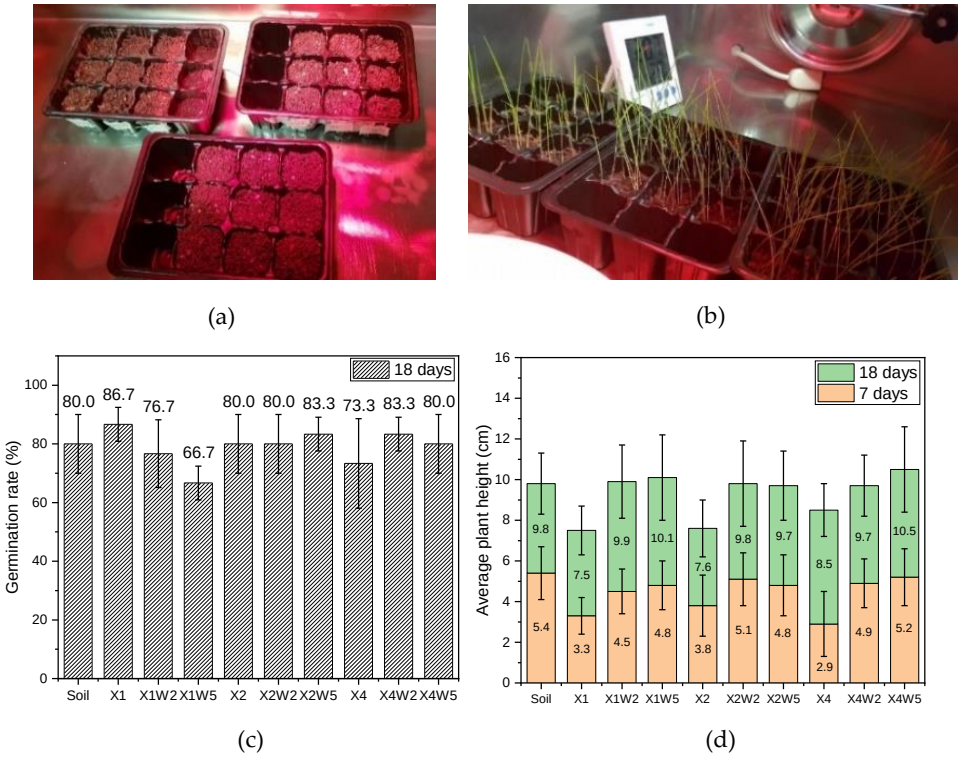

Figure 5.8 Representative images of (a) the grass seeds planted in the different biopolymer-soil culture media and of (b) the grass growth after 18 days. (c) Germination rate after 18 days and (d) average plant height over time.

From Figure 5.8b it can be noticed that, after 18 days, the grass is fully grown in all types of culture media, which means that the selected materials are not harmful to plants. In addition, Figure 5.8c shows that the presence of the SCs does not affect the initial germination of the seeds and the overall growth of sprouts. Indeed, the germination rate, defined as the ratio of the number of germinated seeds to the number of planted seeds, is similar for each pot. This means that these composites are not thought to be used to promote seed germination

rate but are more suitable to support the growth and reduce the mortality of already hatched seedlings. From Figure 5.8d it can be observed that the average plant height is unaffected by the presence of the SC samples. In particular, the overall average plant height after 18 days is 9.7 ± 1.7 cm.
Figure 5.9 shows an image of the grass after 7 days of the interruption of the water supply.

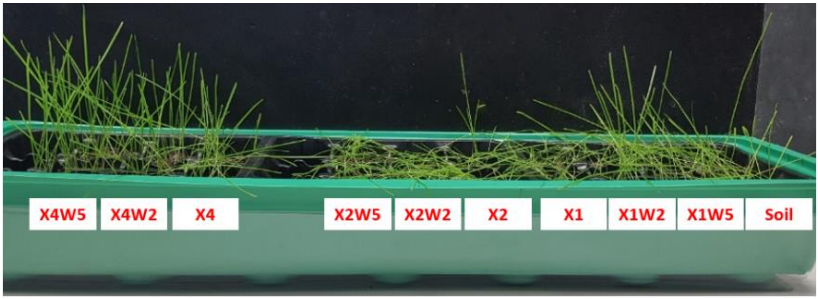

Figure 5.9 Image of the grass after 7 days of interruption of water supply (25 days from the beginning of the experiment).

From Figure 5.9 it can be observed that, after 7 days of drought conditions, the grass is still lush for some specific formulations. In particular, the soil mixed with X1W2, X4W2, and X4W5 samples shows the best results in terms of grass survival rate. As already reported in Figure 5.3 these three formulations show a good balance between a good moisture absorption capacity and slow water release, with consequent beneficial effects in case of a prolonged absence of water supply. However, for X1W2 and X4W5 formulations, mold has formed on the top layer of the soil. Mold growth in these systems can be explained by the high concentrations of cellulose fibers with respect to the amount of xanthan gum, which can induce accelerated biodegradation of the composite with consequent proliferation of bacteria and fungi, especially at elevated humidity conditions. The X4W2 sample possesses the optimized ratio of xanthan gum and cellulose fibers, demonstrating the applicability of this composition as

a soil conditioner to support grass growth in drought conditions, without the formation of molds. In Figure 5.10(a–d) the results for a second plant cultivation experiment, with comparison between the soil treated with the best formulation (i.e., X4W2), untreated soil and soil mixed with commercial Idrogea, are reported.

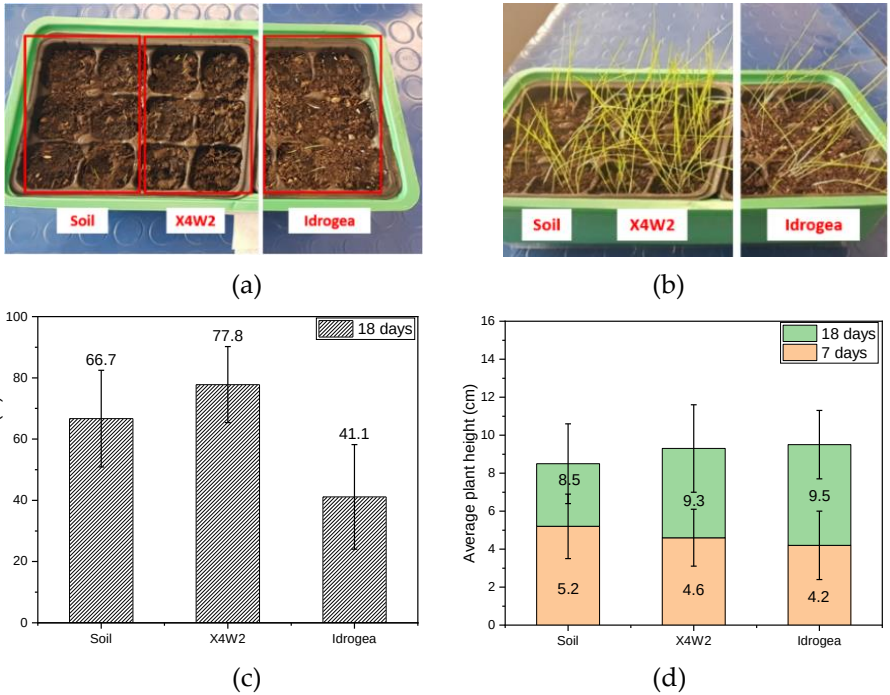

Figure 5.10 Representative images of (a) grass seeds planted in soil, soil treated with X4W2 and with commercial product, (b) grass growth after 14 days. (c) Germination rate after 18 days and (d) average plant height over time.

From Figure 5.10c it is possible to observe that, in this case, the germination rate for the culture medium consisting of the soil treated with X4W2 is two times that of the soil treated with the commercial product. From Figure 5.10d it can be seen that the average plant height is very similar for each sample, in particular, the overall height is 4.7

± 1.7 cm and 9.1 ± 2.1 cm, after 7 and 18 days, respectively, which is very similar to those of the previous experiment. From these studies it can be concluded that the presence of XG and cellulose fibers in the soil helps to better retain water, which is delivered to the plant more gradually than in the neat soil, giving plants the chance for better survival rates under water scarcity conditions.

5.1.3 Conclusions

Novel bio-based SCs produced from xanthan gum and cellulose fibers were developed with the aim of promoting plant growth. It can be hypothesized that the addition of natural cellulose fibers resulted in an increased water retention capability, thanks to the formation of a physical network between the soil and xanthan gum. Among the different produced compositions, the one with XG and cellulose fibers in ratio 2:1 (X4W2) showed interesting moisture absorption and water retention capacity, good rheological properties and mold resistance. The addition of 1.8 wt% of X4W2 to the soil improved the ability to absorb water by 60% with respect to the neat soil, and it also increased the water retention by slowing the rate of water evaporation from the soil. From practical experiments conducted on the growth of herbaceous plants, it was observed that the presence of xanthan gum-cellulose fiber composites in the soil helped to better retain water, which was released to the plant more gradually than in untreated soil, thus enabling a more vigorous growth and an increased survival rate under drought conditions.

5.2 Effect of different cellulose fillers on xanthan-based SCs

Published paper:

Sorze, A; Valentini, F; Smolar, J; Logar, J; Pegoretti, A; Dorigato, A. Effect of different cellulose fillers on the properties of xanthan-based composites for soil conditioning applications. *Materials*, **2023**, 16 (23), 7285.

As demonstrated in Section 5.1, the combination of xanthan gum with cellulose fibers, specifically at a relative weight ratio 2:1, could be an interesting solution for the development of soil conditioners able to increase soil water regulation properties. Therefore, the aim of this work is to further study the effect of different types of natural cellulose-based fillers, of varied fiber length and oxide ash content, on the properties of xanthan gum-based soil conditioners.

5.2.1 Materials and methods

5.2.1.1 Materials

The materials employed in the production of SCs are listed in Table 5.5. A more detailed description can be found in Section 3.1.

Table 5.5 List of materials employed for the preparation of optimized SCs.

Material	Label
Xanthan gum	XG
Arbocel R	R
Arbocel FT 400	FT
Arbocel ZZC 500	ZZC
Cellugrün	CG
Arbocel ZZ 8-2 CA1	ZZ8
Arbocel Adsorb 2	ADS
STEICO flex 036 (milled)	ST

Two different commercial SCs based on potassium polyacrylate were also used as benchmarks. Idrogea [167], was purchased by Endofruit Srl (Verona, Italy) and Be-Grow Boost M [168], kindly provided by the University of Freiburg (Germany) and produced by Be-Grow GmbH (Neustadt an der Weinstraße, Germany). According to the technical datasheet, the concentrations of these products to be used in the dry soil are 0.13 wt% and 0.4 wt%, respectively.
Two types of soils were used in this investigation:

- (S1) A top soil layer sampled from a garden in the Department of Industrial Engineering of the University of Trento (46.06° N, 11.15° E, altitude 398 asl) and characterized by Fondazione Edmund Mach (San Michele all'Adige, Trento, Italy). The main properties of this soil are listed in Table 5.6.
- (S2) A top soil layer sampled in Alpine forests from the Ljubelj area (Slovenia, E(D96/TM) 443431, N (D96/TM) 144159, altitude 1100 asl) [69]. This is fine-grained soil and can be classified according to USCS (ASTM D2487-17 [70]) as organic silt of high plasticity (OH). The average value of natural gravimetric water content, determined according to ISO 17892-1 [71], is 42.9%. The main properties of this soil are listed in Table 5.6.

Table 5.6 Results of the chemical analysis of the soil S1 and soil S2.

Determination	**Soil S1**	**Soil S2**
Sand (2.0–0.05 mm)	412 g/kg	202 g/kg
Silt (0.05–0.002 mm)	458 g/kg	493 g/kg
Clay (<0.002 mm)	130 g/kg	305 g/kg
pH (in water ratio 1:2.5)	8.1	7.5
Total limestone	349 g/kg $CaCO_3$	17 g/kg $CaCO_3$
Active limestone	15 g/kg $CaCO_3$	-
Organic substance	33 g/kg	82 g/kg
Phosphorus	27 mg/kg P_2O_5	<60 mg/kg P_2O_5
Potassium	166 mg/kg K_2O	<100 mg/kg K_2O
Magnesium	317 mg/kg MgO	-

5.2.1.2 Sample preparation

Soil conditioners were produced by dissolving xanthan gum powder in hot water (T = 60 °C) at a concentration of 4 wt%. The mixing was carried out using a Dispermat® F1 mixer (VMA-Getzmann Gmbh, Reichshof, Germany), operating at 5000 rpm for 15 min, in order to obtain a homogeneous mixture without lumps. The fillers were gradually added during the mixing operations at a concentration of 2 wt% (relative to the water solution). In this way, it was possible to obtain seven different compositions, as reported in Table 5.7. The neat XG was also studied as a reference. For some analysis, samples were used in the dried state, and therefore, the produced composites were put in an oven at 50 °C for 72 h. Finally, the prepared materials were ground for 3 min using a Piovan® RN166/1 granulator (Piovan SpA, Venice, Italy) to obtain samples in the form of dried powder.

Table 5.7 List of prepared SCs samples.

Sample	Type of Filler
SC_R	Arbocel R
SC_FT	Arbocel FT 400
SC_ZZC	Arbocel ZZC 500
SC_CG	Cellugrün
SC_ZZ8	Arbocel ZZ 8-2 CA 1
SC_ADS	Arbocel Adsorb 2
SC_ST	STEICO flex 036
XG	-

5.2.1.3 Experimental techniques

The techniques used to characterize the prepared samples are listed in Table 5.4. A more detailed description can be found in Section 3.2.2.

Table 5.8 List of experimental techniques used to characterize the produced SCs.

Technique	Parameters
Rheological properties	Section 3.2.2.1
FT-IR	Section 3.2.2.2
Light microscopy	Section 3.2.2.3
Moisture absorption	Section 3.2.2.4
Maximum water holding capacity (MWHC) of the soil	Section 3.2.2.6
Water retention capacity of the soil	Section 3.2.2.7
Water absorption of the soil (DIN 18132)	Section 3.2.2.9
Determination of the Soil Water Retention Curve (SWRC	Section 3.2.2.8
Evaluation of the plant growth	Section 3.2.2.10

5.2.2 Results and discussion

5.2.2.1 Rheological properties

Figure 5.11a shows the results of the rheological investigations performed on the prepared SCs in the wet state. Figure 5.11b and Table 5.9 display the yield stress values obtained by fitting the shear stress data using the Casson model (see Equation (3.10)).

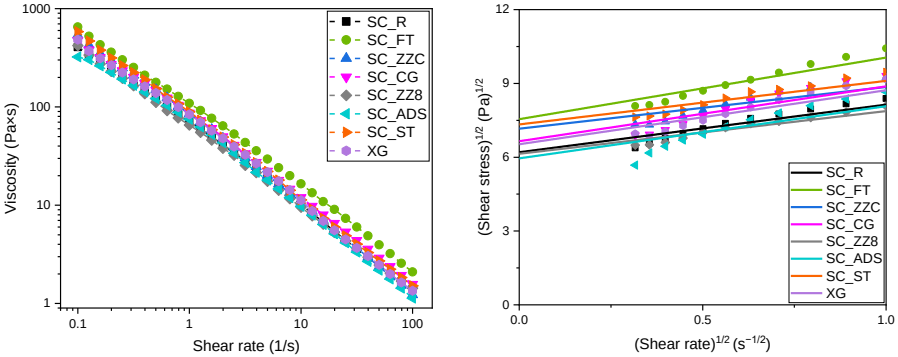

(a) (b)

Figure 5.11 Rheological tests on the prepared SCs in the wet state. (a) Trend of shear viscosity with respect to the shear rate. (b) Linear interpolation of shear stress values for evaluation of the yield stress, using the Casson model (see Equation (3.10)).

Table 5.9 Values of yield stress for the prepared samples obtained through the Casson model (see Equation (3.10)). Different letters indicate that results are statistically different ($p<0.05$

Sample	Yield Stress [Pa]
SC_R	38.5 ± 1.6 ^{ac}
SC_FT	56.9 ± 2.3 ^{b}
SC_ZZC	51.3 ± 2.5 ^{b}
SC_CG	44.2 ± 2.7 ^{a}
SC_ZZ8	37.7 ± 1.2 ^{ac}
SC_ADS	35.5 ± 3.1 ^{c}
SC_ST	53.8 ± 1.8 ^{b}
XG	42.6 ± 2.2 ^{a}

From Figure 5.11a it is possible to observe that rheological properties are closely related to the morphology of the fillers constituting the samples. For instance, fillers with a high aspect ratio (see Table 3.1)

may interlace and form tangled networks [201]. Indeed, the addition of fillers with a high aspect ratio leads to an increase in both the viscosity and the shear stress with respect to the neat xanthan gum (XG). In particular, SC_FT, which is constituted by the filler with the highest aspect ratio, is characterized by the highest viscosity. However, several factors besides aspect ratio are hypothesized to affect the viscosity of these samples. For example, the presence of oxide ash in the fillers may lead to a reduction of the viscosity and the shear stress. In fact, despite the good aspect ratio, sample SC_ZZ8 has the lowest rheological properties, which can be explained by considering the elevated content of oxide ash (50%) in this filler. Moreover, the sample SC_ADS is composed of very fine particles of cellulose dextrose derivate (30–250 μm) that may not form a good network with the xanthan gum, resulting in lower viscosity. From Figure 5.11b and Table 5.9 it is possible to notice that the values of yield stress are also influenced by the aspect ratio of the fillers and by the oxide ash content. In general, samples with a filler characterized by a high aspect ratio and low oxide ash content, like SC_FT, SC_ST, and SC_ZZC, exhibit statistically higher yield stress ($p<0.05$) with respect to neat xanthan gum, evidencing an improvement of the gel network strength.

5.2.2.2 FT-IR Spectroscopy

In Figure 5.12 (a,b) the results for the FT-IR analysis performed on the xanthan gum, fillers, and corresponding soil conditioners are displayed.

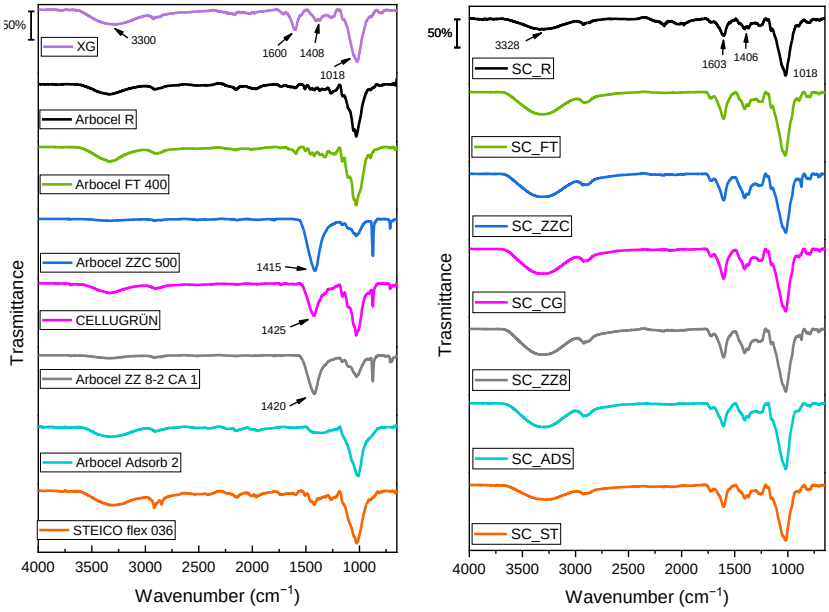

(a) (b)

Figure 5.12 FT-IR spectra of (a) neat xanthan gum and cellulose-based fillers and (b) the corresponding SCs.

From Figure 5.12a it is possible to compare the spectra of cellulose fillers with that of xanthan gum. In particular, the broad absorption peak observed in the XG spectrum at around 3300 cm^{-1} corresponds to the O-H stretching vibration of the hydroxyl group, while the peaks at 1600 and 1408 cm^{-1} are associated with the asymmetrical and symmetrical C=O stretching vibration of carboxylate anion (-COO-), respectively. For Arbocel ZZC 500, Cellugrün, and Arbocel ZZ 8-2 CA 1, the absorption peak around 1420 cm^{-1} is more evident with respect to the other fillers. This can be explained by the very high oxide ash content of these fillers (see Table 3.1), associated with the presence of more C=O bonds. The characteristic peak at 1014 cm^{-1} for C-O stretching of primary alcohols is also observed for all the samples. From Figure 5.12b it is clearly visible that the characteristic spectra of

SC samples are very similar to each other and to that of neat xanthan gum (XG), which is the main constituent of the soil conditioners. Moreover, the similar chemical structure of the cellulose fillers to the xanthan gum does not allow for the identification of the significant differences between SC spectra.

5.2.2.3 Light microscopy

In Figure 5.13(a–g) the light microscopy images for the dried SCs are shown.

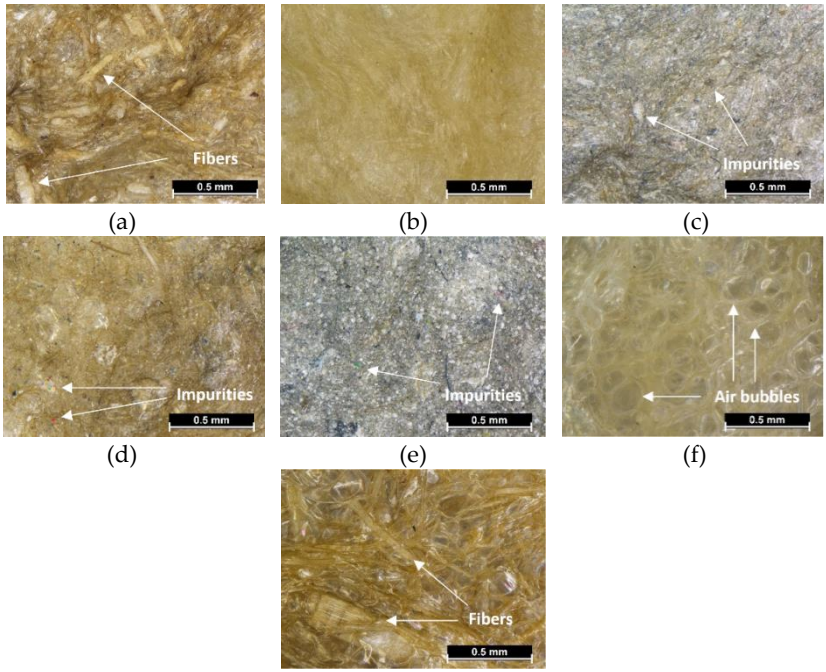

Figure 5.13 Light microscope images of the dried SCs: (a) SC_R, (b) SC_FT, (c) SC_ZZC, (d) SC_CG, (e) SC_ZZ8, (f) SC_ADS, and (g) SC_ST.

From Figure 5.13(a,g) it can be observed that SC_R and SC_ST samples are composed of fillers with a wide distribution of fiber length, as also reported in Table 3.1. Figure 5.13f shows that the SC_ADS sample is full of air bubbles formed during the mixing process, and this may affect the final density of the material. From Figure 5.13(c–e), it can be seen that SC_ZZC, SC_CG, and SC_ZZ8 show lot of impurities that were already present in their cellulose fibers and, together with the high oxide ash content, contribute to the darker color of the image. Overall, it is possible to notice that for every sample the structure appears quite homogeneous, without the presence of biopolymer lumps or filler aggregates. This indicates that a good mixing procedure was carried out, as also demonstrated by the good dispersion of the polymer and the fillers in the water solution. This homogeneous mixture leads to the formation of a network between cellulose fillers and XG structure that may result in a reinforcing and stabilizing effect of the composite when applied to the soil [199,200].

5.2.2.4 Moisture absorption and water retention capability

In the results of the moisture absorption and water release tests for the different SCs are displayed.

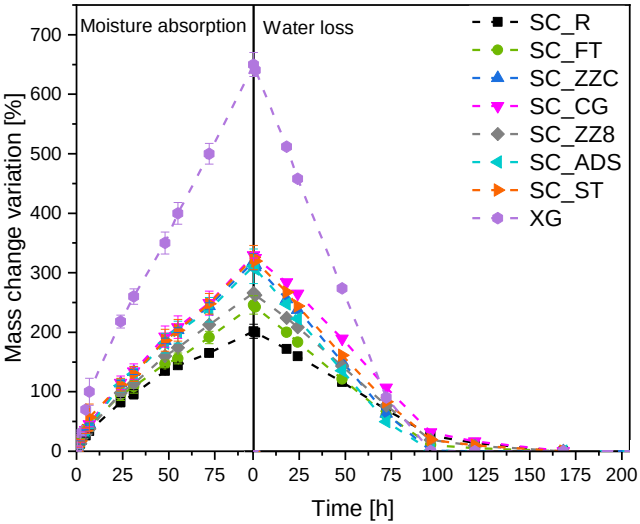

Figure 5.14 Evaluation of the moisture absorption (left) and the residual water content (right) for the different SCs.

Figure 5.14 shows that the moisture absorption of the tested samples increases parabolically with time. Overall, the addition of cellulose fillers to the xanthan gum solution leads to a decrease in the moisture absorption capacity. The observed behaviour can be attributed to the chemical similarity between xanthan gum and cellulose, which facilitates strong interfacial adhesion between the two components. This physical interaction can somehow hinder the diffusion of water molecules in the SC [179]. The test was conducted under high humidity conditions (Section 3.2.2.4); therefore, the analysis was stopped before it reached the plateau due to the formation of molds in the samples. In the right part of Figure 5.14, from the water retention test, there is an initial linear decrease in mass over time. In this case, the presence of the fillers in the samples leads to a slower water release compared to XG, which reaches complete drying after 96 h. For the other samples, this occurs between 120 h and 168 h (5–6 days). Furthermore, the presence of fillers in the solution helps to limit the volumetric shrinkage during the drying, which is also very significant for the XG sample. These tests indicate that the most

promising compositions for a practical application are those that couple good moisture absorption capacity with a slow water release, such as SC_CG, SC_ST, and SC_ZZ8.

5.2.2.5 Evaluation of the water holding capacity (WHC) of the soil

The analysis was performed on soil S1 mixed with 1.8 wt% of dry SCs. Moreover, to demonstrate the positive effect of adding fillers to xanthan-based solutions, a soil mixed with 1.2 wt% of neat xanthan gum powder (which is the amount of xanthan gum present in the SC samples) was also tested.
The results of WHC tests are shown in Figure 5.15.

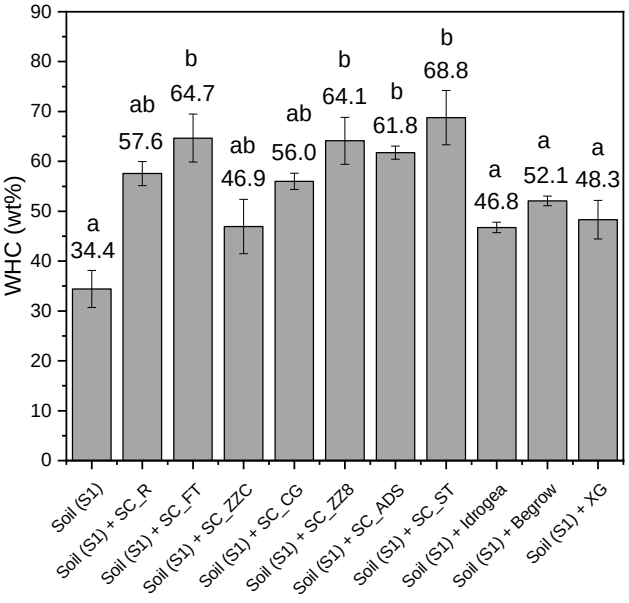

Figure 5.15 Water holding capacity of soil S1 with the different soil conditioners and commercial products. Different letters indicate that results are statistically different ($p<0.05$).

Figure 5.15 shows that the water holding capacity (WHC) of the soil increases when xanthan-based soil conditioners are added. In particular, the reference untreated soil S1 has a WHC of 34.4%, which means that saturation is reached when 35 mL of water is poured into 100 g of dry soil. The addition of 1.8 wt% of the prepared soil conditioners to the soil increases WHC values up to 68.8% (SC_ST sample), i.e., double that of the untreated soil. Moreover, xanthan-based soil conditioners exhibit good water absorption properties, in most of the cases statistically higher to those of commercial products ($p<0.05$). In particular, the SC_ZZC sample has a water holding capacity as high as 46.9%, which is the lowest value among the cellulose-filled SCs. However, it is still comparable with that of soil treated with commercial products (Idrogea and BeGrow), which show WHC values of 46.8% and 52.1%, respectively. Moreover, the WHC value cannot be increased by further increasing the amount in weight of commercial products in the soil, as it was experienced that this would lead to a significant increase in soil volume with the formation of an incoherent gelatinous mixture of polymer and soil (Section 5.3). In a practical application, this may lead to an evident swelling, which will be investigated in future work as part of geotechnical investigations of forest soils treated with developed SCs. Furthermore, for all the samples, the WHC values increase or are equivalent compared to neat xanthan gum (48.3%), demonstrating the advantages of adding fillers to the biopolymer solution.

5.2.2.6 Evaluation of the water retention capacity of the soil

As for the evaluation of WHC, the analysis was performed on soil S1 mixed with 1.8 wt% of dry SCs. Moreover, to demonstrate the positive effect of adding fillers to xanthan-based solutions, a soil mixed with 1.2 wt% of neat xanthan gum powder (which is the amount of xanthan gum present in the SC samples) was also tested. In Figure 5.16, the results of the evaluation of the water retention capacity of the untreated and treated soil are reported.

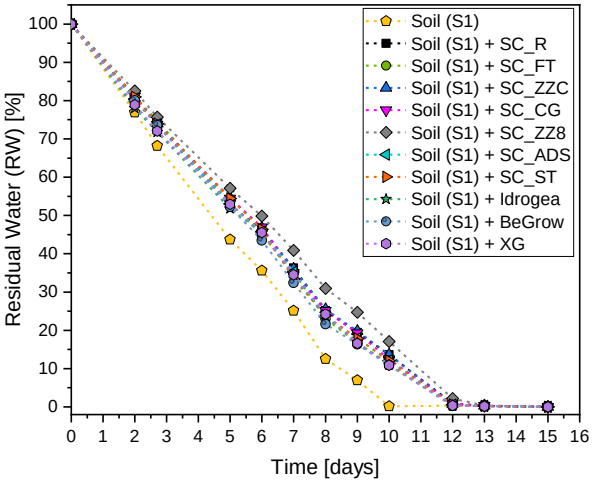

Figure 5.16 Water retention behaviour of soil (S1) mixed with cellulose-filled soil conditioners and commercial products.

Figure 5.16 shows that the presence of soil conditioners leads to an increase in the water retention capacity compared to the untreated soil, which means a slowdown in the water evaporation rate from the soil. In particular, the untreated soil has a weight loss of 56.3% after 5 days and 93.2% after 9 days. For all the other samples, weight loss values are around 45.5% after 5 days and 80.5% after 9 days. SC_ZZ8 shows the best performance, with weight loss values of 48.1% and 80.8% after 5 and 9 days, respectively. Both commercial products lead to weight loss values of 47.7% and 83.6% after 5 and 9 days, respectively. It can be hypothesized that the rate of water evaporation of the cellulose-filled SCs could be lower than that shown by commercial products. This means that composites based on xanthan gum and cellulose fillers are a suitable solution to retain water for a longer time, and this is extremely important for plants in dry climate conditions. Practically, the delay to the dry state between untreated and treated soil is about 2 days.

5.2.2.7 Evaluation of the water absorption with DIN 18132 of soil

Tests were conducted on soil S2 (d_{max} < 0.4 mm) mixed with the compositions SC_R, SC_CG, and SC_ZZC. The dosage of these SCs was defined as the percentage of their mass to the dry mass of the soil: 0.4 wt.% (low dosage) and 1.8 wt.% (high dosage).
Table 5.10 presents the results of water absorption tests carried out on untreated and treated soil S2. The addition of SC generally increases the water absorption of soil. The increase depends on the amount and the type of SC. Activation of SC in soil mixtures does not happen immediately, which is reflected in the absorption time needed to achieve $w_{A\,max}$. In particular, it is possible to observe that treated soil is able to absorb 1.5 times more water than untreated soil, with the highest values reached after 24 h using a high dosage of SC_R. It is also interesting to notice that the use of low amounts of SC_R does not provide any improvement with respect to untreated soil.

Table 5.10 Water absorption of untreated and treated soil S2.

Specimen	**Dosage of SC**	**$w_{A\,24\,h}$ (%)**	**$w_{A\,max}$ (%) ***
Soil (S2) (untreated)		87–89	87–89
Soil (S2) + SC_R	Low	91–99	Not measured
Soil (S2) + SC_R	High	154–162	166–176
Soil (S2) + SC_CG	High	140–150	174–201
Soil (S2) + SC_ZZC	High	131–139	140–175

* End of absorption: untreated soil 15 min, treated soil 2–4 days.

These results are in good agreement with the data obtained for soil S1. Even though the investigations were carried out in two different laboratories, by adopting different experimental procedures and different soils, the influence of SCs on water holding capacity and water absorption is similar. This is confirmed by Figure 5.17, in which

the relative improvement of $w_{A\ 24h}$ and WHC values upon SC insertion for both S1 and S2 soils is reported.

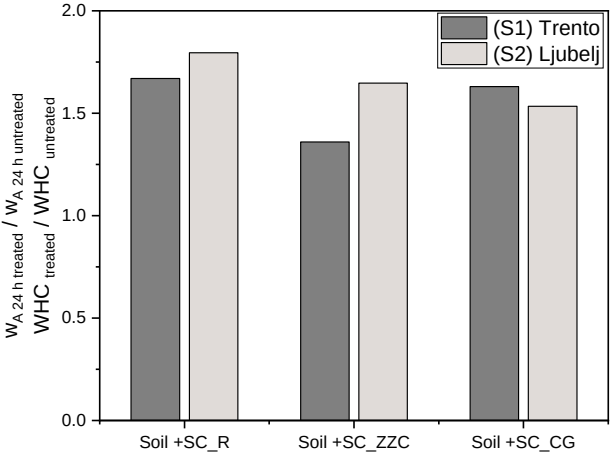

Figure 5.17 The influence of SCs on WHC and $w_{A\ 24h}$ values of S1 and S2 soils. Data elaborated and provided by ULJ.

5.2.2.8 Determination of the soil water retention curve (SWRC)

As for the evaluation of the water absorption with DIN 18132, the analysis was carried out on soil S2 (d_{max} < 0.4 mm) mixed with the compositions SC_R, SC_CG, and SC_ZZC. The dosage of these SCs was defined as the percentage of their mass to the dry mass of the soil: 0.4 wt.% (low dosage) and 1.8 wt.% (high dosage). In Figure 5.18 the results of the soil water retention curves are showed.

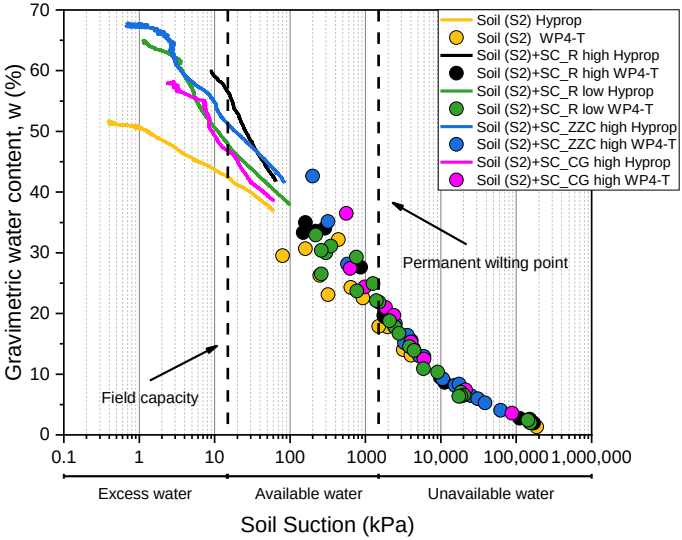

Figure 5.18 Soil water retention curves of untreated and treated soil S2. Data elaborated and provided by ULJ.

Results indicate that SC does not affect suctions higher than 2000 kPa, while there is an increase in available water in the range of low suctions up to 100 kPa when SCs are added to the soil. In the range of suctions between 100 kPa and 2000 kPa, the difference between suction of untreated and treated soil is low, within 5%, and this could be also a result of inhomogeneity of specimens and their preparation. For the assessment of available water for plant growth, two points of the SWRC are particularly important and are indicated in Figure 5.18 by black vertical dashed lines: field capacity at suctions between 10 and 33 kPa and permanent wilting point at suction approximatively 1500 kPa [202]. As can be seen from Figure 5.18, the addition of SCs has a beneficial effect on the available water for plants in the zone between field capacity and permanent wilting point. In the zone of excess water, the SCs increase the water content. During the saturation of treated soil specimens, swelling was observed. As a result of

swelling, porosity increases, and consecutively, the water content of the saturated specimen increases. The initial density of the saturated specimens thus affects the position of SWRC. In Figure 5.18, the increase in energy needed to suck water from the treated soil can be observed in the range of low suctions (up to 100 kPa). At the same water content, the SWRCs of treated soil are shifted to the right compared to the SWRC of untreated soil. However, this does not represent a limitation for the use of SCs, because the phenomenon is observed in the area of excess water and at the transition to available water for plants, where sucking energy is low. Conversely, at high suction (>1000 kPa), corresponding to the condition of almost no available water for the plant (drought), the presence of SC in the soil does not increase the energy necessary to extract water from the soil with respect to the untreated soil.

5.2.2.9 Evaluation of the grass germination in soil S1

In Figure 5.19 a schematization of the experiment is reported.

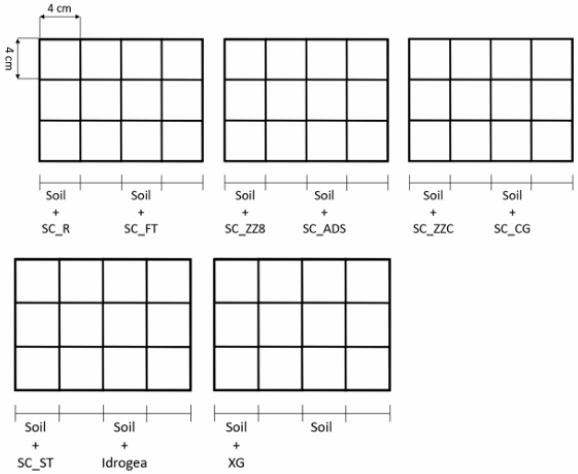

Figure 5.19 Schematization of the experiment planned for the evaluation of the grass growth with soil conditioners.

In Figure 5.20(a–c) the results of the grass cultivation experiments with the different soil conditioner compositions are displayed.

(a)

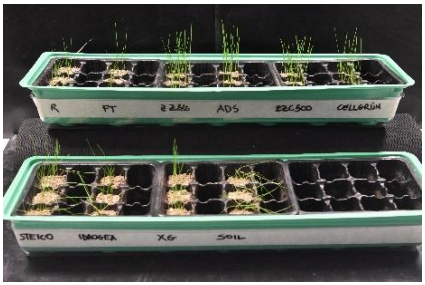

(b)

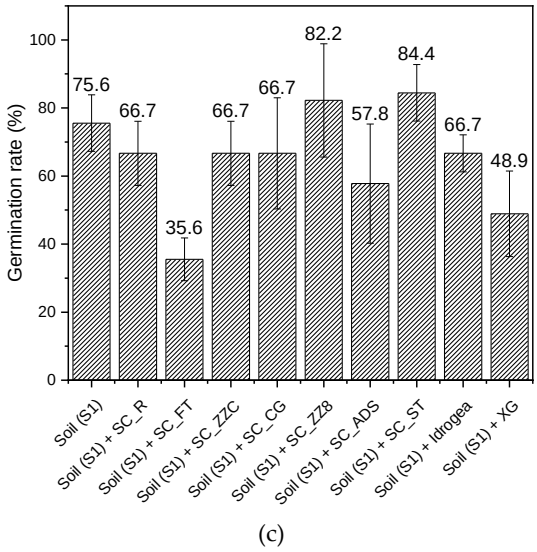

(c)

Figure 5.20 Representative images of (a) the grass seeds planted in the soil S1 treated with different SCs, (b) the grass growth after 25 days, and (**c**) the germination rate after 18 days.

Figure 5.20b shows that grass fully develops in all types of soil samples after 18 days, demonstrating the non-harmful nature of the materials investigated. Additionally, Figure 5.20c indicates that the initial germination of seeds and the overall growth of sprouts are quite variable depending on the soil conditioner used. Indeed, the germination rate, defined as the ratio of the number of germinated seeds to the number of planted seeds, is higher for the soil treated with SC_ZZ8 and SC_ST with respect to the untreated soil. For the soil mixed with SC_R, SC_CG, SC_ZZC and SC_ADS the germination rate is comparable to those of untreated soil and soil mixed with commercial products, while for the soil treated with SC_FT and with neat XG, it is lower. These results are quite coherent with those reported for water absorption and water retention tests. The most performing samples are those that show a good balance between good moisture absorption (Figure 5.14), high WHC when mixed in the soil (Figure 5.15), and slow water release (Figure 5.14) and Figure 5.16). However, as already seen in Section 5.1.2.7, these xanthan-based SCs are not designed to promote seed germination rate but are more suitable to reduce the mortality of already hatched seedlings under drought conditions. Indeed, from Figure 5.20b, it is also possible to observe that the grass in pots with untreated soil is rather perished, while in the other pots it is still thriving, despite the very low amount of daily water supplied. Therefore, this study confirms that the addition of cellulose fillers to xanthan gum for the production of bio-based soil conditioners improves the water regulation capability of the soil, increasing the probability of plants survival under drought conditions. Due to the hydrophilic properties of their components, the prepared composites enhance the ability of soil to retain water, creating an environment that is more favorable for plant cultivation. A possible limitation of these materials could result from the poor durability of the biopolymers in soil, which may affect their long-term efficiency. However, literature studies on the use of XG in agricultural

applications have shown that its performance in soil is still good even after 2 years [170].

5.2.3 Conclusions

In this work, soil conditioners based on xanthan gum and different cellulose fillers were characterized to have a comprehensive evaluation of their influence on the water absorption, water retention, and water availability of soil. Light microscopy observations showed the homogeneous dispersion of these fillers within the xanthan gum matrix, resulting in the formation of a reinforcing and stabilizing network. The water holding capacity of soil was increased from 34% (untreated soil) up to 69% (soil treated with 1.8 wt% of SC_ST), with good performance, comparable (in some cases even statistically higher) to that of commercial products. Moreover, treated soil exhibited a water retention capability delayed by around two days with respect to untreated soil. Soil water retention curves, determined using the Hyprop evaporation and Dew Point Potentiometer methods, showed that the addition of SCs had beneficial effects on the following: (i) the available water for plants in the zone between field capacity and permanent wilting point; (ii) in cases of excess water, avoiding water stagnation; and (iii) in drought conditions, not increasing the pressure necessary to extract water from the soil with respect to the untreated soil. The results also confirmed the suitability of geotechnical investigations for the determination of the influence of SCs and showed a comparable influence of the SCs on water absorption, determined using two different methods on different soil samples. Finally, a case study application demonstrated the non-harmful nature of the SCs and highlighted the beneficial effect played by cellulose fillers on the water regulation properties of the soil.

5.3 Investigation of the geotechnical properties of soil treated with SCs

Published paper:

Fortuna, B; Logar, J; Sorze, A; Valentini, F; Smolar, J. Influence of xanthan gum-based soil conditioners on the geotechnical properties of soils. *Applied Sciences*, **2024**, 14, 4044.

This work was conducted in collaboration with the Faculty of Civil and Geodetic Engineering of the University of Ljubjana (Slovenia) (ULJ). **The experimental analysis and the results were carried out by ULJ. All the reported images and data were kindly elaborated and provided by ULJ**.

The main objective of this research was the assessment of influence of xanthan gum-based SCs on geotechnical properties of forest soils. Specimens constituted of different soils mixed with different SCs compositions were investigated in saturated state, where their mechanical properties are expected to be the lowest. The properties of the developed SCs and their influence on soil properties were to some extend already demonstrated in Section 5.2. In the present study, the influence of different fillers on the mitigation of XG-based SCs sensitivity to water was investigated from a geotechnical point of view. The focus was on drained shear strength and compressibility, index properties, water absorption capacity and hydraulic conductivity of three different types of forest soils treated with three types of newly developed XG-based soil conditioners.

5.3.1 Materials and methods

5.3.1.1 Materials

The materials employed in the production of soil conditioners are listed in Table 5.11. A more detailed description can be found in Section 3.1.

Table 5.11 List of materials employed for the preparation of SCs for the geotechnical investigations.

Material	Label
Xanthan gum	XG
Arbocel R	R
Arbocel ZZC 500	ZZC
Cellugrün	CG

Laboratory investigations were carried out on three types of soils from different forest areas in Europe, i.e., Ljubelj in Alpine part of Slovenia (S1), Catalonia, Northeastern Spain (S2) and Heldburg, Germany (S3). Soil samples at their natural water content are shown in Figure 5.21. The samples were taken from approx. 10-20 cm below the organic layer which consisted mostly of fresh leaves and needles. Organic content of soil S1 was 8.2% per dry matter (DM), whereas S2 and S3 had organic contents ranging between 1.8% and 5.2% DM. Before laboratory investigations, older and partially decomposed large organic particles were manually removed from soils at their natural water content. The cleared soils were then stored in tightly closed containers until the investigations were conducted.

Figure 5.21 Soils used for the laboratory tests to evaluate the geotechnical properties. Images kindly provided by ULJ.

5.3.1.2 Sample preparation

The samples chosen to investigate the geotechnical properties of the soil were the compositions SC_R, SC_CG and SC_ZC produced according to procedure described in Section 5.2.1.2. These compositions were selected among others as they showed the most promising water absorption and retention properties. All the tests were carried out on soils without SC (untreated soils) and on mixtures of soils with the SCs (mixtures). The soil conditioner SC_R was used in low (L) and high (H) dosage with 0.4% and 1.8% of SC per dry soil mass, respectively, while the soil conditioners SC_CG and SC_ZZC were used only in high (H) dosage. The mixtures for the determination of water absorption (w_A) were prepared from dry soil and dry soil conditioners, while the mixtures for the other tests were prepared from soil at natural water content with the addition of dry SC.

5.3.1.3 Experimental techniques

The techniques used to investigate the geotechnical properties of the prepared samples are listed in Table 3.2. A more detailed description can be found in Section 3.2.2.9.

5.3.2 Results and discussion

5.3.2.1 Liquid limit of untreated soils and mixtures

Figure 5.22 illustrates the liquid limits for untreated soils and soils treated with SC_R (* represents the identification number of the soil).

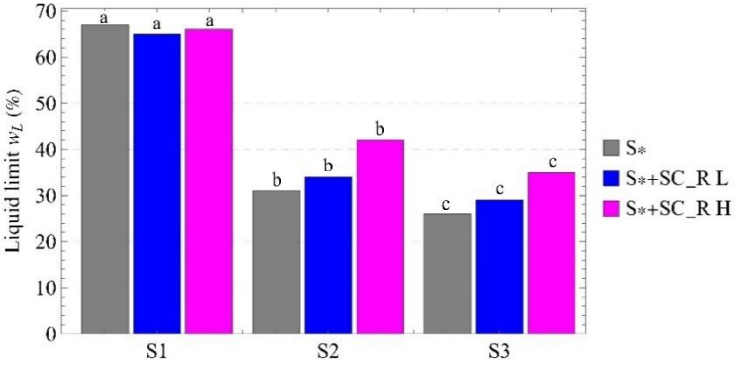

Figure 5.22 Liquid limit of untreated soils and soil mixed with low (L) and high (H) dosage of SC_R. (* Represents the identification number of the soil). Letters indicate significantly different means of the groups of specimens ($p<0.05$). Data elaborated and provided by ULJ.

The impact of SC on liquid limit are strongly affected by the index properties of the untreated soil. In the case of silt with sand S1, the SC has negligible effect on liquid limit, with small differences in values that could be consequence of the specimen's heterogeneity. For the sandy clays S2 and S3 with lower liquid limit, the influence of the SC is more evident. The liquid limit rises with increasing SC content, and this influence is quite similar for both soils S2 and S3. For instance, with low dosage, the liquid limit increases by approximately 10% for both S2 and S3 and by approximately 35% for high dosage of SC_R. This is in line with the study [19], where w_L for untreated soil was 22% and the increase of 13% in w_L was observed for 0.5% addition of XG

and 39% increase in w_L for 2% addition of XG (results for 50/50 mixture of river sand and residual soil).

5.3.2.2 Water absorption of untreated soils and mixtures

The water absorption of soils and mixtures, with an initial dry mass of 1.0 g per specimen, are presented in Figure 5.23 (* represents the identification number of the soil).

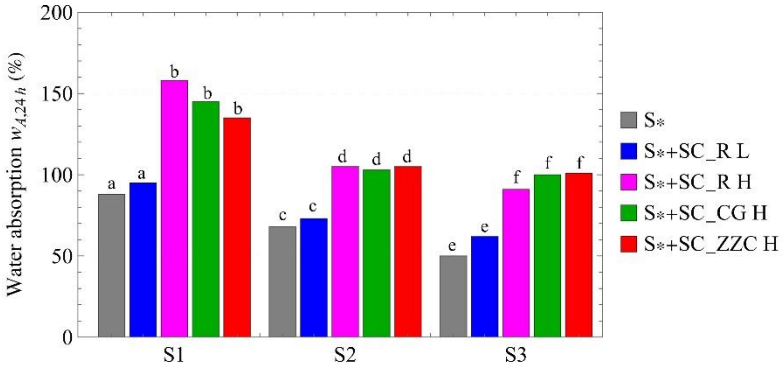

Figure 5.23 Average water absorption of untreated soils and soils with different SCs after 24 h. (* Represents the identification number of the soil). Letters indicate significantly different means of the groups of specimens ($p<0.05$). Data elaborated and provided by ULJ.

Due to the comparable measured values of the tests performed in two or more replicates, the water absorption is given as their average value. Following the standard recommendation, the water absorption was assessed after a test duration of 24 hours. In general, the addition of SCs increases the wA for all types of soils. High dosage of SC_R results in approx. 80% increase of wA compared to the wA of untreated soils S1 and S3, while for S2 the increase is 54%. The overall highest increase of wA is observed for the mixtures of soil S3, specifically with SC_CG H and SC_ZZC H which is over 100% in both cases. Soil S2 had similar increase of wA for all three types of SCs at

high dosage that is approx. 53%. The influence of the type of soil on water absorption of mixtures is clearly visible, as is the dosage of the SC. However, the type of SC is not an influential parameter, which was confirmed also by statistical test.

5.3.2.3 Compressibility

In Figure 5.24(a-c) the compressibility curves are shown as the relationship between vertical deformation of specimens and their effective vertical stress. For all untreated soils and mixtures, two repetitions of oedometer test were performed. Both tests yield comparable results. To prevent information overload in the diagrams, only one test per specimen of untreated soils and mixtures is illustrated in Figure 5.24(a-c).

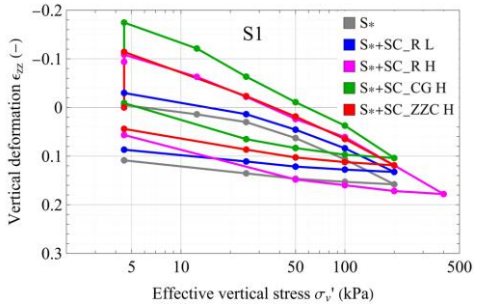

(a)

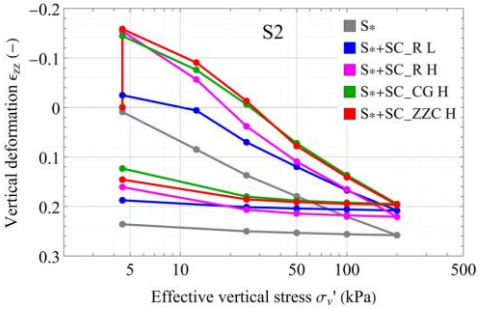

(b)

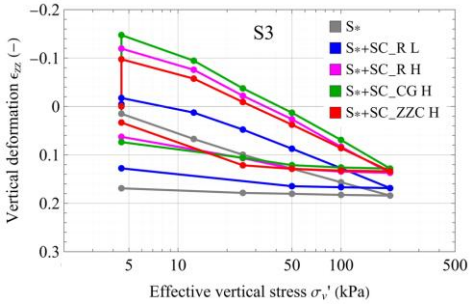

(c)

Figure 5.24 Compressibility curves for untreated and treated soil: (a) S1, (b) S2 and (c) S3. Data elaborated and provided by ULJ.

Despite a comparable initial void ratio of specimens from soil and its mixtures, after soaking and perform swelling deformations at $\sigma_v' = 4.5$ kPa, compressibility curves of mixtures are shifted above the compressibility curves of untreated soils. As previously demonstrated, the addition of SCs increases water absorption capacity of the soils, which is reflected in swelling of the mixtures. Swelling deformation depends on the amount of SC. The statistical analysis of oedometer moduli at individual loading stages performed on all specimens shows that there is a statistically significant difference ($p<0.05$) between specimens with low and high dosage of SC_R. On the other hand, the analysis shows that the influence of the type of SCs is not statistically significant. During unloading no considerable swelling can be observed even at $\sigma_v' = 4.5$ kPa.

Figure 5.25 illustrates the time-dependent swelling, represented by the vertical displacement of the specimen with initial height of 19.3 mm, within the oedometer ring. The measurements for time-dependent swelling were conducted on all specimens after soaking at the loading stage of 4.5 kPa. The results are presented only for soil S1 and its mixtures, however the swelling magnitude was comparable also for soil S2 and S3. The water intake and swelling of the mixtures does not happen instantly, as it was observed also during water

absorption investigation. Thus, the specimens were left to swell for approx. 2 days. The swelling curves illustrate that low dosage of SC_R corresponds to reduced swelling compared to high dosage. In Figure 5.25 (right) the oedometer test specimen is shown, where large swelling deformations after disassembly can be observed.

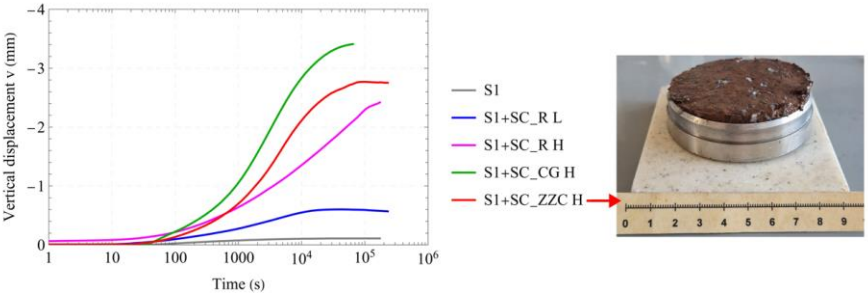

Figure 5.25 Swelling process (σ_v' = 4.5 kPa) of soil S1 and its mixtures (left) and specimen S1+SC_ZZC H after investigation (right). Data elaborated and provided by ULJ.

5.3.2.4 Drained shear strength

Figure 5.26a presents the results of direct shear tests for untreated and treated S1 soil samples prepared with a comparable initial water content and soaked during consolidation and shearing. To enhance the validity of results, two repeatability tests were carried out for soil S1, mixed with SC_R H and SC ZZC_H, as shown in Figure 5.26b.

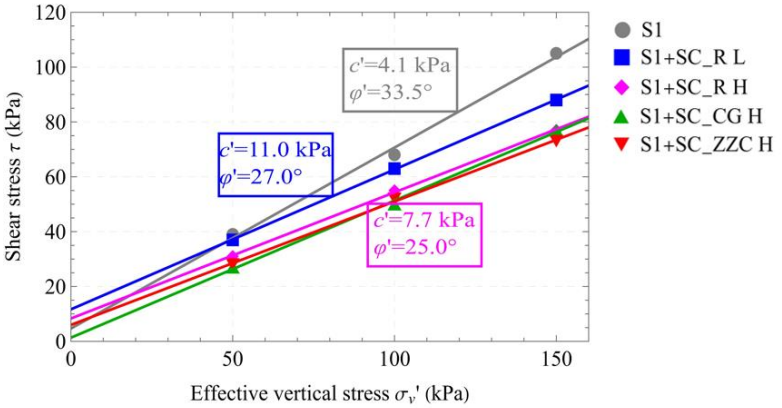

(a)

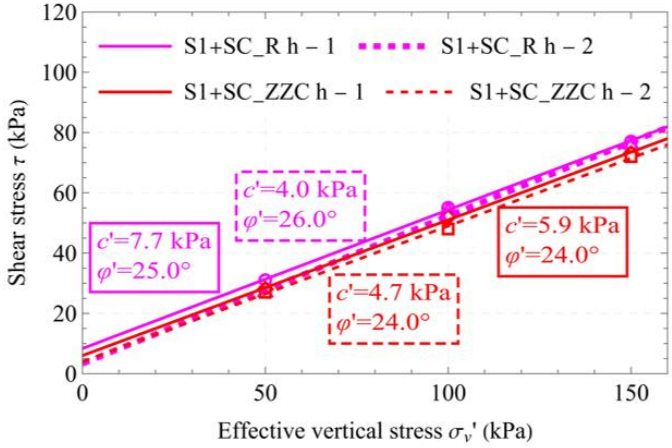

(b)

Figure 5.26 (a) Results of direct shear tests for the soil S1 and its mixtures and (b) repeatability test for two types of SCs mixed with soil S1. Data elaborated and provided by ULJ.

The XG-based soil conditioners in wet environment formed a gel-like structure and inherently caused the swelling of the mixtures. The

swelling could result in a lack of contact between soil particles [124,203]. On the other hand, newly developed SCs contain different fillers which can reduce this effect. The repeatability of the direct shear test results, shown in Figure 5.26b, is very good, especially for the friction angle. The difference between the two tests is within 4% for SC_R H, while for SC_ZZC H, the friction angles are identical. The repeatability for cohesion is not as strong. However, it is crucial to note that all measured cohesions are very low, keeping the differences within the expected range.

Table 5.12 presents measured values for cohesion (c′) and friction angle (φ′) for all treated and untreated soils.

Table 5.12 Measured values of cohesion and friction angle for untreated soils and mixtures. Data elaborated and provided by ULJ.

Specimen	S1[1]		S2		S3	
	c′ (kPa)	*φ′*(°)	*c′* (kPa)	*φ′*(°)	*c′* (kPa)	*φ′*(°)
S*	4.4	33.5	1.4	30.0	12.0	28.0
S* +SC_ R L	11.0	27.0	0.4	31.0	0.0	32.5
S* +SC_ R H	4.0/7.7	26.0/25.0	2.6	25.5	0.0	25.5
S* +SC_ CG H	1.6	26.5	1.7	27.5	0.0	27.0
S* +SC_ ZZC H	4.7/5.9	24.0/24.0	0.0	26.5	1.6	24.5

[1] For specimens with repeated test, both values are given.

The results show that, with the exception of mixtures of S2 and S3 and SC_R L, the friction angle is decreased in all cases, regardless of the soil and SC type. On the other hand, the c′ remains in the same range for all mixtures. It is interesting to note that mixtures with high dosages of SCs have comparable values of friction angles and cohesions, irrespective of the soil type. Two-way ANOVA with a confidence level of 0.05 was performed on all data presented in Table 5.12. It can be seen that there is no significant difference between the friction angle of the three soils, while the mixtures with SC_R H and SC_ZZC H exhibit significantly different friction angles. Due to similar friction angles of the three soils, additional one-way ANOVA

analysis was performed on the data grouped into 3 groups: S*+SC_R H, S*+SC_CG H and S*+ZZC_R H, where S* stands for data of all soils. Within the three groups of soils with high dosages of three different SCs, the mixtures of soils with SC_CG H exhibit significantly higher friction angles, which could be associated with the longest average fiber length of fillers in SC_CG.

These results can appear contradictory to findings in the literature [124,203-208], where increased strength properties (both cohesion and friction angle) of the soil treated with XG are reported. However, it is important to note that much of the strength related research found in the literature focuses on specimens at different curing stages [124] or at the optimum and controlled water content of the mixtures [209]. On the contrary, this research focuses on soils and mixtures at high water content. Some literature suggests that, in a wet, saturated state, treatment with SCs indeed results in decreased shear strength properties, particularly for internal friction angle. The investigation of low plasticity clay (CL) showed a 5% decrease in friction angle [124], while for low plasticity silt (ML) the decrease was more than 24% [203] for the addition of 1% XG. The impact of XG on cohesion is dependent on the cohesion of untreated soil. For high plasticity clay (CH) treated with 1% of XG the cohesion is reported to remain unaffected [205] while approx. 4% increase was observed in the case of low plasticity clay (CL) [124]. For partially saturated sandy materials, treated with 1% of XG the increase in cohesion can be up to 35% [205]. One of the reasons for low shear strength of biopolymer-treated soils with high water content are low viscous biopolymer hydrocolloids, which surround the soil particles. However, during the drying process, the transformation of XG hydrogel into a high-strength biofilm occurs, thereby enhancing the shear strength of the treated soil [210,211].

5.3.2.5 Saturated hydraulic conductivity

Saturated hydraulic conductivity (k) was measured using falling head permeameter at the end of consolidation stages in oedometer. Measurements were carried out at effective vertical stress of 25 kPa

and 50 kPa, except for mixtures of soils S2 and S3 with the SC_R H, where hydraulic conductivity was determined only for effective vertical stress of 25 kPa. In Table 5.13 the mean values of measured hydraulic conductivities are given for all samples of untreated soils and mixtures.

Table 5.13 Saturated hydraulic conductivity of soils and mixtures at effective vertical stresses of 25 kPa and 50 kPa. Data provided by ULJ.

		k (m/s)				
Soil	σ'_v **(kPa)**	**S***	**S* + SC_ R L**	**S* + SC_ R H**	**S* + SC_ CG H**	**S* + SC_ ZZC H**
S1	**25 kPa**	$(9.9 \pm 0.4) \cdot 10^{-7}$	$(9.3 \pm 0.3) \cdot 10^{-7}$	$(2.7 \pm 0.2) \cdot 10^{-10}$	$(3.7 \pm 0.5) \cdot 10^{-9}$	$(2.7 \pm 0.1) \cdot 10^{-10}$
	50 kPa	$(4.4 \pm 0.4) \cdot 10^{-7}$	$(3.1 \pm 0.1) \cdot 10^{-7}$	$(4.0 \pm 0.1) \cdot 10^{-11}$	$(1.1 \pm 0.1) \cdot 10^{-10}$	$(5.8 \pm 0.2) \cdot 10^{-11}$
S2	**25 kPa**	$(4.3 \pm 0.1) \cdot 10^{-7}$	$(2.6 \pm 0.1) \cdot 10^{-7}$	$(1.9 \pm 0.1) \cdot 10^{-10}$	$(6.0 \pm 0.1) \cdot 10^{-10}$	$(2.9 \pm 0.1) \cdot 10^{-10}$
	50 kPa	$(5.3 \pm 0.2) \cdot 10^{-8}$	$(2.0 \pm 0.1) \cdot 10^{-7}$	/	$(7.6 \pm 0.2) \cdot 10^{-10}$	$(6.2 \pm 0.3) \cdot 10^{-10}$
S3	**25 kPa**	$(4.1 \pm 0.1) \cdot 10^{-7}$	$(7.9 \pm 0.1) \cdot 10^{-10}$	$(1.3 \pm 0.2) \cdot 10^{-10}$	$(2.6 \pm 0.1) \cdot 10^{-10}$	$(1.4 \pm 0.1) \cdot 10^{-9}$
	50 kPa	$(1.7 \pm 0.1) \cdot 10^{-8}$	$(3.6 \pm 0.1) \cdot 10^{-10}$	/	$(4.8 \pm 0.8) \cdot 10^{-10}$	$(9.7 \pm 0.2) \cdot 10^{-10}$

In general, the SCs decrease the hydraulic conductivity of all soils. The magnitude of decrease in hydraulic conductivity due to the addition of high dosage of SCs is significant ($p<0.05$), i.e., between 10^2 to 10^4 m/s. Although untreated soils exhibit significantly different hydraulic conductivities, the addition of high dosage of SCs results in similar hydraulic conductivities of the mixtures. The hydraulic conductivity of mixtures with high dosages are unaffected by the effective vertical stresses for soil S3. In the case of S1 and S2, the hydraulic conductivities of high dosage mixtures at effective vertical stress of 25 kPa are significantly higher ($p<0.05$) compared to the ones at effective

vertical stress of 50 kPa. In general, the type of SCs was not recognized as influential parameter.

The results are in agreement with that in the literature [212] where for similar dosages of XG similar magnitude of decrease in hydraulic conductivity was reported, from $1.42 \cdot 10^{-7}$ m/s for untreated soil to $4.46 * 10^{-10}$ m/s for addition of 1% of XG. It is also established that the decrease is highly dependent on the soil type [206,212,213].

5.3.3 Conclusions

Research confirmed that addition of XG-based SCs affected the index properties, water absorption capacity, compressibility, drained shear strength and also hydraulic conductivity of the soil. The main function of developed SCs was the increase of soil water retention for plant growth. Due to this the compressibility, drained shear strength and hydraulic conductivity were determined on saturated specimens of soils and mixtures. The study proved that in saturated state, the XG hydrogels decreased soil strength, stiffness and hydraulic conductivity. By repeating tests on three types of soils it was found that the dosage of the SCs affected the geotechnical soil properties, while the type of filler in the SC did not turn out to be as influential. For investigated untreated soils and mixtures following conclusions can be made:

1. Addition of SCs increased liquid limit only for the soils S2 and S3 with relatively low initial liquid limits, while for the soil S1 with the highest initial liquid limit, the values remained approximately unchanged.
2. The increase of water absorption capacity due to the SCs was notable for all types of soil. The magnitude of increase in water absorption capacity due to SCs was governed by water absorption capacity of untreated soil. The type of SC did not have a considerable impact on water absorption, but the dosage of the SCs does.
3. The addition of the SCs led to the swelling of the mixtures under low effective vertical stress, inherently affecting their

compressibility. Analysis of the results highlighted the importance of the dosage of the SCs, while the type of the SC was not recognized as influential.

4. In terms of drained shear strength, the friction angles of treated soils were reduced compared to those of untreated soils, especially for silt with sand with the highest plasticity index (S1). The addition of a high dosage of SC_R and SC_ZZC yielded similar drained shear strengths, while SC_CG with the longest fibers exhibited somewhat higher friction angles, irrespective of the soil type. The friction angle was shown to be dependent on the dosage of SC.
5. In general, the hydrogel consistency of SCs decreased the hydraulic conductivity of all types of soil. For mixtures with high dosage of SCs, the hydraulic conductivity was independent of the effective vertical stress only in the case of soil S3, while for high dosage mixtures of S1 and S2 a decrease of hydraulic conductivity with increasing effective vertical stress was clearly identified. Generally, the type of SCs did not influence the hydraulic conductivity.
6. Considering that different types of SCs were specified with the amount of oxide ash and cellulose fillers with various fiber lengths, this study postulated that the influence of the fillers and their fiber length on the geotechnical properties of mixtures was limited, i.e., the XG appears to be the main component which governed the water sensitivity and the properties of the saturated mixtures.

The newly developed XG-based SCs exhibited favorable effects on soils in terms of water absorption, water retention capacity and hydraulic conductivity. Their presence could prove beneficial for retaining water and directly mitigating the consequences of extreme climatic events, such as droughts, floods, etc. However, high water content (saturated state) of mixtures had generally negative impact on their geotechnical properties.

While SCs can be highly beneficial in controlled environment (with regulated water inflow and/or controlled water content), special consideration should be taken when applying SCs in a natural environment where conditions are impossible to control and soil modification can result in even more severe consequences compared to the untreated state. In natural environment, soils improved with biopolymers experience cyclic process of rainfall infiltration and evaporation, which is another aspect to be considered and whose influence on the mechanical properties thoroughly investigated.

The impact of SCs on geotechnical properties of soil layer could be negligeable in the case of their use locally in planting holes for trees in small amounts (< 1.8% per dry soil mass). In case of applications on large areas with different thickness and inclination of treated soil layer further attempts should be made to overcome or at least mitigate the SCs sensitivity to water. Despite the fact that positive impact of filler's fiber length was indicated only by drained shear strength, it is believed that fillers with longer fibers could be promising component of SCs. This could counteract the negative effects of XG on soil strength, stiffness and compressibility. By following this approach, it would be possible to develop a universal sustainable SC that not only positively influences soil water retention ability but also enhances the geotechnical properties of forest soil susceptible to erosion and slope instabilities.

6 Planting trials within ONEforest project

According to the tasks outlined in the ONEforest project, different planting trials have been conducted to assess the effect of the produced TSCs and SCs on early plant performance. The TSCs and SCs compositions tested in these planting trials were chosen from the most promising ones, based on the results of the experimental activity described in the previous sections. The aim was to investigate the effect of these formulations in different European forest regions. Specifically, two planting trials have been performed in Germany under continental climate conditions, conducted by the University of Freiburg (UFR), with the use of soil conditioners: the first one in Jessen (Saxony-Anhalt) and the second one in Heldburg (Thuringia). However, the latter experiment failed due to a late frost which caused the death of the majority of the plants, and therefore no data could be reported. Other two planting trials have been performed in Spain under Mediterranean conditions conducted by the Forest Science and Technology Centre of Catalonia (CTFC). In this case, one planting trials have been conducted in Caldes de Montbui with the use of soil conditioners while the other in Girona with the use of topsoil covers. A further experiment was conducted at the University of Trento on tomato plants to investigate the possibility of using the produced TSCs and SCs also in agricultural applications. Further details of these field experiments are given in the following sections.

6.1 Planting trial with SCs in Jessen (Germany)

The field experiment was conducted and coordinated by the University of Freiburg (UFR) and the Saxony-Anhalt State Forest Centre in a forest field in Jessen (Saxony-Anhalt, Germany). The experiment involved the use of different soil conditioner, based on xanthan gum and gelatin, applied in a hydrated state. **All the reported images and data were kindly elaborated and provided by UFR.**

6.1.1 Materials and methods

6.1.1.1 Materials

The materials employed in the production of soil conditioners are listed in Table 6.1. A more detailed description can be found in Section 3.1.

Table 6.1 List of materials employed for the planting trial in Jessen.

Material	Label
Xanthan gum	XG
Arbocel R	R
Gelatin	GEL

As a benchmark, the experiment was also performed using a commercial potassium polyacrylate-based soil conditioner Be-Grow Boost M [168], kindly provided by the University of Freiburg (Germany) and produced by Be-Grow GmbH (Neustadt an der Weinstraße, Germany).

6.1.1.2 Sample preparation

Details about the preparation of xanthan-based soil conditioners are reported in Section 5.2.1. In particular, the composition SC_R was used. The gelatin-based soil conditioners were prepared by mixing

cellulose fibers with gelatin at dry stage with proportions 5:95% (w/w).
Prior to implantation, both xanthan-based and gelatin-based SCs were hydrated with two different water contents (1 liter and 2 liters). In Table 6.2 a summary of the treatments applied for the field experiment are reported.

Table 6.2 List of the applied treatments in the planting trial in Jessen.

Treatment	Composition	Water content (L)
BeGrow_2L	Commercial soil conditioner based on potassium polyacrilate	2.0
SC_R_1L	Soil conditioner based on xanthan gum and Arbocel® cellulose fiber	1.0
SC_R_2L	Soil conditioner based on xanthan gum and Arbocel® cellulose fiber	2.0
SC_GEL_1L	Soil conditioner based on gelatin and Arbocel® cellulose fiber	1.0
SC_GEL_2L	Soil conditioner based on gelatin and Arbocel® cellulose fiber	2.0

6.1.1.3 Experimental techniques

The experiment started on March 29th, 2022 and ended on September 23rd, 2022. The experiment was performed on 180 seedlings of red oaks (*Quercus rubra*) planted in a substrate constituted of sandy soil. For each treatment 30 trees have been tested. In Figure 6.1 pictures of the experimental design are shown.

(a) (b)

Figure 6.1 (a) Picture of the experimental design and (b) example of a planting pit with hydrated SCs. Images kindly provided by UFR.

During the experiment, the death rate and the mean height growth of the seedlings were monitored.

6.1.2 Results and discussion

In Table 6.3 the final results of the Jessen planting experiment are reported.

Table 6.3 Main results of semi-annual growth monitoring for the planting trial in Jessen. Data elaborated and provided by UFR.

Treatment	Death rate (%)	Mean growth (cm)
BeGrow_2L	54	4.2
SC_R_1L	3	2.9
SC_R_2L	27	3.7
SC_GEL_1L	47	0.4
SC_GEL_2L	80	2.1
Control	20	5.8

From Table 6.3 it is possible to observe that the seedlings treated with the xanthan-based SCs hydrated with 1 L water have the lowest

mortality rate, while in all the other cases tree mortality is higher than in the control. Moreover, for all the treatments the mean growth of the plants is lower compared to the control. A possible reason to explain these behaviours could be related to the use of hydrated soil conditioners that may have partially suffocated the roots of the seedlings, thus limiting their growth. In this sense, the use of dry SCs applied directly to the soil may be more advantageous for plant growth because in this way hydration, due to irrigation or rainfall, is more gradual. Moreover, the use of dry powder is also advantageous for a practical application because it saves operators from having to transport large quantities of water to the experiment site.

6.1.3 Conclusions

From the planting trial conducted under continental conditions in Jessen, it was demonstrated that the use of soil conditioners in the hydrated state could suffocate the plant roots, causing a high plant mortality rate and lower plant growth than the control. However, the use of xanthan-based soil conditioners hydrated with 1 L of water seems to improve the mortality rate, thus demonstrating the potential of this product for forestry applications.

6.2 Planting trial with SCs in Caldes de Montbui (Spain)

The field experiment was conducted and coordinated by the Forest Science and Technology Centre of Catalonia (CTFC) in a forest field in Caldes de Montbui (Spain). The experiment involved the use of xanthan-based soil conditioner, applied in the dry state and compared with commercial products. **All the reported images and data were kindly elaborated and provided by CTFC.**

6.2.1 Materials and methods

6.2.1.1 Materials

The materials employed in the production of soil conditioners are listed in Table 6.4. A more detailed description can be found in Section 3.1.

Table 6.4 List of materials employed for the planting trial in Caldes de Montbui.

Material	Label
Xanthan gum	XG
Arbocel R	R

As a benchmark, the experiment was also performed on two commercial products. The first was a potassium polyacrylate-based soil conditioner Be-Grow Boost M [168], kindly provided by the University of Freiburg (Germany) and produced by Be-Grow GmbH (Neustadt an der Weinstraße, Germany). The second was a soil conditioner containing water absorbing, growth stimulating and nutritive components, called TerraCottem Arbor® produced by TerraCottem Intl. SL (Cadiz, Spain).

6.2.1.2 Sample preparation

The details for the production of xanthan-based TSCs are extensively described in Sections 5.2.1. In particular, the composition SC_R was used in two different dosages. In Table 6.5 a summary of the treatments applied for the field experiment are reported.

Table 6.5 List of the applied treatments with the main technical properties.

Treatment	**Composition**	**Dosage (g/tree)**
SC_R_150g	Xanthan gum and cellulose fibers	150
SC_R_75g	Xanthan gum and cellulose fibers	75
TerraCottem	Commercial soil conditioner containing nutrients	40
BeGrow	Commercial soil conditioner based on potassium polyacrilate	1 Tap/tree

6.2.1.3 Experimental techniques

The experiment started on February 16th 2023 and ended on October 19th 2023. All the different treatments were applied to common pear (*Pyrus communis*), which is known to be a very tough plant in both hot and cold conditions. The field soil consisted of 28% clay, 22% silt and 50% sand. Figure 6.2 reports the arrangement of the experimental design. Specifically, a split-plot design with 3 blocks was established. A total of 195 trees, displayed in rows, were planted (39 trees for each treatment).

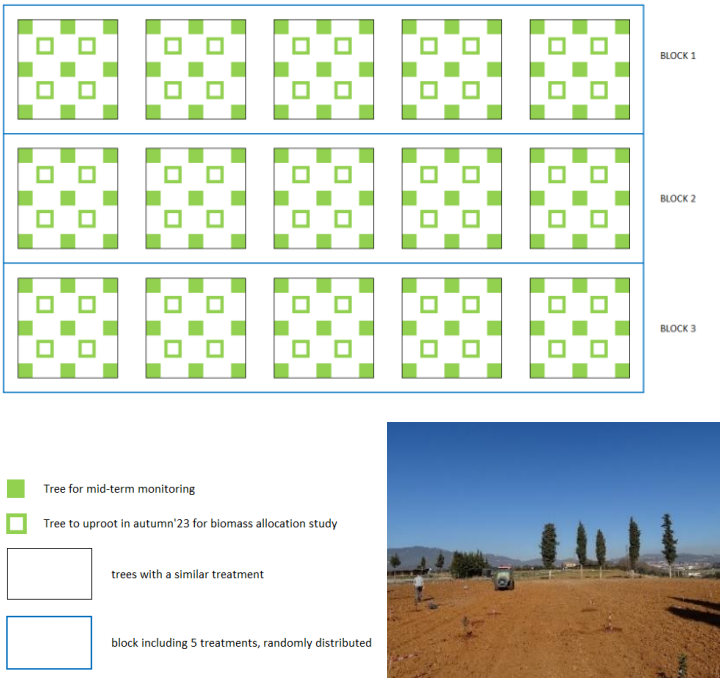

Figure 6.2 Arrangement of the experimental design. Images kindly provided by CTFC.

In October (end of the experiment), the vegetative status of the trees was monitored, assigning each tree to one of the following categories: A (alive and healthy), B (alive but showing vegetative problems like basal sprouting, leaf chlorosis, loss of apical shoot), C (dead).

At the beginning and end of the study, the basal diameter of the trees was measured in tenths of millimeters with a digital caliper (the measuring point was marked with a permanent marker to ensure a constant measuring point) and the total height in centimeters was taken with a measuring tape. The aerial tree volume was evaluated considering a conical shape and the annual diameter growth, annual height growth and annual volume growth as the difference between the final and the initial values. In the end of the experiment, biomass

allocation was also assessed in 12 seedlings per treatment, using the following procedure: trees were carefully uprooted in the laboratory, and the substrate was gently rinsed with tap water without damaging the roots. All broken roots of each seedling were recovered. Thus, seedlings were cut into three components: (i) stem, (ii) coarse roots (>2 mm thick) and (iii) fine roots (<2 mm thick). Root thickness was measured using a digital caliper. Each component was placed in aluminum trays and dried at 65-75 °C for 72 h. Finally, dry components were weighted with an accuracy of 0.1 g (laboratory scale) to calculate the aggregated root biomass and the total seedling biomass. The treatment effect on annual aerial growth (diameter, height, volume - 39 trees) and on each biomass allocation component (12 trees) was assessed by one-way ANOVA with a significance level of 0.05. When the assumptions of normality or homoscedasticity were not met, the data set was transformed by either square root, logarithm or inverse function, while tables and figures show untransformed data. Pairwise differences between treatments were assessed using the post hoc Tukey test. Statistical analyses were performed using R software release 4.3.1 (the R Foundation for Statistical Computing, 2023).

6.2.2 Results and discussion

A number of complications arose during the experiment, particularly with regard to extremely dry weather conditions, i.e., 312 annual precipitation (16 mm of rain recorded in March and April) and damage to the plants due to rabbit outbreaks. To counteract the drought problems, three emergency irrigations were applied: two in spring and one in summer (10 L/tree each). On the other hand, for the rabbit outbreak, shelters were installed, however, 30% of trees were damaged (non-lethally).

In Table 6.6 the results of the vegetative status at the end of experiment (October 2023) are reported.

Table 6.6 Results of the vegetative status at the end of the experiment. Data elaborated and provided by CTFC.

Treatment	Alive, healthy [%]	Alive, low vigour [%]	Dead [%]
SC_R_150g	41	11	48
SC_R_75g	38	15	47
TerraCottem	37	15	48
BeGrow	62	28	10
Control	29	11	61

From Table 6.6 it can be observed that the xanthan-based SC, in both dosages, reduces the plant mortality rates compared to the control and with results comparable to those of TerraCottem, which is a commercial product containing nutrients. The results are lower compared to BeGrow, which is, however, not a bio-based product.
In Table 6.7 the results of the annual growth monitoring are reported.

Table 6.7 Results of annual growth monitoring. The letters indicate that there is a significant difference between treatments according to Tukey test. Data elaborated and provided by CTFC.

Treatment	Diameter growth [mm/year]	Height growth [mm/year]	Volume growth [cm^3/year]
SC_R_150g	1.55 ± 0.19	13.4 ± 1.4	3.53 ± 0.98 ^{ab}
SC_R_75g	1.71 ± 0.22	17.1 ± 1.9	5.71 ± 1.21 ^{a}
TerraCottem	1.51 ± 0.21	18.5 ± 2.0	5.32 ± 1.28 ^{a}
BeGrow	1.81 ± 0.15	18.8 ± 2.2	5.85 ± 1.41 ^{a}
Control	1.47 ± 0.18	12.1 ± 2.6	1.63 ± 0.38 ^{b}

From Table 6.7 it can be seen that the xanthan-based SC is effective in significantly improving the volume growth of the plant compared to

the control and with results comparable to those of both commercial products. With regard to the other parameters studied, such as diameter and height growth, a slight improvement is observed, especially for dosage of 75 g (SC_R_75g), compared to the control.
In Table 6.8 the results of the biomass allocation are reported.

Table 6.8 Results of the biomass allocation (12 trees per treatment). Data elaborated and provided by CTFC.

Treatment	Aerial biomass [g/year]	Fine root biomass [g/tree]	Coarse root biomass [g/tree]	Total root biomass [g/tree]	Total biomass [g/tree]
SC_R_150g	2.95 ± 0.30	0.58 ± 0.09	4.15 ± 0.78	4.74 ± 0.81	7.69 ± 1.03
SC_R_75g	3.79 ± 0.67	0.86 ± 0.17	4.92 ± 0.75	5.78 ± 0.84	9.57 ± 1.43
TerraCottem	4.10 ± 0.65	0.42 ± 0.10	5.30 ± 1.01	5.71 ± 1.08	9.81 ± 1.52
BeGrow	4.04 ± 1.59	0.43 ± 0.11	4.83 ± 1.35	5.27 ± 1.40	9.30 ± 2.96
Control	3.04 ± 0.57	0.56 ± 0.11	3.48 ± 0.51	4.04 ± 0.55	7.07 ± 1.07

From Table 6.8 it is possible to observe that, overall, the xanthan-based SC, in low dosage, leads to an improvement of the studied parameters compared to the control and with similar results compared to the other commercial products.

6.2.3 Conclusions

From the planting trial conducted under Mediterranean conditions in Caldes de Montbui, despite adverse climatic conditions, it was possible to demonstrate and highlight the beneficial effect of SCs produced from xanthan gum and cellulose fibers. Different dosages were tested and the low-dose variation showed promising results in terms of improved volumetric plant growth compared to the control. Moreover, an improvement in the vegetative status and a decrease in the plant mortality rate were observed.

6.3 Planting trial with TSCs in Girona (Spain)

Paper under submission:

Valentini, F; Sorze, A; Coello, J; Chowdhury, A.A; Piergiacomo, F; Casapiccola, G; Brusetti, L; Bösing, J, Hirschmüller, S; Dorigato, A. Xanthan- and gelatin-based composites used as nursery groundcovers: assessment of soil microbiology and seedling performance, **submitted to** *Applied Soil Ecology*.

The field experiment was conducted and coordinated by Forest Science and Technology Centre of Catalonia (CTFC) at the Central Nursery of the public company Forestal Catalana, SA, in Sant Feliu de Buixalleu (Girona, Spain), specialized in producing high quality forest seedlings. The experiment involved the use of different topsoil covers, based on xanthan gum and gelatin, and commercial products. **All the reported images and data were kindly elaborated and provided by CTFC**.

6.3.1 Materials and methods

6.3.1.1 Materials

The materials employed in the production of topsoil covers are listed in Table 6.9. A more detailed description can be found in Section 3.1.

Table 6.9 List of materials employed for the planting trial in Girona.

Material	Label
Xanthan gum	XG
STEICO flex 036 (milled)	ST
Citric acid	CA
Glycerine	GLY
Casein	CAS
Tannic acid	TA
Gelatin	GEL

As a benchmark, the experiment was also performed using a commercial groundcover, Thermodisc® TD-16 produced by MYC-5 (Girona, Spain), composed of 90% natural fibers and 10% synthetic fibers, being fully biodegradable in 6-18 months (according to the producer technical data-sheet). Moreover, woodchips produced by chipping wood residues of the nursery, and applied as a 40 mm layer, were also applied.

6.3.1.2 Sample preparation

The details for the production of xanthan-based TSCs are extensively described in Sections 4.2.1 and 4.3.1. In particular, for this planting trial the composition CA60_cas has been used. The details for the production of gelatin-based TSCs are extensively described in Section 4.3.1. In particular, for this planting trial the composition ID8 (Table 4.12) has been used. In Table 6.10 a summary of the treatments applied for the field experiment are reported.

Table 6.10 List of the applied treatments with the main technical properties.

Code (Treatment)	**Composition**	**Thickness (mm)**	**Grammage (g/m²)**
T1 (CA60_cas)	Xanthan gum and wood fibers cross-linked with citric acid and coated with casein	3	900
T2 (ID8)	Gelatin and wood fibers cross-linked with tannic acid	8	2400
T3	Natural + synthetic fibers (Thermodisc®)	3	375
T4	Woodchips	40	-
T5 (control)	-	-	-

6.3.1.3 Experimental techniques

The experiment started on March 7th 2023 and ended on October 19th 2023. The topsoil covers were applied in 3.5 L pots with 160 mm in diameter at the top, on two species with high interest for forest restoration: narrow-leaved ash (*Fraxinus angustifolia)* and alder (*Alnus glutinosa*), both from the Spanish Provenance Region 10 (Coastal Catalonia). Seedlings were transferred from 300 (ash) or 200 (alder) cm^3 containers pots just before installing the topsoil cover. The substrate was composed of forest soil (35%), composted pine bark (35%), blond peat (25%) and sand (5%) to which a slow-release fertilizer, Basacote®, was added at a rate of 3 kg/m^3 substrate. The management during the vegetative period (2023) consisted of regular irrigation with sprinklers until water percolation. The irrigation dose was adapted to the daily temperatures and evapotranspiration. In summer, irrigation was applied every 1-2 nights.

For each species, a split-plot design with 27 trees per treatment was organized in 3 blocks, totalling 135 experimental trees per species. In each block, the treatments were randomly distributed in groups of 9 seedlings, arranged in a 3x3 quincunx design with seedlings 250 mm apart. Buffer trees in the perimeter of each block were also used to reduce possible edge effects. A schematic arrangement of the experiment and a representative picture of the nursery are shown in Figure 6.3 and Figure 6.4.

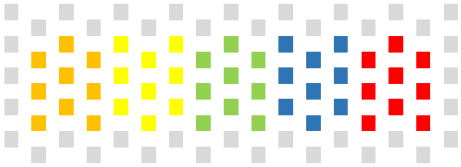

Figure 6.3 Arrangement of the experimental design of one block, for one species. The grey items indicate buffer trees while the rest of colors correspond to experimental trees, randomly assigned to the five experimental treatments. Image kindly provided by CTFC.

Figure 6.4 Picture of the experimental design in the nursery. It is possible to recognize the following samples' blocks (from bottom to top): T1, T2, T3, T4, T5, while the perimeter consists on non-experimental buffer trees. Image kindly provided by CTFC.

In October (end of the experiment), the vegetative status of the trees was monitored, assigning each tree to one of the following categories: A (alive and healthy), B (alive but showing vegetative problems like basal sprouting, leaf chlorosis, loss of apical shoot), C (dead). At the end of June and at the end of the experiment, weed proliferation in each pot was assessed through in three categories: (i) none (no weeds), (ii) low (1-20% of pot mouth covered with weeds), (iii) high (>20% of pot mouth covered with weeds). When weeds were found, their position in the pot mouth was described: (i) center, (ii) radial section of the topsoil cover, (iii) perimeter and (iv) through the topsoil cover.

At the beginning and end of the study, the basal diameter of the trees was measured in tenths of millimeters with a digital caliper (the measuring point was marked with a permanent marker to ensure a consistent evaluation) and the total height in centimeters was taken with a measuring tape. The aerial tree volume was evaluated considering a conical shape and the annual diameter growth, annual

height growth and annual volume growth as the difference between the final and the initial values. In the end of the experiment, biomass allocation was also assessed in 10 ash seedlings per treatment, using the following procedure: trees were carefully uprooted in the laboratory, and the substrate was gently rinsed with tap water without damaging the roots. All broken roots of each seedling were recovered. Thus, seedlings were cut into three components: (i) stem; (ii) coarse roots (>2 mm thick) and (iii) fine roots (<2 mm thick). Root thickness was measured using a digital caliper. Each component was placed in aluminum trays and dried at 65-75 °C for 72 h. Finally, dry components were weighted with an accuracy of 0.1 g (laboratory scale) to calculate the dry matter of each component and the aggregated root biomass, total seedling biomass, and root:shoot ratio.

The treatment effect on annual aerial growth (diameter, height, volume - 27 trees) and on each biomass allocation component (10 trees) was assessed by one-way ANOVA with a significance level of 0.05. When the assumptions of normality or homoscedasticity were not met, the data set was transformed by either square root, logarithm or inverse function, while tables and figures show untransformed data. Pairwise differences between treatments were assessed using the post hoc Tukey test. Statistical analyses were performed using R software release 4.3.1 (the R Foundation for Statistical Computing, 2023).

6.3.2 Results and discussion

The vegetative status of both plant species at the end of the growing season is shown in Figure 6.5.

Figure 6.5 Results of vegetative status evaluations at the end of the experiment. Data elaborated and provided by CTFC.

From Figure 6.5 it is possible to observe that the vegetative status is predominantly good for both species, with no dead seedlings. In the case of ash, the only treatment leading to more than 11% of trees with vegetative problems is T2, amounting to 23%. In the case of alder, vegetative problems affect only 4% of seedlings in T2 and T4, and 7% of T3. The results of weed proliferation are showed in Figure 6.6.

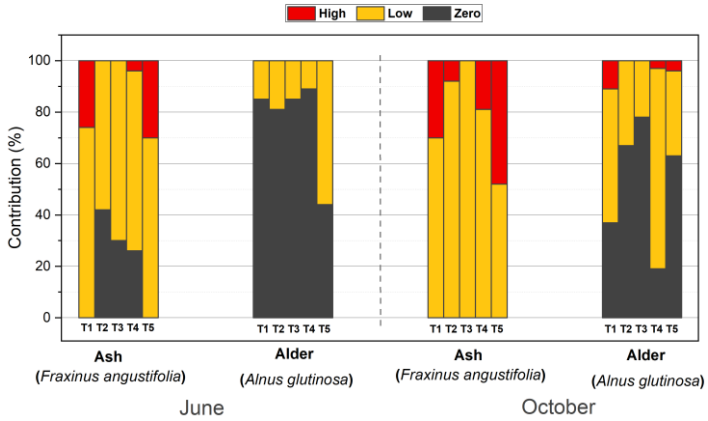

Figure 6.6 Results of weed proliferation evaluation performed in June (left) and October (right). Data elaborated and provided by CTFC.

From the results on weed proliferation, a different trend can be observed in the case of ash and alder trees, with greater weed proliferation in the case of ash trees, probably due to the lower shading capacity. The best results in terms of weed control are obtained for ash trees with treatment T2 in June and T3 in October; for alder trees the treatments are almost equivalent in June while in October the best results are observed with T3 and T2. In Figure 6.7 the weed distribution within the pot is displayed.

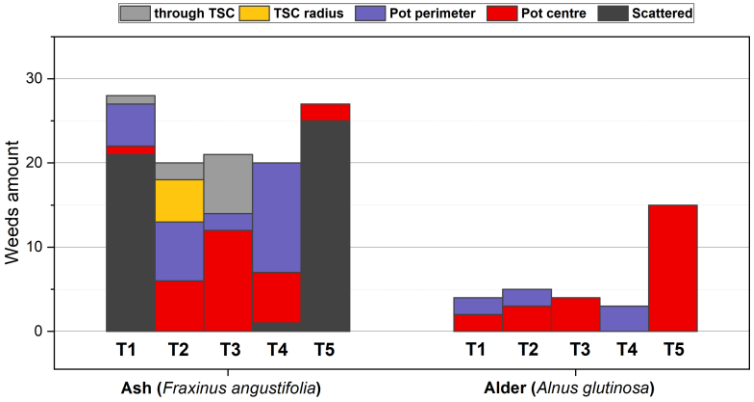

Figure 6.7 Results of weed distribution within the pot (observations of June). Data elaborated and provided by CTFC.

From Figure 6.7 it is possible to observe that T2 is very effective because only few weeds grew through the TSC but mainly on the top perimeter, in center and along the cut on the radius of the TSC. Instead, the reduced efficacy of T1, probably determined by its lower thickness and by a shrinkage observed in the first months, is highlighted by the fact that weeds grew throughout most of the pot without any preferential region. The results of the annual growth monitoring are reported in Table 6.11.

Table 6.11 Results of annual growth monitoring. The letters indicate that there is a significant difference between treatments according to Tukey test. Data elaborated and provided by CTFC.

Tree	Treatment	Diameter growth [mm/year]	Height growth [mm/year]	Aerial volume growth [cm³/year]
Ash	T1	8.2 ± 0.3 [b]	107.7 ± 4.6	45.8 ± 3.2 [b]
	T2	12.2 ± 0.5 [a]	103.0 ± 5.7	84.5 ± 7.8 [a]
	T3	8.0 ± 0.3 [b]	99.0 ± 4.8	41.2 ± 2.5 [b]
	T4	7.7 ± 0.3 [b]	94.6 ± 5.2	38.0 ± 3.5 [b]
	T5 (control)	7.6 ± 0.2 [b]	104.6 ± 4.1	39.5 ± 2.4 [b]
Alder	T1	10.3 ± 0.3	134.8 ± 5.3	108.6 ± 6.4 [ab]
	T2	11.1 ± 0.5	143.0 ± 4.6	128.8 ± 9.0 [a]
	T3	10.6 ± 0.6	134.5 ± 4.1	106.1 ± 8.7 [ab]
	T4	11.7 ± 0.5	136.2 ± 6.2	129.7 ± 8.1 [a]
	T5 (control)	10.3 ± 0.5	133.1 ± 4.5	99.8 ± 7.7 [b]

From the results of seedling growth monitoring, it is possible to observe different trends. In the first case (ash), treatment T2 leads to better plant diameter and aerial growth than all other treatments, doubling the volume growth. In the case of alder, T2 and T4 lead to higher aerial volume growth than control, while T1 and T3 do not show significant differences to any treatment. The aerial volume growth of alder is more than 2 times higher than that of ash and this different behaviour may also be influenced in different ways from the four treatments applied to control the weed growth.

Correlating weed proliferation and vegetative status of plants it is not possible to observe any significative relationship: both for ash and alder, independently from the weed proliferation level, the majority of plants (> 85%) is within the best vegetative status. On the other hand, as shown in Table 6.12, the weed proliferation level seems to

have a certain influence on the volume growth of plants since the highest values are found in case of absence of weeds, probably due to the lower competition between plants and weeds.

Table 6.12 Effect of weed proliferation on the growth parameters of ash and alder trees. Data elaborated and provided by CTFC.

Tree	Growth parameter	Weed proliferation		
		Zero	**Low**	**High**
Ash	Diameter growth [mm/year]	13.4 ± 0.6	11.8 ± 0.2	11.7 ± 0.3
	Height growth [cm/year]	120.6 ± 4.6	117.0 ± 2.7	124.0 ± 6.8
	Volume growth [cm^3/year]	60.8 ± 7.6	46.1 ± 2.4	48.7 ± 5.4
Alder	Diameter growth [mm/year]	15.9 ± 0.2	14.7 ± 0.4	-
	Height growth [cm/year]	173.8 ± 2.7	155.9 ± 6.8	-
	Volume growth [cm^3/year]	122.7 ± 4.2	96.7 ± 6.6	-

The results of the biomass allocation test are reported in Table 6.13.

Table 6.13 Results of biomass allocation on ash trees. The letters indicate that there is a significant difference between treatments according to Tukey test. Data elaborated and provided by CTFC.

Treatment	Stem biomass [g]	Fine roots biomass [g]	Coarse root biomass [g]	Total root biomass [g]	Total biomass [g]	Root:Shoot biomass ratio
T1	25.3 ± 1.6 ^{b}	14.5 ± 1.8	10.7 ± 1.1 ^{b}	25.2 ± 25 ^{ab}	50.5 ± 3.3 ^{b}	1.0 ± 0.1 ^{ab}
T2	51.6 ± 7.1 ^{a}	15.4 ± 2.4	19.1 ± 2.7 ^{a}	34.5 ± 4.1 ^{a}	86.2 ± 10.6 ^{a}	0.8 ± 0.1 ^{a}
T3	24.5 ± 3.1 ^{b}	17.4 ± 1.3	14.7 ± 1.5 ^{ab}	32.1 ± 2.1 ^{ab}	56.6 ± 4.4 ^{ab}	1.4 ± 0.1 ^{b}
T4	19.8 ± 3.6 ^{b}	15.8 ± 1.7	12.4 ± 1.9 ^{ab}	28.1 ± 3.3 ^{ab}	47.9 ± 6.9 ^{b}	1.6 ± 0.2 ^{b}
T5 (control)	25.8 ± 3.5 ^{b}	12.2 ± 1.4	10.3 ± 0.6 ^{b}	22.5 ± 1.7 ^{b}	48.4 ± 4.6 ^{b}	1.0 ± 0.2 ^{ab}

The results of the biomass allocation test performed on ash trees show that T2 leads to the best outcomes in most indicators: higher stem biomass than any other treatment, higher total biomass than all treatments except for T3, and higher root biomass than T5. Fine root biomass does not lead to significant differences between treatments. The root:shoot ratio of T2 is significantly lower than in the case of T3 and T4.

6.3.3 Conclusions

From the planting trial conducted under Mediterranean conditions in Girona it was possible to demonstrate that, in case of ash trees, gelatin-based TSC led to effective weed control and an increase of the aerial volume growth and total root biomass, despite a lower vegetative status than the other treatments. On the other hand, the xanthan-based TSC led to the best vegetative status, but was not effective in preventing weed proliferation and only slightly improved the growth parameters compared to the control and commercial products. In the case of alder, only a slight benefit from the use of TSCs was observed, with less weed proliferation in all treatments and with increases in aerial growth limited to the gelatin-based TSC compared to control.

6.4 Tomato planting trial with TSCs and SCs in Trento (Italy)

Paper in preparation:

Sorze, A; Valentini, F; Nardin, T; Larcher, R; Bösing, J, Hirschmüller, S; Dorigato, A; Pegoretti, A. Influence of bio-based mulching films and soil conditioners on a non-irrigated tomato planting trial.

6.4.1 Introduction

A field experiment was performed in a garden in the Department of Industrial Engineering of the University of Trento (46.06° N, 11.15° E, altitude 398 asl), in order to study the effect of different formulations of TSCs and SCs on plants. In particular, tomato plants (*Solanum lycopersicum L.*) were chosen because it is a crop of great economic importance worldwide and cultivated commercially on all continents. [214]. Tomato is an essential component in the diet of the world population because it has high levels of lycopene and minerals, resulting in benefits to human health [215]. It is also very sensitive to heat and drought stresses, therefore, it is suitable for the purpose of this study in which no irrigation was applied to the plant.

6.4.2 Materials and methods

6.4.2.1 Materials

The materials employed in the production of TSCs and SCs are listed in Table 6.14. A more detailed description can be found in Section 3.1.

Table 6.14 List of materials employed for the tomato planting trial.

Material	Label
Xanthan gum	XG
Arbocel R	R
STEICO flex 036 (milled)	ST
Citric acid	CA
Glycerine	GLY
Casein	CAS
Tannic acid	TA
Gelatin	GEL

As a benchmark, the experiment was also performed using a commercial potassium polyacrylate-based soil conditioner Be-Grow Boost M [168], kindly provided by the University of Freiburg (Germany) and produced by Be-Grow GmbH (Neustadt an der Weinstraße, Germany).

6.4.2.2 Sample preparation

The details for the production of xanthan-based TSCs and SCs are extensively described in Sections 4.2.1, 4.3.1 and 5.2.1. In particular, for this planting trial the TSCs compositions CA60, TA5 and CA60_cas were used, while for the SCs, the composition SC_R was used. The details for the production of gelatin-based TSCs are extensively described in Section 4.3.1. In particular, for this planting trial the composition ID8 (Table 4.12) has been used.
Table 6.15 reports the different compositions used as treatments for the tomato plants.

Table 6.15 List of treatments applied to tomato plants.

Code	Composition	Characteristics
SC_R	Soil conditioner based on xanthan gum and Arbocel® cellulose fiber	15 g/tree
SC_BeGrow	Commercial soil conditioner based on potassium polyacrilate	5 g/tree
TSC_CA60	Mulching film based on xanthan gum and wood fibers cross-linked with citric acid	Disc of 160 mm diameter and 3 mm thickness (grammage 900 g/m^2)
TSC_CA60_cas	Mulching film based on xanthan gum and wood fibers cross-linked with citric acid and coated with casein	Disc of 160 mm diameter and 3 mm thickness (grammage 900 g/m^2)
TSC_TA5	Mulching film based on xanthan gum and wood fibers cross-linked with tannic acid	Disc of 160 mm diameter and 3 mm thickness (grammage 900 g/m^2)
TSC_ID8	Mulching film based on gelatin and wood fibers cross-linked with tannic acid	Disc of 160 mm diameter and 8 mm thickness (grammage 2400 g/m^2)

6.4.2.3 *Experimental techniques*

The experiment started in May 2023 and lasted until December 2023 when all the plants wilted. A total of 72 tomatoes seedlings (*Solanum lycopersicum var. cerasiforme*) purchased from Consorzio Agrario Trento (Italy) were planted in three rows of 24 plants each (3 replications of each treatment per row). Plants with initial height of 90 mm were transplanted by hand, with 60-cm row spacing and 40-cm plant spacing on the seedbed. The experimental design was a randomized block design with eight treatments and nine replications, as described in Figure 6.8.

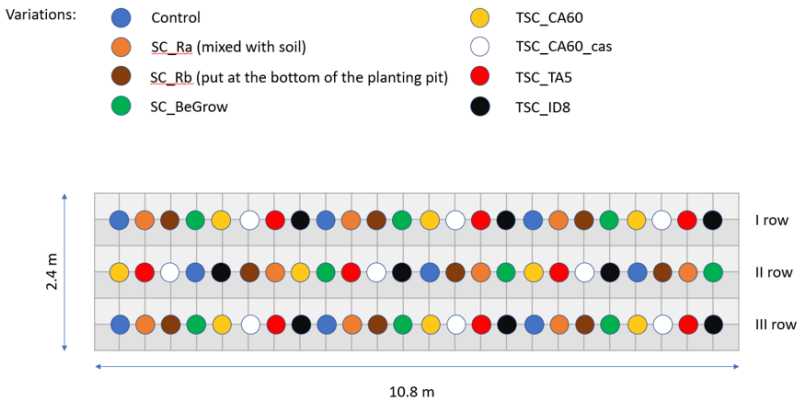

Figure 6.8 Arrangement of the experimental design of the tomato planting trial. The blue dots indicate the reference plants with no treatment while the other colors correspond to the tomato plants treated with TSC or SC.

The treatments consisted of the different SCs and TSCs described in Table 6.15 and the control (not-treated plants). For the composition SC_R, two different treatments were applied: the first (coded as SC_Ra), by mixing the product with the soil used to fill the plant pit after transplantation and the second (coded as SC_Rb), by putting the product at the base of the plant pit before transplantation. In both cases, the amount of SC used was 15 g per plant. The commercial soil

conditioner (SC_BeGrow) was used according to the supplier instructions: 5 g of product put at the base of the plant pit before transplantation.
Samples of the soil in which the test took place were also collected from the border (close to the first row of plants) and the center of the planting area (between second and third rows of plants) and were characterized by Fondazione Edmund Mach (S. Michele all'Adige, Italy). Tests revealed an overall loamy, alkaline, very calcareous soil with a good content of organic matter, potassium and magnesium and low phosphorus content. Composition of the soil in the center part and at the edges of planting zone is reported in Table 6.16.

Table 6.16 Soil analysis results for samples taken from the center and from the edge of the planting zone.

Determination	**Edge**	**Center**
Sand (2.0–0.05 mm)	412 g/kg	405 g/kg
Silt (0.05–0.002 mm)	458 g/kg	465 g/kg
Clay (<0.002 mm)	130 g/kg	130 g/kg
pH (in water ratio 1:2.5)	8.1	8.4
Total limestone	349 g/kg $CaCO_3$	345 g/kg $CaCO_3$
Active limestone	15 g/kg $CaCO_3$	20 g/kg $CaCO_3$
Organic substance	33 g/kg	12 g/kg
Assimilable phosphorus	27 mg/kg P_2O_5	15 mg/kg P_2O_5
Potassium	166 mg/kg K_2O	114 mg/kg K_2O
Magnesium	317 mg/kg MgO	284 mg/kg MgO

Concentration of sand, clay and lime identify the soil at both edges and center of planting area as loam. As observable from Table 6.16, both organic matter and soil nutrients (phosphorous, potassium and magnesium), were more concentrated at the edge of planting zone.

Relative humidity (RH%), rainfall, maximum and minimum air temperature were recorded daily throughout all the duration of the test using of a data logger Rotronic HL-1D (Rotronic AG, Switzerland), located at approximately 10 m from the experimental field. The weather conditions recorded during these tests are the same reported in Figure 3.1.

Before and after transplanting, no fertilizer was added to the plants and the experiment was performed without irrigation throughout all the experiment. The water supply was only provided by the rainfalls. During the experiment, the crop was hand harvested when ripe fruit rate reached about 90% (red stage). At harvest, total fruit yield was determined and marketable yield was assessed considering only red and disease-free fresh fruits.

The fruit quality was investigated through the evaluation of Brix degree and the content of lycopone, β-carotene, lutein and potassium. These analysis were carried out by Fondazione Edmund Mach (S. Michele all'Adige, Italy).

At the end of the experiment, the plants were uprooted and various studies were conducted on the root system. Specifically, the root length and the diameter of the main root, measured at the same depth for each sample, were evaluated using a digital caliper. The water content of the roots was also measured, by taking the weight of the roots just taken out of the soil and after complete drying.

6.4.3 Results and discussion

The experiment was affected by adverse weather conditions. Specifically, as reported in Figure 3.1, the presence of heavy rainfall, especially in the early stages after planting, did not allow the effect of treatments under non-irrigated conditions to be deeply investigated.

6.4.3.1 *Evaluation of the tomato yield*

In Figure 6.9, the results about the yield, intended as the total mass of tomatoes harvested, are reported.

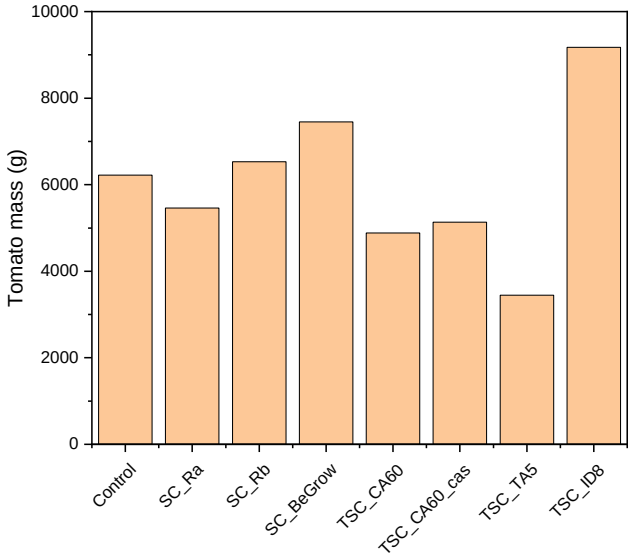

Figure 6.9 Total mass of tomatoes harvested for the different treatments.

From Figure 6.9, it can be seen that the tomato plants treated with the TSC_ID8 are characterized by the highest yield. This TSC formulation is particularly effective in improving the production of the tomato plants with respect to all the other treatments and the control. In Table 6.17 the yield of the treated tomato plants, between the different rows, calculated compared to the untreated plants are reported.

Table 6.17 Yields of treated tomato plants in the three rows calculated with respect to the control plants.

Code	Yield I row (%)	Yield II row (%)	Yield III row (%)
SC_Ra	+17.8	-61.8	-20.1
SC_Rb	+33.9	-47.2	+6.5
SC_BeGrow	+56.3	-23.2	-22.6
TSC_CA60	+6.3	-60.2	-42.1
TSC_CA60_cas	+5.2	-60.5	-12.7
TSC_TA5	-39.8	-49.3	-51.8
TSC_ID8	+55.4	-4.9	+121.8

From Table 6.17 it can be observed that in the first row there is an increase in the yield with respect to the control plants for almost all the different treatments. On the other hand, in the second and third rows, the yield of most treated plant is worse than the control. This behaviour could be related to the very high organic content in the soil in correspondence of the first row (Table 6.16) that, as extensively reported in literature, has a strong effect on the soil water storage capability [216,217]. It can be therefore hypothesized that also the addition of TSCs and SCs takes benefit from the presence of larger organic content in soil allowing to reach their full potential.

6.4.3.2 Evaluation of the fruit quality

It was noticed that the different treatments did not affect the fruit quality but, for all the five investigated parameters, similar values were found. Specifically, for all the treatments the Brix degree ranges from 5.3° to 7.6°. The lycopene and β-carotene contents, ranged from 120 mg/kg to 320 mg/kg and from 50 mg/kg to 170 mg/kg, respectively. The lutein content ranged from 6.3 mg/kg to 14.5 mg/kg, while the potassium content ranged from 2820 mg/kg to 3480 mg/kg.

6.4.3.3 Evaluation of the plant root system

The results of the main root diameter and length showed no statistically significant differences at 0.05 level for the different treatments. Overall, the root diameter values ranged from 0.87 cm to 1.0 cm, while the root length ranged from 32.6 cm to 33.9 cm. Furthermore, the values of final root dry mass and root water content also showed no statistical difference at the 0.05 level for the different treatments. In particular, the root dry mass values ranged from 3.7 g to 11.1 g, while the water content ranged from 76.8% to 80.9%.

6.4.4 Conclusions

From the tomato planting trial, the potential benefits of the applied treatments (both TSC and SC) on tomato plants under non-irrigated conditions could not be fully demonstrated due to the adverse weather conditions. However, it was possible to highlight that the gelatin-based TSC improved the total fruit yield compared to the control. Moreover, good results were also observed for the xanthan-based soil conditioner when applied in the soil with a higher organic content. Overall, no significant differences in fruit quality and plant root system were found for all the treatments applied.

In order to better investigate the effect of xanthan-based TSCs on tomato plants, an additional planting trial conducted in a greenhouse was recently carried out, in collaboration with the University of Bolzano. The investigation regarding this experiment is still ongoing (August 2024).

7 Evaluation of the environmental impacts and costs

The aim of this study was to evaluate the costs of production and the environmental impacts of the developed TSCs and SCs. This analysis was necessary in order to assess the feasibility of these products, i.e., to demonstrate their viability in practical applications and to assess their possible competitiveness on the market compared to commercial products. Specifically, the environmental impacts were evaluated through a Life Cycle Analysis (LCA).

7.1 Life Cycle Assessment (LCA) of TSCs and SCs

7.1.1 Scope definition

7.1.1.1 Analysed products

The analysis has been focused on TSCs and SCs developed by University of Trento (UNITN) and on TSCs developed by Rosenheim Technical University of Applied Sciences (THRO). Specifically, the products developed by UNITN are:

- TSC based on xanthan gum and wood fibers, cross-linked with citric acid and surface-treated with casein (coded as TSC_CA60_cas, see Section 4.3.1.2);
- SC based on xanthan gum and wood fibers (coded as SC_R, see Section 5.2.1.2).

The product developed by THRO is:

- TSC based on gelatin and wood fibers, cross-linked with tannic acid (coded as TSC_ID8, see Section 4.3.1.2).

These specific compositions were chosen because were found to be the most performant from the laboratory tests and were then used for the planting trials described in Sections 6.2 and 6.3.

7.1.1.2 Functional unit

The functional unit is defined in ISO 14040 as "Quantified performance of a product system for use as a reference unit".
LCA analysis assigns the environmental impact to a functional parameter of a product, allowing to quantify and compare this impact with that of other products defined in the same way. The functional unit used in this study was 1 kg of SC and 1 unit of TSC with a diameter of 160 mm. The choice of the functional units was done considering that the SC is provided loose, in form of pellets while the TSC is provided in form of discs. A diameter of 160 mm was selected since used for the planting trials performed for the ONEforest project.

7.1.1.3 Scope and system boundaries

This study considered a "cradle to gate" approach, covering the following stages: extraction of material resources and processing of the materials. It did not consider the use phase, the transport to the plant site and the eventual end-of-life stage.

7.1.2 Life Cycle Inventory (LCI)

The data necessary to model the production processes of the different materials constituting the TSCs and SCs has been found in the literature. Generic data came from the databases Ecoinvent 3.8, Agri-footprint version 6 and Agribalyse version 3.0.1. The inventory has been modelled using the software Simapro 9.3, provided by the company 2B Srl (Mogliano Veneto Italy).

In Table 7.1 the inventory of the production of 1 TSC by UNITN is reported.

Table 7.1 Inventory of the production of 1 unit of TSC developed by UNITN.

Component	Source	Unit	Quantity
Casein	Protein feed, 100% crude | buttermilk, from cow milk to generic market for protein feed | Cut-off, S	kg	0.00025
Citric acid	Citric acid (RER)| production | Cut-off, S	kg	0.003
Glycerine	Glycerine (RER)| market for glycerine | Cut-off, S	kg	0.006
NaOH	Sodium hydroxide, without water, in 50% solution state | market for | Cut-off, S	kg	0.0025
Tannin	See Table 7.7	kg	0.000025
Xanthan gum	See Table 7.4	kg	0.005
Water	Tap water (Europe without Switzerland)| market for | Cut-off, S	kg	0.125
Wood fibers	See Table 7.11	kg	0.005
Electricity for water heating	Electricity, low voltage (IT)| market for | Cut-off, S	kWh	0.0262
Electricity for xanthan gum mixing	Electricity, low voltage (IT)| market for | Cut-off, S	kWh	0.0278
Electricity for casein heating + stirring	Electricity, low voltage (IT)| market for | Cut-off, S	kWh	0.0315
Electricity for cross-linking in oven	Electricity, low voltage (IT)| market for | Cut-off, S	kWh	0.095
Electricity for drying	Electricity, low voltage (IT)| market for | Cut-off, S	kWh	0.072
Production scrap	Biowaste (RoW)| treatment of biowaste, industrial composting | Cut-off, S	kg	0.004
Water, emissions to air	Water	kg	0.125

In Table 7.2 the inventory of the production of 1 kg of SC by UNITN is reported.

Table 7.2 Inventory of the production of 1 kg of SC developed by UNITN.

Component	Source	Unit	Quantity
Xanthan gum	See Table 7.4	kg	0.741
Water	Tap water (Europe without Switzerland)| market for | Cut-off, S	kg	2.2
Wood fibers	See Table 7.11	kg	0.37
Electricity for water heating	Electricity, low voltage (IT)| market for | Cut-off, S	kWh	0.63
Electricity for mixing	Electricity, low voltage (IT)| market for | Cut-off, S	kWh	0.075
Electricity for drying	Electricity, low voltage (IT)| market for | Cut-off, S	kWh	2.16
Production scrap	Biowaste (RoW)| treatment of biowaste, industrial composting | Cut-off, S	kg	0.111
Water, emissions to air	Water	kg	0.125

In Table 7.3 the inventory of the production of 1 unit of TSC by THRO is reported.

Table 7.3 Inventory of the production of 1 unit of TSC developed by THRO.

Component	Source	Unit	Quantity
Gelatin	See Table 7.8	kg	0.04
NaOH	Sodium hydroxide, without water, in 50% solution state | market for | Cut-off, S	kg	0.00102
Tannin	See Table 7.7	kg	0.00601
Wood fibers	See Table 7.11	kg	0.032
Water	Tap water (Europe without Switzerland)| market for | Cut-off, S	kg	0.2
Electricity for water heating	Electricity, low voltage (DE)| market for | Cut-off, S	kWh	0.0246
Electricity for gelatin heating and stirring	Electricity, low voltage (DE)| market for | Cut-off, S	kWh	0.222
Electricity for mixing	Electricity, low voltage (DE)| market for | Cut-off, S	kWh	0.004
Electricity for cutting	Electricity, low voltage (DE)| market for | Cut-off, S	kWh	0.0361
Production scrap	Biowaste (RoW)| treatment of biowaste, industrial composting | Cut-off, S	kg	0.0377

In Table 7.4 the inventory of the production of 1 kg of xanthan gum is listed. Data were obtained from [218-230].

Table 7.4 Inventory of the production of 1 kg of xanthan gum.

Component	Source	Unit	Quantity
Ammonium nitrate (RER)| market for ammonium nitrate | Cut-off, S	Ecoinvent 3.8	kg	0.0193
Calcium chloride (RER)| market for calcium chloride | Cut-off, S	Ecoinvent 3.8	kg	0.00323
Dry milling	See Table 7.6	kg	1
Di ammonium phosphate, as 100% (NH3)2HPO4 (NPK 22-57-0), at plant/RER Mass	Ecoinvent 3.8	kg	0.00372
Electricity, low voltage (RER)| market group for | Cut-off, S (Electricity for ash and nitrogen recovery)	Ecoinvent 3.8	MJ	6.3
Electricity, low voltage (RER)| market group for | Cut-off, S (Electricity for drying)	Ecoinvent 3.8	MJ	7.6
Electricity, low voltage (RER)| market group for | Cut-off, S (Electricity for centrifugation and filtration)	Ecoinvent 3.8	MJ	18.2
Electricity, low voltage (RER)| market group for | Cut-off, S (Electricity for ultrafiltration)	Ecoinvent 3.8	MJ	1.3
Electricity, low voltage (RER)| market group for | Cut-off, S (Electricity for fermentation)	Ecoinvent 3.8	MJ	51.6
Glucose | market for glucose | Cut-off, S	Ecoinvent 3.8	kg	0.762
Inoculum medium	See Table 7.5	kg	2.04
Isopropanol (RER)| market for isopropanol | Cut-off, S	Ecoinvent 3.8	kg	0.379
Magnesium sulfate (RER)| production | Cut-off, S	Ecoinvent 3.8	kg	220.7
Soybean (RoW)| market for soybean | Cut-off, S	Ecoinvent 3.8	kg	0.18
Tap water (Europe without Switzerland)| market for | Cut-off, S	Ecoinvent 3.8	kg	1.28
Emissions to air, carbon dioxide (fermentation)	Ecoinvent 3.8	kg	0.027
Emissions to air, water	Ecoinvent 3.8	kg	2.23
Emissions to air, volatile organic compounds as C	Ecoinvent 3.8	kg	0.38

In Table 7.5 the inventory of the production of 1 kg of inoculum is listed. Data were obtained from [231,232].

Table 7.5 Inventory of the production of 1 kg of inoculum.

Component	Source	Unit	Quantity
Ammonium chloride (GLO)| market for | Cut-off, S	Ecoinvent 3.8	kg	0.00185
Boric acid, anhydrous, powder (GLO)| market for | Cut-off, S	Ecoinvent 3.8	kg	0.0000057
Calcium chloride (RER)| market for calcium chloride | Cut-off, S	Ecoinvent 3.8	kg	0.000017
Citric acid (GLO)| market for | Cut-off, S	Ecoinvent 3.8	kg	0.0019
Glucose (GLO)| market for glucose | Cut-off, S	Ecoinvent 3.8	kg	0.04
Iron(III) chloride, without water, in 14% iron solution state (GLO)| market for | Cut-off, S	Ecoinvent 3.8	kg	0.00000228
Magnesium sulfate (RER)| production | Cut-off, S	Ecoinvent 3.8	kg	0.000238
Phosphoric acid, industrial grade, without water, in 85% solution state (GLO)| market for | Cut-off, S	Ecoinvent 3.8	kg	0.00476
Tap water (Europe without Switzerland)| market for | Cut-off, S	Ecoinvent 3.8	kg	0.951
Zinc monosulfate (RER)| market for zinc monosulfate | Cut-off, S	Ecoinvent 3.8	kg	0.0000114

In Table 7.6 the inventory related to the dry milling process of 1 kg of material is reported. The inventory was obtained modifying an existing process for the dry milling of maize present in the Agri-Footprint database [233].

Table 7.6 Inventory of the dry milling process of 1 kg of material.

Process	Source	Unit	Quantity
Tap water (Europe without Switzerland)| market for | Cut-off, S	Ecoinvent 3.8	kg	0.1
Electricity, low voltage (RER)| market group for | Cut-off, S	Ecoinvent 3.8	MJ	0.29
Heat, district or industrial, natural gas (Europe without Switzerland)| heat production, natural gas, at industrial furnace >100kW | Cut-off, S	Ecoinvent 3.8	MJ	0.174
Wastewater, average (Europe without Switzerland)| market for wastewater, average | Cut-off, S	Ecoinvent 3.8	kg	0.1

In Table 7.7 the inventory of the production of 1 kg of tannin is listed. Data were obtained from [234-237].

Table 7.7 Inventory of the production of 1 kg of tannin.

Process	Source	Unit	Quantity
Bark chips, wet, measured as dry mass (Europe without Switzerland)| market for bark chips, wet, measured as dry mass | Cut-off, S	Ecoinvent 3.8	kg	1
Electricity, low voltage (RER)| market group for | Cut-off, S	Ecoinvent 3.8	kWh	241.9
Tap water (Europe without Switzerland)| market for | Cut-off, S	Ecoinvent 3.8	kg	220.7
Emissions to air, water	Ecoinvent 3.8	kg	60.7
Wastewater, average (Europe without Switzerland)| market for wastewater, average | Cut-off, S	Ecoinvent 3.8	m^3	0.16

In Table 7.8 the inventory of the production of 1 kg of cross-linked gelatin is listed. Data regarding the ratio between gelatin produced through acid and alkaline process were found in [238-241].

Table 7.8 Inventory of the production of 1 kg of cross-linked gelatin.

Process	Source	Unit	Quantity
Gelatin_pig offal (acid process)	See Table 7.9	kg	0.396
Gelatin_beef hides and skin (alkaline process)	See Table 7.10	kg	0.452

In Table 7.9 the inventory of the production of 1 kg of gelatin from pig offal (acid process) is listed. Data regarding the production of gelatin through acid process were obtained from [238,242].

Table 7.9 Inventory of the production of 1 kg of gelatin from pig offal.

Process	Source	Unit	Quantity
Electricity, low voltage (RER)| market group for | Cut-off, S	Ecoinvent 3.8	kWh	14.4
Hydrochloric acid, without water, in 30% solution state (RER)| market for | Cut-off, S	Ecoinvent 3.8	kg	0.27
Offal, pork/FR S	Agribalyse 3.0.1	kg	7.41
Steam, in chemical industry (RER)| production | Cut-off, S	Ecoinvent 3.8	kg	22.5
Sodium hydroxide, without water, in 50% solution state | market for | Cut-off, S	Ecoinvent 3.8	kg	0.296
Tap water (Europe without Switzerland)| market for | Cut-off, S	Ecoinvent 3.8	kg	400
Biowaste (RoW)| market for | Cut-off, S	Ecoinvent 3.8	kg	4.1
Water, emissions to air	Ecoinvent 3.8	kg	22.5
Wastewater, average (Europe without Switzerland)| market for wastewater, average | Cut-off, S	Ecoinvent 3.8	m^3	0.15

In Table 7.10 the inventory of the production of 1 kg of gelatin from beef hides and skin (alkaline process) is listed. Data regarding the production of gelatin through alkaline process were obtained from [238,242].

Table 7.10 Inventory of the production of 1 kg of gelatin from beef hides and skin.

Component	Source	Unit	Quantity
Beef co-product, other, at slaughterhouse (IE) Economic, S	Agri-footprint 6	kg	2.24
Beef co-product, hides and skins, from dairy cattle, at slaughterhouse, PEF compliant/NL Economic/Mass Sistema_S	Agri-footprint 6	kg	2.86
Electricity, low voltage (DE)| market for | Cut-off, S	Ecoinvent 3.8	kWh	4
Hydrochloric acid, without water, in 30% solution state (RER)| market for | Cut-off, S	Ecoinvent 3.8	kg	0.51
Sodium hydroxide, without water, in 50% solution state | market for | Cut-off, S	Ecoinvent 3.8	kg	0.306
Steam, in chemical industry (RER)| production | Cut-off, S	Ecoinvent 3.8	kg	22.5
Tap water (Europe without Switzerland)| market for | Cut-off, S	Ecoinvent 3.8	kg	400
Biowaste (RoW)| market for | Cut-off, S	Ecoinvent 3.8	kg	4.1
Emissions to air, water	Ecoinvent 3.8	kg	22.5
Wastewater, average (Europe without Switzerland)| market for wastewater, average | Cut-off, S	Ecoinvent 3.8	m^3	0.4

In Table 7.11 the inventory of the production of 1 kg of wood fibers is listed. Data regarding the production were obtained from [243-245].

Table 7.11 Inventory of the production of 1 kg of wood fibers.

Process	Source	Unit	Quantity
Electricity, low voltage (RER)| market for | Cut-off, S	Ecoinvent 3.8	kWh	0.4
Wood chips, dry, measured as dry mass (RER)| market for | Cut-off, S	Ecoinvent 3.8	kg	1.18
Waste wood, untreated (RER)| market group for waste wood, untreated | Cut-off, S	Ecoinvent 3.8	kg	0.176

7.1.3 Life Cycle Impact Assessment (LCIA)

The categories used for the environmental impact assessment refer to different methodologies and are listed in Table 7.12.

Table 7.12 Indicators for the description of potential environmental impacts.

Parameters	Unit	Methodology
Abiotic depletion	kg Sb eq	CML-IA (baseline)
Abiotic depletion (fossil fuels)	MJ	CML-IA (baseline)
Global warming (GWP100a)	kg CO_2 eq	CML-IA (baseline)
Ozone layer depletion	kg CFC-11 eq	CML-IA (baseline)
Human toxicity	kg 1,4-DB eq	CML-IA (baseline)
Fresh water aquatic ecotox.	kg 1,4-DB eq	CML-IA (baseline)
Marine aquatic ecotoxicity	kg 1,4-DB eq	CML-IA (baseline)
Terrestrial ecotoxicity	kg 1,4-DB eq	CML-IA (baseline)
Photochemical oxidation	kg C_2H_4 eq	CML-IA (baseline)
Acidification	kg SO_2 eq	CML-IA (baseline)
Eutrophication	kg PO_4^{---} eq	CML-IA (baseline)
Water scarcity footprint	m^3 eq.	AWARE 1.2
Particulate matter	Disease increase	EF 3.0 method
Land use	Pt	EF 3.0 method

7.1.4 Results and discussion

7.1.4.1 LCA results for TSCs

In Figure 7.1 the flow diagram referring to the production of 1 unit of TSC developed by UNITN, according to the impact category GWP is shown.

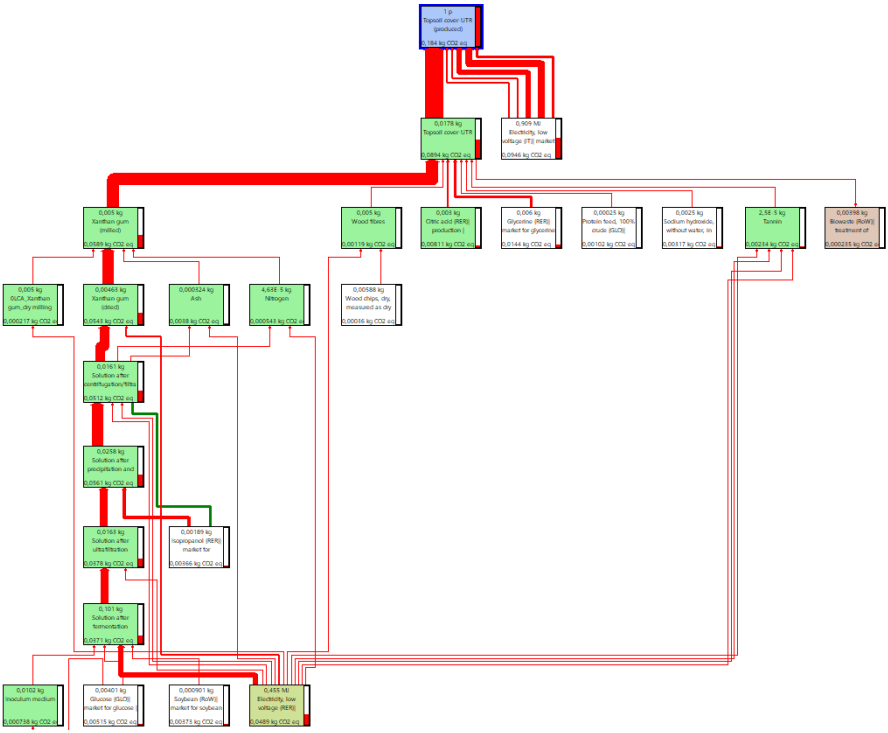

Figure 7.1 Flow diagram referring to the production of 1 unit of TSC developed by UNITN. Impact category GWP, cut-off 0.1%.

It is possible to observe that the impact is mainly caused by the xanthan gum production and in particular due to the electricity consumption for the fermentation and drying processes. A

considerable part of the environmental impact is also caused by the electricity consumption for the production process of the TSC and, minorly, by the use of glycerine and citric acid.
In Figure 7.2 the flow diagram referring to the production of 1 unit of TSC, developed by THRO, according to the impact category GWP is shown.

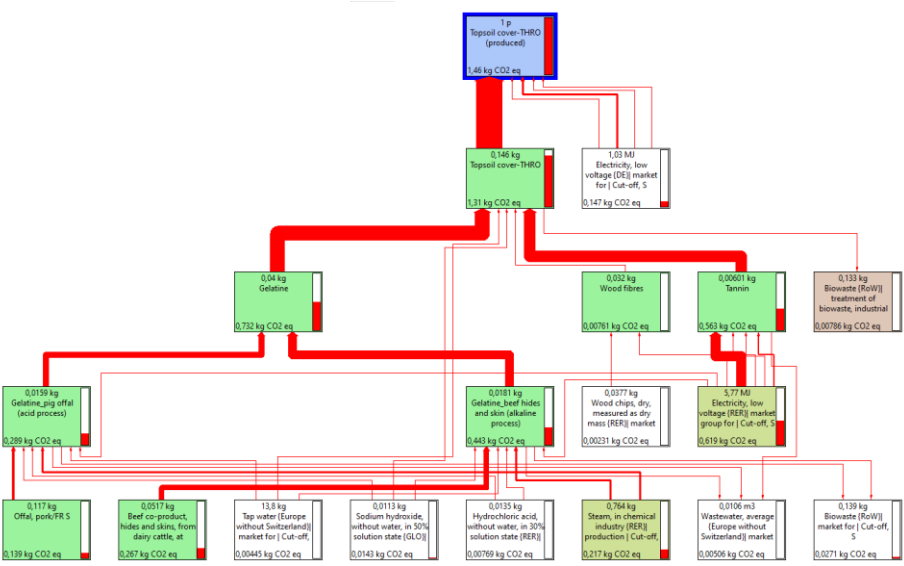

Figure 7.2 Flow diagram referring to the production of 1 TSC developed by THRO. Impact category GWP, cut-off 0.5%.

It is possible to observe that the impact is mainly caused by the use of gelatin and tannin. In case of gelatin production, the impact is derived from the breeding of pigs and beefs.
In Table 7.13 the results for each impact category to produce 1 unit of TSC are reported.

Table 7.13 Results of the life cycle impact assessment of the production of 1 unit of TSC.

Impact category	Unit	TSC (UNITN)	TSC (THRO)
Abiotic depletion	kg Sb eq	1.87E-06	8.08E-06
Abiotic depletion (fossil fuels)	MJ	2.27E+00	1.33E+01
Global warming (GWP100a)	kg CO_2 eq	1.84E-01	1.45E+00
Ozone layer depletion	kg CFC-11 eq	2.02E-08	9.24E-08
Human toxicity	kg 1.4-DB eq	1.13E-01	7.01E-01
Fresh water aquatic ecotox.	kg 1.4-DB eq	1.63E-01	1.09E+00
Marine aquatic ecotox.	kg 1.4-DB eq	2.28E+02	1.77E+03
Terrestrial ecotoxicity	kg 1.4-DB eq	5.55E-03	3.83E-02
Photochemical oxidation	kg C_2H_4 eq	4.12E-05	2.60E-04
Acidification	kg SO_2 eq	8.99E-04	9.76E-03
Eutrophication	kg PO_4^{---} eq	4.34E-04	5.89E-03
Water scarcity footprint	m^3 eq.	1.17E-01	5.82E-01
Particulate matter	Disease increase	5.89E-09	9.52E-08
Land use	Pt	2.45E+00	2.28E+01

Taking the GWP category as a reference, it is possible to observe that the environmental impact of the TSC developed by THRO is much higher with respect to the environmental impact of the topsoil developed by UNITN due to its higher mass (41 g vs. 18 g). On the other hand, this result should be correlated with the functionality of TSC: the material developed by THRO is more durable with respect of that developed by UNITN.

7.1.4.2 LCA results for SCs

In Figure 7.3 the flow diagram referring to the production of 1 kg of SC, developed by UNITN, according to the category GWP is shown.

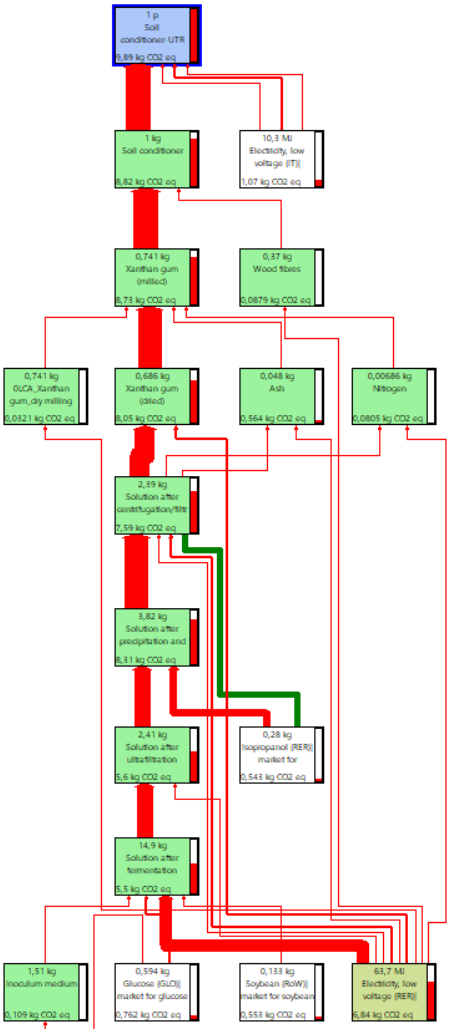

Figure 7.3 Flow diagram referring to the production of 1 kg of SC developed by UNITN. Impact category GWP, cut-off 0.3%.

It is possible to observe that the impact is almost entirely caused by the xanthan gum production and in particular due to the electricity consumption for the fermentation and drying processes.
In Table 7.14 the results for each impact category to produce 1 kg of SC are listed. Due to the unavailability of public data on the environmental impact of commercial products it is not possible to compare the obtained values in order to quantitatively assess their environmental advantage.

Table 7.14 Results of the LCIA of the production of 1 kg of SC.

Impact category	Unit	SC-UNITN
Abiotic depletion	kg Sb eq	9.95E-05
Abiotic depletion (fossil fuels)	MJ	1.17E+02
Global warming (GWP100a)	kg CO_2 eq	9.91E+00
Ozone layer depletion	kg CFC-11 eq	5.21E-07
Human toxicity	kg 1.4-DB eq	7.02E+00
Fresh water aquatic ecotox.	kg 1.4-DB eq	9.89E+00
Marine aquatic ecotox.	kg 1.4-DB eq	1.63E+04
Terrestrial ecotoxicity	kg 1.4-DB eq	1.25E-01
Photochemical oxidation	kg C_2H_4 eq	2.44E-03
Acidification	kg SO_2 eq	4.74E-02
Eutrophication	kg PO_4^{---} eq	2.93E-02
Water scarcity footprint	m^3 eq.	3.49E+00
Particulate matter	Disease increase	2.67E-07
Land use	Pt	9.29E+01

7.1.5 Conclusions

This study quantified the environmental performances of the materials used for the production of topsoil covers and soil conditioners. UNITN developed both these products: the first was based on xanthan gum cross-linked with citric acid, reinforced with wood fibers and coated with casein, while the second was based on

xanthan gum and wood fibers. THRO developed the TSC based on gelatin cross-linked with tannic acid and reinforced with wood fibers. The functional unit was 1 unit of TSC and 1 kg of the SC.

The LCA results have been reported for each impact category. The study was useful to identify the hot-spots in the production processes of the products. In particular, it was clear that the main environmental impact was related to the production of raw materials (xanthan gum, gelatin, tannic acid) at lab scale. Possible advantages could result from the optimization of the production processes at industrial scale and from a rationalization of the production process of these products. It has been found that the global warming potential (GWP) was higher for the TSC based on gelatin (1.45 kg of CO_2eq) in comparison to that of TSC based on xanthan gum (0.18 kg of CO_2eq) due to the larger amount of material used. These results, for a proper interpretation and comparison with those of commercial products, should be correlated with the degradation resistance and efficacy of these products.

7.2 Dataset of costs of TSCs and SCs

The dataset of costs was performed on the TSCs and SCs formulations used for the planting trials described in Section 6.2 and 6.3. The cost evaluation considered the cost of raw materials and electricity costs for the production process (February 2023) [246]. Labour cost was not considered in the calculations.
In Table 7.15 the dataset of costs related to the production of 1 unit of TSC produced is reported.

Table 7.15 Dataset of costs referred for the TSC.

Component	**Source**	**Cost per unit of TSC/tree [€]**
Xanthan gum	Galeno Srl	0.125
Wood Fibers	THRO	0.004
Glycerine	Farmalabor Srl	0.060
Citric acid	Riedel-de Haën GmbH	0.120
Casein	Thermo Fisher Scientific Inc.	0.025
NaOH	Thermo Fisher Scientific Inc.	0.028
Tannic Acid	Galeno Srl	0.00313
Water	Municipality of Trento	0.00013
Energy Consumption	GME [246]	0.045
Total		0.410

In Table 7.16 the dataset of costs related to the production of 1 kg of SC produced is reported.

Table 7.16 Dataset of costs referred for the SC.

Component	**Source**	**Cost per 1 kg of SC/tree [€]**
Xanthan gum	Galeno Srl	18.525
Cellulose fibers	THRO	0.74
Water	Municipality of Trento	0.0022
Total (materials)		19.3
Energy Consumption	GME [246]	0.46
Total		19.72

From the results it is possible to observe that the produced TSC has a cost of around 0.41€/unit, which is comparable with the costs of biodegradable commercial products. In case of SC the cost is around 20 € and even this is comparable to other commercial products present on the market, which range from 5 to 25 €/kg [167,168]. As observed in the evaluation of the environmental impacts, it is important to point out that also cost should always be compared taking into account the performances of the products in order to select the most suitable formulation for the desired application at the lowest possible cost.
Finally, considering that high purity materials are generally not required for these applications and in view of the future industrial upscaling of these products, it is expected that the cost will become more affordable in the near future, allowing thus an extensive use of the materials both in agricultural and forestry application.

8 General conclusions

8.1 Concluding remarks

The aim of this research was to develop innovative and sustainable solutions to support plant growth and, more generally, the revitalization of degraded forests within the objectives of the European project ONEforest. Specifically, laboratory and field studies on selected test sites have been performed in order to develop multifunctional topsoil covers (TSCs) and soil conditioners (SCs). The former are mulching films that aim to improve the regulation of moisture evaporation from the soil and at the same time protect the plant from competing weeds. The latter are products that are mixed with the soil in the planting hole and aim to improve the chemical, physical and water regulation characteristics of the soil. Both products were designed by exploiting the interesting properties and characteristics of xanthan gum, a bio-based polysaccharide.

In Chapter 4, topsoil covers were developed as xanthan-based hydrogels. Different compositions were investigated, testing different types and amounts of fillers (cellulose or wood fibers) and crosslinking agents (citric acid, sodium trimetaphosphate and tannic acid). These hydrogels exhibited excellent water absorption properties, even after multiple absorption/desorption cycles, especially in the case of xanthan gum cross-linked with citric acid, which provided significant water retention and stability. The addition of fibers limited volumetric shrinkage during drying and improved water retention. Moreover, the hydrogels cross-linked with citric acid and reinforced with wood fibers showed water vapor permeance comparable to commercial plastic mulching films and good penetration resistance, crucial for inhibiting weed growth. Additionally, these hydrogels possessed non-flammable characteristics, as demonstrated by flame tests, indicating safe use despite the presence of wood fibers. Outdoor tests confirmed the

stability and biodegradability of these hydrogels, with a significant mass loss over time, indicating environmental friendliness.

In Chapter 5, soil conditioners based on xanthan gum and cellulose fillers were developed and characterized to have a comprehensive evaluation of their influence on the water absorption, water retention, and water availability of soil. Different formulations were tested, changing the type and the concentration of the fillers. Microscopic observations revealed a homogeneous dispersion of fillers within the xanthan gum matrix, forming a network that could enhance soil-water regulation properties. Soil treated with xanthan-based SCs showed a marked improvement in water holding capacity (from 34% of untreated soil to 69% of soil treated with 1.8% of SC) and delayed water loss during drought, outperforming commercial alternatives. Tests on different soil types have shown the ability of these SCs to improve the water absorption capacity of all tested cases. However, in a saturated state and with overdoses, the produced SCs could adversely affect the geotechnical properties of soil, including compressibility, drained shear strength, and hydraulic conductivity. The impact of SCs on the geotechnical properties of the soil layer could be negligible in the case of their local use, in small quantities, in tree planting holes.

In Chapter 6, several field experiments were conducted in collaboration with other project partners to assess the effect of the produced TSC and SC compositions on tree growth under different climate conditions. In particular, experiments showed that the developed TSCs, while not greatly enhancing plant growth, were still able to ensure an excellent vegetative status to plants. On the other hand, the developed SCs demonstrated to improve plant growth, ensure better vegetative health, and reduce mortality rates compared to the control.

Finally, in Chapter 7, the production costs and environmental impacts of the best TSC and SC formulations were evaluated to determine

their sustainability and market competitiveness. Environmental impacts were assessed by a life cycle analysis (LCA), which identified the production of raw materials on a laboratory scale as the main contributing factor. Optimizing production processes at an industrial scale could offer significant environmental benefits. The global warming potential (GWP) was found to be 0.18 kg CO_2eq for producing one TSC unit (a 160 mm diameter disc) and 9.91 kg CO_2eq for producing 1 kg of SC.
Cost analysis estimated that one TSC unit costs around 0.40 €, and 1 kg of SC costs about 20 €, comparable to commercial products, that range from 5 to 25 €/kg. The high cost of xanthan gum, primarily due to its food-grade quality used in the study, was a significant contributor to the overall cost. However, for soil treatment applications, high purity is unnecessary, and the cost is expected to decrease with industrial-scale production. Moreover, the price of xanthan gum has already decreased significantly from 250 to 28 €/kg in recent years, further indicating potential cost reductions.

8.2 Future developments

The interesting results obtained from this PhD thesis give the possibility of upscaling the developed products to an industrial level. However, further optimization of the compositions of both TSCs and SCs could be carried out. Specifically, for TSCs, new efforts could be made in improving their resistance to biodegradation thus extending their service life. This could be done by modifying the composition, i.e., coupling xanthan gum with other biopolymers such as gellan gum or gelatin, or by changing the TSCs geometry, i.e., increasing the thickness and the diameter of the discs.
For SCs, an interesting improvement could be the addition of fillers with longer fiber length, in order to improve the soil shear strength and also the other geotechnical properties.

9 Other activities

During the PhD period, additional research topics were pursued in order to acquire additional skills and knowledge in the field of materials engineering. Specifically, the investigation regarded insulating foams and it is correlated to the topic of the Master's thesis, i.e., the development of polyethylene foams for thermal energy storage applications.

In particular, the following sections will present two of the main side works, both related to investigations on polyurethane foams (PU). PUs are low density thermosetting polymers that are synthesized from the exothermic reaction between polyols and polyisocyanates [247,248]. PUs are widely recognized for their outstanding properties: good thermal insulation, low density, ease of processing, shock wave absorption, low-velocity impact resistance, crashworthiness, and acoustic damping. Therefore, PU have emerged as a preferred choice for insulating applications in several sectors, such as residential and commercial buildings, transportations and military industry [249-252].
The following works have exploited and investigated different aspects of PU foams production and properties. The first study was related to the investigation of the mechanical reprocessing of PU and phenolic foams (PF) to produce novel PU foams with lower environmental impact, containing different amount of recyclates. The second work exploited the properties of PU for the development of multifunctional sandwiches with structural and thermal management properties.

9.1 Mechanical reprocessing of polyurethane and phenolic foams to increase the sustainability of thermal insulation materials

Published paper:

Simonini, L; Sorze, A; Maddalena, L; Carosio, F; Dorigato, A. Mechanical reprocessing of polyurethane and phenolic foams to increase the sustainability of thermal insulation materials. *Polymer testing*, **2024**, 138, 108539.

9.1.1 Introduction

The increasing use of polyurethane (PU) and phenolic (PF) foams in insulation applications has recently led to a growing need for more responsible end-of-life management, and recycling has been recognised as the most effective alternative to reduce their disposal in landfills and increase their sustainability [253,254]. The most common recycling method is mechanical recycling, which involves the physical reprocessing of the foamed polymer waste to produce new materials. Therefore, the aim of this work was to perform, for the first time, a comparative analysis of the potential of the mechanical recycling of PU and PF foams for the development of more eco-sustainable expanded polyurethane panels utilized in thermal insulation of the buildings. At this aim, commercial PU and PF foams were ground into two different particle sizes and incorporated within virgin PU foams at varying concentrations. Although some studies on the mechanical recycling of polyurethane foams already exist in the literature, there are no investigations on the use of recycled PF foams in PU foam boards. With this process, therefore, it might be possible to reduce the use of virgin precursors and increase the recycled content in insulation boards. The obtained foam materials were characterised from a morphological and thermo-mechanical point of view, with a focus on their fire behaviour.

9.1.2 Materials

Polyol (HDR R 150) and isocyanate (ISN 1), having viscosity of 1050 cPs and 200 cPs and density 1.10 g/cm^3 and 1.23 g/cm^3, respectively, were provided as liquids reagents by Kairos Srl (Verona, Italy) and used to prepare the virgin PU foam. Recycled polyurethane foam was obtained by discarded panels having dimensions of 80×100×10 cm^3, supplied by Giona Holding Srl (Santa Maria di Zevio, Italy). These panels had a geometrical density equal to 0.040 g/cm^3 and a thermal conductivity of 0.022 W/m·K at 10 °C, as reported in the datasheet. Recycled phenolic foam was obtained by ISO FEN - VIT VV thermal insulating panels, with dimension of 60×120×10 cm^3, provided by Isolmec Group Spa (Como, Italy). This material had a geometrical density equal to 0.035 g/cm^3 and thermal conductivity of 0.019 W/m·K at 10 °C, as reported in the datasheet. All materials were used as received.

9.1.3 Sample preparation

Polyurethane foams were prepared by mixing the liquid reagents, i.e., polyol and isocyanate, at room temperature in a constant weight ratio of 100:130, as suggested by the supplier. The mixing process was carried out at 300 rpm for 20 seconds to obtain a homogeneous mixture. The obtained mixture was then poured into a preheated (40 °C) mould measuring 250×250×25 mm^3 and placed in an oven for 20 minutes at 40 °C, to allow the foaming process to occur.
Recycled foams were prepared by grinding the discarded panels of PU and PF for 10 minutes by using an Ika Werke M20 mill (Ika AG, Staufer, Germany). The ground material was then sieved to recover granules of sizes ≤ 100 μm and 100-200 μm (denoted with letter "f" and "c", respectively, to indicate a fine and a coarse granulometry). The sieved material was dried at 40 °C overnight, then it was gradually added to the polyol and manually stirred for 20 seconds to obtain a homogeneous mixture. The isocyanate was then added to the mixture at the same relative weight ratio as used for the production of

neat PU foams, and mixed for additional 20 seconds. The mixture was then poured into the preheated mold (40 °C) and subjected to the foaming process previously described for neat PU panels. In this way, foams were prepared with an amount of recycled PF (or PU) of 2.5 wt%, 5.0 wt% and 7.5 wt% (relative to the total weight of liquid PU precursors). These weight concentrations corresponded to a recycled PU content respectively equal to 40.1 %vol, 58.3 %vol and 68.3 %vol, and a recycled PF concentration respectively equal to 50.9 %vol, 73.3 %vol and 85.9 %vol (with respect to the total volume of the liquid PU precursors). The denomination of the prepared samples is summarized in Table 9.1.

Table 9.1 List of the prepared PU samples.

Sample	**Virgin PU (wt%)**	**Size of recycled granules (μm)**	**Recycled PU (wt%)**	**Recycled PF (wt%)**	**Recycled PU (% vol)**	**Recycled PF (% vol)**
PU	100.0	-	-	-	-	-
PF	0.0	-	-	-	-	-
PU2.5fPU	97.5	≤ 100	2.5	-	40.5	-
PU5fPU	95.0	≤ 100	5.0	-	58.3	-
PU7.5fPU	92.5	≤ 100	7.5	-	68.3	-
PU2.5cPU	97.5	100-200	2.5	-	40.5	-
PU5cPU	95.0	100-200	5.0	-	58.3	-
PU7.5cPU	92.5	100-200	7.5	-	68.3	-
PU2.5fPF	97.5	≤ 100	-	2.5	-	50.9
PU5fPF	95.0	≤ 100	-	5.0	-	73.3
PU7.5fPF	92.5	≤ 100	-	7.5	-	85.9
PU2.5cPF	97.5	100-200	-	2.5	-	50.9
PU5cPF	95.0	100-200	-	5.0	-	73.3
PU7.5cPF	92.5	100-200	-	7.5	-	85.9

9.1.4 Experimental techniques

9.1.4.1 Microstructural characterization

The morphological characterization of the foams was carried out with the use of field emission scanning electron microscopy (FESEM) using a Carl Zeiss AG-SUPRA 40 microscope (Carl Zeiss, Oberkochen, Germany) operating at an acceleration voltage of 3.5 kV. Prior the observation, the samples were coated with a thin Pt/Pd 80:20 coating for 20 s to make them conductive, by using a Quorum Q150T ES sputter coater (Quorum Technologies, Lewes, UK).

The porosity of the foams was assessed by calculating the geometrical and theoretical density of the samples. The geometrical density (ρ_{geom}) is defined as the experimental density of a structure including porosity and defects, and it was calculated according to Equation (9.1):

$$\rho_{geom} = \frac{m_{sample}}{V_{geom}} \tag{9.1}$$

where m_{sample} is the weight (in g) and V_{geom} is the geometrical volume (in cm^3) of cylindrical samples, having radius of 12.5 mm and height of 25 mm, cut from the prepared foams. At least 5 specimens were measured for each composition. The theoretical density (ρ_{th}) is defined as the density of a structure without defects and porosity, and it could be obtained from the mixture rule (Equation (9.2)):

$$\rho_{th} = \sum_{i=1}^{n} \varphi_i \cdot \rho_i \tag{9.2}$$

where φ_i and ρ_i are respectively volumetric fractions and the density of each constituent (i.e., polyol, isocyanate and PU/PF recycled foam). For polyol and isocyanate, the density at liquid state has been considered in the calculation, while for the PU/PF recyclate the density at foamed state, corresponding to the geometrical density reported in datasheet, has been taken into account. The apparent

density (ρ_{app}) was measured with an Accupyc 1330 helium pycnometer (Micromeritics Instrument Corporation, Norcross, GA, USA) following ASTM D6226 standard. Measurements were conducted at a temperature of 23 °C, using a 1 cm^3 cell and performing 30 measurements for each sample. The total porosity (P_{tot}) was calculated as reported in Equation (9.3):

$$P_{tot} = \left(1 - \frac{\rho_{geom}}{\rho_{th}}\right) \quad (9.3)$$

The open porosity (P_{open}) was calculated as reported in Equation (9.4):

$$P_{open} = \left(1 - \frac{\rho_{geom}}{\rho_{app}}\right) \quad (9.4)$$

Therefore, the closed porosity (P_{closed}) was calculated as shown in Equation (9.5):

$$P_{closed} = P_{tot} - P_{open} \quad (9.5)$$

9.1.4.2 Thermal characterization

The thermal conductivity (λ) of the prepared foams was determined on specimens of 150×150×25 mm^3 using a Netzsch HFM 446 small lambda instrument (NETZSCH-Gerätebau, Selb, Germany) at constant temperature of 10 °C and according to ASTM C518-21. Three specimens were tested for each composition.

Thermogravimetric analysis on the prepared foams was conducted by using a Mettler TG50 machine (Mettler Toledo, Columbus, OH, USA) under a nitrogen flow of 100 ml/min and imposing a heating ramp from 30 °C to 700 °C and a heating a rate of 10 °C/min. The residual mass at 700 °C (m_{700}), the onset temperature of the degradation (T_{onset}) and the temperature of maximum degradation rate (T_{max}), obtained from the peak of the derivative of TGA thermogram (DTG), were assessed. Only one specimen was tested for each composition.

9.1.4.3 Mechanical characterization

Three-point bending tests were performed using an Instron 5969 machine (Instron®, Norwood, MA, USA), equipped with a load cell of 1 kN, in order to determine the flexural modulus (E_f), the flexural strength (σ_f) and the flexural strain at break (ε_f) according to ISO 1209-2. The flexural properties were then normalized for the geometrical density of the foams. Samples had dimensions of 230×30×15 mm^3, and a span-to-depth ratio of 12 was used. The tests were carried out at constant temperature of 24 °C at a speed of 20 mm/min, and at least 10 specimens for each composition were tested.

Quasi-static compression tests were performed with the Instron 5969 machine (Instron®, Norwood, MA, USA), equipped with a load cell of 1 kN, in order to determine the compressive modulus (E_c) and the compressive strength (σ_c), according to ASTM D1621-16 standard. Even in this case, the compressive properties were normalized for the geometrical density of the foams. Samples had dimensions 50×50×25 mm^3, tests were carried out at constant temperature of 24 °C, with a testing speed of 2 mm/min. At least 10 specimens for each composition were tested.

9.1.4.4 Forced combustion tests

Cone calorimetry measurements (Noselab, Milan, Italy) were conducted following ISO 5660-1 standard considering a 35 kW/m^2 radiative heat flux and setting a distance of 25 mm between the specimens and the radiation source. Specimens with dimensions 100×100×20 mm^3 were preliminarily conditioned at a temperature of 23 ± 0.1 °C and at a relative humidity of 50 ± 0.1% for at least 48 hours in climatic chamber, and all formulations were tested in triplicate. Post combustion cone calorimetry residues were analysed by a Zeiss Evo 15 scanning electron microscope (Carl Zeiss, Oberkochen, Germany) operating at 20 kV. Samples were positioned on conductive tapes and gold sputtered before the measurements.

9.1.5 Results and discussion

9.1.5.1 Microstructural characterization

Representative SEM micrographs of the recycled PU and PF foams, after the sieving process, are reported in Figure 9.1.

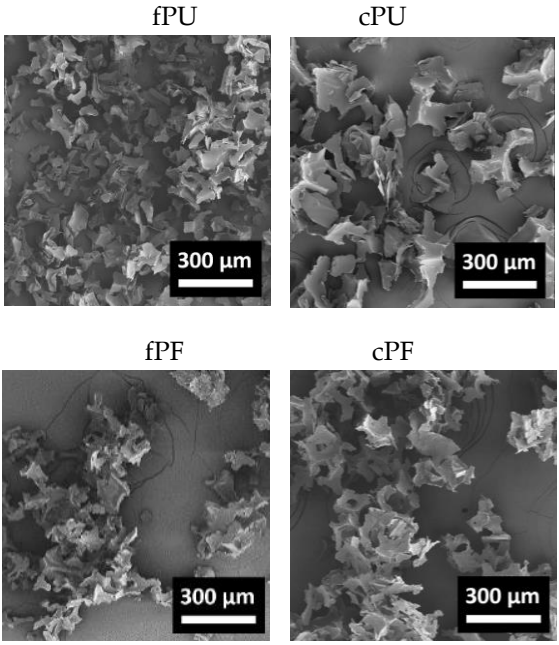

Figure 9.1 SEM micrographs of recycled PU and PF particles.

The sieved materials appear as sharp particles with irregular morphology. Their normal size distribution is shown in Figure 9.2, while their mean dimension is numerically reported in Table 9.2.

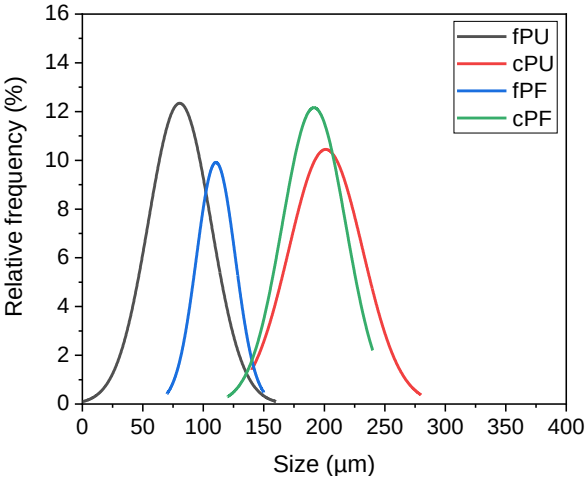

Figure 9.2 Normal size distribution of recycled PU and PF particles after sieving.

Table 9.2. Mean size of recycled PU and PF particles after sieving.

Sample	Size (µm)
fPU	80.4 ± 25.8
cPU	201.2 ± 30.5
fPF	110.4 ± 16.1
cPF	191.5 ± 26.2

The particles size reported in Table 9.2 corresponds to the dimensional ranges denoted as "fine" and "coarse" in Section 9.1.3. Their rather tight size distribution suggests that the materials have been efficiently ground and sieved, resulting in PU and PF foam recyclates with good morphological uniformity.

The cellular morphology of the prepared foams is shown in SEM micrographs displayed in Figure 9.3.

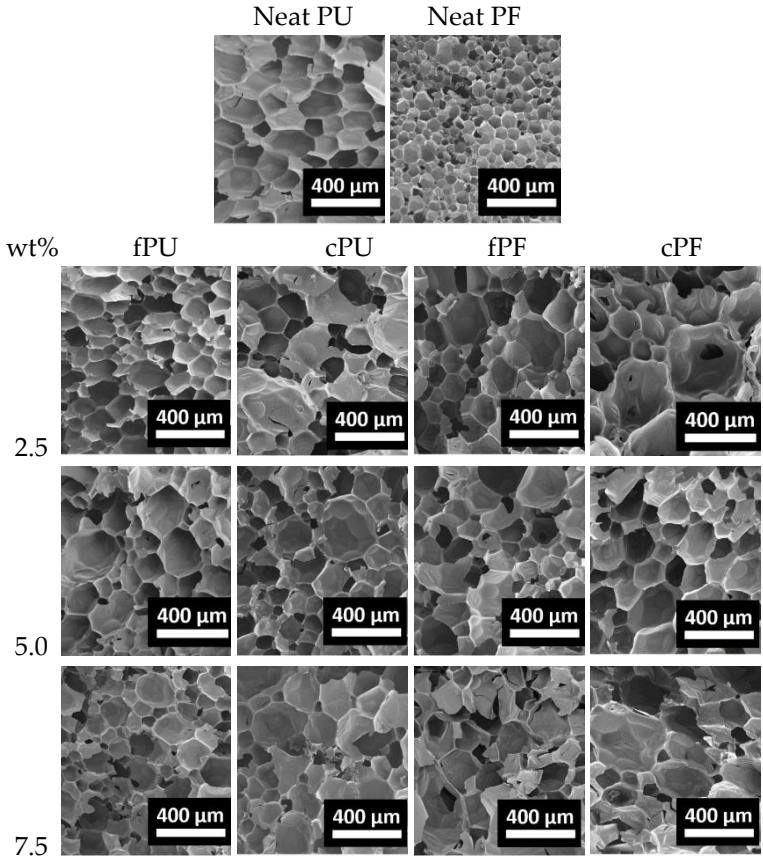

Figure 9.3 SEM micrographs of the prepared foams.

Neat PU and PF foams show a regular cell structure with a uniform porosity and a clear definition of the cell walls. The mechanism of PU cell formation involves the reaction between isocyanate and polyol components, which leads to the generation of gaseous carbon dioxide that acts as a blowing agent, creating the cell structure. The presence of recyclates introduces nucleation sites, leading to the formation of smaller cells. Specifically, as observed from Figure 9.3, the addition of the recycled foam particles allows to substantially maintain the

regularity of the cell structure, but their presence is not clearly visible since they are embedded in the virgin PU foamed matrix. This suggests that, despite the elevated volume fraction of recyclate present in the liquid mixture, the PU precursors adequately wet the recycled particles, ensuring a rapid and efficient foaming process. On the other hand, the addition of PU and PF recyclates at a concentration of 7.5 wt% determines the most significant morphological changes in the cellular structure. Even if in these foams the homogeneity of the cellular structure is not dramatically impaired, the increased viscosity of the liquid matrix due to recyclate addition could have probably slowed down the cross-linking reaction within the PU matrix [255]. Moreover, from these micrographs it is evident that some interconnected porosity is created in the foams upon the introduction of the recycled particles, and this could potentially affect their thermal conductivity. In particular, the brighter zones in the micrographs correspond to the closed pores, whereas the dark sections are related to the open holes. A clear visualization of this phenomenon can be seen in Figure 9.4, where the presence of recycled PF particles induces the formation of open porosity in the foam structure.

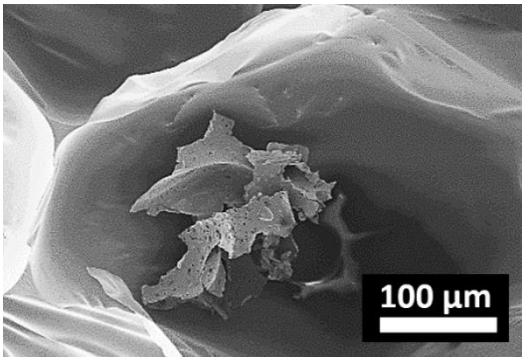

Figure 9.4 SEM image showing the formation of an open pore due to the presence of a recycled PF particle within the virgin PU foam (sample PU7.5cPF).

The normal distribution of the cell size in the prepared foams is represented in Figure 9.5(a,b), while the values of the mean cell size are numerically reported in Table 9.3.

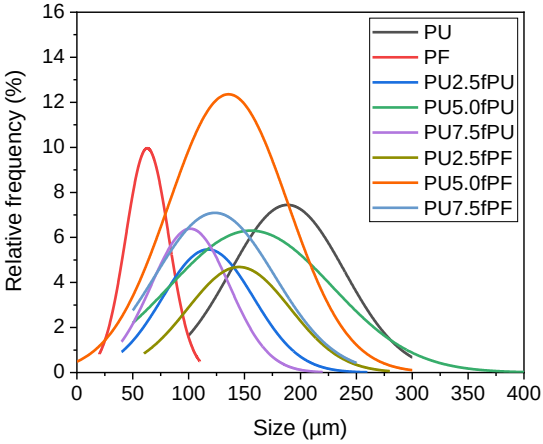

(a)

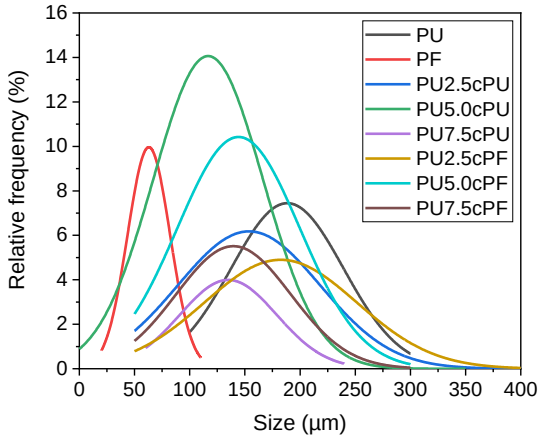

(b)

Figure 9.5 Normal distribution of the cell size of the foams prepared by using neat PU, neat PF and PU/PF recyclates with (a) fine and (b) coarse granulometry.

Table 9.3. Mean pore size of the prepared foams obtained from normal size distribution.

Sample	Size (μm)
PU	188.5 ± 50.9
PF	62.9 ± 19.2
PU2.5fPU	117.4 ± 40.9
PU5.0fPU	155.6 ± 72.8
PU7.5fPU	101.4 ± 34.9
PU2.5cPU	153.7 ± 64.6
PU5.0cPU	116.7 ± 49.6
PU7.5cPU	134.9 ± 43.9
PU2.5fPF	145.1 ± 45.9
PU5.0fPF	135.6 ± 53.2
PU7.5fPF	123.4 ± 53.4
PU2.5cPF	182.4 ± 69.2
PU5.0cPF	144.3 ± 55.5
PU7.5cPF	143.2 ± 83.2

The rather narrow distribution of cell size observed in all the prepared foams indicates that they are characterized by a quite homogeneous cellular structure. Neat PU foam has pores of 188.5 μm, while neat PF is characterized by a mean cell size of 62.9 μm. The lower pore size of PF foam could explain its lower thermal conductivity with respect to the neat PU sample. The introduction of the recycled foams considerably reduces the mean pore dimension, with a drop up to 46% in the case of the PU7.5fPU sample. This could be related to the viscosity increase induced by the recyclate addition. However, there is not a clear trend related to the granulometry, the type and the concentration of the recycled foam added.

The values of theoretical density, geometrical density, apparent density, total and closed porosity are summarized in Table 9.4.

Table 9.4. Values of density and porosity of the prepared foams.

Sample	ρ_{th} (g/cm³)	ρ_{geom} (g/cm³)	ρ_{app} (g/cm³)	P_{tot} (%)	P_{closed} (%)
PU	1.174 ± 0.003	0.044 ± 0.003	0.086 ± 0.009	96.3 ± 2.0	47.4 ± 2.0
PF	-	0.035 ± 0.003	-	-	-
PU2.5fPU	0.686 ± 0.004	0.057 ± 0.006	0.167 ± 0.002	92.1 ± 4.5	25.8 ± 2.5
PU5.0fPU	0.485 ± 0.003	0.062 ± 0.015	0.220 ± 0.007	87.5 ± 4.1	15.4 ± 0.2
PU7.5fPU	0.375 ± 0.012	0.059 ± 0.001	0.208 ± 0.013	84.0 ± 3.2	12.6 ± 1.5
PU2.5cPU	0.686 ± 0.004	0.049 ± 0.001	0.154 ± 0.007	92.2 ± 2.5	24.9 ± 1.1
PU5.0cPU	0.485 ± 0.003	0.048 ± 0.004	0.162 ± 0.010	90.1 ± 3.6	19.7 ± 1.1
PU7.5cPU	0.375 ± 0.012	0.058 ± 0.009	0.114 ± 0.040	85.7 ± 1.4	35.4 ± 1.1
PU2.5fPF	0.646 ± 0.011	0.055 ± 0.010	0.571 ± 0.024	92.3 ± 1.1	1.2 ± 1.1
PU5.0fPF	0.446 ± 0.007	0.048 ± 0.003	0.359 ± 0.013	89.3 ± 2.1	2.6 ± 0.2
PU7.5fPF	0.341 ± 0.003	0.050 ± 0.002	0.316 ± 0.008	87.1 ± 2.6	1.1 ± 0.2
PU2.5cPF	0.646 ± 0.011	0.052 ± 0.007	0.337 ± 0.026	92.6 ± 3.4	7.4 ± 0.1
PU5.0cPF	0.446 ± 0.007	0.055 ± 0.001	0.246 ± 0.002	88.9 ± 3.0	10.1 ± 0.1
PU7.5cPF	0.341 ± 0.003	0.059 ± 0.013	0.305 ± 0.039	93.6 ± 2.4	2.1 ± 1.5

Neat PU foam exhibits a theoretical density of 1.174 g/cm³. The introduction of both PU and PF recyclates, regardless of their granulometry, results in a reduction of the theoretical density. This is attributed to the partial replacement of the liquid precursors with a foamed filler, which has lower density values. Regarding the geometrical density, neat PU foam has density of 0.044 g/cm³, and the addition of the recycled foam leads to a slight ρ_{geom} increase, without a clear dependency on the concentration, type and size of recyclate. A similar observation can be performed analyzing the apparent density values: the neat PU foam shows a ρ_{app} value of 0.086 g/cm³, which increases upon the recyclate introduction. However, the addition of PF involves a stronger increase in ρ_{app}, which can be due to a higher tendency of PF particles to form open pores. In fact, their high polarity can cause a partial agglomeration of the particles and renders more difficult the foaming process [256]. Consequently, also the total

porosity results to be slightly affected by the presence of the recycled foam particles. In particular, the addition of recycled foam, regardless of the type and size, lead to a reduction of total porosity, from 96.3% (neat PU) up to 84.0% (PU7.5fPU). Neat PU shows 47.4% of closed porosity, which is strongly reduced upon the recyclate addition due to the partial breakage of the cell walls. It is important to underline that a closed pores morphology is more suitable for thermal insulation application, while open porosity is desirable when elevated acoustic insulation properties are required [257]. The incorporation of recycled PU particles involves a reduction of closed porosity from 47.4% up to 12.6% (see PU7.5fPU sample), whereas the addition of PF particles results in a P_{closed} reduction up to 1.1% (see PU7.5fPF foam). In general, also for closed porosity, there is not a clear influence played by recycled PU and/or PF foam granulometry.

9.1.5.2 Thermal characterization

Figure 9.6 shows the thermal conductivity (λ) values of the prepared foams at 10 °C.

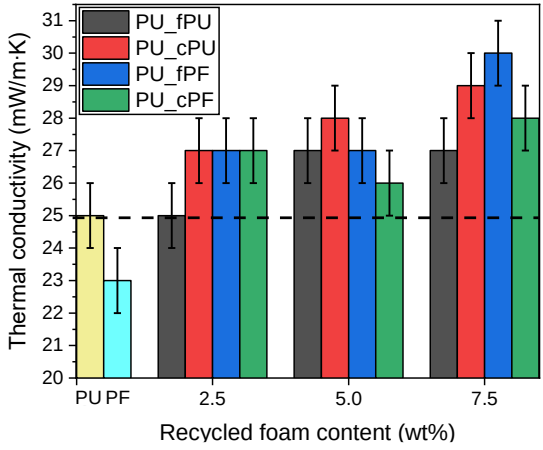

Figure 9.6 Thermal conductivity values at 10 °C of the prepared foams.

Neat PU has a λ value equal to 0.025 W/m·K, while neat PF is characterized by a λ value equal to 0.023 W/m·K, and these values are slightly higher than those reported in the datasheet of the producer. This is probably due to the non-optimal conditions of the foaming process, that was performed by using a lab-made device. At a general level, the introduction of PU and PF recyclates leads to a slight increase of the λ values of the foams. This fact is probably related to the lower values of closed porosity and also to the slight decrease of the total porosity induced by the recycled foam addition. Nevertheless, considering also the standard deviation values associated to these results, it can be clearly seen that this increase is very low, especially up to a recyclate amount of 5 wt%. The most remarkable λ enhancement can be observed in the case of PU7.5fPF foam, where an increase of 16% (0.030 W/m·K) compared to the neat PU foam can be registered. However, this value of thermal conductivity still remains within the λ range of the most common thermal insulating foams diffused on the market [258]. In particular, it is interesting to observe how the insulating capacity of the PU foams containing recycled PF particles is almost retained up to recyclate amount of 7.5 wt%, despite they experience a stronger reduction in the closed porosity. This suggests that the superior thermal insulation power of PF efficiently counteracts the P_{closed} reduction due to recycled PF addition. There is not a distinct trend associated with the recyclate content up to 5 wt%, and the most promising results come from the PU2.5fPU and PU5.0cPF foams, which practically show the same λ values of neat PU. In general, there is no clear influence of the particle size of both PU and PF recyclates on the thermal conductivity of the foams.

In Figure 9.7(a-d) and Figure 9.8(a-d) the TGA and DTG curves obtained from thermogravimetric analysis on the prepared foams are respectively reported, while in Table 9.5 the most important results, expressed in terms of onset degradation temperature (T_{onset}), temperature of maximum degradation (T_{max}) and residual mass at 700 °C (m_{700}) are summarized.

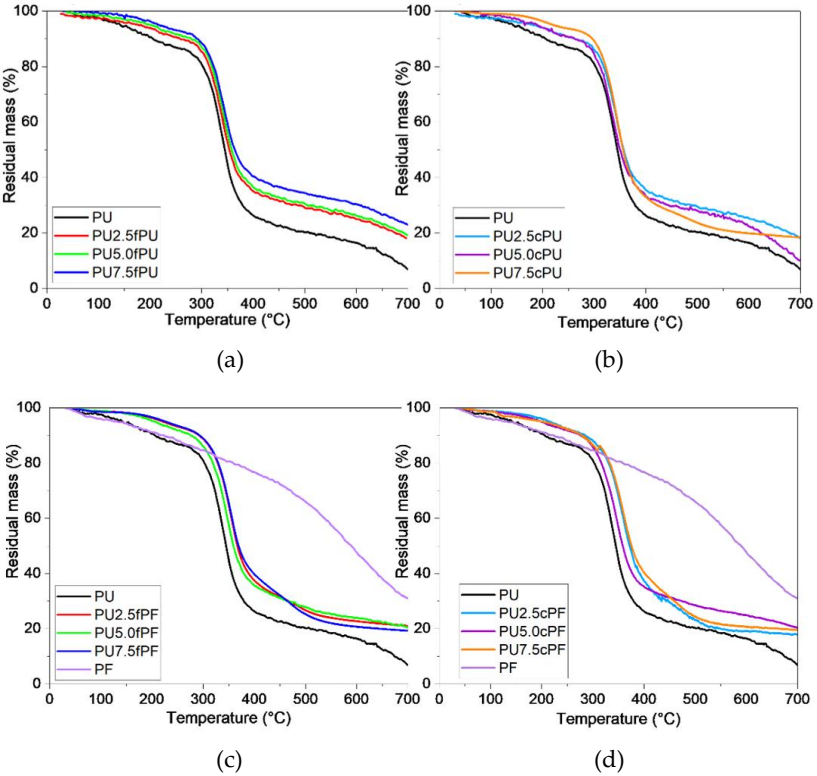

Figure 9.7 TGA curves of neat PU, neat PF and foams with different contents of (a) fPU, (b) cPU, (c) fPF and (d) cPF recycled particles.

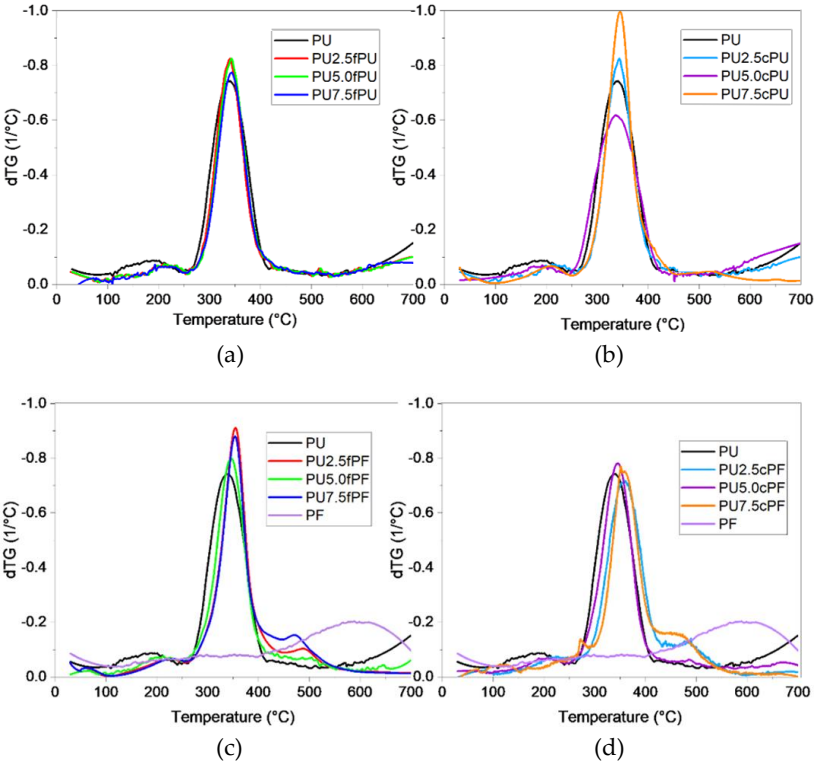

Figure 9.8 DTG curves of neat PU, neat PF and foams with different contents of (a) fPU, (b) cPU, (c) fPF and (d) cPF recycled particles.

Table 9.5. Results of TGA tests on the prepared foams.

Samples	T_{onset} (°C)	$T_{max(PU)}$ (°C)	$T_{max(PF)}$ (°C)	m_{700} (%)
PU	295	336	-	6.8
PF	470	596	578	31.1
PU2.5fPU	297	339	-	19.0
PU5.0fPU	300	342	-	20.0
PU7.5fPU	304	343	-	23.0
PU2.5cPU	311	355	-	8.9
PU5.0cPU	293	340	-	10.0
PU7.5cPU	294	346	-	18.4
PU2.5fPF	295	354	487	23.1
PU5.0fPF	293	352	481	22.7
PU7.5fPF	300	353	498	19.9
PU2.5cPF	308	357	474	18.8
PU5.0cPF	301	352	481	20.2
PU7.5cPF	321	354	478	19.6

The TGA thermogram of neat PU shows a residual mass of approximately 7% at the end of the tests, while the incorporation of recycled PU and PF results in a further m_{700} increase, without a clear correlation with the recyclate concentration. A similar amount of residual mass for PU foams is documented also in the literature [259]. The T_{onset} of neat PU is 295 °C, while that of PF is equal to 470 °C. The introduction of recycled PU increases the T_{onset} values up to 16 °C (see PU2.5cPU sample). However, variations in PU recyclate concentration and granulometry do not seem to significantly influence this increase. The introduction of PF further improves the T_{onset} values, reaching 321 °C in the case of PU7.5cPF foam. Neat PU exhibits a $T_{max(PU)}$ of 336 °C, that is connected to the thermal decomposition of urethane bonds [259], and this value is substantially enhanced by the incorporation of PU recyclate, by reaching 355 °C in the case of the PU2.5cPU foam. This can be explained by the fact that the PU recyclate and the liquid

precursors of the virgin PU foam come from different suppliers and, therefore, they could have a different chemical composition and/or flame retardant concentration (not specified by the supplier). On the other hand, the incorporation of PF has an even more positive impact on $T_{max(PU)}$ values, reaching 357 °C in the case of PU2.5cPF sample. This can be attributed to the fact that PF has a higher maximum degradation temperature ($T_{max(PF)}$) than PU, approximately at 597 °C, as also confirmed in literature [260]. In fact, the degradation of the PF constituent can be detected as a secondary peak in the DTG curves at approximately 480 °C. Also, for the maximum degradation temperatures there is no clear influence of the particle size of both recyclates. Therefore, from TGA tests it can be generally concluded that the introduction of both type of recyclates improves the thermal degradation stability of the resulting foams.

9.1.5.3 Mechanical characterization

In Figure 9.9(a,b) representative stress-strain curves related to the flexural tests on the prepared foams are reported. In particular, Figure 9.9a shows the flexural behaviour of samples produced by using fPU and fPF recyclates, while in Figure 9.9b the flexural properties of samples obtained introducing cPU and cPF recycled foams are shown.

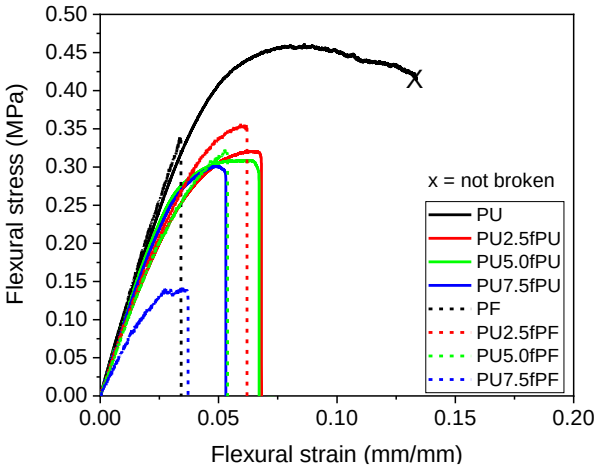

(a)

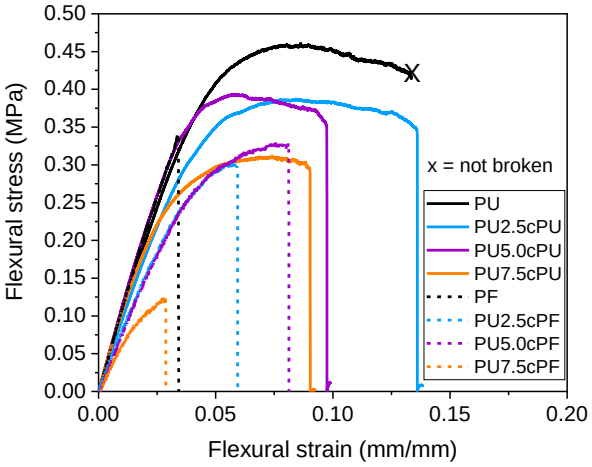

(b)

Figure 9.9 Representative stress-strain curves from flexural tests on the prepared foams. Neat PU, neat PF and foams prepared with different amounts of (a) fPU and fPF, (b) cPU and cPF recyclates.

In Table 9.6 the values of specific flexural strength, flexural modulus and flexural strain at break of samples are summarized, together with the deformation at break.

Table 9.6. Flexural properties of the prepared foams.

Samples	E_f/ρ (MPa/(g/cm³))	σ_f/ρ (MPa/(g/cm³))	ϵ_f (mm/mm)
PU	216.4 ± 22.7	9.5 ± 1.6	-
PF	267.1 ± 97.3	10.0 ± 3.1	0.03 ± 0.01
PU2.5fPU	148.9 ± 24.1	5.8 ± 0.8	0.07 ± 0.01
PU5.0fPU	154.5 ± 44.2	4.7 ± 1.5	0.07 ± 0.02
PU7.5fPU	162.0 ± 9.2	5.1 ± 0.6	0.05 ± 0.01
PU2.5cPU	192.0 ± 10.9	8.2 ± 1.8	0.15 ± 0.04
PU5.0cPU	189.8 ± 20.6	7.9 ± 0.9	0.11 ± 0.03
PU7.5cPU	159.1 ± 37.5	6.0 ± 2.1	0.10 ± 0.04
PU2.5fPF	150.4 ± 31.9	6.4 ± 1.9	0.07 ± 0.03
PU5.0fPF	182.3 ± 30.4	6.7 ± 0.8	0.05 ± 0.02
PU7.5fPF	157.2 ± 32.3	3.0 ± 0.3	0.04 ± 0.02
PU2.5cPF	158.8 ± 28.3	6.0 ± 1.2	0.07 ± 0.02
PU5.0cPF	169.3 ± 18.4	7.8 ± 1.4	0.09 ± 0.04
PU7.5cPF	137.6 ± 60.5	3.1 ± 1.7	0.06 ± 0.01

Neat PU foam behaves as a ductile material under flexural conditions, and it does not break in the strain interval considered. On the other hand, PF foam shows a brittle behaviour, with a catastrophic failure at limited strain levels. Neat PU shows a specific flexural modulus of 216.4 MPa/(g/cm³) and a specific flexural strength of 9.5 MPa/(g/cm³), while neat PF has an E_f/ρ value of 267.1 MPa/(g/cm³) and a σ_f/ρ of 10.0 MPa/(g/cm³). The introduction of increasing amounts of fPU leads to a reduction in modulus and in strength (up to 28.7% and 50.5% for the PU5.0fPU sample, respectively), and to a general embrittlement, with

a strong reduction of ϵ_f values. On the other hand, the addition of fPF has a stronger effect on flexural modulus and strength, with an even more evident degradation of both the properties. In fact, the flexural modulus of the PU7.5fPF foam is 157.2 MPa/(g/cm^3) (-27.4% than PU) and the flexural strength is 3.0 MPa/(g/cm^3) (-68.4% than PU). Regarding the samples containing recyclates with coarse granulometry, it can be noticed that the addition of 7.5 wt% of cPU and 7.5 wt% cPF leads to the reduction of the flexural modulus of 26.5% and 36.4%, respectively, and to a flexural strength drop of 36.8% and 67.4%, respectively. The observed decline in flexural properties may be attributed to several factors. Firstly, poor adhesion between the polyurethane matrix and the recyclates may lead to weak interfacial bonding, compromising the overall structural integrity of the foam. Additionally, a non-uniform distribution of the recyclates within the PU foam could result in localized areas of weakness, contributing to decreased flexural performance. Moreover, the presence of open porosity within the material increases its susceptibility to moisture absorption, which can further weaken the foam structure and negatively impact its flexural properties. This combination of factors underscores the importance of optimizing both material composition and processing parameters to enhance the mechanical performance of foams containing recycled materials.

In Figure 9.10(a,b) representative stress-strain curves related to the compression tests on the prepared foams are reported. In particular, Figure 9.10a shows the compressive behaviour of samples produced by using fPU and fPF recyclates, while in Figure 9.10b the compression properties of the foams obtained introducing cPU and cPF recycled foams are shown.

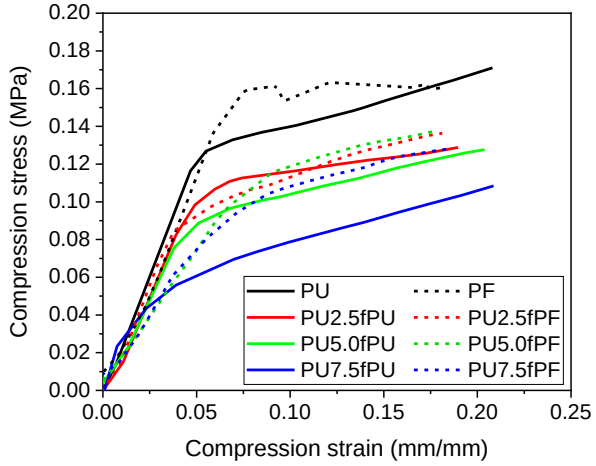

(a)

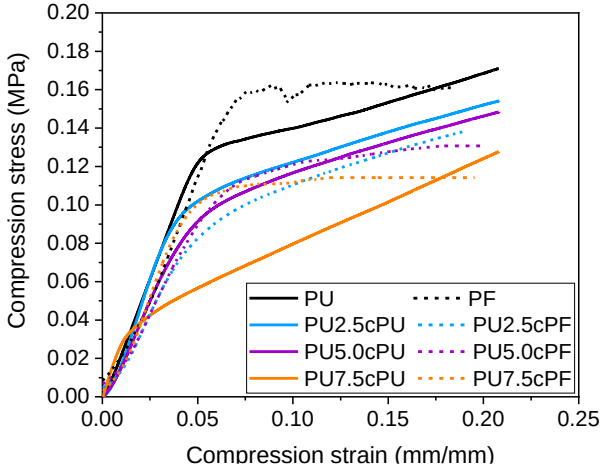

(b)

Figure 9.10 Representative stress-strain curves from compression tests on the prepared foams. Neat PU, neat PF and foams prepared with different amounts of (a) fPU and fPF, (b) cPU and cPF recyclates.

In Table 9.7 the results of compression tests, expressed in terms of specific compressive modulus and strength, are numerically summarized.

Table 9.7. Results of quasi-static compressive tests on the prepared foams.

Samples	E_c/ρ (MPa/(g/cm^3))	σ_c/ρ (MPa/(g/cm^3))
PU	75.9 ± 20.6	3.2 ± 0.7
PF	81.4 ± 20.1	4.3 ± 0.5
PU2.5fPU	59.6 ± 12.9	1.9 ± 0.9
PU5.0fPU	37.6 ± 18.2	1.5 ± 0.7
PU7.5fPU	55.3 ± 13.3	1.2 ± 0.5
PU2.5cPU	71.6 ± 6.2	2.7 ± 0.5
PU5.0cPU	54.6 ± 12.5	2.5 ± 0.6
PU7.5cPU	48.3 ± 23.2	1.0 ± 0.5
PU2.5fPF	51.8 ± 12.7	2.7 ± 0.9
PU5.0fPF	61.0 ± 5.5	2.7 ± 0.4
PU7.5fPF	57.4 ± 8.3	2.8 ± 0.7
PU2.5cPF	53.7 ± 9.7	2.1 ± 0.5
PU5.0cPF	36.4 ± 3.4	2.5 ± 0.6
PU7.5cPF	45.9 ± 15.7	2.9 ± 0.9

The introduction of increasing amounts of PU particles in fine granulometry leads to a slight reduction in the compressive modulus and a stronger reduction in compressive strength. In particular, neat PU shows compressive modulus of 75.9 MPa/(g/cm^3) and a compressive strength of 3.2 MPa/(g/cm^3), while PU7.5fPU sample has a compressive modulus of 55.3 MPa/(g/cm^3) (-27.1% than PU) and compressive strength of 1.2 MPa/(g/cm^3) (-62.5% than PU). On the other hand, the addition of fPF has a milder effect on the compressive strength and a stronger influence on the compressive modulus. In fact,

by introducing 7.5wt% of fPF, the compressive strength results 2.8 MPa/(g/cm^3), but the modulus is reduced of about 24.4%. The use of a recyclate with a coarser granulometry seems to have a stronger effect in the compressive properties than those exhibited in flexural mode. In fact, the introduction of 7.5 wt% of cPU and cPF leads to a reduction of the compressive modulus of 36.4% and 39.5%, respectively, and to a drop of the compressive strength of 68.7% and 9.3%, respectively. Even in this case the observed decline in compressive properties can be attributed to the poor adhesion between the polyurethane matrix and recycled materials, to the uneven recyclate distribution and to the higher fraction of open porosity. In a future work a compatibilizing agent will be used to improve the interfacial interaction between the PU matrix and the recycled foams.

At the end of the morphological and thermo-mechanical characterization, the PU, PF, PU5.0cPU, PU5.0fPF, PU5.0cPF, PU7.5cPF were detected as the most promising ones, and their flame behaviour was characterized through cone calorimetry tests

9.1.5.4 Forced combustion tests

The aim of cone calorimetry measurements was to evaluate whether the inclusion of recycled PU and PF particles had a negative impact on the foam burning behaviour. The tests have been performed under an irradiative heat flux of 35 kW/m^2, which is normally related to the early stages of a developing fire [261]. When exposed to the selected heat flux, the sample releases combustible volatiles that, upon reaching the flammability limits, lead to the flaming combustion of the specimen. The instrument then evaluates the heat release rate (HRR) and the smoke production rate (SPR) as a function of time. Figure 9.11(a-f) reports the collected plots and integral values (THR and TSR for heat and fumes, respectively) as well as histograms related to the peak of heat release rate and final residue. Table 9.8 collects all the measured parameters.

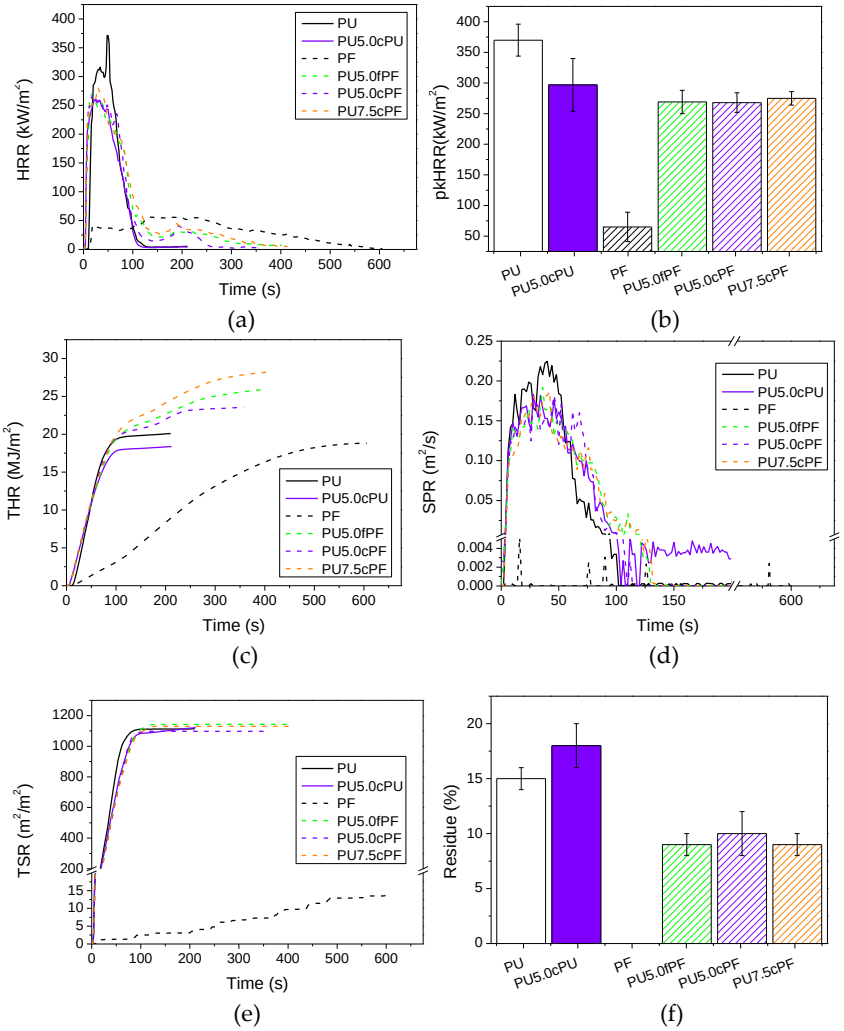

Figure 9.11 Cone calorimetry tests on neat PU, neat PF and foams with optimized composition. (a) Heat release rate (HRR), (b) peak heat release rate (pkHRR), (c) total heat release (THR), (d) smoke production rate (SPR), (e) total smoke release (TSR), (f) residue at the end of cone calorimetry test.

Table 9.8 Results of cone calorimetry tests of neat PU, neat PF and the foams with optimized composition.

Sample	TTI (s)	HRR (kW/m²)	pkHRR (kW/m²)	THR (MJ/m²)	TSR (m²/m²)	Residue (%)
PU	4 ± 1	96 ± 8	370 ± 26	20.0 ± 0.1	1160 ± 100	15 ± 1
PF	10 ± 2	29 ± 3	52 ± 6	19.1 ± 0.3	9 ± 4	<1
PU5.0cPU	2 ± 1	91 ± 8	297 ± 43	19.3 ± 2.1	1164 ± 55	18 ± 2
PU5.0fPF	3 ± 1	70 ± 9	269 ± 19	25.8 ± 2.0	1141± 130	9 ±1
PU5.0cPF	3 ± 1	68 ± 8	268 ± 16	25.0 ± 3.6	1163 ± 143	10 ± 2
PU7.5cPF	3 ± 1	71 ± 3	275 ± 11	26.4 ± 2.0	1121 ± 17	9 ± 1

Figure 9.12 and Figure 9.13 show pictures and SEM micrographs of residues of the same foams after cone calorimetry tests, respectively.

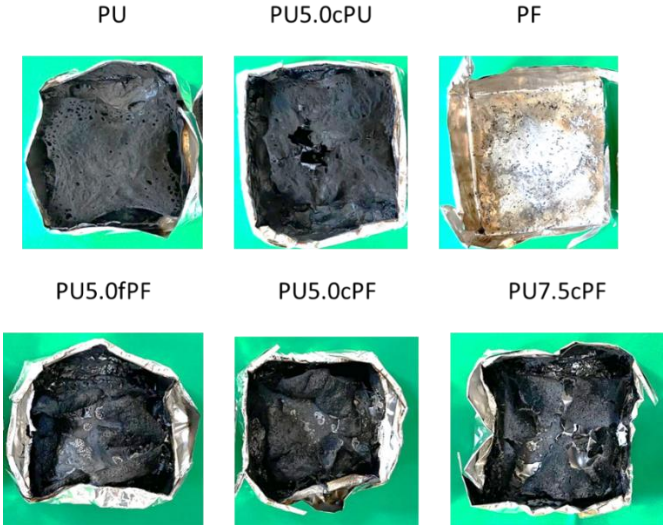

Figure 9.12 Pictures of residues of the prepared foams after cone calorimetry tests.

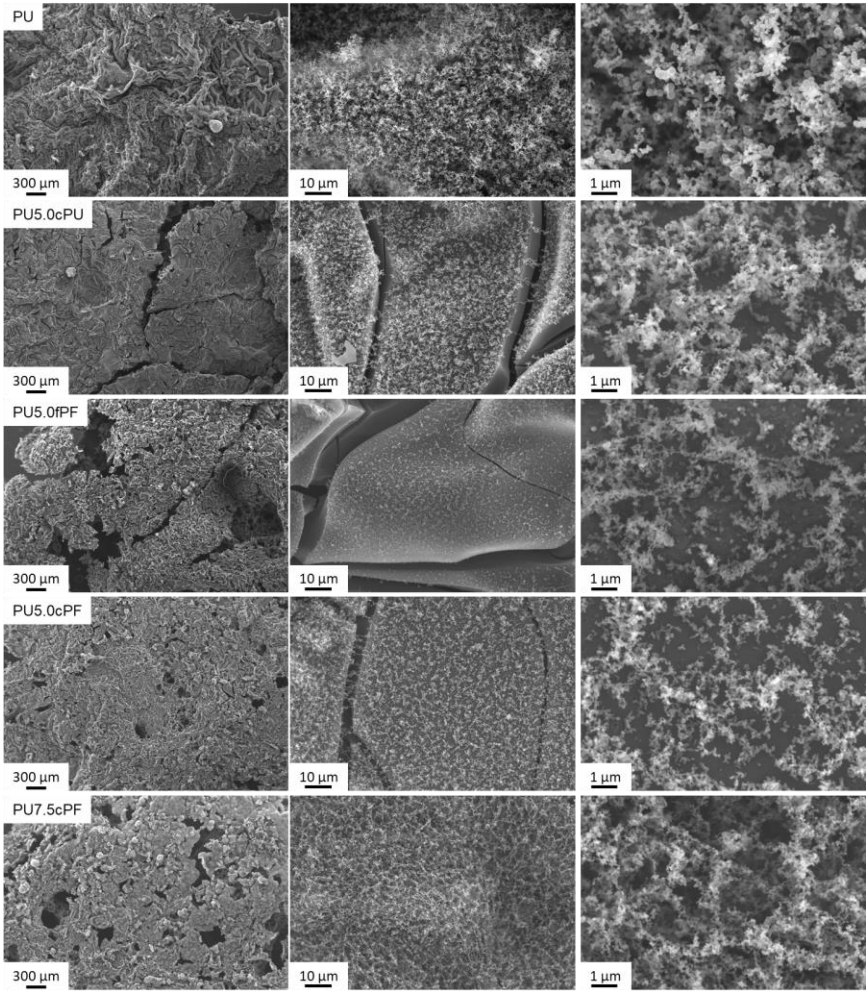

Figure 9.13 SEM micrographs of residues of the prepared foams after cone calorimetry tests.

Upon exposure to the cone heat flux, the PU quickly ignites and burns with vigorous flames. The HRR plots steeply increases reaching a pkHRR at 370 ± 26 kW/m^2. During combustion, the foam structure is gradually consumed leaving a thin and dense charred residue, which accounts for 15% of the original weight. By contrast, the neat PF shows extensive char formation that results in limited HRR values (pkHRR equal to 52 ± 6 kW/m^2) as well as reduced amount of smoke released. After the flame extinguishes, the charred residue is completely consumed by smoldering combustion (i.e., flameless combustion characterized by low HRR values). This behaviour is a well-known characteristic of PF and extends the overall testing time [262,263].

As far as the samples containing recycled particles are concerned, the inclusion of cPU particles does not modify the burning behaviour of the neat PU but produces a reduction in pkHRR (-20%) and a slight increase in the final residue (+20%). The other parameters remain mostly unchanged and within the experimental error. Similarly, during flaming combustion, the good char forming ability and low HRR of PF particles produces a substantial reduction in the pkHRR (up to -28% for the PU5.0cPF foam). As the flame extinguishes, as already observed for the neat PF, the characteristic smoldering behaviour of this latter is also displayed by the recycled foams. This is apparent from the low and prolonged HRR signal collected for samples PU5.0cPF, PU5.0fPF and PU7.5cPF after flame out. The smoldering duration seems to be directly related to the PF concentration. Interestingly, despite a different PF concentration, PU5.0fPF and PU7.5cPF show a similar behaviour thus suggesting an effect of the granulometry where the higher surface exposed of the fine particles likely compensates for their reduced amount in the recycled foam with respect to the coarse ones. The occurrence of a smoldering combustion produces an increase in the THR and a subsequent reduction of the final residue. Smoke parameters remain unchanged with respect to the neat PU. The post combustion residues have been investigated by SEM (Figure 9.13). The performed micrographs point out no substantial differences between the neat PU

and the PU5.0cPU foams, highlighting the formation of a dense and compact char layer for both samples. Conversely, PF containing samples yield partially damaged structures characterized by holes that are likely ascribed to the observed smoldering behaviour.

At a general level, it can be concluded that the inclusion of mechanically recycled foam particles in expanded PU panels results in a positive effect by reducing the pkHRR, that is often considered as one of the main fire safety parameters [264]. This can be ascribed to an improved char forming ability linked to the presence of PU and PF particles (as also observed by TGA, see Figure 9.7). Indeed, during combustion, the neat PU gradually collapses to a thin and dense charred structure that controls and partially limits the release of volatiles feeding the flame. The efficiency of such barrier is improved, to different extent, by the inclusion of PU and PF particles. Indeed, the PU5.0cPU sample yielded a rather compact and dense char layer that eventually achieved the highest wt% residue. Conversely, the superior char forming ability of PF particles only improved the char layer during flaming combustion as after flame out the residual char from PF was consumed by smoldering. This behaviour produced small holes and defects within the residue (Figure 9.13) and led to an overall reduction of the final wt% residue.

9.1.5.5 General comparison of properties

A general comparison between the most important physical properties of the investigated foams is shown in Figure 9.14 as radar plot. This comparative analysis has been performed in terms of thermal conductivity (λ), specific flexural modulus (E_f/ρ) and strength (σ_f/ρ), specific compression modulus (E_c/ρ) and strength (σ_c/ρ), and peak heat release rate (pkHRR).

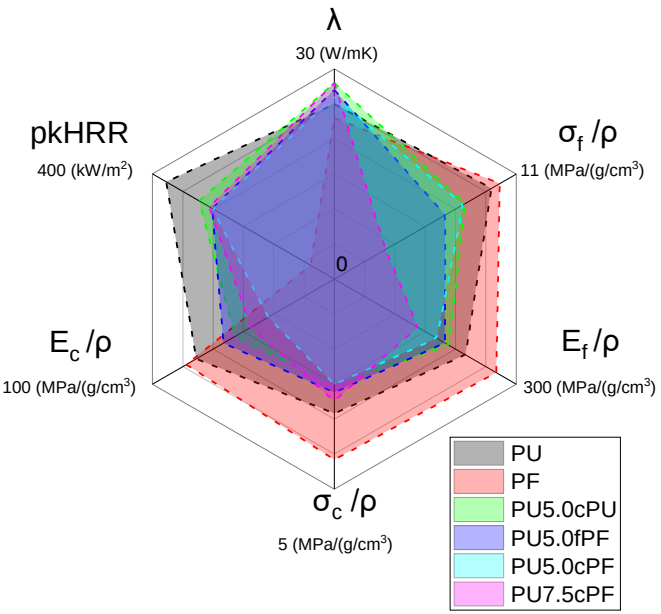

Figure 9.14 Radar plot of the investigated physical properties: thermal conductivity (λ), specific flexural modulus (E_f/ρ) and strength (σ_f/ρ), specific compression modulus (E_c/ρ) and strength (σ_c/ρ), and peak heat release rate (pkHRR).

From the radar plots it is evident the difference in properties between the samples that incorporate PU or PF recyclates compared to neat PU foam. PU foam shows a balanced distribution of properties from both mechanical and thermal point of view. However, its reaction to fire, expressed by the peak heat release rate (pkHRR), is significantly high, reaching a value of 370 ± 26 kW/m^2. This implies a higher heat release during combustion and faster burning, increasing the risk of fire spread. On the other hand, neat PF foam exhibits slightly superior mechanical properties, although the material is inherently more brittle compared to PU. Additionally, PF foam shows lower thermal conductivity than PU, making it more effective as a thermal insulator. The main advantage of PF foam is the significant decrease in pkHRR, which is around 52 ± 6 kW/m^2, compared to neat PU foam. This value

is particularly important in terms of fire safety, as it indicates lower heat release and slower burning, thus reducing the risk of fire spread and providing more time for evacuation. However, it should be noted that the introduction of recycled foams compromises, albeit not drastically, the flexural and compressive properties. In particular, the foams with the highest PU and PF recyclate content show the greatest reduction in mechanical properties, especially under flexural conditions. On the other hand, the thermal conductivity is not substantially compromised by the addition of recycled foams. In the case of recycled PF particles, their higher thermal insulating performance counterbalances the negative effects played on the foam morphology. Among the samples tested, the most promising results emerge for the PU5.0fPF foam, as it highlights a suitable combination of mechanical strength, thermal insulating performance and fire behaviour.

9.1.6 Conclusions

In this work discarded PU and PF panels were ground into two different particle sizes and incorporated at various amounts into expanded PU, in order to limit the consumption of virgin material and promote a novel circular economy approach for thermal insulating materials. SEM microscopy revealed a coherent cell structure in the new formulations, due to efficient wetting by the liquid PU precursors that allowed for an efficient foaming process. The incorporation of PU/PF recyclates led to a slight increase in foam density, resulting in a reduction of closed porosity and, thus, an enhancement in thermal conductivity, up to 16% compared to pure PU, without drastically compromising the thermal insulating power of these foams. Although the addition of PF/PU recyclate marginally improved the thermal stability, it adversely affected the flexural and compression properties of the foams, possibly because of the rather poor adhesion between virgin PU matrix and the recyclates and the higher degree open porosity. Nonetheless, according to cone calorimetry tests, the inclusion of recycled foams notably reduced the peak heat release rate by 28% compared to neat PU, improving fire safety.

9.2 Multifunctional sandwich composites with optimized phase change material content for simultaneous structural and thermal performance

Published paper:

Fredi, G; Boso, E; Sorze, A; Pegoretti, A. Multifunctional sandwich composites with optimized phase change material content for simultaneous structural and thermal performance. *Composites Part A*, **2024**, 186, 108382.

9.2.1 Introduction

Sandwich composite structures, consisting of two thin but stiff face sheets separated by a lightweight core material, have gained significant attention due to their exceptional specific stiffness and strength, especially to flexural load [265]. These properties make sandwich composites attractive for various applications, including aerospace, automotive, marine, and construction industries, where weight reduction is crucial [266]. One of the main advantages associated with sandwich structures is the availability of a diverse range of core designs and materials. Every core has its unique properties in terms of specific strength and stiffness, weight, energy absorption capability, and, ultimately, cost on the market.

Besides the mechanical performance, enhancing the thermal management capabilities of sandwich composite structures has emerged as an area of significant interest, driven by the growing demand for energy-efficient systems and temperature regulation in diverse applications. This can be reached by decreasing the thermal diffusivity of the foam core, but also with the introduction of a Phase Change Material (PCM) [267,268]. PCMs are substances capable of storing and releasing substantial amounts of latent heat during phase transitions, typically between solid and liquid states, within a narrow temperature range [269,270].

The integration of PCMs into polymer foam cores, particularly PU foams, has been extensively investigated in recent years [271,272]. Numerous studies have focused on encapsulating PCMs within PU foams, producing materials with enhanced thermal energy storage (TES) and thermal buffering properties [273-278]. The introduction of PCMs into PU foams has been shown to modify the microstructure, with the PCM microcapsules influencing the cell morphology, size distribution, and overall porosity of the foam [279,280], which in turn affects their mechanical properties. Although the introduction of PCM in PU foams has been largely investigated, the use of PCM-enhanced PU foams to produce structural sandwich panels has been surprisingly limited.

In view of this, the incorporation of PCMs into structural composites presents an appealing multifunctional concept that simultaneously addresses load-bearing and thermal energy storage requirements [281,282]. The obtained results suggested that integrating PCMs within the core of sandwich composite structures may confer a synergistic advantage by combining the latent heat storage capability of PCMs with the exceptional specific strength and stiffness inherent to sandwich designs. This approach facilitates the development of lightweight, energy-efficient composites capable of meeting the stringent demands for thermal management and mechanical robustness in various applications, such as the automotive, aerospace, and refrigerated transportation fields [283-286]. By strategically utilizing PCM-enhanced cores in sandwich composites, the necessity for separate structural and thermal management units can be circumvented, thereby enabling significant mass and volume savings at the system level [282].

Hence, to exploit the known advantages of PCM-enhanced PU foams and fill the mechanical property gap that prevents their extensive use in structural applications, this work proposes, for the first time, the development and comprehensive characterization of a novel sandwich composite system combining the advantages of PU/PCM foams as the core material and high-performance epoxy/carbon fiber

laminates as the structural skins. By optimizing the PCM content within the PU foam core, this multifunctional composite aims to strike an optimal balance between mechanical properties, crucial for structural applications, and thermal management capabilities facilitated by the latent heat storage of the PCM. The research methodology employed in this study involves three subsequent steps. First, PU foams containing various fractions of microencapsulated PCMs were produced and characterized with a PCM content of up to 30 wt%, to identify the optimal composition. Then, sandwich panels were fabricated by using the selected PU/PCM foam as the core material and epoxy/carbon fiber laminates as the skins, and then characterized by microstructural, thermal, and mechanical point of view.

9.2.2 Materials

Polyol HDR R 150 (viscosity at 23 °C = 1050 mPa·s, density at 23 °C = 1.1 g/cm^3) and isocyanate ISN 1 (viscosity at 23 °C = 200 mPa·s, density at 23 °C = 1.23 g/cm^3) were both provided by Kairos Srl (Verona, Italy). As suggested by the producer's datasheet, PU foams for the sandwich cores were produced by mixing polyol and isocynate in a ratio of 100:130. MPCM 32D® microencapsulated phase change material was supplied by Microtek Laboratories Inc. (OH, USA) in the form of a dry powder with a mean particle size of 15-30 μm, a density of 0.9 g/cm^3, a nominal melting point of 32 ± 2 °C, and a latent heat of fusion of 160 J/g. The core constitutes the 85% of the capsule volume and the shell is made of melamine formaldehyde.

For the epoxy/carbon sandwich skins preparation, an epoxy base Elan-tech® EC 152 (viscosity at 25 °C = 1200-1800 mPa·s) and the hardener Elan-tech® W 152 MR (viscosity at 25 °C = 30-60 mPa·s) were kindly provided by Elantas Europe Srl (Parma, Italy) and mixed at a ratio 100:30. Balanced plain weave carbon fabric Angeloni GG 200 P (mass per unit area = 192 g/cm^3) were supplied by G. Angeloni Srl (Venezia, Italy).

9.2.3 Sample preparation

9.2.3.1 Preparation of foams

First, the required amounts of polyol and isocyanate were weighed and poured into separate beakers. For the PCM-containing compositions, the necessary PCM mass was weighed and split equally into the two beakers. Primary mixing by hand was then performed in each beaker using a spatula. Then, the content of the two beakers was combined, mechanically mixed for approx. 25-30 s, and then poured into a mold with an inner cavity of 250 × 250 × 20 mm^3, preheated at 40 °C. The mold was lined internally with PTFE sheets and polyethylene film to facilitate sample extraction. The mold was rapidly covered and cured in an oven at 40 °C for 20 min. Appropriate clamping was applied to counteract the pressure developed during cross-linking and foaming. After the first 15 min, the cover was removed and the mold left open to complete curing. The preparation was repeated for both neat and PCM-containing PU foams, and at least two specimens were prepared for each composition. The prepared foams with the nominal weight compositions are listed in Table 9.9.

9.2.3.2 Preparation of sandwich panels

After the characterization of the foams, the sample PU-PCM20 presented an optimal balance between thermal and mechanical properties. Hence, composite sandwich panels were prepared with either neat PU or PU-PCM20 core materials (Table 9.9). After production, the foams were milled on both surfaces to remove the thin, denser layer on the outer surface and to reach the desired size of 200 × 200 × 15 mm^3. Then, sandwich panels were prepared by hand layup and vacuum bagging. Three carbon fiber (CF) laminae were impregnated with the epoxy/hardener mixture and placed on the top of a flat steel plate. Then, the foam panel was placed onto them, and finally, three more CF laminae were added on top, each one of them

impregnated with the epoxy/hardener mixture. During stacking, both surfaces of the foam were wet with additional epoxy/hardener mixture, to ensure a proper interfacial adhesion. The vacuum bag was then sealed, and the composite was left curing under vacuum for 24 h at room temperature. Each sandwich panel was then demolded and post-cured at 60 °C for 15 h, as recommended by the epoxy resin producer's datasheet. Two specimens were produced with the neat PU foam as a core and two additional specimens with the PU-PCM20 foam as a core.

Table 9.9. List of the prepared samples with nominal composition.

Foam samples	**Polyol + isocyanate (wt%)**	**PCM (wt%)**
PU	100	0
PU-PCM10	90	10
PU-PCM20	80	20
PU-PCM30	70	30
Sandwich panels	Core	Skin
S-PU	PU	Epoxy/carbon laminate
S-PU-PCM20	PU-PCM20	Epoxy/carbon laminate

9.2.4 Experimental techniques

9.2.4.1 Characterization of the foams

Microstructural characterization

Scanning electron microscopy (SEM) was performed to characterize the microstructure of the prepared foam samples. The specimens were cryofractured, coated with Pt-Pd, and observed with a Zeiss Supra 40 (Carl Zeiss AG, Oberkochen, Germany) field emission scanning

electron microscope (FE-SEM) operating at an accelerating voltage of 3.5 kV. The SEM micrographs were analyzed to measure the cell size distribution via the software ImageJ.

The density of the prepared foams was measured to calculate the total, open, and closed porosity as a function of the PCM concentration. This evaluation was carried out as already described in Section 9.1.4.1 and the total, open and closed porosity were calculated according to Equations (9.3),(9.4) and (9.5).

Thermal characterization

Differential scanning calorimetry (DSC) was performed via a Mettler DSC 30 (Mettler Toledo Inc., Columbus, Ohio, USA). Specimens of approx. 10 mg were sealed in aluminum crucibles and subjected to a heating/cooling/heating cycle between -50 °C to 100 °C at ±10 °C/min, under a constant nitrogen flow of 100 ml/min. The tests allowed measuring the melting and crystallization temperatures (T_m and T_c) and enthalpies (ΔH_m and ΔH_c) of the PCM contained in the foams. From the enthalpy values, the relative enthalpy (ΔH_r) was calculated for each sample and each of the three DSC scans through Equation (9.6):

$$\Delta H_r = \frac{\Delta H_{exp}}{\Delta H_{PCM} \cdot W_{PCM}} \tag{9.6}$$

where ΔH_{exp} and ΔH_{PCM} are the melting or crystallization enthalpies experimentally measured on foam samples and on neat PCM, respectively, and W_{PCM} is the nominal PCM concentration in each sample. Hence, $\Delta H_{PCM} \cdot W_{PCM}$ is a measurement of the theoretical enthalpy each sample would have developed if no PCM were lost or damaged in the process.

Thermal conductivity tests were performed on specimens of 200 × 200 × 20 mm^3 with a heat flow meter HFM 446 Lambda (Netzsch Gmbh, Selb, Germany), at mean temperatures of 10 °C (i.e., with solid PCM), 30 °C, and 50 °C (i.e., with molten PCM), with a temperature difference between the specimen sides of 20 °C.

The thermal behaviour of the foams was also analyzed with the FLIR E6 IR thermal imaging camera (Teledyne FLIR llc, NH, USA), to evaluate the thermal management capability of the foams on a sample bigger than that evaluated with DSC. The test was performed in two configurations, i.e., under heating and cooling conditions. For the experiment under heating conditions, the specimens were conditioned at -18 °C for at least 12 hours and then placed in an oven at 50 °C and left heating while the surface temperature was recorded with the thermal camera. For the experiment under cooling conditions, the specimens were conditioned at 70 °C for at least 12 h and then placed at 10 °C and left cooling while the surface temperature was recorded with the thermal camera. The goal of such a procedure was to evaluate how the PCM influenced the heating and cooling speeds. The test was performed on one specimen per composition, with dimensions 200 × 200 × 20 mm^3. The emissivity of the material was set to 0.96.

Mechanical characterization

Mechanical testing was performed with an Instron 5969 universal testing machine (Instron, Norwood, MA, USA), equipped with a 1 kN load cell and a thermal chamber allowing measurements at different temperatures. Three-point flexural and uniaxial compression tests were performed for each sample composition at 20 °C and 40 °C, i.e., below and above the melting temperature of the PCM.

Three-point flexural tests were performed according to the standard ISO 1209, on specimens with nominal dimensions of 200 × 20 × 10 mm^3, with a span length of 120 mm and a crosshead speed of 20 mm/min. Five specimens were tested for each composition at each testing temperature. The test allowed the measurement of the flexural modulus (E_f), flexural strength (R_f) and strain at maximum load (ε_{Rf}).

Compression tests were performed following the standard ASTM D1621-16 on specimens with nominal dimensions of 50 × 50 × 20 mm^3, with a crosshead speed of 2 mm/min (i.e., 10% of the specimen height,

according to the standard). Five specimens were tested for each composition at each testing temperature. The test allowed the measurement of the compressive modulus (E_c) and compressive strength (R_c). More specifically, R_c was calculated as the yield stress, if yielding occurred at strains of less than 10%, or as the stress at 10% strain, in the other cases.

Statistical analyses were performed using R Studio version 2023.12.1 (RStudio, Inc., Boston, MA, USA). To assess the effects of the experimental factors (composition and testing temperature) and their potential interaction, a two-way analysis of variance (ANOVA) was conducted. In cases where the ANOVA revealed statistically significant differences, Tukey's honest significant difference (HSD) post-hoc test was employed to identify specific group comparisons that were significantly different from one another. All statistical tests were evaluated at a significance level of 0.05.

9.2.4.2 Characterization of sandwich panels

Microstructural characterization

Light microscopy was performed to qualitatively assess the core-skin interfacial adhesion. Samples were embedded in epoxy resin, polished with polishing papers, and observed with a Zeiss AXIO Imager.A1m optical microscope (Carl Zeiss AG, Oberkochen, Germany) at different magnification levels. Both the top and bottom skins were observed in this way.

Thermal characterization

DSC tests were performed on the skins of the sandwich panels to measure the glass transition temperature of the cured epoxy resin, so to evaluate the applied curing cycle. DSC scans were performed with the same equipment and testing parameters described above for the foam characterization. The test was performed on specimens from all the prepared panels, taken from the top and the bottom skins.

Thermal conductivity tests were carried out using the HFM machine described for the foam samples, equipped with a specific instrumental kit for testing rigid materials. As for the foams, three tests were performed for each specimen by changing the temperature applied on the top and bottom sides, to reach average temperatures of 10 °C, 30 °C, and 50 °C, with a temperature difference between the specimen sides of 20 °C. The analysis not only helped quantify the effect of conductive epoxy/carbon skins but also that of the possible penetration of epoxy in the open foam porosity on the overall insulation performance.

Mechanical characterization

The mechanical characterization, carried out at 20 °C with the same testing machine described for the foams, involved three-point flexural, edgewise compression, and flatwise tensile tests. The used load cell was a 10 kN cell for the first two tests and a 1 kN cell for the third.

Three-point flexural tests were conducted according to the ASTM C393/C393M-20 standard, on six specimens per sample with nominal dimensions of 200 × 30 × 15 mm^3, with a span length of 150 mm and a crosshead speed of 3 mm/min. From the recorded load-displacement curves, the core shear ultimate strength (σ_s^{ult}) was calculated as in Equation (9.7):

$$\sigma_s^{ult} = \frac{P_{max}}{(d + c) \cdot b} \tag{9.7}$$

where P_{max} is the maximum load observed before failure, d is the sandwich thickness, c is the core thickness, and b is the specimen width. Moreover, the bending stress observed in the facings at the maximum applied load, denoted as facing stress (σ_{fac}), was also determined as reported in Equation (9.8):

$$\sigma_{fac} = \frac{S \cdot P_{max}}{2t \cdot (d + c) \cdot b} \tag{9.8}$$

where S is the span length and t is the facing thickness, calculated as $(d - c)/2$.

Edgewise compression tests were performed according to the ASTM C364/C364M-16 standard on six rectangular specimens per sample with nominal dimensions of 60 × 50 × 15 mm^3. The specimens were oriented so that the uniaxial compressive load was applied parallel to the laminate plane on a cross-sectional area of 50 × 15 mm^2. The crosshead speed was fixed at 0.75 mm/min. From the load-displacement curves, the ultimate edgewise compressive strength (σ_{ec}^{ult}) was determined according to Equation (9.9):

$$\sigma_{ec}^{ult} = \frac{P_{max}}{2t_{fs} \cdot w} \tag{9.9}$$

where P_{max} is the maximum load before failure, t_{fs} is the face sheet thickness, calculated as half of the difference between the sandwich thickness and the core thickness, and w is the specimen width. Moreover, the analysis focused on determining the residual mechanical strength of the sandwich structure loaded by edgewise compression after the first failure. For this purpose, two out of six specimens for both foam compositions were tested by applying the compressive load until the first damage occurred, unloading the specimen immediately after the failure to recover the deformation, and applying the compressive load again, to evaluate the residual mechanical strength.

Finally, flatwise tensile tests were carried out according to the ASTM C297/C297M-16 standard on six specimens per sample with nominal dimensions of 25 × 25 × 15 mm^3. The uniaxial tensile load was applied in the direction orthogonal to the laminate skins, trying to separate the core from the face sheets. This aimed at evaluating the core-skin adhesive strength. The crosshead speed was fixed to 0.5 mm/min. From the recorded load-displacement curves, the ultimate flatwise tensile strength (σ_t^{ult}) was calculated via Equation (9.10):

$$\sigma_t^{ult} = \frac{P_{max}}{A} \quad (9.10)$$

where P_{max} is the maximum load before failure and A is the cross-sectional area.

The mechanical results were statistically treated using R Studio v. 2023.12.1 (RStudio, Inc., Boston, MA, USA). A one-way analysis of variance (ANOVA) was conducted to assess the effect of the composition on the various mechanical parameters. Differences were considered significant with a p-value lower than 0.05.

9.2.5 Results and discussion

9.2.5.1 Characterization of the foams

Microstructural properties of the foam samples

The microstructural characterization of the foam samples revealed significant modifications in cell shape and size with increasing PCM content (Figure 9.15(a-h)). The neat PU foam (Figure 9.15a) exhibits the typical polyhedral closed-cell structure characterized by pentagonal or hexagonal cells, which regulates the foam's thermal and mechanical properties [287,288]. As the PCM content increases, the cell shape is transformed from polyhedral to more spherical, and the cell dimensions appear to decrease (Figure 9.15b). At higher PCM loadings, substantial changes in the cell structure are observed, transitioning from a closed-cell to an open-cell configuration. This transition is facilitated by the rupture of struts between adjacent cells, extensively deforming the original cell shape. The strut rupture mechanism is primarily responsible for the formation of very large cells at higher PCM contents (Figure 9.15(e,f)). This phenomenon is further evidenced by higher magnification micrographs, which reveal that the microcapsules are preferentially located at the interface between adjacent cells. The cell struts and walls change from smooth to rough, indicating that the PCM is primarily incorporated in these regions rather than inside the cells.

In most cases, the PCM shell is observed to detach from the fractured surface, suggesting poor adhesion between the capsules and the PU foam matrix. This poor adhesion can detrimentally affect the mechanical behaviour by impairing the load transfer from the polymer matrix to the capsules. However, instances are observed where the capsule shells remain attached to the matrix, indicating that the bonds are strong enough to induce crack propagation through the microcapsule.

The analysis of the average cell size and distribution (Figure 9.15i) reveals that the mean cell diameter ranges between 200 μm and 500 μm for all foam compositions, consistently with previous studies on PU foams [271,289]. The addition of 10 wt% and 20 wt% PCM appeared to decrease the mean cell size compared to the neat PU foam, attributable to the nucleation effect promoted by the microcapsules [279,290]. However, the same result is not observed with 30% PCM content, where strut rupture and degradation are dominant and the main effect of this is a broadening of the cell size distribution. This cell opening effect promoted by the PCM is responsible for the density and porosity trends represented in Figure 9.15(j,k).

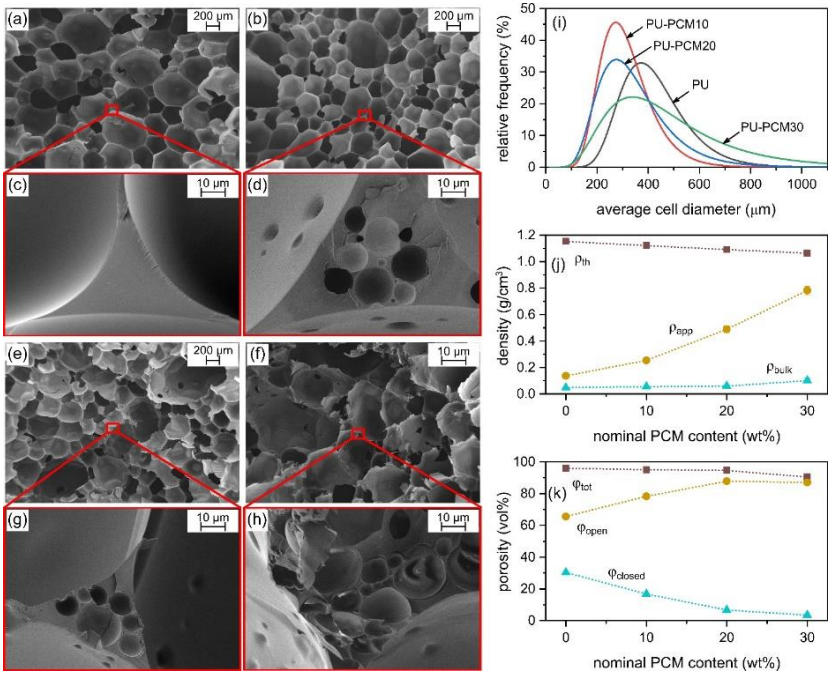

Figure 9.15. Microstructural and physical characterization of the prepared foams. (a-h) SEM micrographs of the cryofracture surface of the samples (a-b) PU, (c-d) PU-PCM10, (e-f) PU-PCM20, (g-h) PU-PCM30, (i) Log-normal fit of the average foam cell size distribution obtained from the analysis of the SEM micrographs of foam samples, (j) theoretical, apparent, and bulk density of the prepared foams as a function of the PCM concentration, (k) total, open, and closed porosity of the prepared foams as a function of the PCM concentration.

The apparent and bulk densities are observed to increase with the PCM concentration, which is attributed to the PCM weakening the cell walls and promoting the transformation into an open-cell structure, as evidenced by the micrographs. In fact, the volume fraction of closed cells decreases from approx. 30 vol% of neat PU down to approx. 3 vol% of PU-PCM30, and the addition of 30 wt% PCM causes an increase in the open porosity of approx. 32% compared to neat PU. In

summary, the addition of PCM to the PU foam influences the cell structure, resulting in a decrease in total porosity, an increase in open porosity, and a reduction in the volume fraction of closed cells. These microstructural modifications significantly impact the thermal and mechanical properties of the foams [291], as described in the next sections.

Thermal properties of the foam samples

The DSC results are reported in Figure 9.16 and Table 9.10.

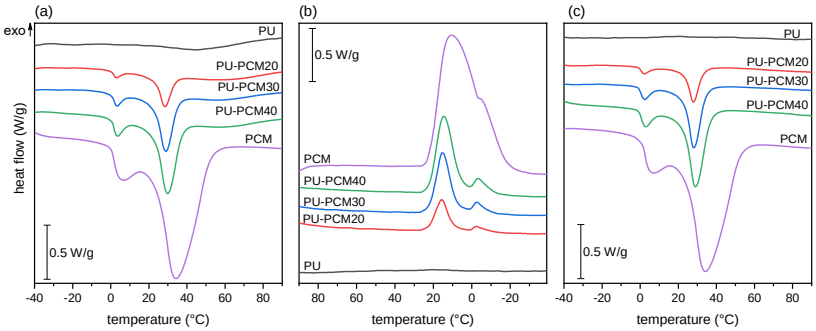

Figure 9.16. DSC thermograms of the prepared foam samples. (a) First heating scan, (b) cooling scan, (c) second heating scan.

Table 9.10. Main results of the DSC tests on the prepared foam samples.

Sample	T_{m1} (°C)	ΔH_{m1} (J/g)	T_c (°C)	ΔH_c (J/g)	T_{m2} (°C)	ΔH_{m2} (J/g)	$\Delta H_{r,m1}$ (%)	$\Delta H_{r,c}$ (%)	$\Delta H_{r,m2}$ (%)
PU	n.a.	n.a.	n.a.	n.a.	n.a.	n.a.	n.a.	n.a.	n.a.
PU-PCM10	28.5	14.5	15.7	15.3	27.8	14.7	82.6	86.4	82.8
PU-PCM20	28.9	28.7	15.3	29.7	28.1	29.1	81.8	84.0	82.2
PU-PCM30	29.8	42.0	14.5	44.4	29	42.5	79.6	83.8	80.0
PCM	29.4	175.6	15.6	176.8	29.6	176.8	n.a.	n.a.	n.a.

$T_{m1}, \Delta H_{m1}$= melting temperature and enthalpy (first heating scan); $T_c, \Delta H_c$= crystallization temperature and enthalpy (cooling scan); $T_{m2}, \Delta H_{m2}$= melting temperature and enthalpy (second heating scan); $\Delta H_{r,m1}, \Delta H_{r,c}, \Delta H_{r,m2}$ = relative phase change enthalpy in the first heating, cooling, and second heating scans, respectively. n.a. = not applicable.

The results reveal that the neat PU foam does not exhibit any evident transition in the analyzed temperature range. However, all PU-PCM samples display signals attributable to the melting/crystallization process of the PCM. Two well-separated peaks are observed in both heating and cooling scans, which may arise from the molecular weight distribution of the paraffin wax and the rotator phase transition of n-alkanes [292]. As the PCM content increases from 10 wt% to 30 wt%, the specific enthalpy stored during heating increases from 14.5 J/g to 42.0 J/g, thus confirming an improved TES capability with higher PCM loading. However, the relative melting and crystallization enthalpy values are always approx. 80%, which indicates that the effective PCM weight fractions able to melt and crystallize are lower than the nominal values. This is likely due to material remaining inside the beaker before mold casting, which advocates for an improvement in the foam preparation procedure.
During the first heating scan, all foam samples also exhibit a slight exothermic signal after 50 °C, which is absent during the second heating scan. This signal may be attributed to the residual cross-linking of polyurethane, suggesting that the foam production method could be optimized to obtain full curing from the onset.

Although an increase in the PCM concentration increases the heat that can be stored and released by the foam, thereby enhancing the thermal buffering capabilities, it also detrimentally modifies the foam cell structure and decreases the volume fraction of closed cells, which diminishes the insulating capability of the foams. This is clear from the results of the HFM tests, reported in Figure 9.17.

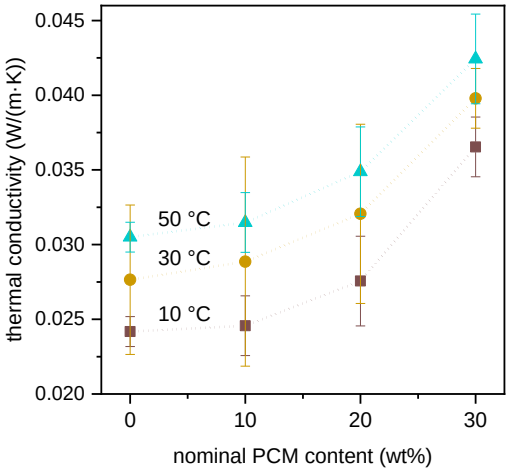

Figure 9.17. Thermal conductivity of the prepared foam samples as a function of the nominal PCM concentration and the testing temperature.

The thermal conductivity increases with the PCM content, from 0.024 W/(m·K) for neat PU to 0.037 W/(m·K) for PU-PCM30 at 10 °C, with the trends being confirmed at the other investigated temperatures. These results are similar to those found in the literature for similar PU/PCM systems [273,278]. More specifically, the increase in thermal conductivity is quite marginal up to a PCM content of 20 wt%, above which the increase is more significant. Given that the typical conductivity of insulating PU foams is 0.02-0.03 W/(m·K) [291,293-295], the thermal performance of PU-PCM30 samples could still be acceptable when leading to improved TES capabilities. In the end, the experimental results prove that, up to a nominal 30 wt% PCM addition, not only larger heat can be stored by PU foams but also the foam insulating capability may still be satisfactory.

The combination of the increased thermal buffering effect provided by the PCM, as investigated in DSC, and the increase in thermal conductivity, as measured via HFM, was studied on a larger scale via infrared thermography and shown in Figure 9.18(a-d).

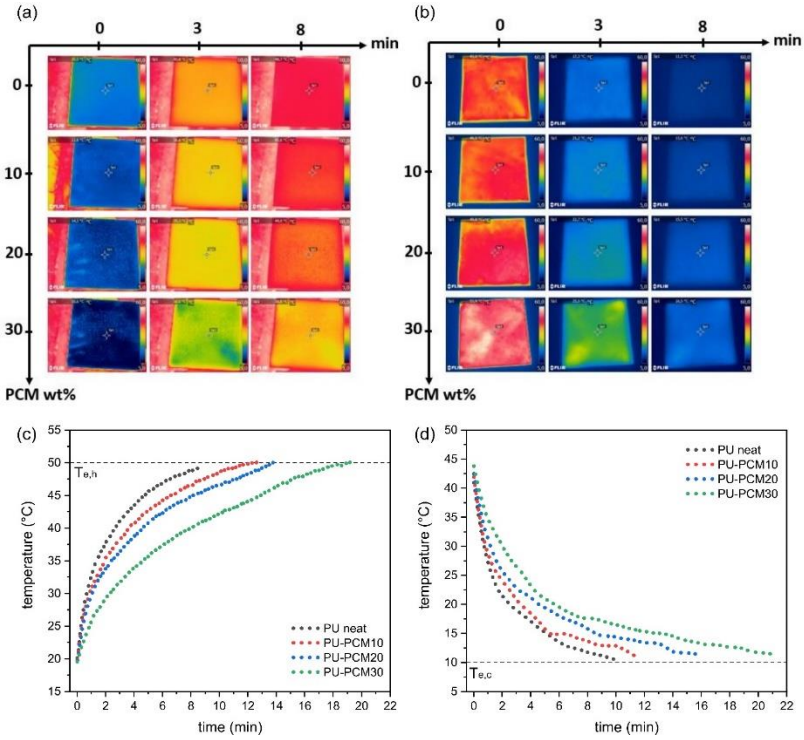

Figure 9.18. Results of infrared thermography on foam samples. (a-b) Camera frames recorded at test start, after 3 min, and after 8 min as a function of the PCM nominal concentration in the heating (a) and cooling (b) experiments. (c-d) Temperature profiles of the foam surfaces (average temperature) as a function of time in the heating (c) and (d) cooling experiments. $T_{e,h}$ and $T_{e,c}$ indicate the environment temperature in the heating and cooling experiments, respectively.

The results of this test demonstrate that an increase in the PCM content prolongs the time required to reach the equilibrium temperature, both during heating and during cooling, due to the heat stored or released by the PCM during its phase transition. For instance, during heating to 50 °C, a nominal addition of 20 wt% PCM extends the time needed from 8 min of neat PU to 14 min of PU-

PCM20. This is also evident by some of the camera frames recorded during the experiment, reported in Figure 9.18(a,b). Interestingly, for PU-PCM30 samples, the camera frames also reveal areas with different temperatures on the same surface, indicating zones with higher PCM concentrations and suggesting potential difficulties in homogeneously incorporating PCM microcapsules at such high PCM contents.

Mechanical properties of the foam samples

The flexural stress-strain curves recorded at 20 °C and 40 °C (Figure 9.19(a,b)) reveal that no fracture occurs for neat PU samples at either temperature. Instead, a continuously increasing vertical deflection is observed during measurement until the specimen starts slipping on the supports, at which point the test was interrupted. This phenomenon is not observed for the PCM-containing compositions, which all undergo fracture before starting to slip. Regarding the flexural modulus (Figure 9.19c), as expected, the increase in temperature from 20 °C to 40 °C causes a decrease in stiffness. This occurs not only for PCM-containing samples but also for neat PU, indicating that the cause is not solely the PCM melting but also the incomplete curing of the polyurethane foams. Moreover, up to a nominal PCM content of 20 wt%, the modulus remains almost constant, while it significantly decreases for samples containing 30 wt% PCM, with a maximum difference of 24% compared to neat PU. Hence, the addition of up to 20 wt% PCM does not dramatically impair the foam modulus and provides satisfactory bending stiffness. Similar considerations can be made for the flexural strength (Figure 9.19d): the maximum stress reached before failure is affected by the softening of non-cured polyurethane upon the temperature rise and remains almost constant for up to 20 wt% nominal PCM content. Furthermore, the flexural strain at maximum load (Figure 9.19e) increases with temperature and decreases with PCM content due to the combined effects of thermal softening and cell structure modifications. These results are in good agreement with those found in the literature for similar systems [290].

The stress-strain curves under compressive loads (Figure 9.19(f,g)) reveal that no yield point is observed in the samples, and the compressive stress continuously increases. Therefore, the stress value at 10% strain is considered the compressive strength, and the values of the compressive modulus (E_c) and compressive strength (R_c) are calculated accordingly. As expected from the microstructural analysis, and similar to what has been reported in the literature [271,273,296], the compressive properties decrease with increasing PCM content. The cell opening effect promoted by the microcapsules, as well as the weakening and deformation of the existing cells, cause the reduction of both E_c (Figure 9.19h) and R_c (Figure 9.19i). The maximum decrease in compressive modulus between samples containing 30 wt% PCM and neat PU is approximately 55%. On the contrary, the compressive strength decreases by a maximum of 39% when adding a nominal 30 wt% PCM content, while the flexural strength shows a higher maximum drop of approximately 57%. This suggests that the PCM primarily impairs the compressive stiffness and the flexural strength of the polyurethane-PCM foams. Regarding temperature and PCM melting, the modulus and strength seem to decrease with a temperature increase from 20 °C to 40 °C. However, all data are affected by a large deviation due to the non-homogeneous foam structure, and the two trends can be partially superimposed. Hence, molten PCM does not appear to significantly impair the compressive properties of the analyzed foams. Additionally, since the lower threshold of compressive strength for PU foams qualified to be used in load-bearing applications (e.g., in the building sector) is 0.1 MPa [279], all the produced foams are suitable for this application.

The comprehensive experimental investigation conducted on the different foam compositions allowed to identify the most suitable PCM content able to provide TES functions without compromising excessively the thermal insulation capability, while also ensuring the necessary mechanical properties for structural applications and uses in sandwich panels. When added to PU foam, the PCM tends to be located inside the cell struts, promoting the weakening of the closed-

cell structure in favor of an open-celled structure. Additionally, the higher the PCM weight fraction, the larger the thermal energy that can be stored in the foam, making it more suitable for TES applications, as appreciated with both DSC and thermal camera imaging. Moreover, while modifications occurring in the cell structure are responsible for a slight increase in thermal conductivity with PCM contents higher than 20 wt%, the foam remains a good thermal insulator even with a 30 wt% PCM content. Notably, the flexural properties are not significantly impaired up to a nominal 20 wt% PCM content, whereas the compressive properties are more affected by changes in the cell structure, suffering a reduction even with lower PCM contents. Consequently, the composition identified as the most suitable to produce sandwich composites is PU-PCM20, as it provides TES functions while guaranteeing low thermal conductivity and sufficiently good mechanical properties. In particular, the flexural behaviour is primarily considered in the analysis, being less negatively affected than the compressive properties by PCM additions below 20 wt%. The results of the characterization of such composite sandwich panels with both neat PU and PU-PCM20 foam cores are presented hereafter.

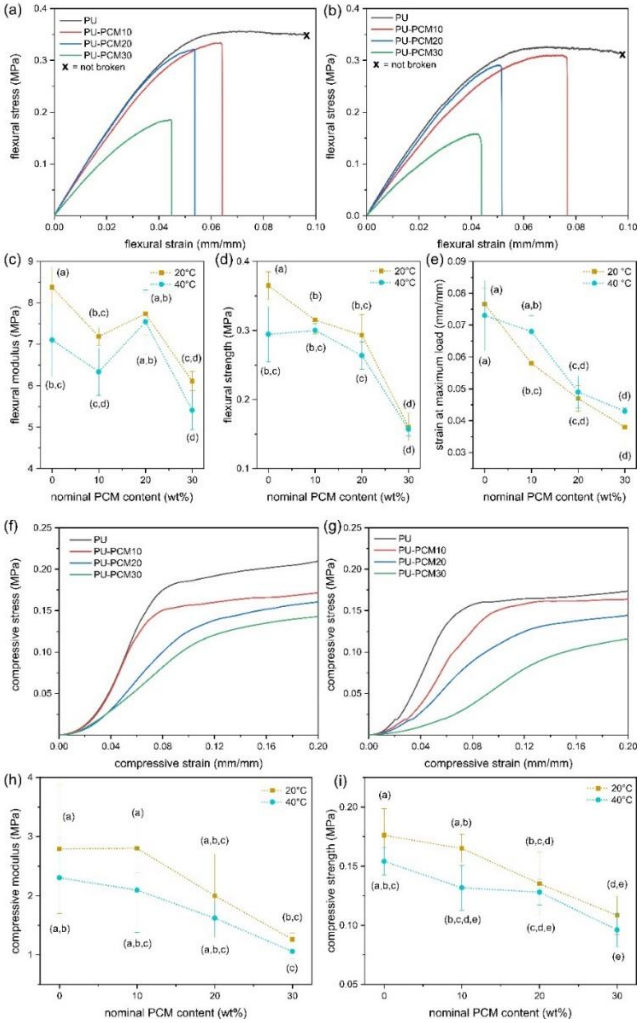

Figure 9.19. Results of the mechanical characterization of the foam samples. (a-b) Flexural tests performed at 20 °C (a) and at 40 °C (b). (c) Elastic modulus, (d) flexural strength and (e) strain at maximum load as a function of the PCM concentration. (f-g) Compressive tests performed at 20 °C (f) and at 40 °C (g). (h) Compressive modulus and (i) compressive strength as a function of the PCM concentration. Letters report the results of Tukey's test.

9.2.5.2 Characterization of sandwich panels

Microstructural properties of the sandwich panels

Figure 9.20(a-d) shows the light micrographs performed on the sandwich panels especially to characterize the core-skin interface and examine the bonding area.

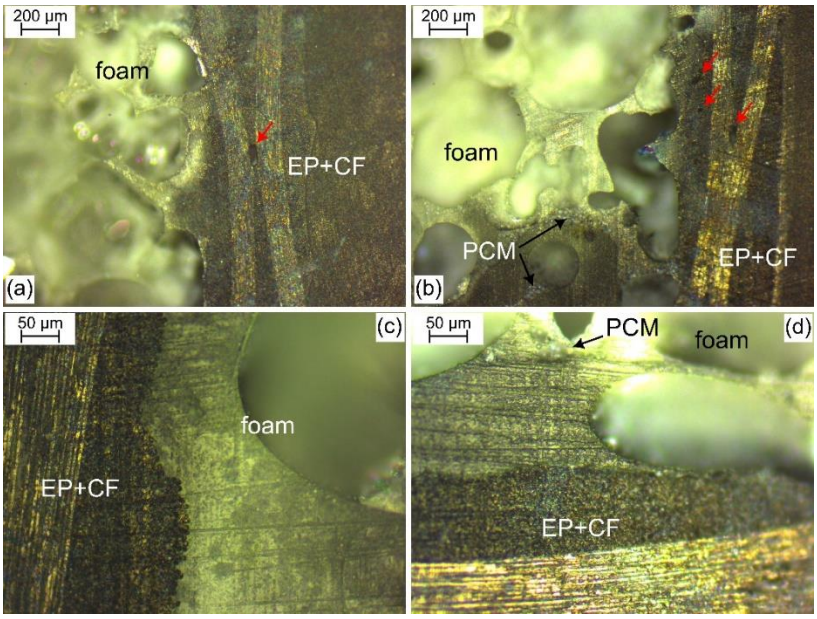

Figure 9.20. Light microscope images of the polished cross-section of the sandwich samples, highlighting the interfacial adhesion. Low (a) and high (c) magnification micrograph of S-PU sample. Red arrows indicate porosity in the epoxy/CF laminate; low (b) and high (d) magnification micrograph of the S-PU-PCM20 sample.

As highlighted in the micrographs, the laminate bonds well with both neat PU and PU-PCM20 foam cores. A continuous adhesion is observed between the two materials, and no voids appear at the interface, revealing a very strong and defect-free interface, at least from the qualitative point of view. The presence of PCM

microcapsules, visible as circular bright elements accumulated in the cell struts, (Figure 9.20b), does not seem to diminish the interfacial adhesion. This is particularly noteworthy because these foams have undergone milling to remove the outermost dense skin and attain the desired foam thickness (see Section 9.2.3.2), which likely led to the exposure of more microcapsules on the foam surface. However, this did not affect the interfacial adhesion. This suggests that the epoxy/hardener mixture added to the foam during the hand layup process is effective in creating a strong and defect-free interface.

If the foam/laminate interface appears strong and defect-free, the laminates themselves contain some porosity, as indicated by red arrows in (Figure 9.20(a,b)), which is certainly detrimental to their mechanical resistance. Such voids and defects are a direct consequence of the hand layup, which, although flexible and simple to perform, is associated with limitations that affect the final obtainable properties. For instance, the manual spread of the epoxy resin cannot guarantee that the reinforcement is homogeneously impregnated in all its parts and with the same amount of resin. Furthermore, if the vacuum is not properly applied or there is leakage, some air may remain trapped inside and generate voids and cavities in the resin. Hence, an automated resin impregnation, the autoclave process, or the use of prepregs could be potential solutions to reduce defects and improve the laminate quality.

Thermal characterization of the sandwich panels

The DSC thermograms of the composite laminate during the first heating, cooling, and second heating scans are reported in Figure 9.21.

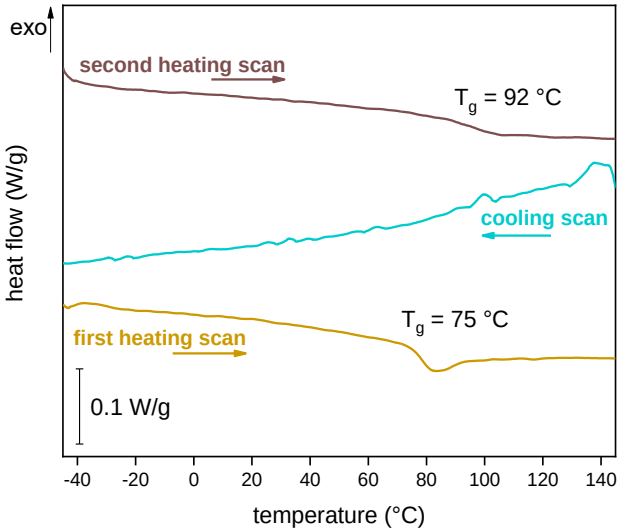

Figure 9.21 Representative DSC thermograms of the skin of the prepared sandwich samples. The glass transition temperatures measured on the two heating scans are indicated close to the corresponding thermograms.

The results do not show any exothermic peaks associated with residual cross-linking, indicating that the curing parameters selected in sample preparation were suitable and effective in producing a composite laminate with the desired properties. The T_g, equal to 75 °C in the first heating scan, increases in the second heating scan as a result of further curing the epoxy receives during the test. In any case, the value obtained from the first heating scan is in accordance with the target property value indicated by the resin producer and well above the target service temperature of these laminates (20-50 °C).

Among the most significant thermal properties of the prepared laminates is thermal conductivity. The values for the thermal conductivity at 10 °C, 30 °C, and 50 °C are reported in Table 9.11.

Table 9.11. HFM thermal conductivity of the prepared sandwich samples and the relative foam core samples after milling, evaluated at 10 °C, 30 °C, and 50 °C.

Sample		$\lambda_{10°C}$ (W/(m·K))	$\lambda_{30°C}$ (W/(m·K))	$\lambda_{50°C}$ (W/(m·K))
Foams	PU	0.031±0.001	0.034±0.001	0.037±0.001
	PU-PCM20	0.033±0.001	0.036±0.001	0.039±0.001
Sandwich panels	S-PU	0.032±0.001	0.035±0.001	0.038±0.002
	S-PU-PCM20	0.036±0.002	0.040±0.002	0.043±0.002

The results show that the addition of two composite laminate skins does not seem to impair the thermal insulation properties of the foam material, as the thermal conductivity does not increase significantly compared to that measured on the skins after milling. A growth in thermal conductivity would have been detected if the epoxy resin had penetrated the foam pores, replacing the poor conductive gas inside them, but this does not seem to be the case. Similar to the analysis of foam samples, the sample containing the microcapsules shows a slightly higher thermal conductivity than the neat sample in all temperature conditions. Thus, the produced sandwich panels preserve both the thermal energy storage and insulation properties that characterize the chosen foam composition. Finally, the data suggest that the operations for preparing the sandwich foam cores played a role in increasing the thermal conductivity of the foam material, with foam milling believed to be the main factor responsible for locally damaging the foam cell structure.

Mechanical characterization of the sandwich panels

The mechanical characterization of the prepared sandwich panels encompassed three-point flexural, edgewise compression, and flatwise tensile tests, and the results of this extensive characterization are reported in Figure 9.22 - Figure 9.25. For flexural tests, the flexural

load-displacement curves (Figure 9.22a) are characterized by a linear load-displacement relationship in the initial part, with a progressively decreasing slope in the region preceeding the maximum load. At the maximum load, the behaviour differs between neat S-PU and S-PU-PCM20 panels. In PCM-containing specimens, failure occurs in two steps: the load drops suddenly after reaching its maximum but then increases again until the second drop. For specimens with a neat PU foam core, the load plateaus and then suddenly drops to zero at much higher displacement values. This difference underlines a different failure mechanism. The sudden load drop in the S-PU specimens core is associated with the top face sheet failure at the contact point with the test fixture, due to the compression-induced local bending of the skin (Figure 9.22b) [297,298]. Conversely, the process observed for S-PU-PCM20 is characterized by a shear failure in the sandwich core, originating in the center foam thickness and propagating diagonally to the face sheets, followed by the bottom facing separating from the core (Figure 9.22c). No failure begins from the interfacial bonding between the foam core and the outer face sheets, confirming good adhesion at the core-skin interface. Since the maximum load reached during the test is comparable across the compositions, the calculated core shear ultimate strength and facing stress values, reported in Figure 9.25a, are only slightly impaired by the PCM and are comparable to values found in the literature for structural sandwich panels [298]. However, since the main failure mechanism for S-PU-PCM20 samples is the shear failure of the foam core, future work might involve the improvement of the foam's shear resistance.

The representative load-displacement curves of the edgewise compression tests (Figure 9.23a) show that the maximum load reached by the PCM-containing sample is significantly lower than that reported for the neat S-PU sample. After the first failure, the load drops gradually with increasing displacement until it stabilizes to a plateau value, which represents the residual mechanical resistance. When reloading the specimens (Figure 9.23b), the maximum load never exceeds that stabilization load value. For the neat S-PU sample,

the load starts increasing again only after a certain displacement, indicating residual deformation after failure. This effect is less evident in S-PU-PCM20 specimens, as they experience limited deflection and reach failure sooner when the load is applied for the first time.

The calculated edgewise compressive strength values (σ_{ec}^{ult}) (Figure 9.25b) of S-PU-PCM20 are lower (-30%) than those of neat S-PU. This result is expected given the decreasing trend of compressive properties with increasing PCM content observed for the foams. However, the compressive strength of neat PU and PCM-containing samples is determined by different failure mechanisms. For neat PU specimens, failure is caused by the face sheet fracturing under compression after buckling of the entire sandwich structure (Figure 9.23c). This damage mechanism, known as overall column buckling, has been extensively studied and reported as one of the most common collapse modes for sandwich structures [299]. When further loading the damaged specimen, the flexural rigidity progressively decreases until the other skin fractures under tension (Figure 9.23d), with the foam core bending extensively and suffering internal shear damage. In contrast, PCM-containing specimens undergo unstable sandwich disintegration [299] with buckling of face sheets in opposite directions. The applied load causes the buckling of either one or both face sheets towards the outside, as the tensile strength of the foam core at the core-skin interface is insufficient to hold the facings bonded together (Figure 9.23(e,f)). A layer of foam material remains adherent to the detached facing, indicating cohesive foam failure and good interface adhesion. The foam core fails at mid-height where the bending load is more intense and propagates rapidly parallel to the face sheets.

Finally, the results of the flatwise tensile tests are reported in Figure 9.24(a-c). The representative load-displacement curves (Figure 9.24a) show a similar trend for both compositions: initially, the load increases slowly, and then the slope increases as the load rises continuously with displacement until failure. Again, the maximum

load reached by neat PU specimens is higher than that of PCM-containing specimens, and a similar tendency occurs for the ultimate flatwise tensile strength (σ_t^{ult}, Figure 9.25c), which drops from 362 kPa of S-PU to 207 kPa of S-PU-PCM20 and is seen depending primarily on the tensile strength of the foam core. Such decreasing trend of the σ_t^{ult} upon PCM addition was expected based on the microstructural and mechanical analysis of the foam materials. However, considering the typical purpose of sandwich structures, an out-of-plane tensile load is unlikely to be applied during normal use, and thus the reduced tensile strength of the PCM-containing sample is not a primary issue. More significantly, a cohesive fracture of the foam core occurred in all tests, regardless of the presence of PCM (Figure 9.24(b,c)), indicating that the adopted production process was very effective in realizing optimal adhesion between the laminates and the foam core.

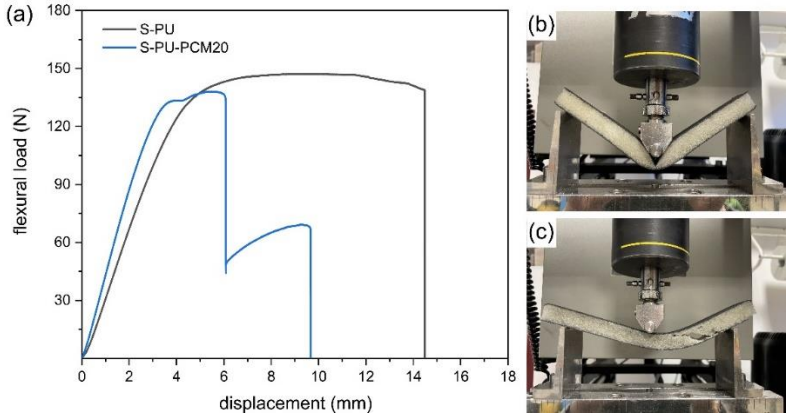

Figure 9.22. (a) Representative load-displacement curves obtained from flexural tests of sandwich samples. (b) Outer facing failure for S-PU specimens, (c) foam core shear failure for S-PU-PCM20 specimens.

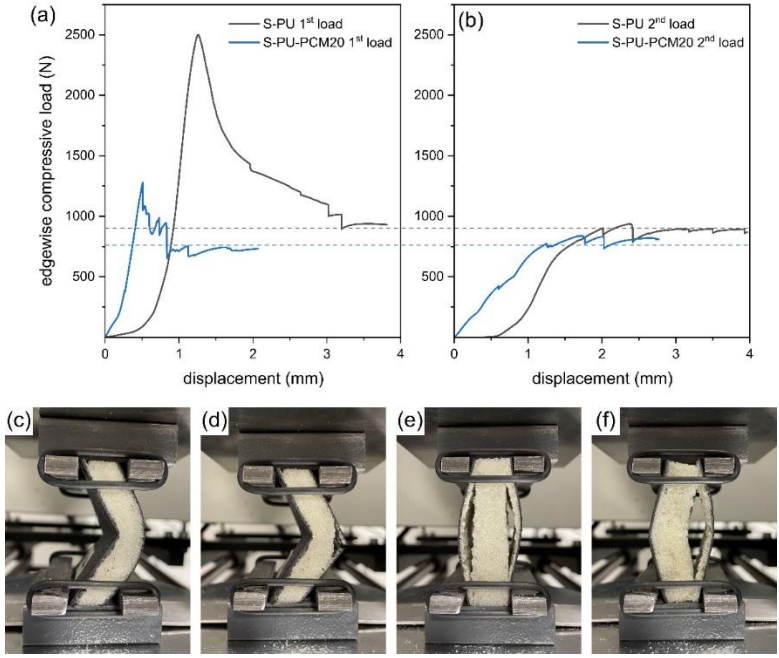

Figure 9.23. Results of the edgewise compression tests on the prepared sandwich samples. (a) Representative load-displacement curves during the first loading, (b) load-displacement behaviour of samples after the first failure. The dashed line represents the maximum load observed for reloaded samples, which is comparable to the load value at stabilization after the first failure. S-PU specimens show overall column buckling as the preferred failure mode: (c) compressive fracture of the left facing, and (d) tensile fracture of the right facing after prolonged application of the load. S-PU-PCM20 specimens show sandwich disintegration with buckling of the outer facings: (e) only one skin is separated from the foam core, and (f) both skins are debonded.

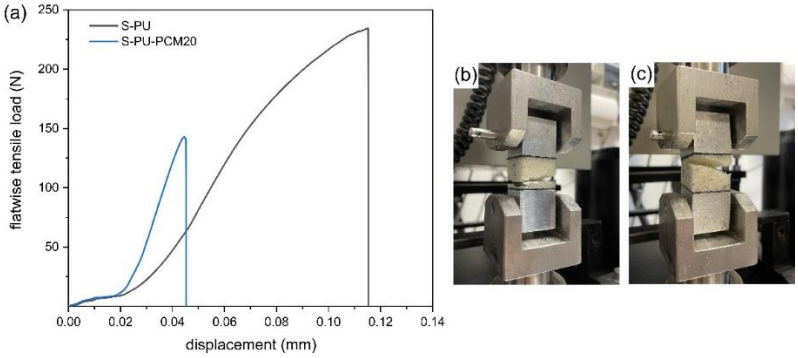

Figure 9.24. Results of the flatwise tensile tests on the prepared sandwich samples. (a) Representative load-displacement curves. For both S-PU (b) and S-PU-PCM20 (c), failure occurs due to core fracturing

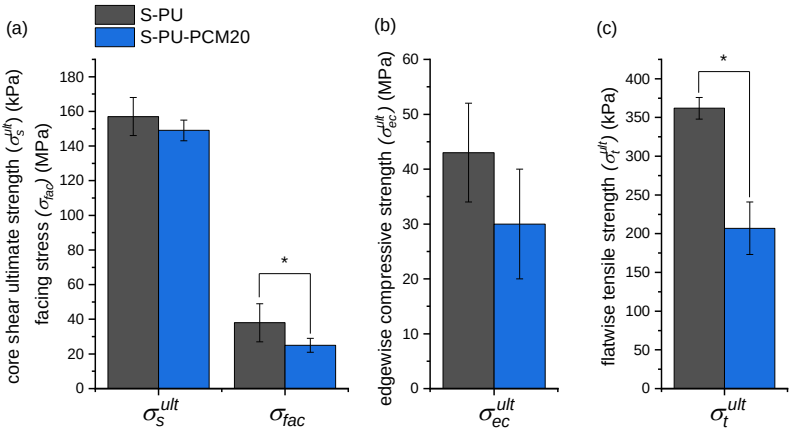

Figure 9.25. Summary of the results of the mechanical properties of the prepared sandwich panels. (a) results of the three-point bending tests, (b) results of the edgewise compression tests, (c) results of the flatwise tensile tests. * indicates statistically significant differences according to one-way ANOVA test (p-value > 0.05).

9.2.6 Conclusions

In this work novel multifunctional sandwich composites that synergistically integrate structural load-bearing capability with thermal management properties were successfully developed and comprehensively characterized. These composites combined PU foam cores containing microencapsulated PCMs with high-performance epoxy/carbon fiber laminate skins.

First, the systematic investigation of PU/PCM foams revealed an optimized PU foam composition with 20 wt% PCM content. This composition (PU-PCM20) provided a balanced combination of adequate thermal energy storage (up to 29 J/g) and low thermal conductivity (0.032 W/(m·K) at 30 °C), while maintaining satisfactory flexural and compressive properties.

Sandwich panels produced with this optimized PU-PCM20 foam core exhibited good structural integrity and interfacial adhesion between the foam core and carbon/epoxy laminate skins. Light microscopy revealed a continuous, defect-free bonding at the core-skin interface with no evidence of voids or delamination. This excellent interfacial adhesion enabled the sandwich panels to withstand flexural, edgewise compression, and flatwise tensile loading conditions characteristic of structural applications. Under three-point flexural loading, the PCM-containing panels achieved comparable core shear strengths of 149 kPa and facing stresses of 25 MPa relative to neat PU sandwich controls. However, the edgewise compressive strength was approx. 30% lower at 30 MPa for PU-PCM20 panels due to premature unstable disintegration from core shear failure rather than overall buckling seen in neat samples, and the flatwise tensile strength also suffered from a significant decrease, dropping to 207 kPa (-42% than neat S-PU sandwich).

In summary, this study demonstrated the feasibility of realizing true multifunctional composites with simultaneous load-bearing and thermal regulation capabilities by judiciously incorporating PCMs within the sandwich foam core architecture.

10 Bibliography

1. Massazza, A.; Ardino, V.; Fioravanzo, R.E. Climate change, trauma and mental health in Italy: a scoping review. *European Journal of Psychotraumatology* **2022**, *13*, 2046374.
2. Clarke, B.; Otto, F.; Stuart-Smith, R.; Harrington, L. Extreme weather impacts of climate change: an attribution perspective. *Environmental Research: Climate* **2022**, *1*, 012001.
3. Masson-Delmotte, V.; Zhai, P.; Pirani, A.; Connors, S.L.; Péan, C.; Berger, S.; Caud, N.; Chen, Y.; Goldfarb, L.; Gomis, M. Climate change 2021: the physical science basis; In: *Contribution of working group I to the sixth assessment report of the intergovernmental panel on climate change*; Cambridge University Press: Cambridge (UK), **2021**, 2391.
4. Fischer, E.M.; Knutti, R. Anthropogenic contribution to global occurrence of heavy-precipitation and high-temperature extremes. *Nature Climate Change* **2015**, *5*, 560-564.
5. Lionello, P.; Scarascia, L. The relation between climate change in the Mediterranean region and global warming. *Regional Environmental Change* **2018**, *18*, 1481-1493.
6. Noto, L.; Cipolla, G.; Pumo, D.; Francipane, A. Climate change in the Mediterranean Basin (Part II): A review of challenges and uncertainties in climate change modeling and impact analyses. *Water Resources Management* **2023**, *37*, 2307-2323.
7. Schelhaas, M.J.; Nabuurs, G.J.; Schuck, A. Natural disturbances in the European forests in the 19th and 20th centuries. *Global Change Biology* **2003**, *9*, 1620-1633.
8. Xu, R.; Yu, P.; Abramson, M.J.; Johnston, F.H.; Samet, J.M.; Bell, M.L.; Haines, A.; Ebi, K.L.; Li, S.; Guo, Y. Wildfires, global climate change, and human health. *New England Journal of Medicine* **2020**, *383*, 2173-2181.

9. Marino, E.; Hernando, C.; Planelles, R.; Madrigal, J.; Guijarro, M.; Sebastián, A. Forest fuel management for wildfire prevention in Spain: a quantitative SWOT analysis. *International Journal of Wildland Fire* **2014**, *23*, 373-384.
10. Carreiras, M.; Ferreira, A.J.D.; Valente, S.; Fleskens, L.; Gonzales-Pelayo, Ó.; Rubio, J.L.; Stoof, C.R.; Coelho, C.O.A.; Ferreira, C.S.S.; Ritsema, C. Comparative analysis of policies to deal with wildfire risk. *Land Degradation Development* **2014**, *25*, 92-103.
11. Shakesby, R.A. Post-wildfire soil erosion in the Mediterranean: Review and future research directions. *Earth-Science Reviews* **2011**, *105*, 71-100.
12. Lovreglio, R.; Leone, V.; Giaquinto, P.; Notarnicola, A. Wildfire cause analysis: four case-studies in southern Italy. *iForest-Biogeosciences Forestry* **2010**, *3*, 8-15.
13. Moreira, F.; Pe'er, G. Agricultural policy can reduce wildfires. *Science* **2018**, *359*, 1001-1001.
14. Haque, K.S.; Uddin, M.; Ampah, J.D.; Haque, M.K.; Hossen, M.S.; Rokonuzzaman, M.; Hossain, M.Y.; Hossain, M.S.; Rahman, M.Z. Wildfires in Australia: a bibliometric analysis and a glimpse on 'Black Summer'(2019/2020) disaster. *Environmental Science Pollution Research* **2023**, *30*, 73061-73086.
15. Stevens-Rumann, C.S.; Kemp, K.B.; Higuera, P.E.; Harvey, B.J.; Rother, M.T.; Donato, D.C.; Morgan, P.; Veblen, T.T. Evidence for declining forest resilience to wildfires under climate change. *Ecology Letters* **2018**, *21*, 243-252.
16. Castrofino, A. Desertification. In: *Encyclopedia of Sustainable Management*; Springer International Publishing: Basel (CH), 2022; 1-8.
17. Le Houérou, H.N. Climate change, drought and desertification. *Journal of Arid Environments* **1996**, *34*, 133-185.
18. Charney, J.G. Dynamics of deserts and drought in the Sahel. *Quarterly Journal of the Royal Meteorological Society* **1975**, *101*, 193-202.

19. Giannini, A.; Biasutti, M.; Verstraete, M.M. A climate model-based review of drought in the Sahel: Desertification, the re-greening and climate change. *Global Planetary Change* **2008**, *64*, 119-128.
20. Rodrigo-Comino, J.; Salvia, R.; Egidi, G.; Salvati, L.; Giménez-Morera, A.; Quaranta, G. Desertification and Degradation Risks vs Poverty: A Key Topic in Mediterranean Europe. *Cuadernos de Investigacion Geografica* **2022**, *48*, 23-40.
21. Middleton, N. Rangeland management and climate hazards in drylands: dust storms, desertification and the overgrazing debate. *Natural Hazards* **2018**, *92*, 57-70.
22. Chelli, S.; Wellstein, C.; Campetella, G.; Canullo, R.; Tonin, R.; Zerbe, S.; Gerdol, R. Climate change response of vegetation across climatic zones in Italy. *Climate Research* **2017**, *71*, 249-262.
23. Norton, M.R.; Malinowski, D.P.; Volaire, F. Plant drought survival under climate change and strategies to improve perennial grasses. A review. *Agronomy for Sustainable Development* **2016**, *36*, 1-15.
24. Ibáñez, J.; Martínez, J.; Schnabel, S. Desertification due to overgrazing in a dynamic commercial livestock–grass–soil system. *Ecological Modelling* **2007**, *205*, 277-288.
25. Manickavelu, A.; Kawaura, K.; Oishi, K.; Shin-I, T.; Kohara, Y.; Yahiaoui, N.; Keller, B.; Abe, R.; Suzuki, A.; Nagayama, T. Comprehensive functional analyses of expressed sequence tags in common wheat (Triticum aestivum). *DNA Research* **2012**, *19*, 165-177.
26. Khan, S.; Anwar, S.; Yu, S.; Sun, M.; Yang, Z.; Gao, Z.-q. Development of drought-tolerant transgenic wheat: achievements and limitations. *International Journal of Molecular Sciences* **2019**, *20*, 3350.
27. Yan, H.; Harrison, M.T.; Liu, K.; Wang, B.; Feng, P.; Fahad, S.; Meinke, H.; Yang, R.; Li Liu, D.; Archontoulis, S. Crop traits

enabling yield gains under more frequent extreme climatic events. *Science of the Total Environment* **2022**, *808*, 152170.

28. Sabatini, F.M.; Bluhm, H.; Kun, Z.; Aksenov, D.; Atauri, J.A.; Buchwald, E.; Burrascano, S.; Cateau, E.; Diku, A.; Duarte, I.M. European primary forest database v2. 0. *Scientific data* **2021**, *8*, 220.
29. Martinez del Castillo, E.; Zang, C.S.; Buras, A.; Hacket-Pain, A.; Esper, J.; Serrano-Notivoli, R.; Hartl, C.; Weigel, R.; Klesse, S.; Resco de Dios, V. Climate-change-driven growth decline of European beech forests. *Communications Biology* **2022**, *5*, 163.
30. Bertini, G.; Amoriello, T.; Fabbio, G.; Piovosi, M. Forest growth and climate change: evidences from the ICP-Forests intensive monitoring in Italy. *iForest-Biogeosciences Forestry* **2011**, *4*, 262.
31. Albrich, K.; Rammer, W.; Seidl, R. Climate change causes critical transitions and irreversible alterations of mountain forests. *Global Change Biology* **2020**, *26*, 4013-4027.
32. Fischer, A.; Lindner, M.; Abs, C.; Lasch, P. Vegetation dynamics in central European forest ecosystems (near-natural as well as managed) after storm events. *Folia Geobotanica* **2002**, *37*, 17-32.
33. Jakoby, O.; Lischke, H.; Wermelinger, B. Climate change alters elevational phenology patterns of the European spruce bark beetle (Ips typographus). *Global Change Biology* **2019**, *25*, 4048-4063.
34. Chirici, G.; Giannetti, F.; Travaglini, D.; Nocentini, S.; Francini, S.; D'Amico, G.; Calvo, E.; Fasolini, D.; Broll, M.; Maistrelli, F. Stima dei danni della tempesta" Vaia" alle foreste in Italia. *Forest@* **2019**, *1*, 3-9.
35. Hlásny, T.; König, L.; Krokene, P.; Lindner, M.; Montagné-Huck, C.; Müller, J.; Qin, H.; Raffa, K.F.; Schelhaas, M.-J.; Svoboda, M. Bark beetle outbreaks in Europe: state of

knowledge and ways forward for management. *Current Forestry Reports* **2021**, *7*, 138-165.

36. Hazubska-Przybył, T.; Wawrzyniak, M.K.; Kijowska-Oberc, J.; Staszak, A.M.; Ratajczak, E. Somatic embryogenesis of Norway spruce and Scots pine: Possibility of application in modern forestry. *Forests* **2022**, *13*, 155.
37. Salvadori, C.; Stergulc, F. Indirizzi selvicolturali per il contenimento dei danni da bostrico nelle foreste delle Alpi orientali. In: Riassunti III Congresso Nazionale di Selvicoltura (Ciancio O ed), Taormina (Italy), 16th-18th October, **2008**.
38. Salvadori, C.; Tolotti, G.; Confalonieri, M. Bostrico tipografo. *Terra Trentina* **2020**, *65*, 60-62.
39. Kurz, W.A.; Dymond, C.; Stinson, G.; Rampley, G.; Neilson, E.; Carroll, A.; Ebata, T.; Safranyik, L. Mountain pine beetle and forest carbon feedback to climate change. *Nature* **2008**, *452*, 987-990.
40. Schneider, K.; Van der Werf, W.; Cendoya, M.; Mourits, M.; Navas-Cortés, J.A.; Vicent, A.; Oude Lansink, A. Impact of Xylella fastidiosa subspecies pauca in European olives. *Proceedings of the national academy of sciences* **2020**, *117*, 9250-9259.
41. Ali, B.M.; Van Der Werf, W.; Lansink, A.O. Assessment of the environmental impacts of Xylella fastidiosa subsp. pauca in Puglia. *Crop Protection* **2021**, *142*, 105519.
42. McElrone, A.J.; Sherald, J.L.; Forseth, I.N. Effects of water stress on symptomatology and growth of Parthenocissus quinquefolia infected by Xylella fastidiosa. *Plant Disease* **2001**, *85*, 1160-1164.
43. Bajocco, S.; Raparelli, E.; Bregaglio, S. Assessing the driving role of the anthropogenic landscape on the distribution of the Xylella fastidiosa-driven "olive quick decline syndrome" in Apulia (Italy). *Science of the Total Environment* **2023**, *896*, 165231.

44. Fettig, C.J.; Klepzig, K.D.; Billings, R.F.; Munson, A.S.; Nebeker, T.E.; Negrón, J.F.; Nowak, J.T. The effectiveness of vegetation management practices for prevention and control of bark beetle infestations in coniferous forests of the western and southern United States. *Forest Ecology Management* **2007**, *238*, 24-53.
45. Hoogstra, M.A.; Schanz, H. Future orientation and planning in forestry: a comparison of forest managers' planning horizons in Germany and the Netherlands. *European Journal of Forest Research* **2009**, *128*, 1-11.
46. Diaz-Balteiro, L.; Romero, C. Sustainability of forest management plans: a discrete goal programming approach. *Journal of Environmental Management* **2004**, *71*, 351-359.
47. Fettig, C.J.; Gibson, K.E.; Munson, A.S.; Negrón, J.F. Cultural practices for prevention and mitigation of mountain pine beetle infestations. *Forest Science* **2014**, *60*, 450-463.
48. von Detten, R.; Hanewinkel, M. Strategies of handling risk and uncertainty in forest management in Central Europe. *Current Forestry Reports* **2017**, *3*, 60-73.
49. Ćosović, M.; Bugalho, M.N.; Thom, D.; Borges, J.G. Stand structural characteristics are the most practical biodiversity indicators for forest management planning in Europe. *Forests* **2020**, *11*, 343.
50. Bouriaud, L.; Marzano, M.; Lexer, M.; Nichiforel, L.; Reyer, C.; Temperli, C.; Peltola, H.; Elkin, C.; Duduman, G.; Taylor, P. Institutional factors and opportunities for adapting European forest management to climate change. *Regional Environmental Change* **2015**, *15*, 1595-1609.
51. Wang, H.-H.; Finney, M.A.; Song, Z.-L.; Wang, Z.-S.; Li, X.-C. Ecological techniques for wildfire mitigation: Two distinct fuelbreak approaches and their fusion. *Forest Ecology Management* **2021**, *495*, 119376.
52. Cui, X.; Alam, M.A.; Perry, G.L.; Paterson, A.M.; Wyse, S.V.; Curran, T.J. Green firebreaks as a management tool for

wildfires: Lessons from China. *Journal of Environmental Management* **2019**, *233*, 329-336.

53. Vega, J.; Fernández, C.; Fonturbel, T. Throughfall, runoff and soil erosion after prescribed burning in gorse shrubland in Galicia (NW Spain). *Land Degradation Development* **2005**, *16*, 37-51.
54. Francos, M.; Úbeda, X. Prescribed fire management. *Current Opinion in Environmental Science Health* **2021**, *21*, 100250.
55. Ryan, K.C.; Knapp, E.E.; Varner, J.M. Prescribed fire in North American forests and woodlands: history, current practice, and challenges. *Frontiers in Ecology the Environment* **2013**, *11*, 15-24.
56. Fukai, S.; Cooper, M. Development of drought-resistant cultivars using physiomorphological traits in rice. *Field Crops Research* **1995**, *40*, 67-86.
57. Humpenöder, F.; Popp, A.; Dietrich, J.P.; Klein, D.; Lotze-Campen, H.; Bonsch, M.; Bodirsky, B.L.; Weindl, I.; Stevanovic, M.; Müller, C. Investigating afforestation and bioenergy CCS as climate change mitigation strategies. *Environmental Research Letters* **2014**, *9*, 064029.
58. Kreidenweis, U.; Humpenöder, F.; Stevanović, M.; Bodirsky, B.L.; Kriegler, E.; Lotze-Campen, H.; Popp, A. Afforestation to mitigate climate change: impacts on food prices under consideration of albedo effects. *Environmental Research Letters* **2016**, *11*, 085001.
59. Doelman, J.C.; Stehfest, E.; van Vuuren, D.P.; Tabeau, A.; Hof, A.F.; Braakhekke, M.C.; Gernaat, D.E.; van den Berg, M.; van Zeist, W.J.; Daioglou, V. Afforestation for climate change mitigation: Potentials, risks and trade-offs. *Global Change Biology* **2020**, *26*, 1576-1591.
60. Cerasoli, S.; Yin, J.; Porporato, A. Cloud cooling effects of afforestation and reforestation at midlatitudes. *Proceedings of the national academy of sciences* **2021**, *118*, 3-7.

61. Zomer, R.J.; Trabucco, A.; Bossio, D.A.; Verchot, L.V. Climate change mitigation: A spatial analysis of global land suitability for clean development mechanism afforestation and reforestation. *Agriculture, ecosystems environment* **2008**, *126*, 67-80.
62. Trabucco, A.; Zomer, R.J.; Bossio, D.A.; van Straaten, O.; Verchot, L.V. Climate change mitigation through afforestation/reforestation: a global analysis of hydrologic impacts with four case studies. *Agriculture, ecosystems environment* **2008**, *126*, 81-97.
63. Schirmer, J.; Bull, L. Assessing the likelihood of widespread landholder adoption of afforestation and reforestation projects. *Global Environmental Change* **2014**, *24*, 306-320.
64. Thomas, S.; Dargusch, P.; Harrison, S.; Herbohn, J. Why are there so few afforestation and reforestation Clean Development Mechanism projects? *Land Use Policy* **2010**, *27*, 880-887.
65. Díaz-Pérez, J.C.; Batal, K.D. Colored plastic film mulches affect tomato growth and yield via changes in root-zone temperature. *Journal of the American Society for Horticultural Science* **2002**, *127*, 127-135.
66. Kasirajan, S.; Ngouajio, M. Polyethylene and biodegradable mulches for agricultural applications: a review. *Agronomy for Sustainable Development* **2012**, *32*, 501-529.
67. Sintim, H.Y.; Flury, M. Is biodegradable plastic mulch the solution to agriculture's plastic problem? *Environmental Science & Technology* **2017**, *51*, 1068-1069.
68. Yang, N.; Sun, Z.-X.; Feng, L.-S.; Zheng, M.-Z.; Chi, D.-C.; Meng, W.-Z.; Hou, Z.-Y.; Bai, W.; Li, K.-Y. Plastic film mulching for water-efficient agricultural applications and degradable films materials development research. *Materials and Manufacturing Processes* **2015**, *30*, 143-154.
69. Ramakrishna, A.; Tam, H.M.; Wani, S.P.; Long, T.D. Effect of mulch on soil temperature, moisture, weed infestation and

yield of groundnut in northern Vietnam. *Field Crops Research* **2006**, *95*, 115-125.

70. Han, Q.; Harayama, H.; Uemura, A.; Ito, E.; Utsugi, H.; Kitao, M.; Maruyama, Y. High biomass productivity of short-rotation willow plantation in boreal Hokkaido achieved by mulching and cutback. *Forests* **2020**, *11*, 505.
71. Vitone, A.; Coello, J.; Piqué, M.; Rovira, P. Use of innovative groundcovers in Mediterranean afforestations: aerial and belowground effects in hybrid walnut. *Annals of Silvicultural Research* **2016**, *40*, 140-147.
72. Briassoulis, D.; Giannoulis, A. Evaluation of the functionality of bio-based food packaging films. *Polymer Testing* **2018**, *69*, 39-51.
73. Ma, Z.; Zhang, X.; Zheng, B.; Yue, S.; Zhang, X.; Zhai, B.; Wang, Z.; Zheng, W.; Li, Z.; Zamanian, K. Effects of plastic and straw mulching on soil microbial P limitations in maize fields: Dependency on soil organic carbon demonstrated by ecoenzymatic stoichiometry. *Geoderma* **2021**, *388*, 114928.
74. Novamont. Available online: https://northamerica.novamont.com/leggi_evento.php?id_event=21 (accessed on 27th July 2024).
75. Ray, S.K.; Chowdhury, P.; Deka, B.C. Scientific Approaches for Arresting and Restoration of Degraded Land. Chapter 2. In: *Conservation of Natural Resources and Its Efficient Utilization for Sustaining Hill Agriculture*; Joint Director ICAR Research Complex for NEH Region: Jharnapani Nagaland (India), 2016.
76. lovethegarden. Available online: https://www.lovethegarden.com/uk-en/article/finish-your-garden-decorative-bark (accessed on 28th August 2024).
77. Dobbs, S.H. Mulching garden soils; Oklahoma Cooperative Extension Service: Oklahoma (USA), 2010.
78. Silagy, D.; Demay, Y.; Agassant, J.F. Study of the stability of the film casting process. *Polymer Engineering Science* **1996**, *36*, 2614-2625.

79. Touchaleaume, F.; Martin-Closas, L.; Angellier-Coussy, H.; Chevillard, A.; Cesar, G.; Gontard, N.; Gastaldi, E. Performance and environmental impact of biodegradable polymers as agricultural mulching films. *Chemosphere* **2016**, *144*, 433-439.
80. Briassoulis, D.; Babou, E.; Hiskakis, M.; Kyrikou, I. Analysis of long-term degradation behaviour of polyethylene mulching films with pro-oxidants under real cultivation and soil burial conditions. *Environmental Science Pollution Research* **2015**, *22*, 2584-2598.
81. Qi, Y.; Beriot, N.; Gort, G.; Lwanga, E.H.; Gooren, H.; Yang, X.; Geissen, V. Impact of plastic mulch film debris on soil physicochemical and hydrological properties. *Environmental Pollution* **2020**, *266*, 115097.
82. Palanna, A.P.; Sayantan, D. A primary study on the degradation of low-density polyethylene treated with select oxidizing agents and starch. *Journal of Applied Natural Science* **2023**, *15*, 884-889.
83. Bucki, P.; Siwek, P.; Domagała-Świątkiewicz, I.; Puchalski, M. Effect of Agri-Environmental Conditionson the Degradation of Spunbonded Polypropylene Nonwoven with a Photoactivator in Mulched Organically Managed Zucchini. *Fibres Textiles in Eastern Europe* **2018**, 55-60.
84. Qi, Y.; Yang, X.; Pelaez, A.M.; Huerta Lwanga, E.; Beriot, N.; Gertsen, H.; Garbeva, P.; Geissen, V. Macro- and micro-plastics in soil-plant system: Effects of plastic mulch film residues on wheat (Triticum aestivum) growth. *Science of the Total Environment* **2018**, *645*, 1048-1056.
85. Wang, J.; Lv, S.; Zhang, M.; Chen, G.; Zhu, T.; Zhang, S.; Teng, Y.; Christie, P.; Luo, Y. Effects of plastic film residues on occurrence of phthalates and microbial activity in soils. *Chemosphere* **2016**, *151*, 171-177.

86. Sudesh, K.; Abe, H.; Doi, Y. Synthesis, structure and properties of polyhydroxyalkanoates: biological polyesters. *Progress in Polymer Science* **2000**, *25*, 1503-1555.
87. Farah, S.; Anderson, D.G.; Langer, R. Physical and mechanical properties of PLA, and their functions in widespread applications—A comprehensive review. *Advanced Drug Delivery Reviews* **2016**, *107*, 367-392.
88. Jamshidian, M.; Tehrany, E.A.; Imran, M.; Jacquot, M.; Desobry, S. Poly-lactic acid: production, applications, nanocomposites, and release studies. *Comprehensive Reviews in Food Science Food Safety* **2010**, *9*, 552-571.
89. Vallejo, V.R.n.; Smanis, A.; Chirino, E.; Fuentes, D.; Valdecantos, A.; Vilagrosa, A. Perspectives in dryland restoration: approaches for climate change adaptation. *New Forests* **2012**, *43*, 561-579.
90. Bu, L.-d.; Liu, J.-l.; Zhu, L.; Luo, S.-s.; Chen, X.-p.; Li, S.-q.; Hill, R.L.; Zhao, Y. The effects of mulching on maize growth, yield and water use in a semi-arid region. *Agricultural Water Management* **2013**, *123*, 71-78.
91. Gu, X.-B.; Li, Y.-N.; Du, Y.-D. Biodegradable film mulching improves soil temperature, moisture and seed yield of winter oilseed rape (Brassica napus L.). *Soil Tillage Research* **2017**, *171*, 42-50.
92. Sun, T.; Zhang, Z.; Ning, T.; Mi, Q.; Zhang, X.; Zhang, S.; Liu, Z. Colored polyethylene film mulches on weed control, soil conditions and peanut yield. *Plant, Soil and Environment* **2015**, *61*, 79-85.
93. Wang, K.; Sun, X.; Long, B.; Li, F.; Yang, C.; Chen, J.; Ma, C.; Xie, D.; Wei, Y. Green Production of Biodegradable Mulch Films for Effective Weed Control. *ACS Omega* **2021**, *6*, 32327-32333.
94. Minuto, G.; Pisi, L.; Tinivella, F.; Bruzzone, C.; Guerrini, S.; Versari, M.; Pini, S.; Capurro, M. Weed control with biodegradable mulch in vegetable crops. In: International

Symposium on High Technology for Greenhouse System Management: GreenSys 801, Naples (Italy), 4th-6th October, **2007**, 291-298.

95. Benigno, S.M.; Dixon, K.W.; Stevens, J.C. Increasing Soil Water Retention with Native-Sourced Mulch Improves Seedling Establishment in Postmine Mediterranean Sandy Soils. *Restoration Ecology* **2013**, *21*, 617-626.
96. Chen, N.; Li, X.; Šimůnek, J.; Shi, H.; Hu, Q.; Zhang, Y. Evaluating the effects of biodegradable and plastic film mulching on soil temperature in a drip-irrigated field. *Soil Tillage Research* **2021**, *213*, 105116.
97. Zhang, D.; Liu, H.-b.; Hu, W.-l.; Qin, X.-h.; Yan, C.-r.; Wang, H.-y. The status and distribution characteristics of residual mulching film in Xinjiang, China. *Journal of Integrative Agriculture* **2016**, *15*, 2639-2646.
98. Botterell, Z.L.; Beaumont, N.; Dorrington, T.; Steinke, M.; Thompson, R.C.; Lindeque, P.K. Bioavailability and effects of microplastics on marine zooplankton: A review. *Environmental Pollution* **2019**, *245*, 98-110.
99. Hauser, R.; Calafat, A. Phthalates and human health. *Occupational Environmental Medicine* **2005**, *62*, 806-818.
100. Briassoulis, D.; Degli Innocenti, F. Standards for soil biodegradable plastics. In: *Soil degradable bioplastics for a sustainable modern agriculture*; Springer: New York (USA), **2017**; 139-168.
101. Coello, J.; Ameztegui, A.; Rovira, P.; Fuentes, C.; Piqué, M. Innovative soil conditioners and mulches for forest restoration in semiarid conditions in northeast Spain. *Ecological Engineering* **2018**, *118*, 52-65.
102. Shinde, R.; Sarkar, P.K.; Thombare, N. Soil conditioners. *Agriculture Food: e-newsletter* **2019**, *1*, 1-5.
103. Donn, S.; Wheatley, R.E.; McKenzie, B.M.; Loades, K.W.; Hallett, P.D. Improved soil fertility from compost amendment

increases root growth and reinforcement of surface soil on slopes. *Ecological Engineering* **2014**, *71*, 458-465.

104. Deshpande, A.; Kamble, B.; Shinde, R.; Gore, S. Effect of primary treated biomethanated spentwash on soil properties and yield of sunflower (Helianthus annuus L.) on sodic soil. *Communications in Soil Science Plant Analysis* **2012**, *43*, 730-743.
105. Sharma, K.; Shankar, G.M.; Chandrika, D.S.; Grace, J.K.; Sharma, S.; Thakur, H.; Jain, M.; Sharma, R.; Chary, G.R.; Srinivas, K. Effects of conjunctive use of organic and inorganic sources of nutrients on soil quality indicators and soil quality index in sole maize, maize+ soybean, and sole soybean cropping systems in hot semi-arid tropical vertisol. *Communications in Soil Science Plant Analysis* **2014**, *45*, 2118-2140.
106. Gore, S.; Shinde, R.; Belhekar, B. Effect of application of post biomethanated spentwash on the population of phosphate solubilizing bacteria in sodic soil. *Asian Journal of Soil Science* **2011**, *6*, 251-252.
107. James, A.; Sánchez, A.; Prens, J.; Yuan, W. Biochar from agricultural residues for soil conditioning: Technological status and life cycle assessment. *Current Opinion in Environmental Science Health* **2022**, *25*, 100314.
108. Kalita, B.; Bora, S.S.; Gogoi, B. Zeolite: a soil conditioner. *International Journal of Current Microbiology Applied Sciences* **2020**, *9*, 1184-1206.
109. Lentz, R.D. Polyacrylamide and biopolymer effects on flocculation, aggregate stability, and water seepage in a silt loam. *Geoderma* **2015**, *241-242*, 289-294.
110. Somé, Y.S.C.; Traoré, D.; Zoromé, M.; Ouoba, P.A.; Da, D.E.C. Assessment of the effectiveness of potassium polyacrylate on crop production. *Journal of Agricultural Chemistry Environment* **2021**, *10*, 113.
111. Thombare, N.; Mishra, S.; Siddiqui, M.Z.; Jha, U.; Singh, D.; Mahajan, G.R. Design and development of guar gum based

novel, superabsorbent and moisture retaining hydrogels for agricultural applications. *Carbohydrate Polymers* **2018**, *185*, 169-178.

112. Chang, I.; Lee, M.; Tran, A.T.P.; Lee, S.; Kwon, Y.-M.; Im, J.; Cho, G.-C. Review on biopolymer-based soil treatment (BPST) technology in geotechnical engineering practices. *Transportation geotechnics* **2020**, *24*, 100385.
113. Gupta, B.S.; Ako, J.E. Application of guar gum as a flocculant aid in food processing and potable water treatment. *European Food Research Technology* **2005**, *221*, 746-751.
114. Chang, I.; Im, J.; Cho, G.-C. Introduction of Microbial Biopolymers in Soil Treatment for Future Environmentally-Friendly and Sustainable Geotechnical Engineering. *Sustainability* **2016**, *8*, 251-274.
115. Orts, W.J.; Sojka, R.E.; Glenn, G.M.J.I.C.; Products. Biopolymer additives to reduce erosion-induced soil losses during irrigation. *Industrial Crops and Products* **2000**, *11*, 19-29.
116. Chang, I.; Prasidhi, A.K.; Im, J.; Shin, H.-D.; Cho, G.-C. Soil treatment using microbial biopolymers for anti-desertification purposes. *Geoderma* **2015**, *253-254*, 39-47.
117. Bolan, N.; Kunhikrishnan, A.; Thangarajan, R.; Kumpiene, J.; Park, J.; Makino, T.; Kirkham, M.B.; Scheckel, K. Remediation of heavy metal (loid) s contaminated soils–to mobilize or to immobilize? *Journal of Hazardous materials* **2014**, *266*, 141-166.
118. Liu, L.; Chen, H.; Cai, P.; Liang, W.; Huang, Q. Immobilization and phytotoxicity of Cd in contaminated soil amended with chicken manure compost. *Journal of Hazardous materials* **2009**, *163*, 563-567.
119. Doyle, J.; Hamlyn, F. Effects of different cropping systems and of a soil conditioner (VAMA) on some soil physical properties and on growth of tomatoes. *Canadian Journal of Soil Science* **1960**, *40*, 89-98.
120. Nimah, M.; Ryan, J.; Chaudhry, M. Effect of synthetic conditioners on soil water retention, hydraulic conductivity,

porosity, and aggregation. *Soil Science Society of America Journal* **1983**, *47*, 742-745.

121. Sojka, R.; Bjorneberg, D.; Entry, J.; Lentz, R.; Orts, W. Polyacrylamide in agriculture and environmental land management. *Advances in Agronomy* **2007**, *92*, 75-162.
122. Chang, I.; Cho, G.-C. Strengthening of Korean residual soil with β-1,3/1,6-glucan biopolymer. *Construction and Building Materials* **2012**, *30*, 30-35.
123. Khatami, H.R.; O'Kelly, B.C. Improving Mechanical Properties of Sand Using Biopolymers. *Journal of Geotechnical and Geoenvironmental Engineering* **2013**, *139*, 1402-1406.
124. Cabalar, A.F.; Awraheem, M.H.; Khalaf, M.M. Geotechnical Properties of a Low-Plasticity Clay with Biopolymer. *Journal of Materials in Civil Engineering* **2018**, *30*, 04018170.
125. Fatehi, H.; Abtahi, S.M.; Hashemolhosseini, H.; Hejazi, S.M. A novel study on using protein based biopolymers in soil strengthening. *Construction and Building Materials* **2018**, *167*, 813-821.
126. Huang, M.; Zhu, Y.; Li, Z.; Huang, B.; Luo, N.; Liu, C.; Zeng, G. Compost as a Soil Amendment to Remediate Heavy Metal-Contaminated Agricultural Soil: Mechanisms, Efficacy, Problems, and Strategies. *Water, Air, & Soil Pollution* **2016**, *227*.
127. Dearfield, K.L.; Abernathy, C.O.; Ottley, M.S.; Brantner, J.H.; Hayes, P.F. Acrylamide: its metabolism, developmental and reproductive effects, genotoxicity, and carcinogenicity. *Mutation Research-Reviews in Genetic Toxicology* **1988**, *195*, 45-77.
128. Christensen, L.H.; Breiting, V.B.; Aasted, A.; Jørgensen, A.; Kebuladze, I. Long-Term Effects of Polyacrylamide Hydrogel on Human Breast Tissue. *Plastic and Reconstructive Surgery* **2003**, *111*, 1883-1890.
129. Besaratinia, A.; Pfeifer, G.P. DNA adduction and mutagenic properties of acrylamide. *Mutation Research/Genetic Toxicology Environmental Mutagenesis* **2005**, *580*, 31-40.

130. Khachatoorian, R.; Petrisor, I.G.; Kwan, C.-C.; Yen, T.F. Biopolymer plugging effect: laboratory-pressurized pumping flow studies. *Journal of Petroleum Science Engineering* **2003**, *38*, 13-21.
131. Becker, A.; Katzen, F.; Pühler, A.; Ielpi, L. Xanthan gum biosynthesis and application: a biochemical/genetic perspective. *Applied Microbiology and Biotechnology* **1998**, *50*, 145-152.
132. Garcıa-Ochoa, F.; Santos, V.; Casas, J.; Gómez, E. Xanthan gum: production, recovery, and properties. *Biotechnology Advances* **2000**, *18*, 549-579.
133. Berninger, T.; Dietz, N.; Gonzalez Lopez, O. Water-soluble polymers in agriculture: xanthan gum as eco-friendly alternative to synthetics. *Microbial Biotechnology* **2021**, *14*, 1881-1896.
134. Jesus, M.; Mata, F.; Batista, R.A.; Ruzene, D.S.; Albuquerque-Júnior, R.; Cardoso, J.C.; Vaz-Velho, M.; Pires, P.; Padilha, F.F.; Silva, D.P. Corncob as carbon source in the production of xanthan gum in different strains Xanthomonas sp. *Sustainability* **2023**, *15*, 2287.
135. Gils, P.S.; Ray, D.; Sahoo, P.K. Characteristics of xanthan gum-based biodegradable superporous hydrogel. *International Journal of Biological Macromolecules* **2009**, *45*, 364-371.
136. Elella, M.H.A.; Goda, E.S.; Gab-Allah, M.A.; Hong, S.E.; Pandit, B.; Lee, S.; Gamal, H.; Rehman, A.; Yoon, K.R. Xanthan gum-derived materials for applications in environment and eco-friendly materials: A review. *Journal of Environmental Chemical Engineering* **2021**, *9*, 104702.
137. Katzbauer, B.J.P.d.; Stability. Properties and applications of xanthan gum. *Polymer Degradation and Stability* **1998**, *59*, 81-84.
138. Chaturvedi, S.; Kulshrestha, S.; Bhardwaj, K.; Jangir, R. A review on properties and applications of xanthan gum. *Microbial Polymers* **2021**, 87-107.

139. Bueno, V.B.; Bentini, R.; Catalani, L.H.; Petri, D.F. Synthesis and swelling behavior of xanthan-based hydrogels. *Carbohydrate Polymers* **2013**, *92*, 1091-1099.
140. Tao, Y.; Zhang, R.; Xu, W.; Bai, Z.; Zhou, Y.; Zhao, S.; Xu, Y.; Yu, D. Rheological behavior and microstructure of release-controlled hydrogels based on xanthan gum crosslinked with sodium trimetaphosphate. *Food Hydrocolloids* **2016**, *52*, 923-933.
141. Alavarse, A.C.; Frachini, E.C.G.; da Silva, R.L.C.G.; Lima, V.H.; Shavandi, A.; Petri, D.F.S. Crosslinkers for polysaccharides and proteins: Synthesis conditions, mechanisms, and crosslinking efficiency, a review. *International Journal of Biological Macromolecules* **2022**, *202*, 558-596.
142. Berovic, M.; Legisa, M. Citric acid production. *Biotechnology Annual Review* **2007**, *13*, 303-343.
143. Schrieber, R.; Gareis, H. *Gelatine handbook: theory and industrial practice*; John Wiley & Sons: New York, 2007.
144. Ramshaw, J.A.; Glattauer, V. *Biophysical and Chemical Properties of Collagen: Biomedical Applications*; IOP Publishing: Bristol, 2019.
145. Hjelmgaard, T.; Svendsen, J.O.; Kohler, B.; Pawelzyk, P.; Lybye, D.; Schmucker, C.M.; Reiter, P.; Reihmann, M.; Thorsen, P.A. Gelatin-Tannin-Based Greener Binder Technology for Stone Shot and Stone Wool Materials: A Detailed Study. *ACS Omega* **2021**, *6*, 33874-33882.
146. García, M.P.M.; Gómez-Guillén, M.C.; López-Caballero, M.E.; Barbosa-Cánovas, G.V. *Edible films and coatings: fundamentals and applications*; Crc Press: Boca Raton, 2016.
147. Chen, H.; Wang, J.; Cheng, Y.; Wang, C.; Liu, H.; Bian, H.; Pan, Y.; Sun, J.; Han, W. Application of protein-based films and coatings for food packaging: A review. *Polymers* **2019**, *11*, 2039.

148. Quideau, S.; Deffieux, D.; Douat-Casassus, C.; Pouységu, L. Plant polyphenols: chemical properties, biological activities, and synthesis. *Angewandte Chemie International Edition* **2011**, *50*, 586-621.
149. Zhang, X.; Do, M.D.; Casey, P.; Sulistio, A.; Qiao, G.G.; Lundin, L.; Lillford, P.; Kosaraju, S. Chemical cross-linking gelatin with natural phenolic compounds as studied by high-resolution NMR spectroscopy. *Biomacromolecules* **2010**, *11*, 1125-1132.
150. Zhang, X.; Do, M.D.; Casey, P.; Sulistio, A.; Qiao, G.G.; Lundin, L.; Lillford, P.; Kosaraju, S. Chemical modification of gelatin by a natural phenolic cross-linker, tannic acid. *Journal of agricultural food chemistry* **2010**, *58*, 6809-6815.
151. Haslam, E.; Cai, Y. Plant polyphenols (vegetable tannins): gallic acid metabolism. *Natural product reports* **1994**, *11*, 41-66.
152. Peña, C.; De La Caba, K.; Eceiza, A.; Ruseckaite, R.; Mondragon, I. Enhancing water repellence and mechanical properties of gelatin films by tannin addition. *Bioresource Technology* **2010**, *101*, 6836-6842.
153. Strauss, G.; Gibson, S.M. Plant phenolics as cross-linkers of gelatin gels and gelatin-based coacervates for use as food ingredients. *Food Hydrocolloids* **2004**, *18*, 81-89.
154. Selke, S.E.; Wichman, I. Wood fiber/polyolefin composites. *Composites Part A: Applied Science Manufacturing* **2004**, *35*, 321-326.
155. Gowthaman, S.; Nakashima, K.; Kawasaki, S. A State-of-the-Art Review on Soil Reinforcement Technology Using Natural Plant Fiber Materials: Past Findings, Present Trends and Future Directions. *Materials (Basel)* **2018**, *11*.
156. Maslinda, A.; Majid, M.A.; Ridzuan, M.; Afendi, M.; Gibson, A. Effect of water absorption on the mechanical properties of hybrid interwoven cellulosic-cellulosic fibre reinforced epoxy composites. *Composite Structures* **2017**, *167*, 227-237.

157. John, M.J.; Thomas, S. Biofibres and biocomposites. *Carbohydrate Polymers* **2008**, *71*, 343-364.
158. Zakikhani, P.; Zahari, R.; Sultan, M.; Majid, D. Extraction and preparation of bamboo fibre-reinforced composites. *Materials Design* **2014**, *63*, 820-828.
159. Bordoloi, S.; Hussain, R.; Garg, A.; Sreedeep, S.; Zhou, W.-H. Infiltration characteristics of natural fiber reinforced soil. *Transportation geotechnics* **2017**, *12*, 37-44.
160. Bordoloi, S.; Garg, A.; Sreedeep, S. Potential of uncultivated, harmful and abundant weed as a natural geo-reinforcement material. *Advances in Civil Engineering Materials* **2016**, *5*, 276-288.
161. Sykacek, E.; Hrabalova, M.; Frech, H.; Mundigler, N. Extrusion of five biopolymers reinforced with increasing wood flour concentration on a production machine, injection moulding and mechanical performance. *Composites Part A: Applied Science Manufacturing* **2009**, *40*, 1272-1282.
162. Agnantopoulou, E.; Tserki, V.; Marras, S.; Philippou, J.; Panayiotou, C. Development of biodegradable composites based on wood waste flour and thermoplastic starch. *Journal of Applied Polymer Science* **2012**, *126*, 273-281.
163. Asyraf, M.R.M.; Syamsir, A.; Ishak, M.R.; Sapuan, S.M.; Nurazzi, N.M.; Norrrahim, M.N.F.; Ilyas, R.A.; Khan, T.; Rashid, M.Z.A. Mechanical properties of hybrid lignocellulosic fiber-reinforced biopolymer green composites: a review. *Fibers and Polymers* **2023**, *24*, 337-353.
164. Shanmugam, V.; Mensah, R.A.; Försth, M.; Sas, G.; Restás, Á.; Addy, C.; Xu, Q.; Jiang, L.; Neisiany, R.E.; Singha, S. Circular economy in biocomposite development: State-of-the-art, challenges and emerging trends. *Composites Part C: Open Access* **2021**, *5*, 100138.
165. J. Rettenmaier & Söhne Gmbh. Available online: https://www.jrs.de/de/ (accessed on 15th January 2023).

166. STEICO. Available online: https://www.steico.com/it/ (accessed on 15th January 2023).
167. Endrofruit Srl. Available online: https://endofruit.com/idrogea/ (accessed on 14th February 2023).
168. Be-Grow GmbH. Available online: https://be-grow.com/ (accessed on 23rd February 2023).
169. Macosko, C.W. *Rheology principles*; VCH Publishers Inc.: New York (USA), 1994; pp. 1-174.
170. Chang, I.; Im, J.; Prasidhi, A.K.; Cho, G.-C. Effects of Xanthan gum biopolymer on soil strengthening. *Construction and Building Materials* **2015**, *74*, 65-72.
171. Yu, J.; Shi, J.G.; Dang, P.F.; Mamedov, A.I.; Shainberg, I.; Levy, G.J. Soil and Polymer Properties Affecting Water Retention by Superabsorbent Polymers under Drying Conditions. *Soil Science Society of America Journal* **2012**, *76*, 1758-1767.
172. Ni, B.; Liu, M.; Lü, S. Multifunctional slow-release urea fertilizer from ethylcellulose and superabsorbent coated formulations. *Chemical Engineering Journal* **2009**, *155*, 892-898.
173. Maček, M.; Smolar, J.; Petkovšek, A. Extension of measurement range of dew-point potentiometer and evaporation method. In: 18th international conference on soil mechanics and geotechnical engineering, Paris, France, 2013, 1137-1142.
174. Schindler, U.; Durner, W.; von Unold, G.; Mueller, L.; Wieland, R. The evaporation method: Extending the measurement range of soil hydraulic properties using the air-entry pressure of the ceramic cup. *Journal of Plant Nutrition and Soil Science* **2010**, *173*, 563-572.
175. Mudgil, D.; Barak, S.; Khatkar, B.S. Guar gum: processing, properties and food applications—a review. *Journal of Food Science and Technology* **2014**, *51*, 409-418.

176. Osmałek, T.; Froelich, A.; Tasarek, S. Application of gellan gum in pharmacy and medicine. *International Journal of Pharmaceutics* **2014**, *466*, 328-340.
177. Moghal, A.A.B.; Vydehi, K.V. State-of-the-art review on efficacy of xanthan gum and guar gum inclusion on the engineering behavior of soils. *Innovative infrastructure solutions* **2021**, *6*, 1-14.
178. Pan, S.; Ragauskas, A.J. Preparation of superabsorbent cellulosic hydrogels. *Carbohydrate Polymers* **2012**, *87*, 1410-1418.
179. Wan, Y.Z.; Luo, H.; He, F.; Liang, H.; Huang, Y.; Li, X.L. Mechanical, moisture absorption, and biodegradation behaviours of bacterial cellulose fibre-reinforced starch biocomposites. *Composites Science and Technology* **2009**, *69*, 1212-1217.
180. Sreekala, M.S.; Goda, K.; Devi, P.V. Sorption characteristics of water, oil and diesel in cellulose nanofiber reinforced corn starch resin/ramie fabric composites. *Composite Interfaces* **2008**, *15*, 281-299.
181. Oliveira, J.P.; Bruni, G.P.; Lima, K.O.; Halal, S.; Rosa, G.S.D.; Dias, A.R.G.; Zavareze, E.D.R. Cellulose fibers extracted from rice and oat husks and their application in hydrogel. *Food Chemistry* **2017**, *221*, 153-160.
182. Sorze, A.; Valentini, F.; Dorigato, A.; Pegoretti, A. Development of a Xanthan Gum Based Superabsorbent and Water Retaining Composites for Agricultural and Forestry Applications. *Molecules* **2023**, *28*, 1952.
183. Li, Y.; Zhang, D.; Ash, J.; Jia, X.; Leone, A.; Templeton, A. Mechanism and Impact of Excipient Incompatibility: Cross-Linking of Xanthan Gum in Pediatric Powder-for-Suspension Formulations. *Journal of Pharmaceutical Sciences* **2019**, *108*, 3609-3615.
184. Shalviri, A.; Liu, Q.; Abdekhodaie, M.J.; Wu, X.Y. Novel modified starch–xanthan gum hydrogels for controlled drug

delivery: Synthesis and characterization. *Carbohydrate Polymers* **2010**, *79*, 898-907.

185. Wahyono, T.; Astuti, D.A.; Gede Wiryawan, I.K.; Sugoro, I.; Jayanegara, A. Fourier Transform Mid-Infrared (FTIR) Spectroscopy to Identify Tannin Compounds in The Panicle of Sorghum Mutant Lines. *IOP Conference Series: Materials Science and Engineering* **2019**, *546*.
186. Langer, R.S.; Peppas, N.A. Present and future applications of biomaterials in controlled drug delivery systems. *Biomaterials* **1981**, *2*, 201-214.
187. Peppas, N.A. *Hydrogels in medicine and pharmacy*; CRC press: Boca Raton, FL (USA), 1986; Volume 1.
188. Ulu, A.; Birhanlı, E.; Ateş, B. Tunable and tough porous chitosan/β-cyclodextrin/tannic acid biocomposite membrane with mechanic, antioxidant, and antimicrobial properties. *International Journal of Biological Macromolecules* **2021**, *188*, 696-707.
189. Long, J.; Zhang, W.; Zhao, M.; Ruan, C.-Q. The reduce of water vapor permeability of polysaccharide-based films in food packaging: A comprehensive review. *Carbohydrate Polymers* **2023**, *321*, 121267.
190. Bertuzzi, M.A.; Vidaurre, E.C.; Armada, M.; Gottifredi, J. Water vapor permeability of edible starch based films. *Journal of Food Engineering* **2007**, *80*, 972-978.
191. Guilbert, S.; Gontard, N.; Cuq, B. Technology and applications of edible protective films. *Packaging Technology and Science* **1995**, *8*, 339-346.
192. Zhang, S.; Jin, X.; Gu, X.; Chen, C.; Li, H.; Zhang, Z.; Sun, J. The preparation of fully bio-based flame retardant poly (lactic acid) composites containing casein. *Journal of Applied Polymer Science* **2018**, *135*, 46599.
193. Carosio, F.; Di Blasio, A.; Cuttica, F.; Alongi, J.; Malucelli, G. Flame retardancy of polyester and polyester–cotton blends

treated with caseins. *Industrial Engineering Chemistry Research* **2014**, *53*, 3917-3923.

194. Wang, Y.-T.; Zhao, H.-B.; Degracia, K.; Han, L.-X.; Sun, H.; Sun, M.; Wang, Y.-Z.; Schiraldi, D.A. Green approach to improving the strength and flame retardancy of poly (vinyl alcohol)/clay aerogels: incorporating biobased gelatin. *ACS applied materials interfaces* **2017**, *9*, 42258-42265.
195. Zhu, F.; Chen, L.; Feng, Q. Waste gelatin based layer by layer assembly for sustainable solution to cotton fabrics flame retardancy. *Progress in Organic Coatings* **2022**, *163*, 106688.
196. Picchio, M.L.; Linck, Y.G.; Monti, G.A.; Gugliotta, L.M.; Minari, R.J.; Alvarez Igarzabal, C.I. Casein films crosslinked by tannic acid for food packaging applications. *Food Hydrocolloids* **2018**, *84*, 424-434.
197. Wang, Y.T.; Zhao, H.B.; Degracia, K.; Han, L.X.; Sun, H.; Sun, M.; Wang, Y.Z.; Schiraldi, D.A. Green Approach to Improving the Strength and Flame Retardancy of Poly(vinyl alcohol)/Clay Aerogels: Incorporating Biobased Gelatin. *ACS Appl Mater Interfaces* **2017**, *9*, 42258-42265.
198. Talukdar, M.M.; Vinckier, I.; Moldenaers, P.; Kinget, R. Rheological characterization of xanthan gum and hydroxypropylmethyl cellulose with respect to controlled-release drug delivery. *Journal of Pharmaceutical Sciences* **1996**, *85*, 537-540.
199. Agrawal, A.; Rahbar, N.; Calvert, P.D. Strong fiber-reinforced hydrogel. *Acta Biomaterialia* **2013**, *9*, 5313-5318.
200. Barrientos-Sanhueza, C.; Mondaca, P.; Tamayo, M.; Álvaro, J.E.; Díaz-Barrera, A.; Cuneo, I.F. Enhancing the mechanical and hydraulic properties of coarse quartz sand using a water-soluble hydrogel based on bacterial alginate for novel application in agricultural contexts. *Soil Science Society of America Journal* **2021**, *85*, 1880-1893.
201. Serra-Parareda, F.; Tarres, Q.; Mutje, P.; Balea, A.; Campano, C.; Sanchez-Salvador, J.L.; Negro, C.; Delgado-Aguilar, M.

Correlation between rheological measurements and morphological features of lignocellulosic micro/nanofibers from different softwood sources. *International Journal of Biological Macromolecules* **2021**, *187*, 789-799.

202. Shortt, R.; Verhallen, A.; Fisher, P. *Monitoring soil moisture to improve irrigation decisions*; Ministry of Agriculture, Food and Rural Affairs: Canada, 2011; pp. 1-12.
203. Bagheri, P.; Gratchev, I.; Rybachuk, M. Effects of xanthan gum biopolymer on soil mechanical properties. *Applied Sciences* **2023**, *13*, 887.
204. Cabalar, A.F.; Wiszniewski, M.; Skutnik, Z. Effects of xanthan gum biopolymer on the permeability, odometer, unconfined compressive and triaxial shear behavior of a sand. *Soil mechanics foundation engineering* **2017**, *54*, 356-361.
205. Soldo, A.; Miletić, M. Study on shear strength of xanthan gum-amended soil. *Sustainability* **2019**, *11*, 6142.
206. Dehghan, H.; Tabarsa, A.; Latifi, N.; Bagheri, Y. Use of xanthan and guar gums in soil strengthening. *Clean Technologies Environmental Policy* **2019**, *21*, 155-165.
207. Kwon, Y.-M.; Chang, I.; Lee, M.; Cho, G.-C. Geotechnical engineering behavior of biopolymer-treated soft marine soil. *Geomechanics and Engineering* **2019**, *17*, 453-464.
208. Ayeldeen, M.; Negm, A.; El-Sawwaf, M.; Kitazume, M. Enhancing mechanical behaviors of collapsible soil using two biopolymers. *Journal of Rock Mechanics and Geotechnical Engineering* **2017**, *9*, 329-339.
209. Soldo, A.; Miletić, M.; Auad, M.L. Biopolymers as a sustainable solution for the enhancement of soil mechanical properties. *Scientific Reports* **2020**, *10*, 267.
210. Chang, I.; Kwon, Y.-M.; Im, J.; Cho, G.-C. Soil consistency and interparticle characteristics of xanthan gum biopolymer–containing soils with pore-fluid variation. *Canadian Geotechnical Journal* **2019**, *56*, 1206-1213.

211. Chang, I.; Im, J.; Lee, S.-W.; Cho, G.-C. Strength durability of gellan gum biopolymer-treated Korean sand with cyclic wetting and drying. *Construction Building Materials* **2017**, *143*, 210-221.
212. Anandha Kumar, S.; Sujatha, E. Assessing the potential of xanthan gum to modify in-situ soil as baseliners for landfills. *International Journal of Environmental Science Technology* **2022**, *19*, 1-12.
213. Singh, S.P.; Das, R. Geo-engineering properties of expansive soil treated with xanthan gum biopolymer. *Geomechanics Geoengineering* **2020**, *15*, 107-122.
214. Sun, Y.; Holm, P.; Liu, F. Alternate partial root-zone drying irrigation improves fruit quality in tomatoes. *Horticultural Science* **2014**, *41*, 185-191.
215. Perveen, R.; Suleria, H.A.R.; Anjum, F.M.; Butt, M.S.; Pasha, I.; Ahmad, S. Tomato (Solanum lycopersicum) carotenoids and lycopenes chemistry; metabolism, absorption, nutrition, and allied health claims—A comprehensive review. *Critical reviews in food science nutrition* **2015**, *55*, 919-929.
216. Sun, Y.; Tao, C.; Deng, X.; Liu, H.; Shen, Z.; Liu, Y.; Li, R.; Shen, Q.; Geisen, S. Organic fertilization enhances the resistance and resilience of soil microbial communities under extreme drought. *Journal of Advanced Research* **2023**, *47*, 1-12.
217. Sullivan, P. *Drought resistant soils*; ATTRA: Fayetteville (USA), 2000.
218. Robinson, R.K. *Encyclopedia of food microbiology*; Elsevier: London (UK), 2014.
219. Jungbunzlauer Suisse AG. Xanthan gum as soil improver. Available online: https://www.jungbunzlauer.com/en/news/view/xanthan-gum-as-soil-improver (accessed on 24th March 2023).
220. Arifin, S.; Chien, I.-L. Design and control of an isopropyl alcohol dehydration process via extractive distillation using

dimethyl sulfoxide as entrainer. *Industrial & Engineering Chemistry Research* **2008**, *47*, 790-803.

221. Dai, Y.; Li, S.; Meng, D.; Yang, J.; Cui, P.; Wang, Y.; Zhu, Z.; Gao, J.; Ma, Y. Economic and Environmental Evaluation for Purification of Diisopropyl Ether and Isopropyl Alcohol via Combining Distillation and Pervaporation Membrane. *ACS Sustainable Chemistry & Engineering* **2019**, *7*, 20170-20179.
222. de Monaco Lopes, B.; Lopes Lessa, V.; More Silva, B.; Da Silva Carvalho, M.A.; Schnitzler, E.; Lacerda, L.G. Xanthan gum: properties, production conditions, quality and economic perspective. *Journal of Food and Nutrition Research* **2015**, *54*, 185-194.
223. Garcia-Ochoa, F.; Santos, V.E.; Alcon, A. Simulation of xanthan gum production by a chemically structured kinetic model. *Mathematics and Computers in Simulation* **1996**, *42*, 187-195.
224. Grisales Díaz, V.H.; Olivar Tost, G. Energy efficiency of a new distillation process for isopropanol, butanol, and ethanol (IBE) dehydration. *Chemical Engineering and Processing: Process Intensification* **2017**, *112*, 56-61.
225. Garcia-Ochoa, F.; Santos, V.E.; Casas, J.A.; Gomez, E. Xanthan gum: production, recovery and properties. *Biotechnology advances* **2000**, *18*, 549-579.
226. Güngörmüşler, M.; Başınhan, İ.; Üçtuğ, F.G. Optimum formulation determination and carbon footprint analysis of a novel gluten-free pasta recipe using buckwheat, teff, and chickpea flours. *Journal of Food Processing and Preservation* **2020**, *44*, 14701.
227. Guo, C. Energy-economic analysis of ionic liquids extractive-heat pump distillation process for recovery of ethanol and isopropyl alcohol from wastewater. *Separation and Purification Technology* **2021**, *276*, 119338.
228. Shengdong, Z.; Yuanxin, W.; Ziniu, Y.; Haibao, T.; Dachang, C.; Decheng, X. Improving xanthan fermentation in a

mechanically stirred aerated fermenter via external loop. *Research Journal of Microbiology* **2006**, *1*, 70-75.

229. Silman, R.W.; Rogovin, P. Continuous fermentation to produce xanthan biopolymer: effect of dilution rate. *Biotechnology and Bioengineering* **1972**, *14*, 23-31.
230. Szepessy, S.; Thorwid, P. Low Energy Consumption of High-Speed Centrifuges. *Chem Eng Technol* **2018**, *41*, 2375-2384.
231. Hartanto, D.; Handayani, P.A.; Sutrisno, A.; Anugrahani, V.W.; Mustain, A.; Khoiroh, I. Isopropyl Alcohol Purification through Extractive Distillation using Glycerol as an Entrainer: Technical Performances Simulation and Design. *Jurnal Bahan Alam Terbarukan* **2019**, *8*, 133-143.
232. Katzbauer, B. Properties and applications of xanthan gum. *Polymer degradation and Stability* **1998**, *59*, 81-84.
233. Letisse, F.; Chevallerau, P.; Simon, J.-L.; Lindley, N. The influence of methabolic network structures and energy requirements on xanthan gum yields. *Journal of Biotechnology* **2002**, *99*, 307-317.
234. Lo, Y.-M.; Yang, S.-T.; Min, D.B. Ultrafiltration of xanthan gum fermentation broth: process and economic analyses. *Journal of food engineering* **1997**, *31*, 219-236.
235. Ding, T.; Bianchi, S.; Ganne-Chédeville, C.; Kilpeläinen, P.; Haapala, A.; Räty, T. Life cycle assessment of tannin extraction from spruce bark. *iForest - Biogeosciences and Forestry* **2017**, *10*, 807-814.
236. Xu, X.; Jayaraman, K.; Morin, C.; Pecqueux, N. Life cycle assessment of wood-fibre-reinforced polypropylene composites. *Journal of Materials Processing Technology* **2008**, *198*, 168-177.
237. Zhang, X.; Do, M.D.; Casey, P.; Sulistio, A.; Qiao, G.G.; Lundin, L.; Lillford, P.; Kosaraju, S. Chemical modification of gelatin by a natural phenolic cross-linker, tannic acid. *Journal of Agricultural and Food Chemistry* **2010**, *58*, 6809-6815.

238. Luo, H.; Liang, K.; Li, W.; Li, Y.; Xia, M.; Xu, C. Comparison of Pressure-Swing Distillation and Extractive Distillation Methods for Isopropyl Alcohol/Diisopropyl Ether Separation. *Industrial & Engineering Chemistry Research* **2014**, *53*, 15167-15182.
239. Ahmad, T.; Ismail, A.; Ahmad, S.A.; Khalil, K.A.; Kee, L.T.; Awad, E.A.; Adeyemi, K.D.; Sazili, A.Q. Autolysis of bovine skin, its endogenous proteases, protease inhibitors and their effects on quality characteristics of extracted gelatin. *Food Chem* **2018**, *265*, 1-8.
240. Alipal, J.; Mohd Pu'ad, N.A.S.; Lee, T.C.; Nayan, N.H.M.; Sahari, N.; Basri, H.; Idris, M.I.; Abdullah, H.Z. A review of gelatin: Properties, sources, process, applications, and commercialisation. *Materials Today: Proceedings* **2021**, *42*, 240-250.
241. Ahmad, T.; Ismail, A.; Ahmad, S.A.; Khalil, K.A.; Kee, L.T.; Awad, E.A.; Sazili, A.Q. Extraction, characterization and molecular structure of bovine skin gelatin extracted with plant enzymes bromelain and zingibain. *Journal of food science technology* **2020**, *57*, 3772-3781.
242. Murphy, F.; Devlin, G.; McDonnell, K. Greenhouse gas and energy based life cycle analysis of products from the Irish wood processing industry. *Journal of Cleaner Production* **2015**, *92*, 134-141.
243. Sampaio, A.P.C.; de Sá M. de Sousa Filho, M.; Castro, A.L.A.; de Figueirêdo, M.C.B. Life cycle assessment from early development stages: the case of gelatin extracted from tilapia residues. *The International Journal of Life Cycle Assessment* **2016**, *22*, 767-783.
244. Sanchez, A.; Ramirez, M.E.; Torres, L.G.; Galindo, E. Characterization of xanthans from xanthomonas strains cultivated under constant dissolved oxygen. *World Journal of Microbiology & Biotechnology* **1997**, *13*, 443-451.

245. Skinner, C.; Stefanowski, B.K.; Heathcote, D.; Charlton, A.; Ormondroyd, G.A. Life cycle assessment of pilot-scale wood fibre production using mechanical disc refining at different pressures. *International Wood Products Journal* **2016**, *7*, 149-155.
246. Gestore Mercati Energetici (GME). Available online: https://www.mercatoelettrico.org/it/ (accessed on 20th February 2023).
247. Saint-Michel F; Chazeau L; Cavaillé JY; E, C. Mechanical properties of high density polyurethane foams: I. Effect of the density. *Composites Science and Technology* **2006**, *66*, 2700-2708.
248. Zhang, H.; Fang, W.Z.; Li, Y.M.; Tao, W.Q. Experimental study of the thermal conductivity of polyurethane foams. *Applied Thermal Engineering* **2017**, *115*, 528-538.
249. Gama, N.V.; Ferreira, A.; Barros-Timmons, A. Polyurethane foams: Past, present, and future. *Materials* **2018**, *11*, 1841-1876.
250. Ates, M.; Karadag, S.; Eker, A.A.; Eker, B. Polyurethane foam materials and their industrial applications. *Polymer International* **2022**, *71*, 1157-1163.
251. Galvagnini, F.; Dorigato, A.; Valentini, F.; Fiore, V.; La Gennusa, M.; Pegoretti, A. Multifunctional polyurethane foams with thermal energy storage/release capability. *Journal of Thermal Analysis and Calorimetry* **2022**, *147*, 297-313.
252. Galvagnini, F.; Valentini, F.; Dorigato, A. Development of polymeric insulating foams for low-temperature thermal energy storage applications. *Journal of Applied Polymer Science* **2022**, *139*, 1-11.
253. Quadrini, F.; Bellisario, D.; Santo, L. Recycling of thermoset polyurethane foams. *Polymer Engineering & Science* **2013**, *53*, 1357-1363.
254. Magnin, A.; Entzmann, L.; Bazin, A.; Pollet, E.; Avérous, L. Green Recycling Process for Polyurethane Foams by a Chem-Biotech Approach. *Chemistry Europe* **2021**, *14*, 4234-4241.
255. Beran, R.; Zarybnicka, L.; Machova, D. Recycling of rigid polyurethane foam: Micro-milled powder used as active filler

in polyurethane adhesives. *Journal of Applied Polymer Science* **2020**, *137*, 49095-49106.

256. Mougel, C.; Garnier, T.; Cassagnau, P.; Sintes-Zydowicz, N. Phenolic foams: A review of mechanical properties, fire resistance and new trends in phenol substitution. *Polymer* **2019**, *164*, 86-117.
257. Drozdov, A.; Claville, C. The effect of porosity on elastic moduli of polymer foams. *Journal of Applied Polymer Science* **2020**, *137*, 1-10.
258. Papadopoulos, A.M. State of the art in thermal insulation materials and aims for future developments. *Energy and buildings* **2005**, *37*, 77-86.
259. Trovati, G.; Sanches, E.A.; Neto, S.C.; Mascarenhas, Y.P.; Chierice, G.O. Characterization of Polyurethane Resins by FTIR, TGA, and XRD. *Journal of Applied Polymer Science* **2010**, *115*, 263-268.
260. Sui, X.; Wang, Z. Flame-retardant and mechanical properties of phenolic foams toughened with polyethylene glycol phosphates. *Polymers for advanced technologies* **2013**, *24*, 593-599.
261. Schartel, B.; Hull, T.R. Development of fire-retarded materials. Interpretation of cone calorimeter data. *Fire and Materials* **2007**, *31*, 327-354.
262. Hidalgo, J.P.; Torero, J.L.; Welch, S. Fire performance of charring closed-cell polymeric insulation materials: Polyisocyanurate and phenolic foam. *Fire and Materials* **2018**, *41*, 358-373.
263. Tang, K.; He, X.; Xu, G.; Tang, X.; Ge, T.; Zhang, A. Effect of formaldehyde to phenol molar ratio on combustion behavior of phenolic foam. *Polymer Testing* **2022**, *111*, 107626-107634.
264. Babrauskas, V.; Peacock, R.D. Heat release rate: the single most important variable in fire hazard. *Fire safety journal* **1992**, *18*, 255-272.

265. Corigliano, A.; Rizzi, E.; Papa, E. Experimental characterization and numerical simulations of a syntactic-foam/glass-fibre composite sandwich. *Composites Science and Technology* **2000**, *60*, 2169-2180.
266. Pareta, A.S.; Gupta, R.; Panda, S.K. Experimental investigation on fly ash particulate reinforcement for property enhancement of PU foam core FRP sandwich composites. *Composites Science and Technology* **2020**, *195*, 108207.
267. Castellón, C.; Medrano, M.; Roca, J.; Cabeza, L.F.; Navarro, M.E.; Fernández, A.I.; Lázaro, A.; Zalba, B. Effect of microencapsulated phase change material in sandwich panels. *Renewable Energy* **2010**, *35*, 2370-2374.
268. Hasse, C.; Grenet, M.; Bontemps, A.; Dendievel, R.; Sallée, H. Realization, test and modelling of honeycomb wallboards containing a Phase Change Material. *Energy and buildings* **2011**, *43*, 232-238.
269. Pielichowska, K.; Pielichowski, K. Phase change materials for thermal energy storage. *Progress in Materials Science* **2014**, *65*, 67-123.
270. Yadav, M.; Pasarkar, N.; Naikwadi, A.; Mahanwar, P. A review on microencapsulation, thermal energy storage applications, thermal conductivity and modification of polymeric phase change material for thermal energy storage applications. *Polymer Bulletin* **2022**, *80*, 5897-5927.
271. Mahajan, U.R.; Emmanuel, I.; Rao, A.S.; Mhaske, S.T. Development of rigid polyurethane foam incorporating phase change material for a low-temperature thermal energy storage application. *Polymer International* **2023**, *72*, 490-499.
272. Nandy, A.; Houl, Y.; Zhao, W.; D'Souza, N.A. Thermal heat transfer and energy modeling through incorporation of phase change materials (PCMs) into polyurethane foam. *Renewable and Sustainable Energy Reviews* **2023**, *182*, 113410.

273. Vatankhah, E.; Abasnezhad, M.; Nazerian, M.; Barmar, M.; Partovinia, A. Thermal energy storage and mechanical performance of composites of rigid polyurethane foam and phase change material prepared by one-shot synthesis method. *Journal of Polymer Research* **2022**, *29*, 1-11.
274. Sarkar, S.; Mestry, S.; Mhaske, S.T. Developments in phase change material (PCM) doped energy efficient polyurethane (PU) foam for perishable food cold-storage applications: A review. *Journal of Energy Storage* **2022**, *50*, 104620.
275. Naikwadi, A.T.; Samui, A.B.; Mahanwar, P.A. Fabrication and experimental investigation of microencapsulated eutectic phase change material-integrated polyurethane sandwich tin panel composite for thermal energy storage in buildings. *International Journal of Energy Research* **2021**, *45*, 20783-20794.
276. Ikutegbe, C.A.; Farid, M.M. Application of phase change material foam composites in the built environment: A critical review. *Renewable and Sustainable Energy Reviews* **2020**, *131*, 110008.
277. Amaral, C.; Pinto, S.C.; Silva, T.; Mohseni, F.; Amaral, J.S.; Amaral, V.S.; Marques, P.A.A.P.; Barros-Timmons, A.; Vicente, R. Development of polyurethane foam incorporating phase change material for thermal energy storage. *Journal of Energy Storage* **2020**, *28*, 101177.
278. Amaral, C.; Vicente, R.; Ferreira, V.M.; Silva, T. Polyurethane foams with microencapsulated phase change material: Comparative analysis of thermal conductivity characterization approaches. *Energy and buildings* **2017**, *153*, 392-402.
279. Yang, C.; Fischer, L.; Maranda, S.; Worlitschek, J. Rigid polyurethane foams incorporated with phase change materials: A state-of-the-art review and future research pathways. *Energy and buildings* **2015**, *87*, 25-36.
280. Galvagnini, F.; Dorigato, A.; Valentini, F.; Fiore, V.; La Gennusa, M.; Pegoretti, A. Multifunctional polyurethane

foams with thermal energy storage/release capability. *Journal of Thermal Analysis and Calorimetry* **2020**, *147*, 297-313.

281. Fredi, G.; Dorigato, A.; Fambri, L.; Pegoretti, A. Multifunctional structural composites for thermal energy storage. *Multifunctional Materials* **2020**, *3*, 042001.
282. Fredi, G.; Dorigato, A.; Fambri, L.; Pegoretti, A. Evaluating the multifunctional performance of structural composites for thermal energy storage. *Polymers* **2021**, *13*, 3108.
283. Umate, T.B.; Sawarkar, P.D. A review on thermal energy storage using phase change materials for refrigerated trucks: Active and passive approaches. *Journal of Energy Storage* **2024**, *75*, 109704.
284. Selvnes, H.; Allouche, Y.; Manescu, R.I.; Hafner, A. Review on cold thermal energy storage applied to refrigeration systems using phase change materials. *Thermal Science and Engineering Progress* **2021**, *22*, 100807.
285. Roy, A.; Kale, S.; Lingayat, A.B.; Sur, A.; Arun, S.; Sengar, D.; Gawade, S.; Wavhal, A. Evaluating energy-saving potential in micro-cold storage units integrated with phase change material. *Journal of the Brazilian Society of Mechanical Sciences and Engineering* **2023**, *45*, 1-25.
286. Fioretti, R.; Principi, P.; Copertaro, B. A refrigerated container envelope with a PCM (Phase Change Material) layer: Experimental and theoretical investigation in a representative town in Central Italy. *Energy Conversion and Management* **2016**, *122*, 131-141.
287. Kuhn, J.; Ebert, H.-P.; Arduini-Schuster, M.; Büttner, D.; Fricke, J. Thermal transport in polystyrene and polyurethane foam insulations. *International journal of heat mass transfer* **1992**, *35*, 1795-1801.
288. Serrano, A.; Borreguero, A.M.; Garrido, I.; Rodríguez, J.F.; Carmona, M. The role of microstructure on the mechanical properties of polyurethane foams containing

thermoregulating microcapsules. *Polymer Testing* **2017**, *60*, 274-282.

289. Gaidukovs, S.; Gaidukova, G.; Ivdre, A.; Cabulis, U. Viscoelastic and Thermal Properties of Polyurethane Foams Obtained from Renewable and Recyclable Components. *Journal of Renewable Materials* **2018**, *6*, 755-763.
290. You, M.; Zhang, X.-x.; Wang, X.-c.; Zhang, L.; Wen, W. Effects of type and contents of microencapsuled n-alkanes on properties of soft polyurethane foams. *Thermochimica Acta* **2010**, *500*, 69-75.
291. Berardi, U. The impact of aging and environmental conditions on the effective thermal conductivity of several foam materials. *Energy* **2019**, *182*, 777-794.
292. Zhang, X.X.; Fan, Y.F.; Tao, X.M.; Yick, K.I. Crystallization and prevention of supercooling of microencapsulated n-alkanes. *Journal of Colloid Interface Science* **2005**, *281*, 299-306.
293. Gama, N.V.; Ferreira, A.; Barros-Timmons, A. Polyurethane Foams: Past, Present, and Future. *Materials (Basel)* **2018**, *11*.
294. Kabakci, E.; Sayer, G.; Suvaci, E.; Uysal, O.; Güler, İ.; Kaya, M. Processing-structure-property relationship in rigid polyurethane foams. *Journal of Applied Polymer Science* **2017**, *134*, 44870.
295. Zhang, H.; Fang, W.-Z.; Li, Y.-M.; Tao, W.-Q. Experimental study of the thermal conductivity of polyurethane foams. *Applied Thermal Engineering* **2017**, *115*, 528-538.
296. Mane, J.V.; Chandra, S.; Sharma, S.; Ali, H.; Chavan, V.M.; Manjunath, B.S.; Patel, R.J. Mechanical Property Evaluation of Polyurethane Foam under Quasi-static and Dynamic Strain Rates- An Experimental Study. *Procedia Engineering* **2017**, *173*, 726-731.
297. Steeves, C.A.; Fleck, N.A. Collapse mechanisms of sandwich beams with composite faces and a foam core, loaded in three-point bending. Part II: experimental investigation and

numerical modelling. *International Journal of Mechanical Sciences* **2004**, *46*, 585-608.

298. Junaedi, H.; Khan, T.; Sebaey, T.A. Characteristics of Carbon-Fiber-Reinforced Polymer Face Sheet and Glass-Fiber-Reinforced Rigid Polyurethane Foam Sandwich Structures under Flexural and Compression Tests. *Materials (Basel)* **2023**, *16*, 5101.
299. Mamalis, A.G.; Manolakos, D.E.; Ioannidis, M.B.; Papapostolou, D.P. On the crushing response of composite sandwich panels subjected to edgewise compression: experimental. *Composite Structures* **2005**, *71*, 246-257.

Scientific production

(Updated to August 30th, 2024)

From Master's thesis work:

- Sorze, A; Valentini, F; Dorigato, A; Pegoretti, A. Salt leaching as a green method for the production of polyethylene foams for thermal energy storage applications. *Polymer Engineering and Science*, **2022**, 62 (5), 1650-1663.

From PhD's thesis work:

Published

- Sorze, A; Valentini, F; Dorigato, A; Pegoretti, A. Development of a xanthan gum based superabsorbent and water retaining composites for agricultural and forestry applications. *Molecules*, **2023**, 28 (4), 1952.
- Sorze, A; Valentini, F; Smolar, J; Logar, J; Pegoretti, A; Dorigato, A. Effect of different cellulose fillers on the properties of xanthan-based composites for soil conditioning applications. *Materials*, **2023**, 16 (23), 7285.
- Fortuna, B; Logar, J; Sorze, A; Valentini, F; Smolar, J. Influence of xanthan gum-based soil conditioners on the geotechnical properties of soils. *Applied Sciences*, **2024**, 14, 4044.
- Sorze, A; Valentini, F; Burin Mucignat, M; Pegoretti, A; Dorigato, A. Multifunctional xanthan gum/wood fibers based hydrogels as novel topsoil covers for forestry and agricultural applications. *Carbohydrate Polymer Technologies and Applications*, **2024**, 7, 100520.
- Fortuna, B; Logar, J; Sorze, A; Valentini, F; Maček, M; Pulko, B; Smolar, J. Reducing drought vulnerability of forest soils

using Xanthan gum-based soil conditioners, *Heliyon,* **2024,** *10*, e39974.

Submitted

- Valentini, F; Sorze, A; Coello, J; Chowdhury, A.A; Piergiacomo, F; Casapiccola, G; Brusetti, L; Bösing, J, Hirschmüller, S; Dorigato, A. Xanthan- and gelatin-based composites used as nursery groundcovers: assessment of soil microbiology and seedling performance, **submitted to** *Sustainability*.
- Auriemma, S; Chowdhury, A.A; Sorze, A; Valentini, F; Piergiacomo, F; Dorigato, A; Brusetti, L. Wood-derived Topsoil Cover Positively Influences the Diversity and Activity of Tomato Plant Rhizobacteria, **submitted to** *Environmental Technology & Innovation*.

In preparation

- Sorze, A; Valentini, F; Nardin, T; Larcher, R; Bösing, J, Hirschmüller, S; Dorigato, A; Pegoretti, A. Influence of the application of different bio-based mulching films and soil conditioners on a non-irrigated tomato planting trial.
- Bösing, J; Sorze, A; Hirschmüller, S. Cross-linked gelatine as binder in wood-fiber composites for topsoil protection.
- Sorze, A; Bösing, J; Hirschmüller, S; Dorigato, A. Investigation of the flame behaviour and thermal degradation of gelatin- and xanthan-based wood fibers composites used as topsoil covers for forestry applications.

From the side research activities:

- Simonini, L; Sorze, A; Maddalena, L; Carosio, F; Dorigato, A. Mechanical reprocessing of polyurethane and phenolic foams to increase the sustainability of thermal insulation materials. *Polymer Testing*, **2024**, 138, 108539.

- Fredi, G; Boso, E.; Sorze, A; Pegoretti, A. Multifunctional sandwich composites with optimized phase change material content for simultaneous structural and thermal performance. *Composites Part A*, **2024**, 186, 108382.

Awards

(Updated to August 30th, 2024)

Macrogiovani 2023 AIM – Best Oral Presentation Award - "Development of superabsorbent xanthan-based hydrogel composites for forestry and agricultural application". Associazione Italiana di Scienza e Tecnologia delle Macromolecole (AIM), June 21st - 23rd 2023, Catania (Italy).

Participation to Congress and Schools

(Updated to September 30th, 2024)

National congress contributions

- Sorze A, Valentini F, Dorigato A, Pegoretti A. **"Development of polyethylene foams through salt leaching method for thermal energy storage applications"**. Associazione Italiana di Ingegneria dei Materiali (AIMAT), September 15-19th 2021, Cagliari (Italy).
- Sorze A, Valentini F, Dorigato A, Pegoretti A. **"Development of polyethylene foams for thermal energy storage applications through salt leaching method"**. National Interuniversity Consortium of Materials Science and Technology (INSTM), January 23-26th 2022, Sestriere (Italy).
- Sorze A, Valentini F, Dorigato A, Pegoretti A. **"Novel biodegradable hydrogel composites to promote plant growth and forest protection"**. Associazione Italiana di

Scienza e Tecnologia delle Macromolecole (AIM), September 4-7th 2022, Trento (Italy).

- Sorze A, Valentini F, Dorigato A, Pegoretti A. **"Development of biodegradable hydrogels for plant growth and forest protection".** Consorzio Interuniversitario Nazionale per la Scienza e Tecnologia dei Materiali (INSTM), January 22-25th 2023, Bressanone (Italy).
- Sorze A, Valentini F, Dorigato A, Pegoretti A. **"Development of superabsorbent xanthan-based hydrogel composites for forestry and agricultural application"**. Associazione Italiana di Scienza e Tecnologia delle Macromolecole (AIM - Macrogiovani), June 21-23th 2023, Catania (Italy).
- Sorze A, Valentini F, Smolar J, Logar J, Pegoretti A, Dorigato A. **"Investigation of the effects of cellulose fillers on the properties of xanthan-based soil conditioners"**. Associazione Italiana di Scienza e Tecnologia delle Macromolecole (AIM - Macrogiovani), June 12-13th 2024, Rimini (Italy).
- Sorze A, Valentini F, Pegoretti A, Dorigato A. **"Xanthan/wood fibers based hydrogels for the production of multifunctional topsoil covers"**. Associazione Italiana di Scienza e Tecnologia delle Macromolecole (AIM), September 8-11th 2024, Napoli (Italy).

International congress contributions

- Sorze A, Valentini F, Dorigato A, Pegoretti A. **"Evaluation of salt leaching method for the production of polyolefin foams for thermal energy storage applications"**. Times of Polymer and Composites (TOP), September 5-9th 2021, Ischia (Italy).
- Sorze A, Fredi G, Dorigato A, Pegoretti A. **"Novel xanthan-based hydrogel composites to promote plant growth and**

forest protection". Milan polymers days (MIPOL), June 19-21th 2022, Milan (Italy).

- Sorze A, Fredi G, Dorigato A, Pegoretti A. **"Novel biopolymer-based composites as soil conditioners to promote plant growth and forest protection".** European Polymer Congress (EPF), 26th June -01st July 2022, Prague (Czechia).
- Sorze A, Valentini F, Dorigato A, Pegoretti A. **"Novel superabsorbent xanthan-based hydrogel composites for forestry application"**. Times of Polymer and Composites (TOP), June 11-15th 2023, Ischia (Italy).
- Sorze A, Valentini F, Dorigato A, Pegoretti A. **"Novel biodegradable xanthan-based hydrogels to promote plant growth and forest protection"**. International Conference on Composite Materials (ICCM), August 1-6th 2023, Belfast (Northern Ireland).
- Sorze A, Valentini F, Pegoretti A, Dorigato A. **"Development of xanthan-based bio-composites for the production of topsoil covers"**. European Conference on Composite Materials (ECCM), July 2-5th 2024, Nantes (France).

Summer school

21th AIMAT School "**I Materiali nella Transizione Energetica**". AIMAT, July 13-16th 2022, Ischia (Italy).

22th AIMAT School "**Intelligenza Materiale: dagli Smart Materials all'Intelligenza Artificiale**". AIMAT, July 14-17th 2024, Ischia (Italy).

Visiting period abroad

(Updated to August 30th, 2024)

Visiting PhD Student at the University of Applied Sciences - Rosenheim (Germany) from 15/02/2024 to 15/05/2024.

Teaching activities

(Updated to August 30th, 2024)

- Tutor activity for the laboratory part of the course of "**Polymeric and composite materials engineering – mod. 1 Polymeric materials**" during the second semester of the A.Y. 2023-24, Master Degree in Materials engineering, University of Trento, Department of Industrial Engineering.
- Tutor activity for the laboratory part of the course of "**Polymeric and composite materials engineering – mod. 2 Composite materials**" during the second semester of the A.Y. 2023-24, Master Degree in Materials engineering, University of Trento, Department of Industrial Engineering.